



HAL
open science

Modelling and experimental analysis of a geothermal ventilated foundation

Kevin Taurines

► **To cite this version:**

Kevin Taurines. Modelling and experimental analysis of a geothermal ventilated foundation. Civil Engineering. Université de Lyon, 2017. English. NNT : 2017LYSEI100 . tel-01940870

HAL Id: tel-01940870

<https://theses.hal.science/tel-01940870>

Submitted on 30 Nov 2018

HAL is a multi-disciplinary open access archive for the deposit and dissemination of scientific research documents, whether they are published or not. The documents may come from teaching and research institutions in France or abroad, or from public or private research centers.

L'archive ouverte pluridisciplinaire **HAL**, est destinée au dépôt et à la diffusion de documents scientifiques de niveau recherche, publiés ou non, émanant des établissements d'enseignement et de recherche français ou étrangers, des laboratoires publics ou privés.



N°d'ordre NNT
2017LYSEI100

THESE de DOCTORAT DE L'UNIVERSITE DE LYON

opérée au sein de

L'Institut National des Sciences Appliquées de Lyon

Ecole Doctorale N° 162

Mécanique, Energétique, Génie civil, Acoustique

Spécialité/ discipline de doctorat :

Génie civil

Soutenue publiquement le 26/10/2017, par :

Kevin TAURINES

Modelling and experimental analysis of a geothermal ventilated foundation

Devant le jury composé de :

| | | |
|---------------------------|---|------------------------|
| Ghiaus, Christian | Professeur à l'INSA de Lyon | Président |
| Woloszyn, Monika | Professeure à l'Univ. Savoie Mont-Blanc | Rapporteuse |
| Fossa, Marco | Professeur à l'Univ. de Gènes (Italie) | Rapporteur |
| Janssen, Hans | Professeur à l'Univ. KU Leuven (Belgique) | Examineur |
| Gan, Guohui | Maître de conférences à l'Univ. de Nottingham (Royaume-Uni) | Examineur |
| Ménézo, Christophe | Professeur à l'Univ. Savoie Mont-Blanc | Directeur de thèse |
| Giroux--Julien, Stéphanie | Maître de conférences HDR à l'UCBL | Co Directrice de thèse |

Département FEDORA – INSA Lyon - Ecoles Doctorales – Quinquennal 2016-2020

| SIGLE | ECOLE DOCTORALE | NOM ET COORDONNEES DU RESPONSABLE |
|------------------|--|---|
| CHIMIE | <p>CHIMIE DE LYON http://www.edchimie-lyon.fr</p> <p>Sec : Renée EL MELHEM Bat Blaise Pascal 3^e etage secretariat@edchimie-lyon.fr Insa : R. GOURDON</p> | <p>M. Stéphane DANIELE Institut de Recherches sur la Catalyse et l'Environnement de Lyon IRCELYON-UMR 5256 Equipe CDFA 2 avenue Albert Einstein 69626 Villeurbanne cedex directeur@edchimie-lyon.fr</p> |
| E.E.A. | <p>ELECTRONIQUE, ELECTROTECHNIQUE, AUTOMATIQUE http://edeea.ec-lyon.fr</p> <p>Sec : M.C. HAVGOUDOUKIAN Ecole-Doctorale.eea@ec-lyon.fr</p> | <p>M. Gérard SCORLETTI Ecole Centrale de Lyon 36 avenue Guy de Collongue 69134 ECULLY Tél : 04.72.18 60.97 Fax : 04 78 43 37 17 Gerard.scorletti@ec-lyon.fr</p> |
| E2M2 | <p>EVOLUTION, ECOSYSTEME, MICROBIOLOGIE, MODELISATION http://e2m2.universite-lyon.fr</p> <p>Sec : Sylvie ROBERJOT Bât Atrium - UCB Lyon 1 04.72.44.83.62 Insa : H. CHARLES secretariat.e2m2@univ-lyon1.fr</p> | <p>M. Fabrice CORDEY CNRS UMR 5276 Lab. de géologie de Lyon Université Claude Bernard Lyon 1 Bât Géode 2 rue Raphaël Dubois 69622 VILLEURBANNE Cédex Tél : 06.07.53.89.13 cordey@univ-lyon1.fr</p> |
| EDISS | <p>INTERDISCIPLINAIRE SCIENCES-SANTE http://www.ediss-lyon.fr</p> <p>Sec : Sylvie ROBERJOT Bât Atrium - UCB Lyon 1 04.72.44.83.62 Insa : M. LAGARDE secretariat.ediss@univ-lyon1.fr</p> | <p>Mme Emmanuelle CANET-SOULAS INSERM U1060, CarMeN lab, Univ. Lyon 1 Bâtiment IMBL 11 avenue Jean Capelle INSA de Lyon 696621 Villeurbanne Tél : 04.72.68.49.09 Fax : 04 72 68 49 16 Emmanuelle.canet@univ-lyon1.fr</p> |
| INFOMATHS | <p>INFORMATIQUE ET MATHEMATIQUES http://edinfomaths.universite-lyon.fr</p> <p>Sec : Renée EL MELHEM Bat Blaise Pascal, 3^e étage Tél : 04.72. 43. 80. 46 Fax : 04.72.43.16.87 infomaths@univ-lyon1.fr</p> | <p>M. Luca ZAMBONI Bâtiment Braconnier 43 Boulevard du 11 novembre 1918 69622 VILLEURBANNE Cedex Tél : 04 26 23 45 52 zamboni@maths.univ-lyon1.fr</p> |
| Matériaux | <p>MATERIAUX DE LYON http://ed34.universite-lyon.fr</p> <p>Sec : Marion COMBE Tél:04-72-43-71-70 -Fax : 87.12 Bat. Direction ed.materiaux@insa-lyon.fr</p> | <p>M. Jean-Yves BUFFIERE INSA de Lyon MATEIS Bâtiment Saint Exupéry 7 avenue Jean Capelle 69621 VILLEURBANNE Cedex Tél : 04.72.43 71.70 Fax 04 72 43 85 28 Ed.materiaux@insa-lyon.fr</p> |
| MEGA | <p>MECANIQUE, ENERGETIQUE, GENIE CIVIL, ACOUSTIQUE http://edmega.universite-lyon.fr/</p> <p>Sec : Marion COMBE Tél:04-72-43-71-70 -Fax : 87.12 Bat. Direction mega@insa-lyon.fr</p> | <p>M. Philippe BOISSE INSA de Lyon Laboratoire LAMCOS Bâtiment Jacquard 25 bis avenue Jean Capelle 69621 VILLEURBANNE Cedex Tél : 04.72 .43.71.70 Fax : 04 72 43 72 37 Philippe.boisse@insa-lyon.fr</p> |
| ScSo | <p>ScSo* http://ed483.univ-lyon2.fr/ Sec : Viviane POLSINELLI Brigitte DUBOIS Insa : J.Y. TOUSSAINT Tél : 04 78 69 72 76 viviane.polsinelli@univ-lyon2.fr</p> | <p>M. Christian MONTES Université Lyon 2 86 rue Pasteur 69365 LYON Cedex 07 Christian.montes@univ-lyon2.fr</p> |

*ScSo : Histoire, Géographie, Aménagement, Urbanisme, Archéologie, Science politique, Sociologie, Anthropologie

ACKNOWLEDGMENTS

More than 3 years and a half of hard-work, this thesis was the results of sharing, discussions and amazing encounters, otherwise it wouldn't be possible.

I first would like to warmly thank my supervisors, Professor Christophe Ménézo and Stéphanie Giroux--Julien. They trusted me all along and did handle my stubborn nature. It was for me a great opportunity to develop my own thinking and approach for solving a complex problem. I wish to thank Professor Monika Woloszyn and Professor Marco Fossa for their interest in my work and for being my reviewers. I also thank my examiners Professor Christian Giauss, Guohui Gan and Professor Hans Janssen for the relevance of their questions about my work. I especially thank Professor Monika Woloszyn and Professor Hans Janssen. I highly appreciated your availability, your kindness and your skills. The very interesting scientific exchanges we had about heat and moisture transfers numerical modelling helped me a lot.

This work wouldn't be possible without advice of skilled and attentive colleagues from CETHIL: my thanks go to Professor Shihe Xin, Abdlekrim Trabelsi and Gilles Russaouën. I especially thank Serge Buathier who made a very nice job with the experimental facilities setting up. Without him, I would still be wrapped with my sensor wires.

A part of this work was carried out from New Zealand, 'The land of the long white cloud'. Many thanks Kévyne Johannes and Christophe Ménézo who gave me this amazing opportunity. My thanks also go to Professor Mohammed Farid who supervised me during this stay. I would never forget the Persian guys who welcomed me in this beautiful country, Reza, Samira and my roommate Nima. Nima, keep on playing târ! You are not from NZ but I met you there and I don't forget you: Luisa, Yoram, thank you!

Huge thanks to all the CETHIL PhD students and friends who shared this experience with me. Adrien, Ankita, Aurelia, Daha, Damien Gl., Damien Go., Eloïse, Etienne, Khriscia, Loïc F., Martin, Nicolas C., Olivier D., Quentin, Rémi, Sandra, Thibault, Yiqin, even when I was struggling against my Matlab code, your good mood at the CETHIL Kfêt made my days much easier! I pay a tribute to all my officemates Benjamin, Loïc R., Priscila, Samuel, Virginia, because "c'est pas facile tous les jours" to stand me.

To my friends and mentors from Lyon... or further: Ali, Auline, Bruno, Denis, Geri, Leon, Lucie, Olivier, Pierrick, Romain, Tere, these four years were incredible thanks to you!

Because this period of my life was not devoted only to work, I thank the Taekwondo club of Vaulx en Velin. More particularly, I thank my masters Kader (except for all the kicks I received from him), Zaïr, Romain, Driss and Nadir. I also have a thought for my dear black belt friends Mohamed T. and Mohamed O. Please guys don't stop this sport! See you soon for a fight! Cha ryuth! Kyung nae!

I cannot forget my friends from Aveyron, what great memories with you for now about two decades! Bruno, Ben, Cindy, Cyril, Fabrice, Flavie, Ghislain, Julie, Titi, Xavier, you are the best! I would like to thank Matthieu, but he actually should to thanks me for supporting him all that time!

Many thanks to my family, especially Joël, Nadège, Juline and Louan. Thank you to my parents who would be my (0,0,0) coordinates whether my life was a Cartesian system.

I devote the last lines to Music that helped me so much for years:

Gojira. "Liberation." *Magma*

ABSTRACT

The concept of Fondatherm is close of an earth-to-air heat exchanger (EAHE). A fan forces the circulation of outdoor air in a buried channel over several dozen meters. This enables to preheat or to cool it down with relatively low energy consumption. The main question is: considering the system costs resulting from the pipe burying, is that technique of energy supply (both for heating and cooling) competitive compared to gas, fuel or electricity? Studies about EAHE showed that the development of competitive systems is possible, but required a careful designing process. Several design variables such as the pipe buried depth, diameter, and length, or still the airflow rate can enhances or downgrade the thermal transfers. Furthermore, the surroundings factors (as for instance the soil hygrothermal properties, the season, the climate, the operation time and more generally the control strategy) are key factors that strongly influence the EAHE operation and performance.

In this context, the Fondatherm specifications have been discerned. The main difference lies in its integration within the building frame, implying a stronger coupling. This can be considered as an improvement. Indeed it results in a multi-functional building envelop component, since Fondatherm allows to recover heat while it is participating as a structure element. It allows saving materials (mainly concrete) which is better from an embodied energy and carbon balance point of view. However from a thermal and energy point of view, this strong coupling with the building is not well known and therefore needs to be mastered. In order to improve the knowledge of the geothermal ventilated foundation, the proposed approach consisted in, on the one hand to develop two numerical models and on the other hand to set up a full scale monitoring of a building equipped with two 50 *m* long foundation.

Considering the modelling, the need for two levels of complexity quickly appeared. The first one has a clear objective: improve the knowledge of the Fondatherm operation conditions and of the complex governing heat transfers that are involved in the foundation behaviour. This required a detailed model. Consequently, a coupled heat and moisture transfer within the soil and the concrete foundation has been developed. Finite volume and Newton-Raphson method have been used to solve the conservation equations. The second level is concerning need of a designing tool. A trade-off between accuracy and computational time is here mandatory. For this reason, a sensible heat transfer model, reduced by a balanced realization technique (also called Moore method) has been proposed. The detailed model is satisfactory regarding the soil, the foundation and the airflow domain behaviour reproduction. The sensible (simplified) model is less accurate regarding the soil and the foundation domain description but reproduce correctly the airflow temperature variations within the foundation cavity.

The performance evaluation of the two models has been possible thanks to experimental measurements carried out on a retirement home. These results also allowed carrying out an energy and a thermal survey of Fondatherm. The energy survey proved that its performances are interesting both for heating and cooling operating modes. It is as efficient as a traditional EAHE, and even more while considering only the heating potential. The thermal analysis based on a whole year statistical analysis demonstrates that the heat transfers within the cavity are not symmetric at all. In heating mode, the main contribution comes from the upper

horizontal and the internal vertical walls. In cooling mode, the main contribution comes from the lower and the external walls.

KEY WORDS: geothermal, earth-to-air heat exchanger, energy, thermal, modelling, finite volumes, experimental, coupled heat and moisture transfer.

RESUME

Le principe de fonctionnement de Fondatherm est proche de celui d'un échangeur air-sol (EAHE). Il s'agit simplement de forcer l'air extérieur à circuler dans un réseau de conduites enterrées, et ceci généralement sur plusieurs dizaines de mètres de longueurs. Cela permet de préchauffer ou de rafraîchir cet air avec une consommation énergétique modeste. La question est : prenant en compte le coût d'achat et d'installation tel que l'enfouissement des tuyaux, ce système permet-il de fournir de l'énergie à un prix raisonnable par rapport au gaz, fioul ou à l'électricité ? Les études menées sur les EAHE montrent que le développement de systèmes compétitifs est possible, mais nécessite une conception soignée. De multiples variables telles que la profondeur d'enfouissement, le diamètre et la longueur des tuyaux ou encore le débit améliorent ou au contraire dégradent les transferts thermiques. Des facteurs liés à l'environnement (tels que les propriétés hygrothermiques du sol, la saison considérée, le climat, la durée et le mode de fonctionnement) influencent grandement le fonctionnement des EAHE.

Dans ce contexte, les spécificités de Fondatherm ont été identifiées et analysées. La principale différence repose sur son intégration au sein de la structure du bâtiment, ce qui induit un fort couplage avec ce dernier. Ceci peut être un avantage. La multifonctionnalité ainsi générée – puisque la fondation géothermique a simultanément un rôle d'échangeur thermique et structurel – réduit l'utilisation de matériaux et assure un gain de place. Le produit est donc meilleur d'un point de vue énergétique et bilan carbone qu'un EAHE classique. Cependant, si l'on considère les transferts thermiques, ce couplage avec le bâtiment n'est pas maîtrisé. Dans le but d'améliorer les connaissances sur cette fondation géothermique, l'approche proposée consiste d'une part à développer deux modèles numériques, et d'autre part de mettre en place une importante instrumentation d'un bâtiment équipé de deux fondations de 50 m de long.

Le besoin de deux niveaux de modélisation est apparu nécessaire. L'objectif du premier niveau est clair : améliorer la compréhension du fonctionnement de Fondatherm et des transferts de chaleurs complexes en son sein. Cela requiert un modèle détaillée. Un modèle de transferts couplés de chaleur et d'humidité, à la fois dans le sol et dans la fondation en béton a donc été développé. Les méthodes de volume finis et de Newton-Raphson ont été utilisées pour résoudre les équations continues qui en résultent. Le deuxième niveau résulte du besoin d'un outil de dimensionnement. Un compromis entre précision et temps de calcul est donc indispensable. Pour ce faire, un modèle de transferts sensible a été développé puis réduit par une méthode de réalisation équilibrée (également appelée méthode de Moore). La reproduction du comportement du sol, de la fondation et du flux d'air par le modèle détaillé est satisfaisante. Le modèle sensible est moins précis sur les domaines sol et fondation, mais reproduit tout de même correctement les variations de température du flux d'air.

L'évaluation de ces deux modèles a été possible grâce aux mesures expérimentales réalisées sur un EHPAD. Ces résultats ont également permis de mener des analyses thermiques et énergétiques de Fondatherm. L'étude énergétique a montré que ses performances sont significatives à la fois en refroidissement et en chauffage. Le système est aussi performant qu'un EAHE traditionnel, et parfois même plus si l'on considère simplement le potentiel en chauffage. L'analyse thermique a démontré grâce à une synthèse statistique

menée sur une année complète que les échanges au sein de la cavité ne sont pas symétriques. En mode chauffage, la principale contribution de la fondation vient de ses parois internes supérieure et intérieure. En mode refroidissement, la principale contribution provient des parois inférieure et externe.

MOTS-CLÉS : géothermie, échangeur air-sol, énergie, thermique, modélisation, volume finis, expérimental, transferts couplés de chaleur et d'humidité.

NOMENCLATURE

Greek letters

| | | |
|--------------------------------|--|-------------------------------|
| α | VGM coefficient for the soil water retention curve | – |
| α_p | VGM coefficient for the concrete water retention curve | Pa^{-1} |
| α_i | VGM coef. for the concrete water retent. curve for the pore size subsystem i | Pa^{-1} |
| α_s | thermal diffusivity | $m^2 \cdot s^{-1}$ |
| β | contact angle between the liquid and solid phases | rad |
| γ | water surface tension factor | K^{-1} |
| δ | penetration depth of the outdoor thermal wave | m |
| δ_v | concrete vapour permeability | s |
| δ_r | concrete vapour permeability coefficient | s |
| δ_e | concrete vapour permeability coefficient | – |
| $\delta x, \delta y, \delta z$ | mesh width, length, height | m |
| δS | mesh section area | m^2 |
| ε | emissivity | – |
| ε | efficiency | – |
| ζ_n | phase of the thermal wave associated to the n th pulsation | |
| η | porosity | – |
| θ | volumetric water content | $m^3 \cdot m^{-3}$ |
| θ_a | volumetric air content | $m^3 \cdot m^{-3}$ |
| θ_k | transition (liquid water phase continuous / discontinuous) water content | $m^3 \cdot m^{-3}$ |
| θ_m | virtual saturated volumetric water content (at $\Psi \geq \Psi_{sat}$) | $m^3 \cdot m^{-3}$ |
| θ_q / θ_{nq} | volumetric content of quartz / non quartz elements | $m^3 \cdot m^{-3}$ |
| θ_r | residual volumetric water content | $m^3 \cdot m^{-3}$ |
| θ_s | saturated water content | $m^3 \cdot m^{-3}$ |
| θ_{sc} | solar chimney slope | rad |
| κ | von Karman constant | – |
| λ | thermal conductivity | $W \cdot m^{-1} \cdot K^{-1}$ |
| λ_0 | concrete thermal conductivity coefficient | $W \cdot m^{-1} \cdot K^{-1}$ |

| | | |
|---------------------|--|-------------------------------------|
| λ_w | concrete thermal conductivity coefficient | $W.m^{-1}.K^{-1}$ |
| ν | mass flow factor for the soil vapour diffusivity | — |
| ξ_i | ratio of the thermal gradient of the phase i and the global thermal gradient | — |
| ξ | correction factor for the soil thermal vapour diffusivity | — |
| ρ | density | $kg.m^{-3}$ |
| σ | Boltzmann constant | — |
| σ | surface tension | — |
| τ | VGM coefficient for the hydraulic conductivity curve | — |
| ν | tortuosity factor | — |
| φ | air layer stability coefficient | — |
| φ | relative humidity | — |
| ϕ | surface flow | $W.m^{-2}$ or $kg.m^{-2}.s^{-1}$ |
| ω_a | air specific humidity | $kg_{vap}.kg_{dry\ air}^{-1}$ |
| ω / ω_n | pulsation / nth pulsation of the outdoor thermal wave | s^{-1} |
| Ψ | matric head potential | m |
| Φ | total hydraulic head | m |
| Φ | volumetric flow rate | $m^3.s^{-1}$ |

Latin letters

| | | |
|----------------|--|-------------------|
| a | ground top surface albedo | — |
| c | specific heat | $J.kg^{-1}K^{-1}$ |
| c_{TT} | thermal capacity in the heat transfer equations | $J.m^{-3}K^{-1}$ |
| $c_{T\Psi}$ | hygric capacity in the matric head based heat transfer equations | $J.m^{-4}$ |
| c_{TP_c} | hygric capacity in the capillary pressure based heat transfer equations | — |
| $c_{\Psi T}$ | thermal capacity in the matric head based moisture transfer equations | K^{-1} |
| $c_{P_c T}$ | thermal capacity in the capillary pressure based moisture transfer equations | $kg.m^{-3}K^{-1}$ |
| $c_{\Psi\Psi}$ | hygric capacity in the matric head based moisture transfer equations | m^{-1} |
| $c_{P_c P_c}$ | hygric capacity in the capillary pressure based moisture transfer equations | $s^2.m^{-2}$ |
| cf | cloud factor | — |

| | | |
|---------------------------------|--|----------------------------|
| e | volumetric energy | $J.m^{-3}$ |
| f | enhancement factor for the soil vapour diffusivity | – |
| f_w | fitting parameter for the ground thermal conductivity model | – |
| g | gravity | $m.s^{-2}$ |
| g_i | fitting parameter for the ground thermal conductivity model | – |
| h_{sc} | solar chimney height | m |
| h_c | convective heat exchange coefficient | $W.m^{-2}.K^{-1}$ |
| h_v | convective vapour exchange coefficient | $kg.m^{-2}.s^{-1}.Pa^{-1}$ |
| k_{TT} | thermal conductance in heat transfer equations | $W.m^{-1}.K^{-1}$ |
| $k_{T\Psi}$ | hygric conductance in the matric head based heat transfer equations | $W.m^{-2}$ |
| k_{TP_c} | hygric conductance in the capillary pressure based heat transfer equations | $m^{-2}.s^{-1}$ |
| $k_{\Psi T}$ | thermal conductance in the matric head based moisture transfer equations | $m^2.s^{-1}.K^{-1}$ |
| $k_{P_c T}$ | thermal conductance in the capillary pressure moisture transfer equations | $kg.m^{-1}.s^{-1}.K^{-1}$ |
| $k_{\Psi\Psi}$ | hygric conductance in the matric head based moisture transfer equations | $m.s^{-1}$ |
| $k_{P_c P_c}$ | hygric conductance in the capillary pressure moisture transfer equations | s |
| l_i | weight factor for concrete hydraulic conductivity of the pore size subsystem i | – |
| l_{sc} | solar chimney width | m |
| m | VGM coefficient for the water retention curve | – |
| \dot{m}_a | mass airflow rate | $kg.s^{-1}$ |
| m_i | VGM coefficient for the water retention curve of the pore size subsystem i | – |
| n | VGM coefficient for the water retention curve | – |
| n_i | VGM coefficient for the water retention curve of the pore size subsystem i | – |
| q | heat flow per unit length | $W.m^{-1}$ |
| q_0 | fitting parameter for the ground thermal conductivity model | – |
| r | pore radius / pipe radius | m |
| r_s | additional series resistance for the moisture exchange on ground top surface | $s.m^{-1}$ |
| t | time | s |
| $\vec{u}_x \vec{u}_y \vec{u}_z$ | unitary vectors | – |
| w | mass water content | $kg.m^{-3}$ |

| | | |
|----------------|---|---------------------|
| w_{sat} | saturated mass water content | $kg.m^{-3}$ |
| $x y z$ | coordinates width, length, height (positive upward) | m |
| A | area | m^2 |
| A_n | amplitude of the outdoor thermal wave associated to the nth pulsation | K |
| ACR | crawl space air change rate | hr^{-1} |
| B_T | boundary vector for matrix heat transfer equation | W |
| B_Ψ | boundary vector for matrix moisture transfer equation | $m^3.s^{-1}$ |
| C_d | coefficient of discharge of air channel inlet (0.57) | – |
| C_{TT} | thermal capacity matrix in the matrix heat transfer equation | $J.K^{-1}$ |
| $C_{T\Psi}$ | moisture capacity matrix in the matrix heat transfer equation | $J.m^{-1}$ |
| $C_{\Psi T}$ | thermal capacity matrix in the matrix moisture transfer equation | $m^3.K^{-1}$ |
| $C_{\Psi\Psi}$ | moisture capacity matrix in the matrix moisture transfer equation | m^2 |
| D_v | soil effective vapour diffusivity | $m^2.s^{-1}$ |
| $D_{v,a}$ | water vapour diffusivity in air | $m^2.s^{-1}$ |
| D_{Tv} | soil thermal vapour diffusivity | $m^2.s^{-1}.K^{-1}$ |
| $D_{\Psi v}$ | soil hydraulic vapour diffusivity | $m.s^{-1}$ |
| G | solar global irradiance on a horizontal plan | $W.m^{-2}$ |
| G_T | load vector for matrix heat transfer equation | W |
| G_Ψ | load vector for matrix moisture transfer equation | $m^3.s^{-1}$ |
| H | enthalpy | J |
| K_0 | matching point for the hydraulic conductivity | $m.s^{-1}$ |
| K_i | concrete hydraulic permeability for a pore size subsystem i | s |
| K_h | soil hydraulic conductivity | $m.s^{-1}$ |
| K_p | concrete liquid permeability | s |
| K_{sat} | saturated soil hydraulic conductivity | $m.s^{-1}$ |
| $K_{p,sat}$ | saturated concrete hydraulic permeability | s |
| K_{TT} | thermal conductance in the matrix heat transfer equation | $W.K^{-1}$ |
| $K_{T\Psi}$ | moisture conductance in the matrix heat transfer equation | $W.m^{-1}$ |
| $K_{\Psi T}$ | thermal conductance in the matrix moisture transfer equation | $m^3.s^{-1}.K^{-1}$ |
| $K_{\Psi\Psi}$ | moisture conductance in the matrix moisture transfer equation | $m^2.s^{-1}$ |

| | | |
|-------------------|---|--------------------------------|
| L | length | m |
| L_v | heat of vaporization of water | $J \cdot kg^{-1}$ |
| L_{MO} | Monin-Obukhov instability length | m |
| NTU | Number of Transfer Units | – |
| P | perimeter | m |
| P | pressure | Pa |
| $P_{v,a}^f$ | partial water vapour pressure of the flowing air within the foundation | Pa |
| Q | heat | W |
| R | gas constant | $J \cdot kg^{-1} \cdot K^{-1}$ |
| R_i | Richardson number | – |
| S | saturation level | – |
| S_0 | modified saturation level | – |
| S_a | sand fraction | – |
| S_i | concrete saturation level for the pore size subsystem i | – |
| S_T | corrective vector for a conservative scheme in the matrix heat equation | W |
| S_Ψ, S_{P_c} | corrective vector for a conservative scheme in the matrix moisture equation | m^3 and kg |
| T | temperature | K |
| T_a^f | temperature of the flowing air within the foundation | K |
| U | unknown vector | K and m or Pa |
| \vec{U} | fluid apparent velocity | $m \cdot s^{-1}$ |
| U_e | aerodynamic conductance on ground top surface | $m \cdot s^{-1}$ |
| V | volume | m^3 |
| V_a / \vec{V}_a | air velocity / air velocity vector | $m \cdot s^{-1}$ |
| W | wind speed | $m \cdot s^{-1}$ |
| \vec{W} | fluid local velocity | $m \cdot s^{-1}$ |
| Z_0 | length of the ground top surface roughness | m |
| Z_e | height of the wind speed measurement | m |

Subscript

| | |
|----------------|--|
| <i>0</i> | at T_0 |
| <i>a</i> | air |
| <i>base</i> | at ground base layer |
| <i>c</i> | capillary |
| <i>cav</i> | foundation cavity walls |
| <i>conv</i> | convection |
| <i>cool</i> | cooling mode |
| <i>CS</i> | ground top surface to the crawl space air |
| <i>d</i> | dispersion |
| <i>e</i> | elementary volume |
| <i>EAHE</i> | of the earth-to-air heat exchanger |
| <i>evap</i> | evaporation / condensation |
| <i>f</i> | fluid |
| <i>found</i> | foundation / Fondatherm |
| <i>h</i> | heat |
| <i>heat</i> | heating mode |
| <i>HRU</i> | heat recovery unit |
| <i>i, j, k</i> | mesh index along the x, y and z direction respectively |
| <i>in</i> | indoor |
| <i>inlet</i> | at the foundation inlet section |
| <i>l</i> | liquid |
| <i>lw</i> | long wave radiation |
| <i>m</i> | moisture |
| <i>outlet</i> | at the foundation outlet section |
| <i>prec</i> | precipitation (rain or snow) |
| <i>PCM</i> | Phase change material |
| <i>ref</i> | reference |
| <i>s</i> | solid / soil |
| <i>sat</i> | saturation |

| | |
|--------------------|--|
| <i>sc</i> | solar chimney |
| <i>sens</i> | sensible heat |
| <i>sky</i> | celestial sphere |
| <i>slab</i> | building slab |
| <i>surf</i> | at ground top surface |
| <i>sw</i> | short wave radiation |
| <i>v</i> | vapour |
| <i>e w n s t b</i> | east, west, north, south top and bottom meshes surfaces of the mesh <i>P</i> |
| <i>E W N S T B</i> | east, west, north, south top and bottom meshes adjacent to the mesh <i>P</i> |

Superscript

| | |
|------------|-------------------|
| <i>ext</i> | outdoor (ambient) |
| <i>f</i> | foundation |
| <i>g</i> | ground |
| <i>CS</i> | crawl space air |
| <i>*</i> | equivalent |

Abbreviation

| | |
|-------------------------|--|
| <i>AHU</i> | air handling unit |
| <i>COP</i> | coefficient of performance - thermodynamic definition, based on fan electric consumption |
| <i>COP_{pl}</i> | coefficient of performance – pressure loss based definition |
| <i>EAHE</i> | earth-to-air heat exchanger |
| <i>HRU</i> | heat recovery unit |
| <i>PCM</i> | phase change material |

CONTENTS

| | |
|--|-----------|
| ACKNOWLEDGMENTS | 5 |
| ABSTRACT | 6 |
| RESUME | 8 |
| NOMENCLATURE | 10 |
| CONTENTS | 17 |
| LIST OF TABLES..... | 21 |
| LIST OF FIGURES..... | 22 |
| CHAPTER 1. GENERAL INTRODUCTION | 1 |
| 1.1. Context | 1 |
| 1.2. A geothermal foundation | 3 |
| 1.3. Thesis Objectives and Fondatherm project outlines | 6 |
| CHAPTER 2. GROUND HEAT EXCHANGERS, EARTH-TO-AIR HEAT EXCHANGERS: STATE OF THE ART | 9 |
| 2.1. General knowledge about ground heat exchangers and earth-to-air heat exchangers | 9 |
| 2.1.1 Ground heat exchangers and earth-to air heat exchanger: definitions, configurations and physics..... | 9 |
| 2.1.2 Design factors influencing the EAHE performances | 12 |
| 2.1.3 Evaluation of the EAHE performances | 19 |
| 2.1.4 external parameters: environment and operation modes | 22 |
| 2.2. On the modelling of EAHE | 32 |
| 2.2.1 Analytical modelling | 32 |
| 2.2.2 Numerical modelling | 37 |
| 2.3. FONDATHERM specifications and conclusions | 51 |
| 2.3.1 Depth | 51 |
| 2.3.2 Cavity size and shape | 51 |
| 2.3.3 Duct thickness and material | 52 |
| 2.3.4 Positioning in relation to the building..... | 52 |
| 2.3.5 Conclusions | 52 |

CHAPTER 3. GROUND HEAT TRANSFER PHENOMENA & COUPLED HEAT AND MOISTURE TRANSFER WITHIN POROUS MEDIA: MATHEMATICAL DESCRIPTION..... 53

| | |
|---|-----------|
| 3.1. Buildings ground heat loss | 53 |
| 3.1.1 Different modelling levels | 53 |
| 3.1.2 Summary: useful information for Fondatherm | 60 |
| 3.2. Coupled heat and mass transfer within porous media: specific case of grounds and concrete | 63 |
| 3.2.1 Porous media: generalities about their mathematical modelling | 63 |
| 3.2.2 Coupled heat and mass transfer equations for porous media and soils | 67 |
| 3.3. Conclusions | 75 |

CHAPTER 4. OBJECTIVES AND DEVELOPMENT OF THE COUPLED HEAT AND MASS TRANSFER MODEL 77

| | |
|---|------------|
| 4.1. Objectives | 77 |
| 4.2. System of conservation law equations | 77 |
| 4.3. Thermal and hydraulic properties of unsaturated soils | 81 |
| 4.3.1 Water retention curve | 81 |
| 4.3.2 Hydraulic conductivity | 82 |
| 4.3.3 Thermal conductivity | 83 |
| 4.3.4 Vapour diffusivity | 85 |
| 4.3.5 Parameter values..... | 86 |
| 4.4. Thermal and hydraulic properties of concrete | 86 |
| 4.4.1 Water retention curve | 87 |
| 4.4.2 Liquid permeability..... | 87 |
| 4.4.3 Vapour permeability..... | 88 |
| 4.4.4 Thermal conductivity..... | 88 |
| 4.5. Boundary conditions description | 88 |
| 4.5.1 Boundary conditions for the ground | 88 |
| 4.5.2 Boundary conditions for the concrete foundation | 94 |
| 4.6. Numerical resolution | 98 |
| 4.6.1 Projection of the conservation equations | 98 |
| 4.6.2 Algorithm procedure, meshing and time step definition | 99 |
| 4.6.3 Implementation of boundary conditions | 107 |
| 4.7. Conclusions | 111 |

| | |
|---|------------|
| CHAPTER 5. OBJECTIVES AND DEVELOPMENT OF THE SENSIBLE HEAT TRANSFER MODEL..... | 113 |
| 5.1. Objectives | 113 |
| 5.1.1 Geometry | 113 |
| 5.1.2 Thermal characteristic..... | 113 |
| 5.1.3 Ground stratification | 114 |
| 5.1.4 Air flow | 114 |
| 5.1.5 Climate | 114 |
| 5.1.6 Building basement configuration | 114 |
| 5.1.7 Simulation time and accuracy | 114 |
| 5.2. State model development and reduction | 115 |
| 5.2.1 State model for conduction within the solids | 115 |
| 5.2.2 State Reduced Order model: Balanced Realization (Moore) method..... | 117 |
| 5.3. Boundary conditions | 118 |
| 5.4. Numerical resolution | 122 |
| 5.5. Conclusions | 124 |
| | |
| CHAPTER 6. FONDATHERM FULL SCALE MONITORING | 125 |
| 6.1. Facilities presentation | 125 |
| 6.2. Experimental results analysis | 135 |
| 6.2.1 Energy behaviour understanding | 135 |
| 6.2.2 Thermal behaviour understanding..... | 140 |
| 6.3. Conclusions | 153 |
| | |
| CHAPTER 7. SIMULATION RESULTS - COMPARISON WITH THE MEASUREMENTS | 155 |
| 7.1. Introduction | 155 |
| 7.1.1 Objectives..... | 155 |
| 7.1.2 Parameters of the models, Simulation period, and divergence problems..... | 156 |
| 7.1.3 Computational time | 157 |
| 7.2. Focus over short periods | 159 |
| 7.2.1 Global analysis of the coupled model behaviour | 159 |
| 7.2.2 Two winter weeks | 161 |
| 7.2.3 Two spring weeks..... | 169 |
| 7.3. Analysis over six months | 176 |
| 7.3.1 Focus on the soil results | 176 |
| 7.3.2 Focus on the foundation middle section results | 178 |
| 7.4. Conclusions | 179 |

| | |
|--|------------|
| CHAPTER 8. INNOVATIVE COUPLINGS WITH OTHER SYSTEMS..... | 181 |
| 8.1. Introduction | 181 |
| 8.2. Coupling with an air handling unit | 181 |
| 8.3. Coupling with a solar chimney | 185 |
| 8.4. Phase change materials combination | 188 |
| 8.5. Conclusions | 191 |
| CHAPTER 9. GENERAL CONCLUSIONS AND OUTLOOKS | 193 |
| 9.1. Conclusions of this work | 193 |
| 9.2. Future outlooks | 196 |
| REFERENCES | 198 |
| ANNEXES..... | 208 |
| APPENDIX A: SYSTEMS OF CONSERVATION LAW EQUATIONS FOR SOIL AND CONCRETE..... | 209 |
| APPENDIX B: SET OF THERMO-HYGRIC CHARACTERISTICS FOR SEVEN SOILS | 211 |
| APPENDIX C: A FINITE VOLUME METHOD | 212 |
| APPENDIX D: A NEWTON-RAPHSON METHOD | 214 |
| APPENDIX E: DESCRIPTION OF THE EXPERIMENTAL ACQUISITION SYSTEM | 216 |
| APPENDIX F: CALCULATION OF THE PRESSURE LOSSES THROUGH THE VENTILATED FOUNDATION..... | 221 |
| APPENDIX G: DIFFERENCES BETWEEN THE MEASUREMENTS AND THE MODELS RESULTS | 222 |
| APPENDIX H: FONDATHERM CONTROL STRATEGY: PREMISES..... | 224 |

LIST OF TABLES

| | |
|---|-----|
| Table 1: Cost of preheating and cooling of several EAHE configurations (Hollmuller and Lachal, 2001)..... | 2 |
| Table 2: Economic analysis of retrofitting solutions integrating EAHE (Bansal et al., 2012a) | 3 |
| Table 3: Cost of energy savings for two building integrating Fondatherm..... | 5 |
| Table 4: Work packages and tasks details of the Fondatherm project..... | 7 |
| Table 5: Comparative advantages of EAHE and BHE..... | 9 |
| Table 6: Performance of three EAHE installations according to four different indicators (Pfafferott, 2003)..... | 20 |
| Table 7: Overview of the EAHE installation characteristics and performances for cooling... | 25 |
| Table 8: Overview of the EAHE installation characteristics and performances for heating .. | 28 |
| Table 9: Most common convective heat transfer coefficient..... | 48 |
| Table 10: EAHE modelling: summary of the main existing models..... | 49 |
| Table 11 : Building ground heat loss modelling: summary of the main existing methods | 62 |
| Table 12 : Main moisture movements within porous media..... | 71 |
| Table 13: Concrete composition and main characteristics for the foundation in Val-de-Mercy | 87 |
| Table 14: Moisture suction curve: parameters for a bi-modal representation of concrete ... | 88 |
| Table 15: Boundary conditions at ground-foundation interface..... | 97 |
| Table 16: Matric head-controlled boundary conditions at ground top surface: moisture equations and transfer coefficients..... | 109 |
| Table 17: Multiplicative corrective factor for the convective heat transfer coefficient of the foundation cavity | 110 |
| Table 18: Thermal characteristics values for the sensible heat transfer model | 116 |
| Table 19: Coefficient for the one dimensional ground temperature model..... | 122 |
| Table 20: Sensors characteristics | 126 |
| Table 21: Acronyms used definitions..... | 141 |
| Table 22: Node number used for the reduced and the full linear model..... | 158 |
| Table 23: Computational time of the full and reduced linear model, and of the coupled model | 158 |
| Table 24: Set of parameters for the suction curve, the hydraulic conductivity and the thermal conductivity analytical models, for seven representative soils..... | 211 |
| Table 25: Details about the box data acquisition system..... | 218 |
| Table 26: Calculation details of the pressure losses through the ventilated foundation | 221 |

LIST OF FIGURES

| | |
|--|----|
| Figure 1: Main components of the Fondatherm technology..... | 4 |
| Figure 2: Comparison between a traditional foundation and the Fondatherm system..... | 5 |
| Figure 3: Two configuration examples: (a) closed loop serpentine layout next to a building and (b) grid open loop layout beneath a building..... | 10 |
| Figure 4: Main physical phenomenon that influence the EAHE thermal performance (heating conditions) | 11 |
| Figure 5: Soil temperature collected for several depths in Val-de-Mercy (France) against analytical model (2.1) | 12 |
| Figure 6: Influence of the pipe depth on the outlet air temperature for eight EAHE models (Tzaferis et al., 1992) | 13 |
| Figure 7: The effect of buried depth on daily (a) and annual (b) phase shift and amplitude dampening (Yang et al., 2016) | 14 |
| Figure 8: Influence of the pipe length on the outlet air temperature for eight EAHE models (Tzaferis et al., 1992) | 15 |
| Figure 9 : Influence of the pipe radius on the outlet air temperature for eight EAHE models (Tzaferis et al., 1992) | 16 |
| Figure 10: Cooling capacity variation of the EAHE for different radii (Wu et al., 2007) | 16 |
| Figure 11: The effect of pipe radius on daily (a) and annual (b) phase shift and amplitude dampening (Yang et al., 2016) | 16 |
| Figure 12 : Influence of air speed on the outlet air temperature for eight EAHE models (Tzaferis et al., 1992) | 18 |
| Figure 13: The effect of airflow rate on daily (a) and annual (b) phase shift and amplitude dampening (Yang et al., 2016) | 19 |
| Figure 14: Simple modeling of an EAHE with (a) and without (b) considering the soil surrounding the tube | 32 |
| Figure 15: EAHE analytical model developed by Hollmuller (2002, 2003) | 36 |
| Figure 16: Cross and longitudinal section of the EAHE finite volume model (Thiers and Peuportier, 2008) | 38 |
| Figure 17: Modelling of the heat and mass flow within the buried pipe (Hollmuller, 2002) | 40 |
| Figure 18 : Cross-sectional view of the EAHE installation modelled by Gauthier et al. (1997) | 41 |
| Figure 19: Principle of EAHE modelling with response factor method (Tittlein et al., 2009) | 45 |
| Figure 20: Fondatherm cross section with crawl space (a) or ground-on-slab (b) configuration: main physical phenomenon | 51 |

| | |
|---|-----|
| Figure 21: Fundamental thermal processes: steady-state (A), periodic (B) and outdoor temperature (C) (Claesson and Hagentoft, 1991)..... | 55 |
| Figure 22: Boundary conditions for the numerical simulation of the soil surrounding a basement wall (a) and total wall heat loss values from day 85 to day 99 for a basement surrounded by a sandy soil (b) (Shen and Ramsey, 1988) | 59 |
| Figure 23: Porous media: definition of the Elementary Representative Volume | 64 |
| Figure 24: Partially saturated porous media | 67 |
| Figure 25: Definition of the capillary strengths within a porous unsaturated media..... | 68 |
| Figure 26: Isotherm suction (a) and corresponding sorption curves (b): classification of the regions..... | 69 |
| Figure 27: Hydraulic (a) and heat (b) transfer coefficients for the moisture equation, and thermal (c) and hydraulic (d) heat (d) transfer coefficient for the heat equation | 80 |
| Figure 28: Difference between the complete equation and the simplified one for the term kTf : impact on the outlet air temperature and relative humidity..... | 80 |
| Figure 29: Suction curve for three different soils with the Janssen-VGM model | 82 |
| Figure 30: Hydraulic conductivity for three different soils with the Janssen-VGM model | 83 |
| Figure 31: Thermal conductivity for three different soils with the de Vries – Janssen model | 85 |
| Figure 32: Hydraulic vapour diffusivity for three different soils according to the Philipp & de Vries model | 86 |
| Figure 33 : Ground top surface boundary conditions: (a) moisture and (b) heat transfers .. | 89 |
| Figure 34: Boundary heat flows on the ground top surface with deactivated concrete cover | 92 |
| Figure 35: Modelling the heat and mass transfer through the interface soil / bituminous coating / foundation (not in scale)..... | 95 |
| Figure 36: Modelling the heat and mass transfer through the interface soil / foundation (not in scale)..... | 96 |
| Figure 37: Algorithm of the 3D finite volume model for the resolution of the coupled heat and moisture equations within the soil and the concrete foundation | 101 |
| Figure 38: Validation of the numerical code over test exercises: (a) infiltration - results from (Milly, 1982) (b) heat and vapour transfer - results from (Janssen, 2002)..... | 102 |
| Figure 39: Domain studied and its limits..... | 103 |
| Figure 40: Comparison of the outlet temperature (a) and relative humidity (b) to the 2D reference case | 104 |
| Figure 41: Trade-off simulation time / Accuracy as a function of the number of nodes for a 2D simulation..... | 105 |
| Figure 42: Trade-off simulation time / Accuracy as a function of the number of nodes for a 3D simulation..... | 105 |

| | |
|--|-----|
| Figure 43: Comparison of the circulating air outlet temperature (a) and (b) and relative humidity (c) and (d) to the 3D reference case | 106 |
| Figure 44: Maximum temperature (a) and water content (d) gradient along the y axis – Temperature (b) and water content (c) evolution through the concrete foundation for the finest grid 34X20X61 | 106 |
| Figure 45: Global meshing a cross-section of the system {soil+foundation}..... | 107 |
| Figure 46: Description of the moisture flow in the flux-controlled (a) and the matric-head controlled case (b) | 108 |
| Figure 47: Boundary conditions for the crawl-space case | 118 |
| Figure 48: Cavity section: j^{th} air node exchanging heat and moisture with n cavity wall surfaces..... | 119 |
| Figure 49: Fondatherm sensible heat transfer model: numerical resolution general procedure | 123 |
| Figure 50: Cross-sectional meshing..... | 124 |
| Figure 51: Overview of the monitored building: (a) general view of the west and east wings, (b) position of the east air intake and inspection window at the foundation inlet and (c) weather station installation | 127 |
| Figure 52 : Ground plan of the monitored building: (a) west wing and (b) east wing | 129 |
| Figure 53: Cross-sectional views of the monitored building: sensors positioning..... | 134 |
| Figure 54: Inspection manhole: access to the foundation cavity..... | 134 |
| Figure 55 : Energy experimental analysis of Fondatherm | 136 |
| Figure 56: Energy experimental analysis of the half length of Fondatherm..... | 138 |
| Figure 57: Comparison of the energy performance of Fondatherm technology against traditional EAHE..... | 139 |
| Figure 58: Vocabulary used - Main sensors positions..... | 140 |
| Figure 59: Fondatherm thermal performance analysis over five typical summer days..... | 143 |
| Figure 60: Fondatherm thermal performance analysis over five typical winter days | 145 |
| Figure 61: Fondatherm thermal performance analysis over five typical spring days..... | 147 |
| Figure 62: Fondatherm thermal performance analysis over five typical autumn days..... | 148 |
| Figure 63: Monthly boxplot diagram of the thermal potentials within the foundations (full line: west wing, dashed line: east wing, blue line: inlet section, green line: middle, red line: outlet)..... | 151 |
| Figure 64: Impact of the ground temperature and water content on the flowing air heating / cooling..... | 152 |
| Figure 65: Comparison of the calculation from the full and from the reduced linear model: temperature and relative humidity differences at the foundation (a) middle section (b) outlet section | 159 |

| | |
|--|-----|
| Figure 66: Temperature and water saturation level fields obtained from the coupled model - cross and longitudinal sections - 12 January 2016, 12h..... | 160 |
| Figure 67: Temperature and water saturation level fields obtained from the coupled model - cross and longitudinal sections – 17 May 2016, 16h..... | 161 |
| Figure 68: Crawl-space modelling results: (a) Air volume (b) Soil 42cm depth..... | 163 |
| Figure 69: Ground free field measurements and modelling results: (a) Weather data (b) Soil surface (c) Soil 80cm depth (d) Soil 160cm depth | 164 |
| Figure 70: Foundation inlet section (section AA') temperature measurements and modelling results: (a) Flowing air (b) Inner walls (c) External outer wall (d) Internal outer wall..... | 167 |
| Figure 71: Foundation middle section (section CC') temperature measurements and modelling results: (a) Flowing air (b) and (d) Inner walls (c) Outer wall..... | 168 |
| Figure 72: Foundation outlet section (section FF') temperature measurements and modelling results: (a) Flowing air (b) Inner walls (c) Outer walls..... | 169 |
| Figure 73: Crawl-space modelling results: (a) Air volume (b) Soil 42cm depth..... | 170 |
| Figure 74: Ground free field measurements and modelling results: (a) Weather data (b) Soil surface (c) Soil 80cm depth (d) Soil 160cm depth | 171 |
| Figure 75: Foundation inlet section (section AA') temp. measurements and modelling results: (a) Flowing air (b) Inner walls (c) External outer wall (d) Internal outer wall | 173 |
| Figure 76: Foundation middle section (section CC') temperature measurements and modelling results: (a) Flowing air (b) and (d) Inner walls (c) Outer wall..... | 174 |
| Figure 77: Foundation outlet section (section FF') temperature measurements and modelling results: (a) Flowing air (b) Inner walls (c) Outer walls..... | 175 |
| Figure 78: Ground modelling results versus measurements: Surface (a) temp., (b) moist. cont., 80cm depth (c) temp., (d) moist. cont., 160 cm depth (e) temp., (f) moist. cont., Crawl-space soil (g) temp., (h) moist. cont..... | 177 |
| Figure 79: Linear and coupled models results comparison against measurements: Flowing air (a) temp., (b) relative humidity, (c) Inner upper, (d) Inner lower, (e) Inner internal, (f) Inner external wall surface temp. | 179 |
| Figure 80: Linear and coupled models results comparison against measurements: (a) Internal outer wall surface temperature, (b) External outer surface wall temperature, (c) Outer walls moisture content..... | 179 |
| Figure 81: Energetic experimental study of the coupling between Fondatherm and the air handling unit..... | 182 |
| Figure 82: Mean daily energy gains of Fondatherm, of the heat recovery unit of the AHU and of the coupling {Fondatherm+AHU} | 184 |
| Figure 83: Net mean daily energy gain of Fondatherm when compared to the heat recovery unit (HRU) or considering the coupling with AHU | 185 |
| Figure 84: Coupling between a solar chimney and Fondatherm (a) and solar chimney model (b)..... | 185 |

| | |
|--|-----|
| Figure 85: Study of the coupling between Fondatherm and a solar chimney..... | 187 |
| Figure 86: Modelling of the PCM incorporation within the Fondatherm ventilated cavity . | 189 |
| Figure 87: Comparison of the Fondatherm outlet air temperature with and without PCM | 190 |
| Figure 88: Mean daily energy gains comparison - Fondatherm with and without PCM..... | 191 |
| Figure 89: 2D meshing for a finite volume method..... | 212 |
| Figure 90: Position of the acquisition boxes and Ethernet connection | 216 |
| Figure 91: SM300 connection to NI 9472 and NI 9205 | 217 |
| Figure 92: Screenshot of the Labview front panel..... | 217 |
| Figure 93: View of box 1 (top right corner) and 5 (bottom left corner)..... | 220 |
| Figure 94: Ground modelling – meas. differences: Surface (a) temp., (b) moist. cont., 80cm depth (c) temp., (d) moist. cont., 160 cm depth (e) temp., (f) moist. cont., Crawl-space soil (g) temp., (h) moist. cont. | 222 |
| Figure 95: Foundation modelling - measurements difference: Air (a) temp., (b) Rel. humidity, (c) Inner horizontal walls surface temp., (d) Inner vertical walls surface temp., (e) External outer wall surface temp., (f) Internal outer wall surface temp., (g) Outer wall surface moist. cont..... | 223 |
| Figure 96: Proposition for a control strategy of the airflow rate | 224 |

Chapter 1. GENERAL INTRODUCTION

1.1. CONTEXT

The building construction is a complex multi-objective problem with a huge amount of decision variables. One can cite for example thermal, acoustic and visual comfort, low energy consumption, low carbon emission and content and almost invariably low financial cost. Several steps are usually followed to design an energy efficient and low carbon building. First, the building energy needs (for heating, cooling or still for lighting) are reduced as much as possible by optimizing decision variables related to the envelope design such as the insulation level, the structure thermal inertia, glazing area and orientation, building location, shape and orientation, etc. Then, the remaining energy needs may be balanced by energy systems like electric heaters, gas or fuel boiler, heat pump, PV or thermal solar PVT panels, ground source heat pumps etc. The selection of one or other of these systems is mainly driven by the initial investment, the thermal efficiency and practical details.

While in theory an earth-to-air-heat exchanger (EAHE) is a good opportunity to save energy, using the ground as a heat source or sink source to pre-heat or cool the air used for building ventilation, it is often underperforming. It even sometimes constitutes a health threat for the building occupants. Indeed, mould growth enhanced by the presence of water due to condensation or infiltration, dust and radon can severely alter the air quality at the pipe outlet.

The reasons for this under-performance are most of the time linked to the design. Although the energy savings can be substantial, they are extremely depending on the geographic localisation (i.e. the local weather), the ground nature and the building use (residential, commercial, agricultural, etc.) (ADEME, 2017). Therefore, the design of the EAHE, namely the number, length, diameter and depth of the pipes, the airflow rate and fan specifications, has to integrate these constraints. Then, monitoring and maintenance procedures should be adopted to ensure its proper efficiency throughout the building operation. Indeed, designers have to deal with several inherent limitations of EAHE:

- The defects mainly due to the choice of the plastic material used for the pipe, the joints between the pipes, and sometimes a too low slope that prevents the evacuation of the condensate,
- The vehicle traffic and planting of plants are prohibited on the soil above the system,
- The ground settlement,
- An important land use when the EAHE is buried next to the building. In France in 2006, the mean individual house and the mean land area surface are respectively around 111 and 600 m²¹ while the trench area² is commonly around 60 m²,

¹ <https://www.insee.fr/fr/statistiques/1281267>

² <https://www.picbleu.fr/page/puits-canadien-ou-provencal-aeration-des-batiments-d-habitation>

- A soil with a buried EAHE is considered as constructed ground (in France), and is thus subjected to property tax.

Furthermore, although energy from EAHE appears as ‘free’, it actually necessitates an important investment for the excavation and refilling as well as an operating cost due to the fan electric consumption. All in all it makes that EAHE are often not economically viable.

Hollmuller and Lachal (2001) were among the firsts to consider energy and economy aspects in the study of EAHE at the same time. Table 1 reproduced from this paper gives a sum up of their work. Considering the capital cost of a traditional EAHE – which comprises the cost for excavation ($13.5 \text{ €} \cdot \text{m}^{-3}$), the cost for the supplying and the lying out of PVC pipes ($13.8 \text{ €} \cdot \text{m}^{-1}$), the cost for the refilling (with concrete in this specific case, $121.5 \text{ €} \cdot \text{m}^{-3}$) and the engineering costs (+28 % of the total previous cost) – they showed that the EAHE is not competitive with traditional oil / electricity based systems for heating, but it competes the electricity prices for cooling with regards to the Swiss energy prices.

Table 1: Cost of preheating and cooling of several EAHE configurations (Hollmuller and Lachal, 2001)

| | Capital | | Heating only | | | Cooling only | | |
|--|--------------------|------------------------|---------------------------------|---------------------------------|---|---------------------------------|---------------------------------|--|
| | Investment (k€) | Repayment* (k€.y-1) | Gains (MWh y ⁻¹) | Cost (c€.kWh ⁻¹) | Equivalent cost** (c€.kWh ⁻¹) | Gains (MWh y ⁻¹) | Cost (c€.kWh ⁻¹) | Equivalent cost*** (c€.kWh ⁻¹) |
| <i>As constructed</i> | 123 | 7.8 | 27 | 28.9 | 21.7 | 19.6 | 40 | 80 |
| <i>Half sized</i> | 43.2 | 2.8 | 22.4 | 12.2 | 9.2 | 18.4 | 14.9 | 29.8 |
| <i>As constructed with high flowrate</i> | 123 | 7.8 | 25.7 | 30.5 | 22.9 | 66.8 | 11.7 | 23.4 |

*Repayment considering 50 years lifetime and 6% interest rate

**For heating, the (primary) cost is multiply by 75 % as for fuel system

***For cooling it is multiply by 200% as for electric system

This trend was already the conclusion of the work in (Bojic et al., 1997). The studied system is more energy and cost efficient in summer than in winter – the cost of energy is double in winter - and this is true regardless the pipe length and number.

Ten years later, Bansal et al., (2012a) analysed several retrofitting solutions reported on Table 2, all including an EAHE - eventually coupled with an evaporative cooler. For both solutions, either a standard, an energy efficient or an inefficient blower generates the airflow. Results indicate first that the inefficiency of the blower plays a critical role in the final choice of the system. An inefficient blower led in most of cases to larger energy consumption than with the existing system which is to be retrofitted. The smallest pay-back period are reached with the energy efficient blower. Secondly, the EAHE (simple as well as coupled with an evaporative cooler) cannot cost-effectively replace an existing energy efficient system. Thirdly, the retrofitting is relevant when the electricity tariff is high. Lastly, the coupling of the EAHE with an evaporative cooler led to better Internal Rate of Return (IRR).

Ozgener and Ozgener (2013) evaluated the EAHE construction cost of a closed loop EAHE assisted with PV panels for a solar greenhouse air conditioning around 6960 €. Ventilation system manufacturers (ATLANTIC, 2016; Eole, 2017; Fiabibat SCOP, 2017) and the French agency for energy ADEME (ADEME, 2017) send EAHE kit, the price of which ranges between 1000 € and 10000 €. As can be noted the investment cost for an EAHE varies a lot according to the system configuration and the country, but is generally substantial. Therefore, the financial viability of an EAHE integrated to the building can only be reached after a multi-

criteria optimization process, considering the energy savings – related to the system sizing – the coupling with the other energy systems and in the case of refurbishment, the existing energy system performance.

Table 2: Economic analysis of retrofitting solutions integrating EAHE (Bansal et al., 2012a)

| | Blower | Simple EAHE | | | EAHE integrated with evaporative cooler | | |
|---|------------------------------------|-------------|--------------|--------------|---|--------------|--------------|
| | | Efficient | Standard | Inefficient | Efficient | Standard | Inefficient |
| <i>Costs (€)</i> | <i>Excavation and back filling</i> | 87 | | | | | |
| | <i>PVC pipe</i> | 84 | | | | | |
| | <i>Blower</i> | 174 | 131 | 87 | 174 | 131 | 87 |
| | <i>Honey comb pad</i> | - | | | 35 | | |
| | <i>Miscellaneous</i> | 56 | | | 66 | | |
| | <i>Total</i> | 393 | 350 | 306 | 445 | 402 | 358 |
| <i>Electrical energy saving existing systems vs proposed system (kWh)</i> | <i>Case 1</i> | 545 | 185 | -169 | 780 | 356 | -63 |
| | <i>Case 2</i> | 640 | 281 | -74 | 917 | 492 | 74 |
| | <i>Case 3</i> | 765 | 405 | 51 | 1097 | 672 | 254 |
| | <i>Case 4</i> | 1774 | 1415 | 1061 | 2051 | 1626 | 1208 |
| <i>IRR* (%) with domestic electric tariff**</i> | <i>Case 1</i> | 5 | Not feasible | Not feasible | 9 | Not feasible | Not feasible |
| | <i>Case 2</i> | 9 | Not feasible | Not feasible | 15 | 1 | Not feasible |
| | <i>Case 3</i> | 14 | 1 | Not feasible | 21 | 9 | Not feasible |
| | <i>Case 4</i> | 52 | 44 | 35 | 54 | 45 | 34 |
| <i>IRR (%) with commercial electric tariff***</i> | <i>Case 1</i> | 24 | Not feasible | Not feasible | 34 | 9 | Not feasible |
| | <i>Case 2</i> | 30 | 7 | Not feasible | 43 | 19 | Not feasible |
| | <i>Case 3</i> | 39 | 17 | Not feasible | 56 | 32 | 4 |
| | <i>Case 4</i> | 170 | 130 | 95 | 187 | 136 | 94 |

*Internal Rate of Return

**0.073 €/kWh⁻¹

***0.14 €/kWh⁻¹

Retrofitted case 1: Cooling with air-conditioner of COP=3.1, Heating with heat-pump of COP=4.1

Retrofitted case 2: Cooling with air-conditioner of COP=2.7, Heating with heat-pump of COP=3.7

Retrofitted case 3: Cooling with air-conditioner of COP=2.3, Heating with heat-pump of COP=3.3

Retrofitted case 4: Cooling with air-conditioner of COP=2.7, Heating with electrical heater of 90% efficiency

1.2. A GEOTHERMAL FOUNDATION

The French company Patrick CESCHIN SAS filed for a patent of an innovating EAHE. The Fondatherm® system concept is to add a thermal function to the structural role of a foundation. In practical terms, the foundation section is given a 'U' shape of cross section area 60 cm x 60 cm. Once the footing is set-up on its top, a hollow is created and constitutes a channel in which air can be blown. One element is 7.2 m length and several blocks can be assembled to form a longer channel. This technology sketched on Figure 1 provides solutions to the limitations cited above:

- Fondatherm is industrially precast, and the checking carried out at the factory allows avoiding numerous defects³ intrinsic to the building site. It is expected that

³ In France, about 8000 damages per year are the consequence of faulty work.

Fondatherm will be set-up by construction professionals (Patrick CESCHIN SAS or partners).

- It furthermore enables to reduce the energy and water consumption, the construction waste, and to speed-up the execution of the work, ensuring optimal security and hygiene for the workers.
- For the same mechanic resistance, a lower quantity of concrete is used, and the transport of the soil material removed is reduced.
- Since Fondatherm does not extend the building footprint contrary to traditional EAHE, the vehicle traffic and ground settlement problems are overcome. No additional land is required, and therefore this system can be set-up for house without land e.g. in an urban zone.

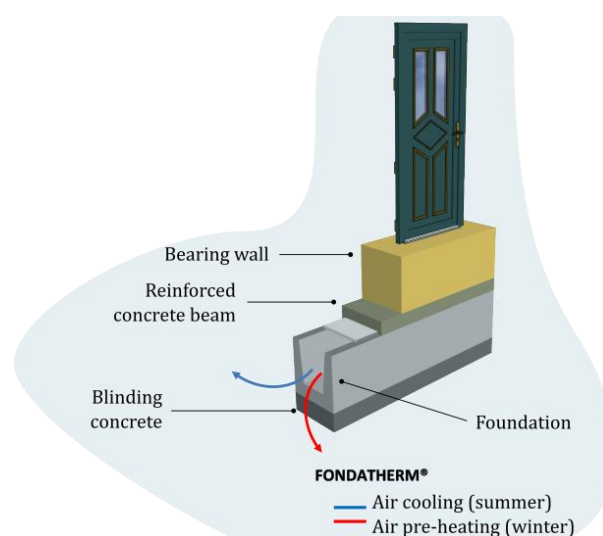


Figure 1: Main components of the Fondatherm technology

Nevertheless, all of these advantages are unnecessary if the technical solution is not economically viable. Indeed Fondatherm won't be set up on new building constructions if it does not mean short investment payback and more generally financial savings. It furthermore has to present a real advantage compared to the traditional EAHE. The total cost (materials, precast and laying) of Fondatherm has been estimated between 350 and 550 $\text{€} \cdot \text{m}^{-1}$ (an average around 450 $\text{€} \cdot \text{m}^{-1}$) by Patrick CESCHIN thanks to feedback on several installation on building construction. This cost has to be compared to that of a traditional foundation (Figure 2) since in all cases it is an inseparable part of the building structure. The company Patrick CESHIN estimated that cost around 235 $\text{€} \cdot \text{m}^{-1}$, consequently the Fondatherm net price is 215 $\text{€} \cdot \text{m}^{-1}$.

In order to study the economic viability and the performance of this innovative solution, prototypes has been installed and monitored on two tests buildings (Table 3) close to Auxerre in France:

- The extension of a retirement home built in 2012 for twelve resident in order to preheat and cool the air for the thermal comfort,
- A wine warehouse built in 2011, in order to maintain the air temperature between 13 °C and 15 °C as required for a good wine storing.

These two test buildings enable to gather data about the potential energy gains and besides the validation of the structural aspect of the foundation, they allow to evaluate the economic competitiveness of Fondatherm. Table 3 shows that even if the yearly energy gains are substantial – more than 4 and over 1 MWh for the retirement home and the wine warehouse respectively – the cost per kWh is not competitive with the gas and electricity prices in all cases: considering the solution 1 for the repayment, the cost of the energy supplied by Fondatherm is around $23 \text{ c}\text{€}.\text{kWh}^{-1}$ for the retirement home and about $92 \text{ c}\text{€}.\text{kWh}^{-1}$ for the wine warehouse against respectively 20.5 and $8.35 \text{ c}\text{€}.\text{kWh}^{-1}$ for the electricity and the gas in the European Union according to the French Ministry of Environment (Ministère de l'Environnement de l'Énergie et de la Mer, 2016).

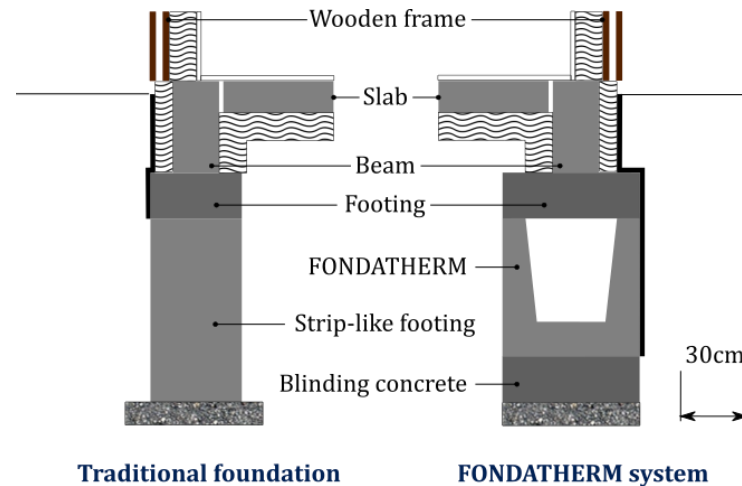


Figure 2: Comparison between a traditional foundation and the Fondatherm system

The financing solution 1 is therefore competitive with electricity prices for the retirement house, but not with the gas prices. Omitting the costs due to interest rate (solution 2), the energy from the geothermal foundation of the retirement home is even competitive with the gas prices. On the contrary, the investment for Fondatherm on the wine warehouse appears to be too expensive.

Table 3: Cost of energy savings for two building integrating Fondatherm

| Tested building | Fondatherm system | | Investment | | Repayment ($\text{k}\text{€}.\text{y}^{-1}$) | | Energy gains ($\text{kWh}.\text{y}^{-1}$) | Cost ($\text{c}\text{€}.\text{kWh}^{-1}$) | |
|-----------------|-------------------|-----------|------------------------------|---------------------------|--|------------|---|---|------------|
| | Length (m) | Depth (m) | Gross ($\text{k}\text{€}$) | Net($\text{k}\text{€}$) | Solution 1 | Solution 2 | | Solution 1 | Solution 2 |
| Retirement home | 80 | 1.5 | 38 | 16 | 1 | 0.32 | 4385 | 23 | 7.3 |
| Wine warehouse | 100 | 1-2 | 45 | 20 | 1.3 | 0.4 | 1200 | 92 | 33.3 |

Solution 1: Repayment considering 50 years lifetime and 6% interest rate
 Solution 2: Repayment considering 50 years lifetime and 0% interest rate

As for the traditional EAHE, Fondatherm appears to be efficient on an energy point of view. As previously explained, it also solved some technical limitations inherent to the EAHE such as the digging. But the analysis of the prototype energy cost showed that there exist both economically viable and unviable configurations, which prove that its integration to buildings has to be carefully analyzed in order to supply the best performances. The understanding and the potential improvements of Fondatherm are the object of the project of the same name.

1.3. *THESIS OBJECTIVES AND FONDATHERM PROJECT OUTLINES*

The technical & scientific objectives of this project are detailed in Table 4 and focus on:

- the mechanical resistance of the concrete,
- the off-site prefabrication optimization and replication easiness,
- the outlet air quality,
- the development of a thermal modelling tool,
- the study of the coupling of the foundation with other energy systems like air handling units and heat recovery units,
- the development of a dashboard to inform the users of the state of the foundation and the energy savings it induced

Five partners shares this work (Table 4): the construction company Patrick CESCHIN SAS at the origin of the project, the French Scientific and Technical Centre for Building (CSTB), the companies CIAT and INDUSTRIELEC and the Centre for Energy and Thermal Sciences of Lyon (CETHIL) which is a laboratory of the engineering school INSA of Lyon, CNRS and Univ. Lyon 1. The general objective of the project is to develop a turnkey solution for the integration of Fondatherm into buildings. The targeted market is new building constructions, mainly those of the tertiary and services sectors. It can eventually be adapted for civil engineering works or agricultural buildings.

The framework of this thesis is thus the Fondatherm project and its content is mainly made of the workpackages D and E (see Table 4). The general objective is the improvement of the understanding of the thermal behaviour of the foundation aiming at being able to develop a system as efficient as possible, from both an energy and a financial point of view.

Hence, starting from the state of the art of EAHE, especially about the way to model it, Chapter 2 identifies the specifications of the geothermal foundation and consequently the constraints and the best modelling approach to be used.

Then, Chapter 3 focuses on the mathematical description of a coupled heat and moisture transfer model within soils and concrete, necessary to finely represent Fondatherm.

Chapter 4 develops the numerical solution and the local validation of the coupled model.

Furthermore, a simpler model, considering only sensible heat transfers within soil and concrete is presented in Chapter 5. This model has been reduced with balanced realization method in order to speed up the calculation and to be able to supply quickly results to building designers and foundation regulation and control.













The experimental facilities are introduced in Chapter 6. The monitoring of a full-scale building allowed the evaluation of the energy performance of Fondatherm over one year. Some conclusions about its thermal behaviour can also be drawn.

Then, the two modelling results are compared against the recorded data in Chapter 7.

The Chapter 8 reports the study of the coupling between the foundation and a double flow air handling unit and suggests some improvements.

Finally, the main conclusions of this work are drawn in Chapter 9, and recommendations for future work are proposed.

Table 4: Work packages and tasks details of the Fondatherm project

|  | | |
|---|---|--|
| Technological and scientific locks | Tasks | Workpackage leader partner |
| A. <i>Foundation block sizing</i> | i. Block sizing in function of the building and the risks exposure (fire, seism, flooding) of the blocks |  <small>www.patrickceschin-btp.fr</small> |
| B. <i>Manufacture process for precasting, execution and assembling</i> | i. Develop the precasting manufacture process ii. Develop the block assembling techniques, allowing easy execution on site and maintenance |  <small>www.patrickceschin-btp.fr</small> |
| C. <i>Outlet air hygienic quality</i> | i. Identify the risks linked to the foundation outlet air quality (bacteriological, chemical, particles, dust, radon, etc) ii. Develop a methodology for the monitoring and maintenance iii. Conception of suitable preventive and curative solutions (chemical treatment of the concrete, cleaning, etc.) |  <small>le futur en construction</small> |
| D. <i>Foundation energy and thermal modelling</i> | i. Literature survey about the traditional EAHE ii. Identify the specifications of the geothermal foundation iii. Define and develop several modelling level iv. Validation of the numerical codes against experimental data v. Study of the coupling of Fondatherm with several energy systems |   <small>INSTITUT NATIONAL DES SCIENCES APPLIQUÉES LYON</small> |
| E. <i>Full scale monitoring of a building equipped with Fondatherm</i> | i. Identification of the required data: meteorological data, ground temperature, ground humidity, foundation concrete temperature, flowing air temperature and relative humidity, etc. ii. Conception of the monitoring: choice of the sensors and the data loggers, connection with the building computer network iii. Analysis of the data and the geothermal foundation thermal and energy behaviour |   <small>INSTITUT NATIONAL DES SCIENCES APPLIQUÉES LYON</small> |
| F. <i>Development of an adapted air handling unit for Fondatherm</i> | i. Sizing of a suitable fan and ventilation ducting for Fondatherm ii. Development of a suitable damper allowing an adapted control of Fondatherm |  |
| G. <i>Control strategy</i> | i. Definition of the rules for the control strategy ii. Definition of the required data for this strategy iii. Definition of the monitoring |   <small>INSTITUT NATIONAL DES SCIENCES APPLIQUÉES LYON</small> |
| H. <i>Dashboard and boxcontrol development</i> | i. Development of the boxcontrol for the data recovering and transmission ii. Development of the user interface and the control tools |  |

Chapter 2. GROUND HEAT EXCHANGERS, EARTH-TO-AIR HEAT EXCHANGERS: STATE OF THE ART

2.1. GENERAL KNOWLEDGE ABOUT GROUND HEAT EXCHANGERS AND EARTH-TO-AIR HEAT EXCHANGERS

Here the functioning principle of an earth-to air heat exchanger and the most common existing configurations are introduced. The influence of the designing factors as well as extrinsic variables on their performances is exposed and analysed. Numerous numerical and experimental results have been gathered and allow getting an idea of the potential energy savings and efficiency, thermal comfort improvement, and the advantages and limitation of this low-tech system.

2.1.1 GROUND HEAT EXCHANGERS AND EARTH-TO AIR HEAT EXCHANGER: DEFINITIONS, CONFIGURATIONS AND PHYSICS

2.1.1.1. Definitions and configurations

Ground coupled heat exchangers (GCHE) simply consists in circulating a fluid in a pipe network buried in the ground (Soni et al., 2015). These systems are used for a wide variety of applications such as space conditioning, water heating, agricultural drying etc. They can be classified according to:

- the connection type of the tube network: parallel or series
- the orientation of the pipes: horizontal or vertical
- the flow substance: air or water

The last consideration is the most common, as lots of features are consequences of the kind of fluid used. In the case of airflow, they are designated by the term earth-to-air heat exchanger (EAHE⁴). If the fluid is water/water+glycol, they are called borehole heat exchangers (BHE).

Table 5: Comparative advantages of EAHE and BHE

| EAHE | BHE |
|---|--|
| Long life | High efficiency |
| Cost effectiveness | Working for all seasons |
| Environmental friendly (no refrigerant) | No air contamination problem |
| Stable capacity with time | No condensation problem within the tubes |
| Simple equipments (no compressor) | |
| Low maintenance cost | |

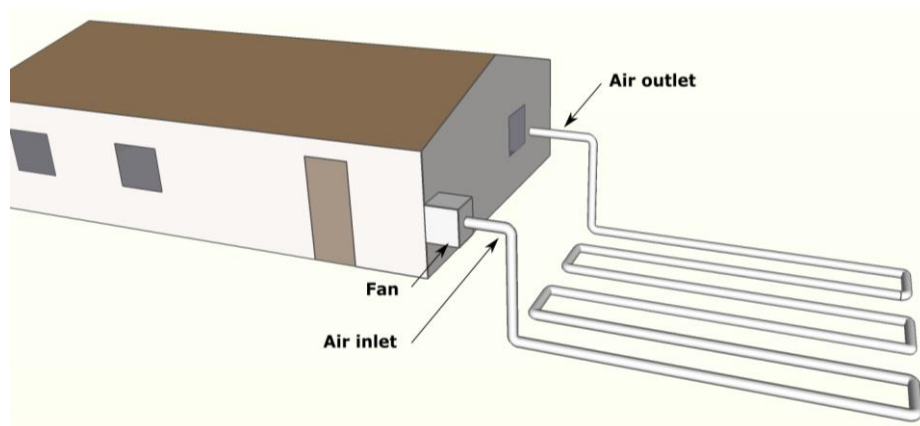
⁴ This is the most common acronym, but EAHX, ETAHE, ATEHE can also be found in the literature.

The assembly of the BHE can be regular or direct. In the regular mounting, the buried pipe in the ground is usually plastic and enables water to circulate and exchange heat with the condenser coil of the heat pump. In the direct mounting, the condenser coil, usually copper, is buried into the ground and allows a refrigerant fluid (usually R134a) to circulate.

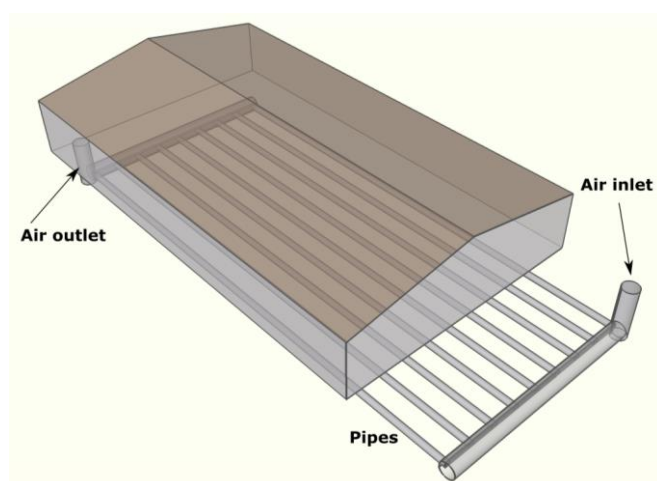
The relative advantages of the two systems are listed in Table 5 (Ozgener, 2011; Soni et al., 2015). The direct BHE are efficient but the economic viability laid on several parameters such as climate, soil nature, operating, etc.

The current work will focus only on the EAHE systems, as the main object of this thesis is actually the study of an innovating EAHE. According to the literature review made by Peretti et al. (2013), an EAHE can be defined by its technical characteristics. It is most of the time composed by:

1. An air intake equipped with a filter. It can be located outdoor, in that case the EAHE is mounted in 'open loop', or indoor and the mounting is thus called 'closed loop',
2. A buried pipe network in the ground. It can be situated in open space or beneath a building. The network can be a grid, a serpentine or a ring layout. Some examples are given on Figure 3. The pipes can be made of plastic, aluminium, steel or concrete,
3. A fan that blows or sucks air through the pipes.



(a)



(b)

Figure 3: Two configuration examples: (a) closed loop serpentine layout next to a building and (b) grid open loop layout beneath a building

2.1.1.2. Physics of the EAHE functioning

Thanks to these equipments, the EAHE systems use the ground's thermal storage capacity to dampen and under certain conditions to shift the ambient air temperature. As illustrated on Figure 4, their performances are influenced by the heat exchanged between the flowing air and the pipes inner surface by convection. This quantity is dissipated mainly by conduction within the surrounding soil. Conduction within the soil and convection between the air and the pipe wall are fundamentally in interaction: the temperature of the soil is disturbed by the presence of the pipes. Then the heat contained in the circulating air is transported by advection due to the air movement. Since the air contains humidity, condensation may occur if the surface temperature of the pipe is lower than the dew point of the air. Reversely, if the pipe inner surface is wet, liquid water evaporates if the air is not saturated. Finally, the moisture quantity and the moisture flow modify the heat transfers in the soil. Its influence is most of the time neglected in the literature. Due to the small pipe radius compared with the buried depth, the channel wall temperatures tend to be uniform: the long wave radiations are thus also commonly neglected.

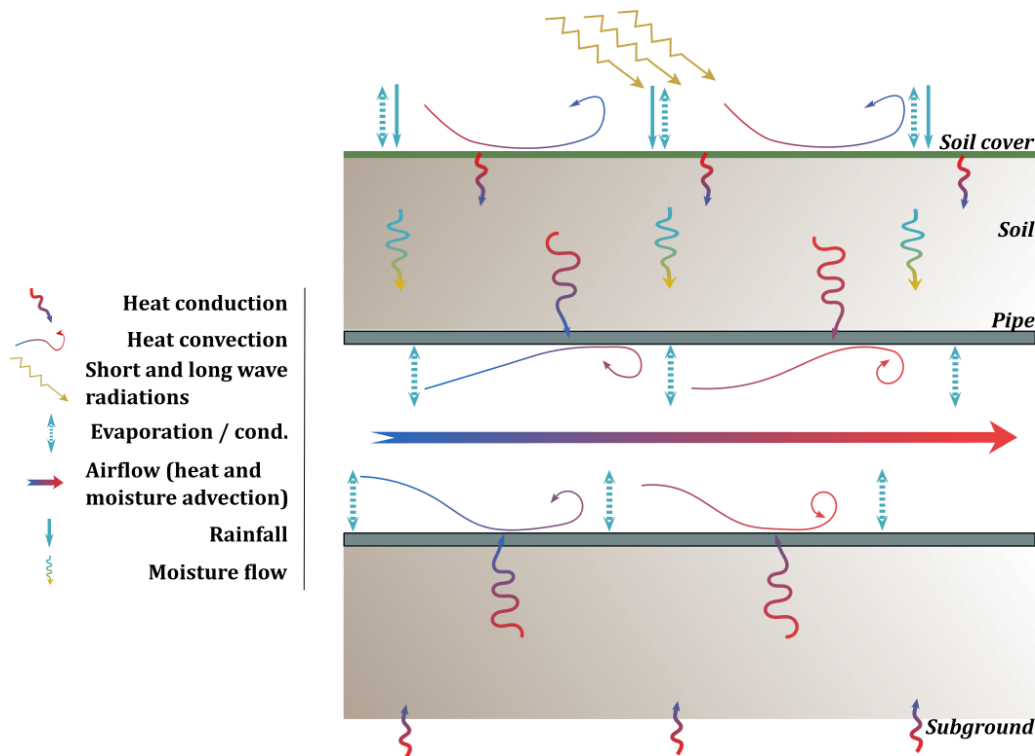


Figure 4: Main physical phenomenon that influence the EAHE thermal performance (heating conditions)

Intrinsic parameters of the EAHE as well as extrinsic parameters enhance or limit the previous transfers. Intrinsic parameters such as pipes depth, diameter, length, air speed, tube spacing and the position of the pipes relative to the building have been widely investigated in the past decades and the main conclusions will be sum up in the next subsection 2.1.2. Furthermore, environmental factors influence the EAHE performances such as climate, soil nature and the control strategy (related to the building use). They will be analyzed in the subsection 2.1.4.

2.1.2 DESIGN FACTORS INFLUENCING THE EAHE PERFORMANCES

2.1.2.1. Pipe buried depth

Solving the heat balance at ground surface and the one-dimensional heat conduction equation led several authors to propose an analytical solution for the undisturbed ground temperature as a function of depth and time. Thiers and Peuportier (2008) wrote for example

$$T_{und}^g(z, t) = \overline{T_{und}^g(z_0)} + \sum_{n=1}^l A_n(z_0) e^{-\frac{z}{\delta(\omega_n)}} \sin\left(\omega_n t - \zeta_n - \frac{z}{\delta(\omega_n)}\right) \quad (2.1)$$

where $\overline{T^g(z_0)}$ is the annual mean ground surface temperature, $A_n(z_0)$ and ζ_n the amplitude and the phase of the sinusoidal thermal wave of pulsation ω_n and δ the penetration depth of the ambient thermal wave, given by (2.2). A daily wave has a penetration depth of about 20 cm, while an annual wave reaches around 3 m depth. Of course these values are indicative and depend on the soil type and the ground cover. As the usual buried depth of an EAHE is between 1-3 m, the ground temperature is often approximated to a sinusoidal function of period one year exponentially dampened with depth. In the previous formula, it means that $l = 1$.

$$\delta(\omega) = \sqrt{\frac{2\alpha_s}{\omega}} \quad (2.2)$$

This is experimentally verified by many authors. An example for the soil temperature evolution throughout the year in Val-de-Mercy (France) is reported on Figure 5. Experimental data were recorded for the year 2016 for the ground surface, 80cm and 1.6m depth. They are compared to the results yield by the formula (2.1) with a daily and an annual pulsation ($l = 2$).

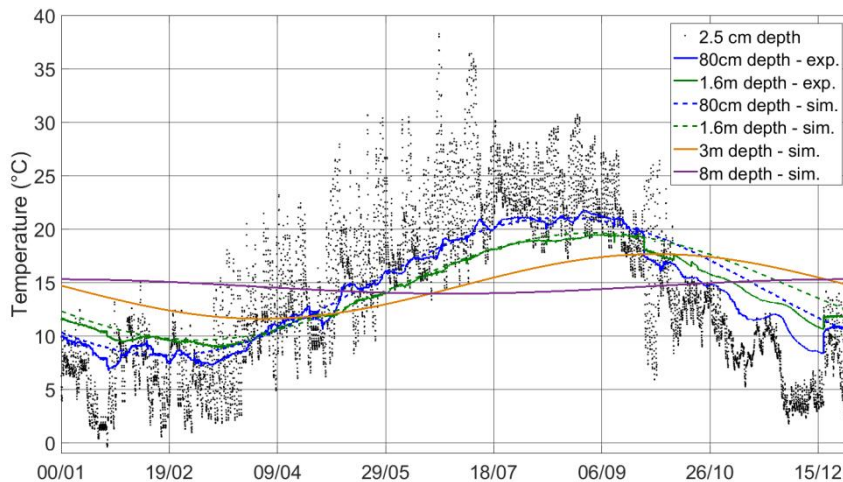


Figure 5: Soil temperature collected for several depths in Val-de-Mercy (France) against analytical model (2.1)

In view of the amplitude dampening and the shifting of the ambient air temperature by the ground, the flowing air in a buried pipe will be most of the time colder than the ground in

winter, and hotter in summer, and that the deeper the pipe will be, the more true it will be. This is consistent with the three zones of the ground that are distinguished by Florides and Kalogirou (2007):

1. The surface zone, from the ground surface to 1m depth, is very sensitive to short time changes of weather conditions,
2. The shallow zone, extending from 1m to between about 8 m – 20 m according to the soil type is characterized by an almost constant ground temperature close to the mean annual average air temperature,
3. The deep zone, below 8m-20m, for which the temperature is constant and very slowly increasing with depth.

The most common EAHE are set in the shallow zone.

Tzaferis et al. (1992) carried out a sensitivity analysis on eight models for several parameters. The influence of the pipe depth on the outlet air temperature is analyzed in summer conditions. As illustrated on Figure 6, even though slight differences exist between the eight models, the tendencies are similar: the deeper the pipe is buried, the lower the outlet air temperature is. Mihalakakou et al. (1996) experimentally studied the outlet air temperature for three different depth (1.2 m, 2 m and 3 m) and showed that the cooling potential (the heat transferred to the soil) was increased with the burying depth. Lee and Strand (2006, 2008) developed an analytical model, implemented it in the building software modelling EnergyPlus, and came to similar conclusion. A steady-state study in summer conditions (cooling) shows that as the pipe depth increases, the outlet air temperature decreases. The amplitude of this decreasing is variable according to the location. Trzaski and Zawada (2011) confirm this tendency both for cooling and for heating. However, Deglin et al. (1999) nuanced these conclusion via experimental results, and observed that the performance increasing was strong for cooling but lower for heating.

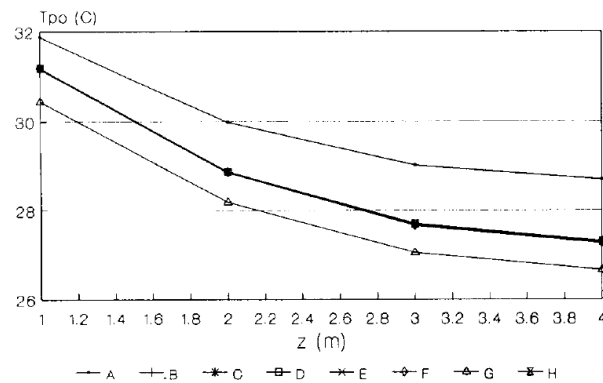


Figure 6: Influence of the pipe depth on the outlet air temperature for eight EAHE models (Tzaferis et al., 1992)

Yang et al. (2016) developed a model assuming periodic oscillations of the ground temperature, and semi-infinite distance diffusion in the soil. This analytical model considers both daily and annual periodic fluctuation of ambient air, pipe air and soil temperature. The interaction between the pipe and the ground is taken into account through an 'excess fluctuating temperature'. The classical conclusions about the influence of buried depth, the pipe radius, the pipe length and the flow rate on the outlet air temperature for a typical

summer day are made. They furthermore proposed an additional analysis, based on the influence of the four latter parameters on the daily and annual phase shift and amplitude fluctuation. As illustrated on Figure 7, they concluded that:

- The daily phase shift is constant when the buried depth is above 1 m,
- The daily fluctuation amplitude decreases and tends toward zero when the buried depth is above 1 m,
- The annual shift increases then decreases with depth, and the maximum time lag is about 43 days,
- The annual fluctuation amplitude is stable from 7 m depth.

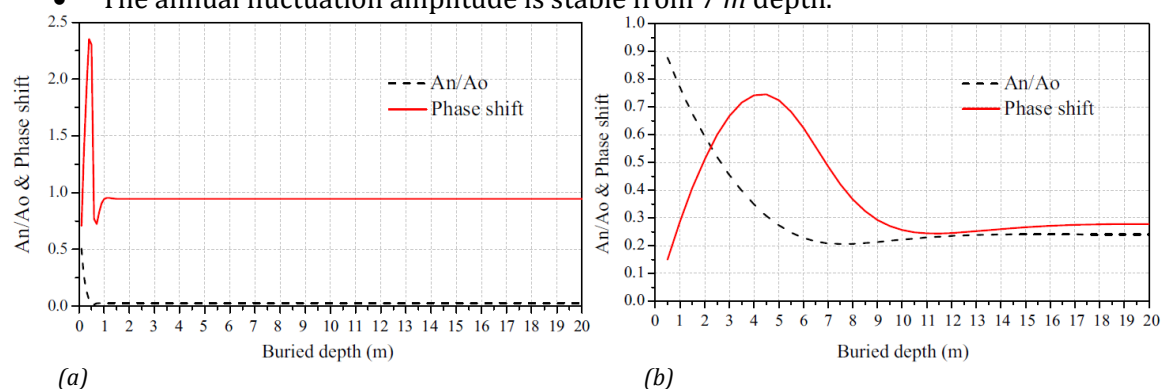


Figure 7: The effect of buried depth on daily (a) and annual (b) phase shift and amplitude dampening (Yang et al., 2016)

2.1.2.2. Pipe length

Logically, the longer the EAHE pipes are, the more heat is exchanged between the flowing air and the soil. In the theoretical case of an infinite EAHE, the outlet air temperature would be equal to the ground temperature. As expected and confirmed by several studies of the past decades, the performance of the EAHE will thus get better. The work published by Tzaferis et al. (1992) led under summer climate for eight models showed a positive impact of the increasing length (Figure 8), and confirmed by a numerical study according to Mihalakakou et al. (1996), in which the authors varied the tube length from 30 to 70 m. Deglin et al. (1999) refined the analysis and observed that the average heat transfer is more important in the first half of the pipe: 70 % of the average heat transfer power comes from the first 10 m according to them. Lee and Strand (2006, 2008) highlighted that the amplitude of the temperature decreasing (in summer conditions) along the pipe length was variable according to the location. The results of Wu et al. (2007) - obtained thanks to a CFD code for the flowing air and a three-dimensional numerical finite volume based model for the soil - were consistent with the latter. Considering both the heating and the cooling potential, Trzaski and Zawada (2011) used their three-dimensional model based on finite element method to prove that extend the pipe length improves the performances of the EAHE: the heating supplied is raised by around 18% and the cooling by about 20 % when the pipes are lengthened from 35 m to 45 m.

Yang et al. (2016) confirmed again the effect of the pipe length on the outlet air temperature, and also observed that:

- The daily phase shift increases linearly with length,
- The daily fluctuation amplitude decreases with length,

- The annual phase shift and fluctuation amplitude follow similar trends.

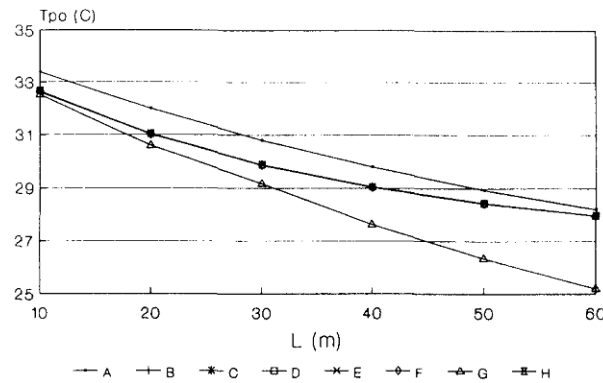


Figure 8: Influence of the pipe length on the outlet air temperature for eight EAHE models (Tzaferis et al., 1992)

Finally, it is noticeable that most of the heat transfers take place in the first part of the pipe length. As shown by Gan (2015), the heat transfer rate per unit length decreases when the pipe length increases. Since the pressure drop increases with the pipe length - and consequently the fan energy consumption - and equally the excavation cost, one has to keep in mind that a trade-off has to be made between the thermal efficiency, the fan consumption and the cost. In practical terms, Ascione et al. (2011) suggested 50 m is the best compromise: while 10 m is too short to ensure a significant temperature drop/rise, more than 70m induces a too high pressure drop resulting in uninteresting system.

2.1.2.3. Pipe diameter

The study of the influence of the pipe diameter (or hydraulic diameter) on the EAHE performances may look a bit confusing as several authors considered different pipe diameter with a constant air velocity, while others considered a constant airflow rate.

Maintaining a constant air velocity, it has been proved that an increase of the outlet air temperature of up to 10°C in summer condition - thus a decrease of the cooling potential - is induced by a change on the pipe radius from 5 cm to 25 cm (cf Figure 9) (Mihalakakou et al., 1996; Tzaferis et al., 1992). This was explained by a reduction of the convective heat transferred. Indeed Deglin et al.(1999) calculated a reduction of about 38% of the specific surface⁵ when the pipe diameter change from 25 cm to 40 cm. A steady-state analysis in summer conditions (cooling) led to similar conclusions (Lee and Strand, 2006, 2008; Niu et al., 2015). It was also mentioned the lowering of the convective heat transfer coefficient as one of the cause of the reduction of the convective heat transferred.

On the other hand, Trzaski and Zawada (2011) studied the influence of the piped diameter with a constant airflow. The area of the exchanging surface is still increased, but the flow velocity is reduced, as well as the heat transfer coefficient. A slight decrease of the cooling and heating potential is observed, but the influence of the diameter is very limited according to the authors.

⁵ the pipe walls' area divided by the volumetric airflow rate in $m^2 \cdot m^{-3} air$

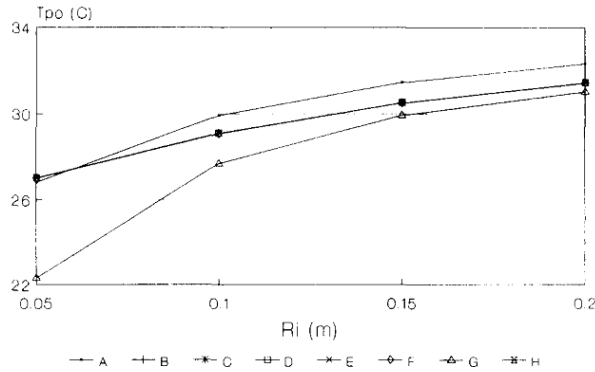


Figure 9 : Influence of the pipe radius on the outlet air temperature for eight EAHE models (Tzaferis et al., 1992)

A transient calculation on 24 hours – study in which the air velocity is kept constant - confirmed the first tendencies: in terms of outlet air temperature, the performance of the EAHE is reduced (Wu et al., 2007). Nevertheless, in terms of energy, the cooling potential of the EAHE is improved as illustrated on Figure 10. The elevation of the outlet air temperature is balanced by the increasing of the airflow.

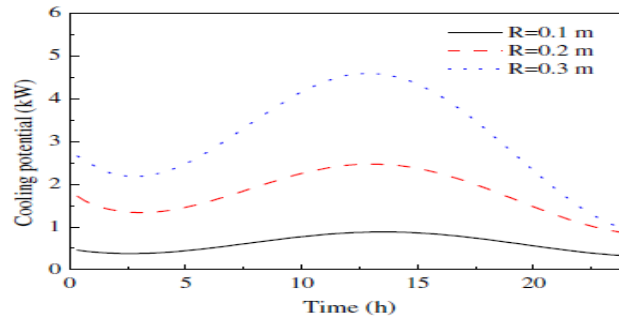


Figure 10: Cooling capacity variation of the EAHE for different radii (Wu et al., 2007)

Yang et al. (2016) confirmed that the outlet air temperature decreases when radius increases. Only a small difference is observed: about 0.6 °C for R from 5 cm to 1 m. They additionally studied the influence of the pipe radius on the daily and the annual phase shift and the amplitude dampening of the ambient air temperature. As showed on Figure 11, the daily phase shift decreases and the daily amplitude dampening increases with radius. The influence on the annual values is more complex: the amplitude dampening decreases then increases with radius, while the phase shift follows opposite trends.

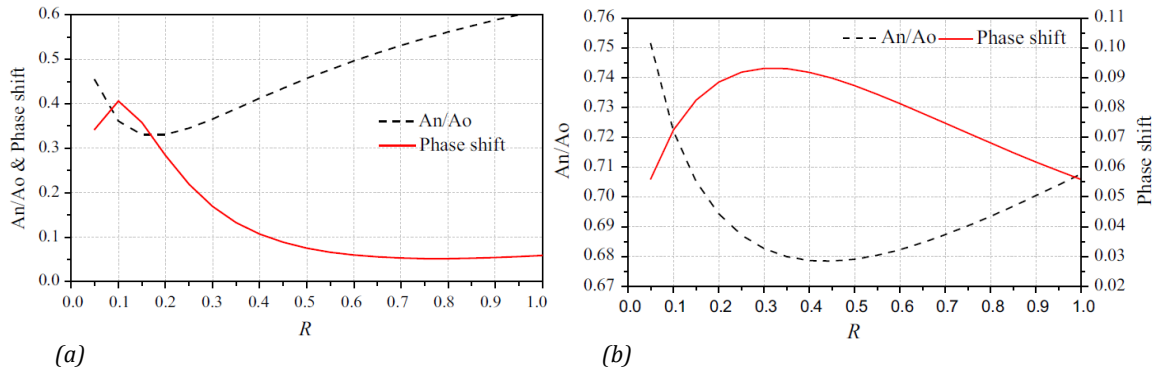


Figure 11: The effect of pipe radius on daily (a) and annual (b) phase shift and amplitude dampening (Yang et al., 2016)

Lastly, another fact should be considered when evaluating the performance of the EAHE: the pressure loss and consequently the fan energy consumption are affected by a change in the pipe diameter, and of course in air velocity which is treated in next subsection.

2.1.2.4. Pipe thickness and material

The observations made in the literature in the case of EAHE, proved that the material of the pipes influences the cost of the installation, and its durability, but not the thermal performance. Badescu (2007) modelled three different materials (copper, PVC and steel) and proved that it has a small influence on the annual energy provided by or supply to the soil. Ascione et al. (2011) tested concrete, plastic and metallic materials, and observed that all lead to very similar energy gains. As the pipe thickness is small (5 mm in the case of PVC, 7 mm for the metallic material 7 cm for the concrete), the thermal resistance of the tube is still low compared to that of the ground. In turn, Serageldin et al. (2016) tried copper, PVC and steel and noted minor changes of the outlet air temperature.

The choice of the tube material has to be made according to other criteria such as the mechanical resistance, the corrosion, and the hygiene (Ascione et al., 2011; Peretti et al., 2013). Indeed, some materials are more favourable to mould growth, and eventually allow radon transfers.

2.1.2.5. Pipe number and spacing

In the design process of a building construction project, the ventilation airflow rate is usually a requirement, given by health standards. In order to supply this airflow, to achieve the energy savings objectives – including the additional fan energy consumption due to pressure loss – and to master the costs, the solution proposed by De Paepe and Janssens (2003) consists in multiplying the number of pipes in parallel and reduce their diameter. As explained by Trząski and Zawada (2011), it increases the exchanging surface and enhance the available volume of soil for the heat storage or release. The drawback is the convection heat exchange coefficient reduction due to the air velocity lowering. However, the numerical simulation showed that multiply the number of pipes increases the performances: two pipes in parallel increase the performance by about 23 % in heating mode and 26 % in cooling mode.

The arising question from the adding of pipes is the influence they have on each other, and the consequences on the whole EAHE performance. Trząski and Zawada (2011) found that both the heating and the cooling potential difference between pipe spacing of 1m and 1.5 m was below 4 %. These moderated but real effects showed that increase the pipe spacing increases the heating and cooling performance. The interaction between the pipes in parallel appeared to be detrimental. This is quite consistent with the rules proposed by De Paepe and Janssens (2003), who advised to space the pipes of at least 1 m.

The complexity of the EAHE layout can be raised and might improve the thermal performance. For that reason, Kepes Rodrigues et al. (2015) proposed the use of the Constructal Desing method to determine the best arrangement geometry of an EAHE. The three-dimensional numerical model developed by Vaz et al. (2011) enable them to evaluate the performance of each configuration in term of thermal potential defined as the monthly average temperature difference between the outlet air and the ambient air temperatures. The

best tested geometrical configurations sometimes change a little bit while considering the cooling or the heating needs, but generally speaking, the four pipes arranged in a rectangular array appears as the optimal one, even if it does not exit one universal shape that maximizes the thermal performance of all the EAHE. This study showed that the influence of the pipe on each other and the soil portion they occupy within the ground are determinant. Diminish the impact of the pipe between them can improve the performance of the installation. Indeed, 'flat shape' like elongated triangle gives better results. The influence of one pipe on the other is minimized, and the pipes tend to be at the same depth.

2.1.2.6. Air velocity or air flow rate

The influence of the air velocity is similar to the influence of the pipe radius. Tzaferis et al. (1992) showed that – for steady-state cooling conditions – increasing the air velocity raises the outlet air temperature (Figure 12). Other studies came to the same trends for air velocity varying until 20m.s^{-1} (Lee and Strand, 2006, 2008; Mihalakakou et al., 1996).

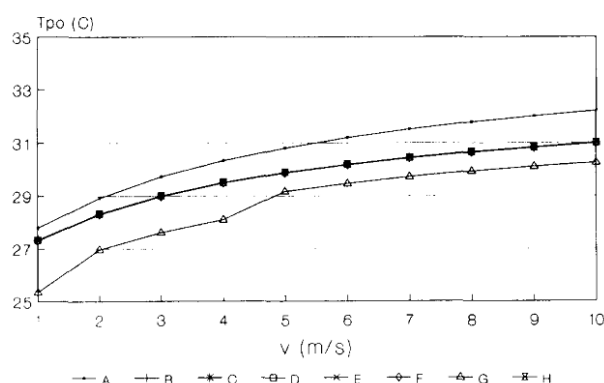


Figure 12 : Influence of air speed on the outlet air temperature for eight EAHE models (Tzaferis et al., 1992)

According to Deglin et al. (1999), when the air velocity increases from 2 m.s^{-1} to 4 m.s^{-1} , the thermal efficiency is reduced by 20 %. The efficiency of the heat exchange for each air volume unit (Wh.m^{-3}) is lower. This decreasing of the thermal performance is accentuated when the ground conductivity declines.

Bansal et al. (2009) studied the heating potential of an EAHE thanks to a CFD model validated against experimental results. The investigation is performed under steady-state conditions on January 12, 2008. The ground temperature is assumed constant, the pipe is buried at 2.7 m depth, its diameter is 15cm, and is 23.42m long. If the air velocity rises from 2 m.s^{-1} to 5 m.s^{-1} , the temperature elevation drops from $4.8\text{ }^{\circ}\text{C}$ to $4.1\text{ }^{\circ}\text{C}$. However, the energy recovered from the ground rose from 423 to 847 kWh. The same study is conducted by Bansal et al. (2010) for summer conditions. The air velocity increasing induces cooling gains increasing from 1.2 to 3.1 MWh, but the temperature drops fall from $12.7\text{ }^{\circ}\text{C}$ to $8\text{ }^{\circ}\text{C}$. These results should nevertheless be treated with care because of the large discrepancies between the simulation and the experimental results: up to $4\text{ }^{\circ}\text{C}$ difference on the temperature outlet.

Taking into account both the sensible and latent exchanges between the circulating air and the pipe walls, it has also been proved that the lower the air velocity is, the faster the air temperature decreases in summer conditions (Niu et al., 2015). Yang et al. (2016) studied the influence of the airflow rate on the daily and the annual phase shift and the amplitude dampening of the ambient air temperature by the EAHE (Figure 13):

- The daily phase shift evolution is complex, but has a maximum value reached for an airflow rate more or less equal to $0.6 \text{ m}^3 \cdot \text{s}^{-1}$,
- The annual phase shift decreases from its maximum values reached for an airflow rate equal to $0.05 \text{ m}^3 \cdot \text{s}^{-1}$,
- Both the daily and the annual amplitude fluctuation increases with an increasing airflow rate.

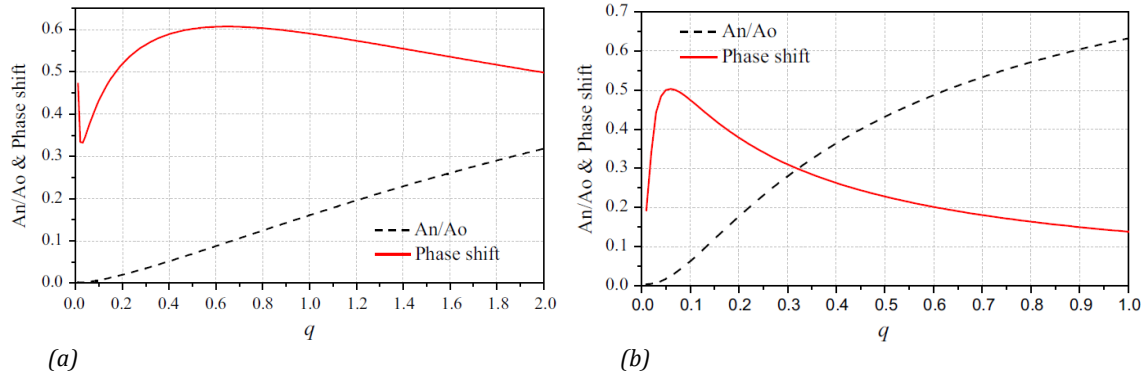


Figure 13: The effect of airflow rate on daily (a) and annual (b) phase shift and amplitude dampening (Yang et al., 2016)

2.1.3 EVALUATION OF THE EAHE PERFORMANCES

2.1.3.1. Efficiency, coefficient of performance and convective heat coefficient

The effects of EAHE intrinsic parameters on the outlet air temperature, on the heat exchanged and on the phase shifting and amplitude dampening of the ambient air temperature have been widely exposed in the previous subsection. However, a global analysis, considering at the same time the thermal exchanges, the pressure loss and the economic aspect are scarce.

Pfafferott (2003) carried out three buildings equipped with EAHE systems. Using four different indicators, it put in evidence that each building is the best according to one indicator, and the worst according to another one, as can be seen in Table 6. The Fraunhofer ISE building is for example the best according to the indicator R_T but the worst according to the efficiency ε and the COP. His first analysis is simply based on the outlet air temperature. In order to measure the intrinsic performance of the EAHE – without including the influence of climate he proposed to use the ratio defined by

$$R_T = \frac{T_{outlet,max} - T_{outlet,min}}{T_{inlet,max} - T_{inlet,min}} \quad (2.3)$$

A second analysis can be made according to the comparison of the energy gains, directly linked to the convective thermal exchange coefficient h_c . The authors proposed an original approach: the energy supplied (heating or cooling) can be sorted according to the ambient air temperature value. Such graph put in evidence the strong need for a regulation as a non negligible part of cooling energy is used at low ambient air temperature, and vice versa, heating energy is sometimes used at high ambient air temperature. As a conclusion he proposed a time control or a temperature control.

A third analysis can be made in terms of efficiency. Considering a sinusoidal evolution for the ambient air and the soil temperature – constant along the pipe - the outlet air temperature can be written:

$$T_{outlet}(t) = T_{und}^g(t) + \left(T_{inlet}(t) - T_{und}^g(t)\right) e^{-NTU} \quad (2.4)$$

where

$$NTU = \frac{h_{c,EAHE} A_{EAHE}}{\dot{m}_a c_a} \quad (2.5)$$

The number of transfer units NTU can be seen as an indicator for the intrinsic thermal efficiency of the EAHE. It is the quotient of the heat transfer from the ground to the air divided by the soil thermal capacity. The coefficient $h_{c,EAHE}$ is here the overall heat transfer coefficient (averaged on the EAHE wall surface). The higher the NTU is the more efficient the EAHE is. Another way to express the efficiency of the EAHE in percentage is given by the equation (2.6). This does not include a global analysis embedding the fan energy consumption.

$$\varepsilon = \frac{T_{inlet}(t) - T_{outlet}(t)}{T_{inlet}(t) - T_{und}^g(t)} = 1 - e^{-NTU} \quad (2.6)$$

The COP of the system corrects this weakness and has been calculated by the author according to (2.7). $\Delta p \Phi_a$ is used instead of fan power consumption because the ventilation unit is installed in a building in all cases.

$$COP_{pl} = \frac{\sum_{t_{op}} (Q_{heat} + Q_{cool})}{\sum_{t_{op}} \Delta p \Phi_a} \quad (2.7)$$

Finally, the authors noted that the soil and the position of the building relative to the EAHE pipes play a role as important as the pipe diameter and other intrinsic parameters.

Table 6: Performance of three EAHE installations according to four different indicators (Pfafferott, 2003)

| | R_T (K.K ⁻¹) | h_c (W.m ⁻² .K ⁻¹) | ε (K.K ⁻¹) | COP (kWh _{th} .kWh _{mech} ⁻¹) |
|-----------------------|----------------------------|---|------------------------------------|---|
| <i>DB Netz AG</i> | 0.28 | 5.5 | 0.944 | 88 |
| <i>Fraunhofer ISE</i> | 0.47 | 5 | 0.766 | 29 |
| <i>Lamparter</i> | 0.36 | 3.2 | 0.804 | 380 |

2.1.3.2. Heating and cooling gains

There is also a dilemma in the way to calculate the heating or cooling potential (i.e. the heat gains). The equation (2.8) for example measures the intrinsic performance of the EAHE, without consideration of the indoor air (Pfafferott, 2003; Sodha et al., 1985).

$$Q_{EAHE} = \dot{m}_a c_a (T_{outlet} - T_{inlet}) \quad (2.8)$$

Al-Ajmi et al. (2006) proposed to add to the previous formula the temperature elevation due to the fan heat dissipation – only for the cases where the fan is placed at the pipe inlet. Trombe et al. (1991) used the formula (2.9) where T_{ref} is successively taken equal to the ambient air temperature and 25 °C representing the comfort temperature. The first case

yields an equation similar to the previous one, while the second case fits more to the 'real' cooling potential of the EAHE. Indeed, the cooling benefits of the EAHE on the room air temperature are taken into account through this latter formulation.

$$Q_{EAHE} = \dot{m}_a c_a (T_{outlet} - T_{ref}) \quad (2.9)$$

Sawhney et al. (1999) chose to use (2.10), similar to (2.9) but where T_{nac} is the air temperature of a non conditioned room, i.e. without air delivery from an EAHE.

$$Q_{EAHE} = \dot{m}_a c_a (T_{outlet} - T_{nac}) \quad (2.10)$$

The formulation given by (2.11) is proposed by Badescu (2007) where T_{app}^g is the apparent ground temperature, assumed equal to 10°C in this work. Again, this expression is similar to the equation (2.8), where the outlet air temperature replaced the ground temperature. This is equivalent to assume that the EAHE has a perfect efficiency.

$$Q_{EAHE} = \dot{m}_a c_a (T_{app}^g - T_{ext}) \quad (2.11)$$

The equation (2.12) is a mixing between the equations (2.9) and (2.11): the outlet air temperature in (2.8) is replaced by the ground temperature at pipe depth, and the evaluation is relative to the room air temperature T_{in} (Chel and Tiwari, 2009; Tiwari et al., 2006).

$$Q_{EAHE} = \varepsilon \dot{m}_a c_a (T_{und}^g (z = \text{pipe depth}) - T_{in}) \quad (2.12)$$

But the gross heat gain calculated thanks to (2.8) is said not to be always relevant according to Hollmuller and Lachal (2014). Instead they proposed to use the formula (2.13) where $\dot{V}_{a,0}$ is the base required flow rate and $\Delta \dot{V}_a$ a possible additional flow rate for the thermal conditioning.

$$Q_{EAHE} = \dot{m}_{a,0} c_a (T_{outlet} - T_{ext}) + \Delta \dot{m}_a c_a (T_{outlet} - T_{in}) \quad (2.13)$$

Thus, if the EAHE is only designed for the hygienic air change, its cooling (or heating) gain is equal to the gross heat gain (see equation (2.8)). But if it is designed to cool the indoor building air, which imply an increase of the base air change rate, the differential of temperature between the outlet of the EAHE and the indoor air has to be considered.

2.1.3.3. General considerations - Summary

Ascione et al. (2011) made a global analysis about EAHE that enable to draw some general conclusions about the EAHE design.

First, they declared about the buried depth that theoretically 8 m seems to be ideal. This is explained by the six months time lag at this depth which means that the ground temperature is minimal in summer, and maximal in winter. Nevertheless, the cost for excavation usually increases with depth and a trade-off has to be made. According to them 3m is usually a good compromise, while 1m is not deep enough to ensure sufficient cooling and heating potential.

The second point is about the air velocity: a too high air speed is generally not beneficial because of the induced pressure loss increase and the fact that the increasing of the heat exchanges is balanced by the decreasing of the inlet/outlet air temperature difference.

Thirdly they tested five different control modes corresponding to several numbers of hours per day of EAHE ventilation during the cooling season. The best mode is that which maximizes the number of hours of utilization (15 h.day^{-1}) even when taking into account the fan energy consumption. The comparison of the EAHE performances with other passive system (such as shadings and night ventilation) completes this analysis and showed that the energy savings by the EAHE are significant.

Finally the parametric analysis has been led for three different Italian climates and this factor appeared as of crucial importance. The highest efficiency is reached for the coldest climate of Italy. For moderated climate, the energy savings don't balance the fan energy consumption. Integrating the economic aspect of the problem, the EAHE use is said to be relevant if the excavation to bury the pipes is easy and cheap.

To conclude, it seems that each project has to be designed according to the specific constraints: climate, building, soil, uses, etc. The impact of the design parameters has to be evaluated thanks to several indicators; among them at least one should include the fan energy consumption due to the pressure drops in the tubes. The control strategy appears to be decisive for the optimization of the usable energy supplying. The role played by all of these inflexible external parameters will be assessed in the next subsection.

2.1.4 EXTERNAL PARAMETERS: ENVIRONMENT AND OPERATION MODES

2.1.4.1. Soil nature and cover

The main thermal characteristics of the ground - density, thermal conductivity and specific heat - are explicitly used in Equation (2.1). Furthermore, the average and the amplitude of the ground surface temperature are given by the writing of the heat balance at soil surface. They are function of ground surface albedo, emissivity, convective coefficient, etc. (Lee et al., 2006). Thus, this simple model allows understanding that both the soil nature and the ground cover strongly influence the ground temperature at depth z and time t . As a result, the heat exchanged between the EAHE pipe's wall and the flowing air is affected by a change of soil nature or ground cover.

Kopecky (2008) conducted a sensitivity analysis on ten parameters of an EAHE analytical model. Three of them are related to the ground characteristics, five to the pipe and the airflow, one is the initial conditions and the last is the inlet air temperature. The parameters with the strongest influence on the total heat exchanged are in the order:

1. The initial temperature
2. The inlet air temperature
3. The pipe length
4. The air speed
5. The ground thermal conductivity
6. The ground specific heat

The parameters linked to the soil nature have therefore a relatively high impact on the EAHE behaviour. Mihalakakou et al. (1996) proved thanks to a numerical model that the cooling potential of an EAHE is enhanced when the soil is covered with grass (instead of the case where it is bare). Trzaski and Zawada (2011) showed that a grass lawn cover instead of a bare ground surface could increase the cooling potential by about 58 %. Nevertheless, the effect on the heating potential looks minor (less than 1 % decreasing). According to Ghosal et al. (2004), when an EAHE is buried in a soil covered with glazing, it improves its heating potential compared to the case of a bare ground surface, but it also reduces the cooling potential.

It is confirmed by several other papers focused on the soil nature. Lee and Strand (2006, 2008) carried out their parametric analysis (about the influence of pipe depth, radius, etc.) for four climates and soil natures. Even if the tendencies observed are similar for the four locations, their amplitude can be greatly different from one to another. Deglin et al. (1999) took into account the soil water content in the calculation of its thermal conductivity and density. They then compared the performance of an EAHE buried in a saturated silt soil and in a dry sand soil for a short-time period of 12 h. The saturated soil gave better performances. Ascione et al. (2011) used the model implemented in EnergyPlus and obtain similar results: the wet and heavy soils are that which supply the best EAHE performances. More specifically, the kind of soil alters differently the EAHE functioning in cooling mode and in heating mode (Trzaski and Zawada, 2011). When a sand soil is modelled instead of a sandy clay loam soil the heating potential is increased by 5 % and the cooling potential decreased by 29.9 %. Bansal et al. (2013a, 2013b) observed a maximal temperature drop between the inlet and outlet air of 15.6 °C, 17.0 °C and 17.3 °C for a soil with a thermal conductivity 0.52 $W.m^{-2}.K^{-1}$, 2.0 and 4.0 $W.m^{-2}.K^{-1}$ respectively. They concluded that if the ground thermal conductivity increases, the EAHE performances are also increased. Thanks to their transient analysis, based on the introduction of a 'derating factor', they found that this is still true, even after a long working period of 36 hours. The lower the ground thermal conductivity is, the faster the decline of the EAHE performances with time are.

It is noteworthy that in all the previously cited studies, the grounds modelled were considered homogeneous. Although the stack of different soil materials can strongly modify the EAHE thermal performance, only a few models allow the inclusion of the ground stratification. It can only be considered in two or three-dimensional numerical models (Bansal et al., 2010; Gauthier et al., 1997; Hollmuller and Lachal, 2001; Tzaferis et al., 1992). Furthermore, the soil thermal properties are highly dependent of the water content, which can vary a lot especially in the shallow ground. However, only a few models take into account the ground moisture variations. Some of them consider for example simultaneous heat and mass transfer within the soil (Kumar et al., 2003; Mihalakakou et al., 1994a). Nevertheless, the ground is modelled as a cylinder surrounding the pipe. With such assumption, the model is not able to represent different boundary conditions at different positions – the undisturbed ground temperature is applied at the ground cylinder outer surface. Gan (2014, 2015) proposed a three-dimensional and coupled heat and moisture transfer model. It thus makes possible the modelling of stratification and non constant soil thermal properties. Finally, complex boundary conditions at the ground top surface – convection, radiation,

evaporation/condensation and rainfall – are implemented, which is a step toward an accurate modelling of the ground cover.

2.1.4.2. Summer day – Hot climate

Many publications can be found about the study of the cooling performances of EAHE. Since there is a wide variety of situations – linked to the climate, the building uses, the EAHE size and configuration – and of analysis – choice of the indicator of performance, see section 2.1.3 - a clear summary of all the investigations is difficult but was undertaken by Santamouris and Kolokotsa (2013). Table 7 adapted from this work shows a selection of buildings coupled with an EAHE for different climates and uses. To sum up and gives a better idea of the cooling efficiency of an EAHE, it can be observed from the available data that:

- The yearly energy gain ranges between 11 and 760 $kWh.m^{-2}.y^{-1}$ ⁶, but the most common values are between 10 and 40 $kWh.m^{-2}.y^{-1}$,
- The daily energy gain ranges between 7 and 512 $kWh.day^{-1}$,
- The usual cooling power of an EAHE ranges between 2.5 and 17 kW,
- The COP ranges between 0.96 and 15.8 (ignoring the COP relative to a whole year),
- The obtained temperature drop varies from 1.5 °C to more than 20 °C.

In view of this figures, the EAHE systems appear to be very efficient for cooling, to decrease the ambient air temperature as well as to save a significant amount of energy. Furthermore, the spreading of the values for the energy gain, the COP and the temperature drop are of course explained by the differences between the configurations, but also by the difference of calculation adopted by the authors (see section 2.1.3.2.).

Nevertheless, when considering the fan energy consumption – via the calculation of the coefficient of performance COP – the EAHE is sometimes inefficient since $COP \cong 1$. When the EAHE cooling performance is compared to other passive cooling method such as natural ventilation it reveals that it is not always a competitive system (Breesch et al., 2005; Hollmuller and Lachal, 2014). Breesch et al. (2005) calculate the impact of several passive cooling techniques on the discomfort hour's number – when the predicted mean vote PMV exceeds 0.5. Without any passive cooling technique, this value is more than 500 *h*, falls to around 350 *h* with the presence of an EAHE (alone) whereas it falls to around 50 *h* with simple night ventilation. The tendencies are accentuated with an increase of the building occupation. For Hollmuller and Lachal (2014), the use of EAHE as a passive cooling technique is similar to night ventilation. Since the outlet air temperature of the buried pipes is generally below the comfort threshold, an increase of the airflow rate enables to remove the heat load excess. They however warn about the electricity overconsumption of the fan, and for an appropriate sizing of the pipes.

⁶ kWh per meter square of pipe surface area per year

Table 7: Overview of the EAHE installation characteristics and performances for cooling

| Reference | Country | Building Type – Surface | Numb. of pipes | EAHE length | EAHE depth | EAHE diam. / sect. | EAHE airflow rate | Closed loop | Period | Temp. drop | Outlet air temp. | Indoor temp. | Energy gains | COP |
|-----------------------------------|---------|---|----------------|-------------|------------|---------------------------|--------------------------------------|-------------|--------------------|---|------------------|--------------|--|----------------------------|
| (Breesch et al., 2005) | Belgium | Office – 2000 m ² | 2 | 40 m | 3 – 5 m | 0.8 m | ~3000 m ³ h ⁻¹ | N | | | Below 22 °C | | -20% – 30% of the discomfort hours | |
| | Germany | Office – 6000 m ² | 26 | 67–107 m | 2 – 4 m | 0.2 m | 10300 m ³ h ⁻¹ | N | 1year | 30°C → 18°C | 5°C – 20°C | | 13.5 kWh.m ⁻² .y ⁻¹ | 88 (global) |
| (Pffafferott, 2003) | Germany | Office – 13150 m ² | 7 | 95 m | 2 m | 0.25 m | 7000 m ³ h ⁻¹ | N | 1year | 36°C → 24°C | 7°C – 20°C | | 23.8 kWh.m ⁻² .y ⁻¹ | 29 (global) |
| | Germany | Office – 1000 m ² | 2 | 90 m | 2.3 m | 0.35 m | 1100 m ³ h ⁻¹ | N | 1year | 30°C → 20°C | 2.5°C – 25°C | | 12.1 kWh.m ⁻² .y ⁻¹ | 380 (global) |
| (Eicker et al., 2006) | Germany | Office – 1488 m ² | 2 | 90 m | 2.8 m | 0.35 m | 1900 m ³ h ⁻¹ | N | | | | | 24 Wh. m ⁻² .day ⁻¹ 18% of the cooling loads, 2.5 – 4.5 MWh.y ⁻¹ | 34.7 – 50.2 (global) |
| | Italy | Educational | 28 | 70 m | 2.6 m | | | N | 1year | | | | 760 kWh.m ⁻² .y ⁻¹ per pipe (sim. results) | |
| | Greece | Educational | 4 | | 1.5 m | | | N | 1year | | | | 33 kWh.m ⁻² .y ⁻¹ | |
| (Santamouris and Kolokotsa, 2013) | Italy | Multifunct. – 382 m ² | | 40 m | 4 m | | | N | | Ambient -5°C | | | | |
| | Greece | Atheltic center | 6 | 40 – 57 m | 3 m | | | N | | | | | The EAHE covers ~60% of the building cooling needs (sim. results) | |
| (Sodha et al., 1985) | India | Hospital | 1 | 80 m | | 2.05 x 1.4 m ² | | N | June. 22-31 (1983) | Inlet: 23.4 – 43.2 °C Outlet: 23.1 – 28.2 °C | 23.1 – 28.2 °C | | 512 kWh.day ⁻¹ Can cool 7 rooms of 16 m ² area | |
| (Burton, 2004) | France | Retirement home – dining room of 380 m ² | 11 | | 2 m | 0.2 m | | N | | | | | Monitoring: 3600 m ³ h ⁻¹ : 9.5 kW 7200 m ³ h ⁻¹ : 14 kW Typically 5 kW after continuous use Sim. extrapolation: 2.2 MWh.y ⁻¹ | 16 (global - sim. results) |

| Reference | Country | Building Type - Surface | Numb. of pipes | EAHE length | EAHE depth | EAHE diam. / sect. | EAHE airflow rate | Closed loop | Period | Temp. drop | Outlet air temp. | Indoor temp. | Energy gains | COP |
|---|----------|------------------------------------|----------------|-------------|------------|--------------------|---|-------------|----------------------------------|--|---|--|---|--------------------------|
| (Badescu, 2007) | Germany | Passive house - 150 m ² | 1 | 36 m | | | | N | | | | | 462 kWh.y ⁻¹ | |
| (Sawhney et al., 1999) | India | House | 2 | 85 m | | 0.5 m | 942 m ³ .h ⁻¹ each | Y | May | Ambient: 22.5°C - 44.2°C Drop: -1.5°C | 25.3°C - 28.4°C | 26.4°C - 32.8°C | 180 kWh average for one day (over one month) | 3.35 |
| (Trombe et al., 1991) | France | House | 1 | 42 m | 2.5 m | 0.2 m | 306 - 450 m ³ .h ⁻¹ | N | 10th day in summer | Ambient: 16°C - 37°C Outlet: 18°C - 25°C | | 3°C lower with than without EAHE during the peak temp. | ~20 kWh per day if the outside air temp. is the ref. temp. ~7 kWh per day if the ref. temp is the comfort temp. (25°C) | |
| (Trombe and Serres, 1994) | France | House - 39 m ² | 1 | 39 m | 2 m | | 70 - 300 m ³ .h ⁻¹ | N | July 5-18 August 22-31 (1991) | | 17°C - 26°C | below 27°C | | |
| (Burton, 2004) | Portugal | House | 2 | 25 m | | 0.16 m | 290 m ³ .h ⁻¹ | N | Summer period | Max. - 8°C | | | Max. power of 2.5 kW | |
| (Al-Ajmi et al., 2006) | Kuwait | House - 100 m ² | 1 | 60m | | 0.25 m | 100 kg.h ⁻¹ | N | May-Sept. | -2.8°C in the peak hour of mid-July | | 28-32°C | 1.693 MWh | |
| (Vaz et al., 2011) | Brazil | House | 1 | 42 m | 2 m | 0.11 m | 113 m ³ .h ⁻¹ | N | | -3°C potentially during summer | | | | |
| (Chel and Tiwari, 2009) | India | House - 94 m ² | 1 | 78 m | 5 m | 0.06 m | 132 m ³ .h ⁻¹ | N | | | | | 2.36 MWh.y ⁻¹ | 1.8 |
| (Wu et al., 2007) | China | | 2 | 60 m | 3.75 m | 0.4 m | 1000 m ³ .h ⁻¹ | N | 1 day July | Inlet: 27.3 °C - 37 °C Outlet: 23.8 - 29.5 °C | | | 27.8 - 47.8 kWh.day ⁻¹ | |
| (Santamouris et al., 1994) | Greece | Greenhouse - 1000 m ² | 5 | 30 m | 1.5 m | 0.22 m | | N | May - Aug. | Ambient: 15°C - 48°C Outlet: 15°C - 25°C | Mean diff. max indoor / outlet air temp.: 20 °C | 15°C - 35°C | | |
| (Tiwari et al., 2006) | India | Greenhouse - 24 m ² | 1 | 39 m Serp. | 1 m | 0.06 m | 150 kg.h ⁻¹ | Y | 1day per week | Ambient: 28 - 39°C Inlet: 29.7°C - 43.3°C | 28.7°C - 33°C | 29.3°C - 45.3°C | 6.1 kWh.day ⁻¹ | 0.96 - 1.41 |
| (Ozgener and Ozgener, 2010; Ozgener et al., 2011) | Turkey | Greenhouse - 49 m ² | 1 | 47 m U-bend | 3 m | 0.56 m | 5300 m ³ .h ⁻¹ | Y | 4 days in Oct. | | | | Max. 16.93 kW | 4.4 - 15.8 Av.: 10.09 |
| (Bansal et al., 2010) | India | House - 15.5 m ² | 2 | 23.4 m | 2.7 m | 0.1 m | 119 m ³ .h ⁻¹ | Y | Steady-st. | Inlet: 42.2 - 43.6°C Outlet: 31 - 33.7°C | | | 1.2 - 3.1 MWh.h ⁻¹ | 1.9 - 2.9 |

2.1.4.3. Winter day – Cold climate

Table 8 gathers several EAHE coupled to buildings, in different climate, for configurations, and attempt to supply data about their performances for heating. It can be observed from these data that:

1. The yearly energy gain ranges between 5.55 and 203 kWh.m⁻².y⁻¹, but the most common values are between 10 and 20 kWh.m⁻².y⁻¹,
2. The daily energy gain ranges between 3.5 and 269 kWh.day⁻¹
3. The only available value for the heating power of an EAHE is around 4 kW,
4. The COP ranges between 0.63 and 5.16 (ignoring the COP relative to a whole year),
5. The obtained temperature rise varies from 2 °C to 8 °C.

These figures illustrate the fact that for the Central European climates the cooling performance is higher than the heating performance. Hollmuller and Lachal (2014) explained this phenomena by the asymmetry of the meteorological constraint. In winter, the daily mean ambient temperature is always below the comfort threshold around 20 °C whereas in summer the daily average temperature never exceeds the 26 °C comfort threshold. Therefore, in winter the heating of the ambient air via an EAHE is related to its potential to dampen the annual outdoor thermal wave, while in summer the cooling only requires to dampen the daily oscillation. Of course the dampening of the daily oscillation does not necessitate the same sizing as the yearly oscillation. In the first case, a 10-20 m per 100 m³.h⁻¹ of air, surrounded by a 20 cm soil layer is sufficient to avoid temperature overshoots according to Hollmuller and Lachal. The second case necessitates a pipe length of 20 – 40 m per 100 m³.h⁻¹ of air and solicits a soil layer of about 3 m.

This raises the question of the relevance of such project. First, burying the pipes is expensive and increases with the tube length and depth. Secondly, the performance of the EAHE is thermally limited by the ground temperature, around 10 °C in winter. In comparison, a simple heat recovery system is at the same time cheaper and more efficient since the temperature of the heat source is around 20 °C. In conclusion, while EAHE can eliminate the need for active cooling, they are not very competitive for (pre-)heating (Hollmuller and Lachal, 2014; Peretti et al., 2013; Soni et al., 2015). Instead, a heat recovery unit is in almost all the cases far better and more cost-effective.

Table 8: Overview of the EAHE installation characteristics and performances for heating

| Reference | Country | Building Type – Surface | Numb. of pipes | EAHE length | EAHE depth | EAHE diam. / sect. | EAHE airflow rate | Closed loop | Period | Temp. rise | Outlet air temp. | Indoor temp. | Energy gains | COP |
|---------------------------|---------|---|----------------|-------------|------------|---------------------------|---|-------------|---------------------|---|------------------|--------------|---|----------------------------|
| | Germany | Office – 6000 m ² | 26 | 67–107 m | 2 – 4 m | 0.2 m | 10300 m ³ h ⁻¹ | N | | | | | 16.8 kWh.m ⁻² .y ⁻¹ | 88 (global) |
| (Pfafferott, 2003) | Germany | Office – 13150 m ² | 7 | 95 m | 2 m | 0.25 m | 7000 m ³ h ⁻¹ | N | | | | | 51.3 kWh.m ⁻² .y ⁻¹ | 29 (global) |
| | Germany | Office – 1000 m ² | 2 | 90 m | 2.3 m | 0.35 m | 1100 m ³ h ⁻¹ | N | | | | | 16.2 kWh.m ⁻² .y ⁻¹ | 380 (global) |
| (Eicker et al., 2006) | Germany | Office – 1488 m ² | 2 | 90 m | 2.8 m | 0.35 m | 1900 m ³ h ⁻¹ | N | | | | | 1.8 – 3 MWh.y ⁻¹ | 34.7 – 50.2 (global) |
| (Sodha et al., 1985) | India | Hospital | 1 | 80 m | | 2.05 x 1.4 m ² | | N | Dec. 22 – 31 (1983) | Inlet : 4 – 24 °C Outlet : 12 – 20°C | 12 – 20°C | | 269 kWh.day ⁻¹ | |
| (Burton, 2004) | France | Retirement home – dining room of 380 m ² | 11 | | 2 m | 0.2 m | | N | | | | | Sim. extrapolation: 6.7 MWh.y ⁻¹ | 16 (global - sim. results) |
| (Badescu, 2007) | Germany | Passive house – 150 m ² | 1 | 36 m | | | | N | | | | | 968 kWh.y ⁻¹ | |
| (Trombe and Serres, 1994) | France | House – 39 m ² | 1 | 39 m | 2 m | | 70 – 300 m ³ h ⁻¹ | N | | | | | -503 – 347 kWh.y ⁻¹ | |
| (Vaz et al., 2011) | Brazil | House | 1 | 42 m | 2 m | 0.11 m | 113 m ³ h ⁻¹ | N | | +8°C potentially during winter | | | | |

Table 8: Overview of the EAHE installation characteristics and performances for heating (continuation)

| Reference | Country | Building Type – Surface | Numb. of pipes | EAHE length | EAHE depth | EAHE diam. / sect. | EAHE airflow rate | Closed loop | Period | Temp. rise | Outlet air temp. | Indoor temp. | Energy gains | COP |
|---|---------|----------------------------------|-----------------------------|----------------|------------|--------------------|--|-------------|---------------------------|--|------------------|-------------------|---|-------------|
| (Chel and Tiwari, 2009) | India | House – 94 m ² | 1 | 78 m | 5 m | 0.06 m | 132 m ³ h ⁻¹ | N | | | | | 3.01 MWh.y ⁻¹ | 2.9 |
| (Santamouris et al., 1994) | Greece | Greenhouse – 1000 m ² | 5 | 30 m | 1.5 m | 0.22 m | | N | Jan. – Feb. | Ambient : 4 – 15 °C Outlet : 10 – 21 °C | 10 °C – 21 °C | 8 °C – 35 °C | | |
| (Tiwari et al., 2006) | India | Greenhouse – 24 m ² | 1 | 39 m Serp. | 1 m | 0.06 m | 150 kg.h ⁻¹ | Y | 1 day per week throughout | Amb.: 8.4 – 18 °C Inlet: 12.3 °C – 24.8 °C | 18.3 – 20.3 °C | 20.8 °C – 27.8 °C | 3.5 kWh.day ⁻¹ | 0.63 – 0.78 |
| (Ozgener and Ozgener, 2010; Ozgener et al., 2011) | Turkey | Greenhouse – 49 m ² | 1 | 47 m U-bend | 3 m | 0.56 m | 5300 m ³ h ⁻¹ | Y | | +2.09 °C | | | Cover of 60% of the heating load Ave.: 3.77 kW Max.: 4.5 kW | 5.16 |
| (Spieler et al., 2000; Wagner et al., 2000) | Germany | Office – 2180 m ² | 4 | 32 m | 1.5 m | 0.5 m | 3100 m ³ h ⁻¹ | N | 1 year | Inlet: -10 °C – 12 °C Outlet: -2 °C – 12 °C | | | 5.55 kWh.m ⁻² .y ⁻¹ | |
| (Bansal et al., 2009) | India | House – 15.5 m ² | 2 | 23.4 m | 2.7 m | 0.1 m | 119 m ³ h ⁻¹ | Y | Steady-st. | Inlet: 20.6 °C Outlet: 24.2 – 25.4 °C | | | 423.4 – 846.7 kWh.h ⁻¹ | |
| (Hollmuller and Lachal, 2001) | Switz. | Comm. – 2900 m ² | 49 – beneath building | 50 m | 0.5 m | 0.125 m | 2400 – 3000 m ³ h ⁻¹ | N | 1 year | | | | 9.4 MWh.y ⁻¹ | |
| (Hollmuller and Lachal, 2001) | Switz. | Comm. – 8050 m ² | 43 – beneath building | 23 m | 6 m | 0.25 m | 6000 – 12000 m ³ h ⁻¹ | N | 1 year | | | | 15.6 MWh.y ⁻¹ | |

2.1.4.4. Mid-season, coupling with buildings and long term functioning

As proved by the number of studies cited in the two previous subsections, the heating and the cooling modes of the EAHE are well understood. On the contrary, a few researches carried out their functioning for mid-season, when the heating and cooling mode can alternate daily. For such periods the EAHE can be very inefficient. Indeed, Pfafferott (2003) talks about 'overlap' of the heating and the cooling period. This sometimes happens in winter when the ambient air temperature decreased as it flows through the pipes, and reversely increased in summer. To face this problem of inexpedient heating/cooling the solution is to identify the periods when undesirable temperature are yield by the EAHE and to by-pass it. The control method can take a variety of forms:

- Time controlled: the EAHE outlet air is by-passed for a given time window,
- Open-loop controlled: the EAHE outlet air is by-passed according to the value of the ambient air temperature,
- Closed-loop controlled: the EAHE outlet air is by-passed according to the value of the indoor air temperature.

According to Trząski and Zawada (2011) in which an assessment is carried out for a whole year with simulation, the by-pass presence considerably improves the EAHE heating as well as cooling performance, particularly for mid-season. Furthermore, when an EAHE is used for the air-conditioning of a building it can work alone or it can be coupled to another system, as an air-handling unit (with or without heat recovery system), a heat pump, a solar chimney, etc. The latter often have their own control systems and by-pass.

About the coupling in series with an heat recovery unit, the contribution of the pipes has been proved to be marginal compared to that of the heat recovery unit (Chlela et al., 2007; Hollmuller and Lachal, 2014; Kopecky, 2008). While an EAHE can improve the thermal comfort in summer, it only ensures preheating in winter. Ensuring a good thermal comfort during the cold season necessitates a coupling: in such case, the EAHE enable to avoid the freezing of a heat recovery unit for example.

The coupling between an EAHE and a conventional air conditioner is analyzed by Misra et al. (2012) in order to investigate the possibilities to enhance its performances. Four arrangements are evaluated:

1. The air conditioner is working alone (the reference case),
2. Both air conditioner and the EAHE supply in parallel cold air to the room,
3. The EAHE blows cold air on the condenser coils of the air conditioner, and the air conditioner supply cold air to the room,
4. The EAHE uses 50 % of its outlet air to cool down the condenser coils of the air conditioner and the remaining 50 % is directly blown to the room.

The mode 4 downgrades the performance and the modes and 3 yield better performances than the reference case. The room air temperature and the electric consumption are reduced in both cases, up to -1.4 °C and -18 % for the mode 3.

Four ventilation devices were analyzed by Bojić (2000) for their potential of energy savings: an air-to-air heat pump, a heat recovery exchanger, an EAHE and an air-mixing

devices. The heat recovery and the air-mixing techniques have been found as having the more significant impact on the energy savings, and the control of the global ventilation system has been proved to be even more significant.

A coupling of an EAHE with an evaporative cooling system was analyzed with both numerical model and experimental measurements (Bansal et al., 2012a). The comparison showed good agreements with a maximal relative error of 8 %. The potential of the two systems – EAHE alone and EAHE coupled with the evaporative cooling system – to meet the requirements of thermal comfort is evaluated by comparison to the scenario where no passive cooling system is set. Without any treatment of the air, the air is comfortable 25.6 % of time. The EAHE alone supplies comfortable conditions 23.3 % of time, while the coupling 'EAHE+ evap. cooler' increases this percentage to 34.2 %. The combined system is thus from an energy point of view more efficient. Bansal et al. (2012b) put in evidence that this system is also better from an economic point of view. Nevertheless, they showed that attention has to be paid to the choice of the fan: if the latter is not efficient, the project is not viable. In a refurbishment project, this system can be relevant only if the current heating and cooling systems are not efficient.

Although it is clearly of high importance, the performance evolution with a long term functioning is another aspect of the EAHE that received little attention. Bansal et al. (2013b) used a transient model in order to prove that a continuous working of 36 hours induces a decrease of the performances compared to the results yield by a stationary model – i.e. considering a constant ground temperature. Through the introduction of a 'derating factor', they also showed that the lower the soil thermal conductivity is, the higher the reduction of the performance is. Kopecky (2008) noted that the ground discharges heat during winter due to the cold air circulation within the pipe. The long term analysis showed that when the airflow is stopped, the ground temperature tends toward the undisturbed ground temperature in a few days only. The intermittent working of the EAHE enables ground heat recovering, and thus raises the EAHE performance. This phenomenon is attenuated in summer: because of a stronger daily temperature variation, the ground temperature stays closer to the undisturbed ground temperature.

The lessons from that section are various. First, the functioning of an EAHE has been widely studied for purely winter or summer conditions but not for intermediate conditions. However, the efficiency for such periods remains very uncertain due to inexpedient heating or cooling. The problem can be partially solved by the adding of a by-pass, correctly programmed. Secondly, the comparison of the EAHE performances with other passive air-conditioning systems showed this is not always a relevant choice, both from an energetic and an economic point of view. In the light of the above sections, only good sizing, material choices, and regulation ensure the success of the use of an EAHE. This necessitates an evaluation for each project since as exposed in the section 2.1.4, the soil nature and the climate strongly influence its behaviour. This evaluation, of course via modelling, has been done for years most of the time with steady state models, using undisturbed ground temperatures and excessively simple boundary conditions.

2.2. ON THE MODELLING OF EAHE

Many solutions to model EAHE has been proposed in the literature. A structured overview is presented in this section. First, the analytical models are reviewed. Then, the main numerical approaches are introduced according to their level of complexity. Finally, a synthesis is made in order to catch the main features of each model.

2.2.1 ANALYTICAL MODELLING

2.2.1.1. Steady-state analytical models

Tzaferis et al. (1992) exposed and compared eight EAHE modelling approaches. The basic idea of the algorithms to calculate the outlet air temperature is to compute the convective sensible heat exchange for a pipe section of length δx and deduce the temperature evolution throughout this section. It necessitates the knowledge of the pipe surface temperature. From there, the authors distinguished two possibilities. The temperature of the pipe surface is either assumed equal to that of the undisturbed ground temperature at the pipe depth (Figure 14 (b)) or the undisturbed ground temperature is applied at the outer surface of a ground volume surrounding the pipe (Figure 14 (a)).

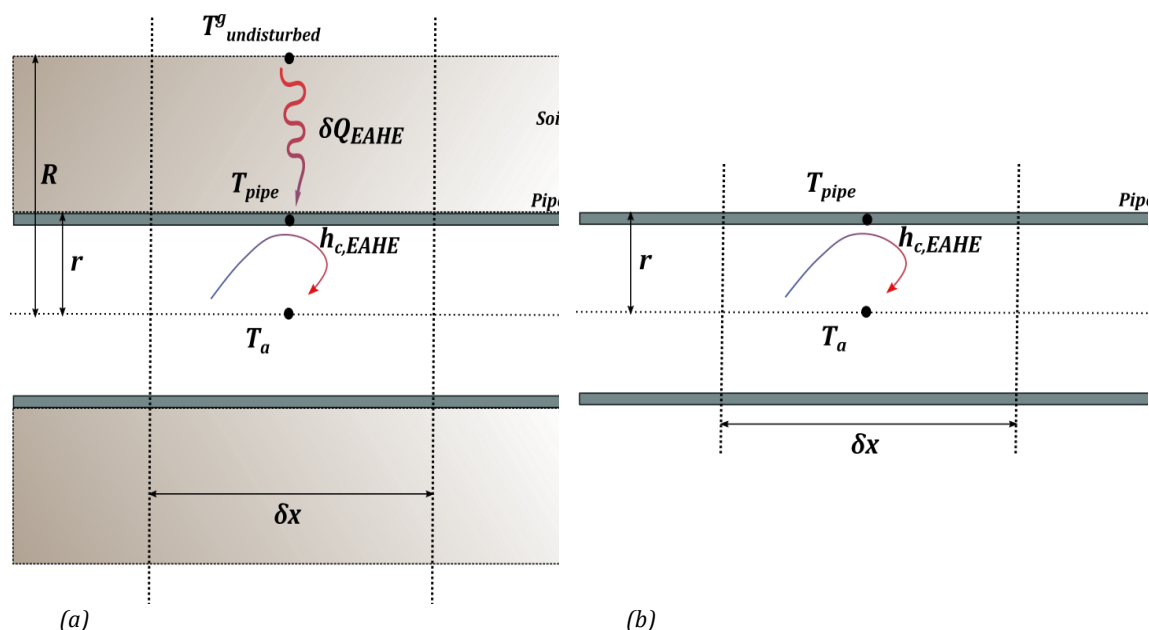


Figure 14: Simple modeling of an EAHE with (a) and without (b) considering the soil surrounding the tube

In both cases the pipe surface temperature is considered isothermal. This reasoning is the base of most of the simpler analytical models as for example those developed by De Paepe and Janssens (2003). This steady-state one dimensional analytical model aims at providing decision help to architect and building designers. The total heat transferred to the air is

$$Q_{EAHE} = \dot{m}_a c_a (T_{outlet} - T_{inlet}) \quad (2.14)$$

Considering that the total heat exchanged by convection can be written

$$Q_{EAHE} = h_{c,EAHE} A_{EAHE} \Delta T_{lm} \quad (2.15)$$

where ΔT_{lm} the logarithmic average temperature difference is given by

$$\Delta T_{lm} = (T_{outlet} - T_{inlet}) \ln \left[\frac{T_{inlet} - T_{pipe}}{T_{outlet} - T_{pipe}} \right]^{-1} \quad (2.16)$$

the solution is thus

$$T_{outlet} = T_{pipe} + (T_{inlet} - T_{pipe}) e^{-NTU} \quad (2.17)$$

where the NTU has been defined by equation (2.5), and $T_{pipe} = T_{und}^g$.

A similar model – with nevertheless some additions - is developed and implemented in the TRNSYS software (Al-Ajmi et al., 2006). The model considers steady-state airflow within a pipe surrounded by a soil annulus whose thickness is equal to the duct radius. The temperature of the outer surface of the soil is equal to the undisturbed ground temperature – varying only with an annual period – at the corresponding time and depth. The calculation of the outlet air temperature is done according to

$$T_{outlet} = T_{inlet} - (T_{inlet} - T_{und}^g) \left(1 - e^{-\frac{U_{EAHE} A_{EAHE}}{c_a \dot{m}_a}} \right) + \frac{\Delta P_t}{\eta_{fan} c_a \rho_a} \quad (2.18)$$

$$U_{EAHE} = \left(\frac{\ln\left(\frac{2r}{r}\right)}{2\pi L_{EAHE} \lambda} + \frac{1}{2\pi r L_{EAHE} h_{c,EAHE}} \right)^{-1} \quad (2.19)$$

where U_{EAHE} is the global heat conductance of the EAHE - due to the convective thermal resistance $\frac{1}{2\pi r L_{EAHE} h_{c,EAHE}}$ and the conduction thermal resistance of the ground $\frac{\ln\left(\frac{2r}{r}\right)}{2\pi L_{EAHE} \lambda}$ - r is the pipe radius, ΔP_t the pressure loss and η_{fan} the fan efficiency.

The final model is evaluated thanks to a comparison against two set of experimental results. For the first set of results, the difference between the predicted and the measured outlet air temperature is below 1.7 °C. For the second set, it is below 4.8 °C for low air speed (0.5 $m.s^{-1}$), but limited to 0.9 °C for higher air speed. According to the authors, the discrepancies can be partially explained by short duration of the study. The TRNSYS type that yield the undisturbed ground temperature is the TYPE 263.

Niu et al. (2015) used an order two polynomial regression to build simple analytical expression to evaluate the sensible, the latent and the total cooling potential of a EAHE as a function of the inlet air temperature, relative humidity and velocity, the pipe diameter, length and temperature. This is based on the results yield by a numerical model, introduced in the next section.

2.2.1.2. Transient analytical models

A more detailed analytical model based on Green's function is developed by Cucumo et al. (2008) in order to calculate the temperature of the pipe wall's. This model considers one-dimensional heat diffusion through the soil, yearly and daily fluctuations of the ground upper surface temperature and heat convection between the pipe wall's and the flowing air in continuous operation. Due to the complexity of this model, and the resulting high computational time, a simplified version is devised based on the principle of superposition. The exact and the simplified solutions are compared and the discrepancies of the temperature at the installation depth of the buried pipe are below 5 % and below 12 % in the vicinity of the pipe. The simplified model considers that the ground temperature at depth z and time t is the sum of four terms, two of which related to the daily and yearly evolution of the ambient air temperature, and two others linked to the EAHE influence. The resulting pipe wall's temperature function is given by (2.20) where $T_{und}^g(z, t)$ is given by equation (2.1), \bar{T}_a is the daily mean air temperature and $\Delta T_{a,d}$ its daily amplitude variation, $\beta = \frac{\lambda}{h_{c,EAHE} \sqrt{\frac{\omega_d}{2\alpha_s}}}$ and $\varepsilon = \arctan\left(\frac{\beta}{\beta+1}\right)$. Using this model, the authors then proposed to evaluate the performance of the EAHE. The approach is different from the traditional one consisting in evaluating the outlet air temperature. In their work, they consider the outlet air temperature is a given parameter. On the contrary their objective is to calculate the length of the pipe and the specific humidity at the outlet. The inlet specific humidity, the pipe depth and diameter, the soil thermal parameters are known. If the inlet air specific humidity is over the saturation condition, condensation occurs and is not negligible.

$$\begin{aligned}
 & T_{pipe}(z, t) \\
 & = T_{und}^g(z, t) \\
 & + \left(\bar{T}_a - T_{und}^g(z, t_0) \right) \left[1 \right. \\
 & \left. - \exp\left(\frac{h_{c,EAHE}^2 \alpha_s (t - t_0)}{\lambda^2} \right) \operatorname{erfc}\left(\frac{h_{c,EAHE} \sqrt{\alpha_s (t - t_0)}}{\lambda} \right) \right] \\
 & + \frac{\Delta T_{a,d}}{\sqrt{1 + 2\beta + 2\beta^2}} \cos(\omega_d (t - t_a^*) - \varepsilon)
 \end{aligned} \tag{2.20}$$

The pipe wall's temperature cannot be considered as constant, especially when phase change is taken into account. Since the isothermal condition is excluded here, the traditional exponential evolution of the air temperature is wrong. Instead, the evolution of the temperature and the relative humidity along the z axis is assumed to be quadratic. This was verified against experimental data. Noting $T^*(z) = T_a(z) - T_{pipe}(z)$, they thus assumed

$$T^*(z) = T_{inlet}^* - 2 \frac{T_{inlet}^* - T_{outlet}^*}{L_{EAHE}} z + \frac{T_{inlet}^* - T_{outlet}^*}{L_{EAHE}^2} z^2 \tag{2.21}$$

and a similar expression for the air specific humidity at saturation. Therefore, the heat exchanged is given by

$$\begin{aligned}
Q_{EAHE} &= \int_0^L h_{c,EAHE} P_{EAHE} (T_a(z) - T_{pipe}(z)) dz \\
&= \int_0^L h_{c,EAHE} P_{EAHE} T^*(z) dz \\
&= \frac{h_{c,EAHE} P_{EAHE} L_{EAHE}}{3} (2T_{outlet}^* + T_{inlet}^*) \\
&= \dot{m}_a (H_{outlet} - H_{inlet})
\end{aligned} \tag{2.22}$$

To calculate the inlet and outlet air enthalpy necessitates the knowledge of the outlet air specific humidity. The authors solved this problem by using an iterative procedure and assuming

$$\begin{aligned}
\omega_{a,outlet} &= (\omega_{a,inlet} - \omega_{a,sat,inlet}) e^{-NTU} \\
&\quad + (\omega_{a,sat,inlet} - \omega_{a,sat,outlet}) \left(\frac{2(1 - e^{-NTU})}{NTU^2} \right. \\
&\quad \left. - \frac{2e^{-NTU}}{NTU} - 1 \right) + \omega_{a,sat,inlet}
\end{aligned} \tag{2.23}$$

It is thus possible to compute L_{EAHE} and $\omega_{a,outlet}$. The results yields by this model have been compared against a numerical finite volume model and experimental data, both in summer conditions, and showed good agreement.

A fully analytical model of an EAHE is developed by Hollmuller (2002, 2003). Heat diffusion through a soil cylinder surrounding the pipe, heat convection between the flowing air and the pipe surface and heat advection along the pipe are the main phenomenon considered, illustrated in Figure 15. Aiming at giving an idea of the accuracy of this model, the main assumptions are recalled here:

- The heat diffusion is radial (neglected in the longitudinal direction),
- The soil thermal properties are homogeneous and constant,
- The air temperature is considered as constant in a pipe cross-section,
- The convective heat transfer coefficient is constant along the tube,
- The tube thickness is neglected,
- The latent heat transfers are neglected,
- The air warming due to the friction on the pipe surface is neglected.

Under these conditions, the equation describing the heat diffusion within the soil cylinder is therefore

$$\alpha_s \left(\frac{\partial^2 T^g}{\partial r^2} + \frac{1}{r} \frac{\partial T^g}{\partial r} \right) = \frac{\partial T^g}{\partial t} \tag{2.24}$$

for which the boundary conditions is

$$\lambda_s \frac{\partial T^g}{\partial r} \Big|_{r=r_0} = h_a (T^g|_{r=r_0} - T_a) \tag{2.25}$$

The equation describing the heat exchanges to the flowing air is

$$c_a \dot{m}_a \left(\frac{\partial T_a}{\partial x} + \frac{1}{v_a} \frac{\partial T_a}{\partial t} \right) = 2\pi r_0 h_a (T^g|_{r=r_0} - T_a) \quad (2.26)$$

To solve this system of equations, Hollmuller considered an harmonic evolution of the inlet air temperature $T_a|_{x=0} = \theta_0 \cos(\omega t)$. Noting $\theta_a^*(x)$ its - complex - longitudinal evolution, the pipe air temperature can be written

$$T_a = \mathcal{R}e(\theta_a^*(x)e^{i\omega t}) \quad (2.27)$$

Considering that the radial $\Gamma_g^*(r)$ and the longitudinal evolution $\theta_g^*(x)$ of the ground temperature are independent, a similar expression can be written for the soil temperature

$$T^g = \mathcal{R}e(\theta_g^*(x)\Gamma_g^*(r)e^{i\omega t}) \quad (2.28)$$

where, choosing $\Gamma_g^*(r_0) = 1$, $\theta_g^*(x)$ is the temperature of the tube.

Taking $h_\Gamma^* = -\lambda \frac{\partial_r \Gamma_g^*(r)}{\Gamma_g^*(r)} \Big|_{r=r_0}$ and decomposing $\frac{h_a h_\Gamma^*}{h_a + h_\Gamma^*}$ under the form $h + ik$, the solution for the air temperature is obtained via the modified Bessel's functions and its real part is given by

$$T_a(x, t) = \theta_0 \cdot \exp\left(-\frac{2\pi r_0}{c_a \dot{m}_a} hx\right) \cdot \cos\left(\omega\left(t - \frac{x}{v_a}\right) - \frac{2\pi r_0}{c_a \dot{m}_a} kx\right) \quad (2.29)$$

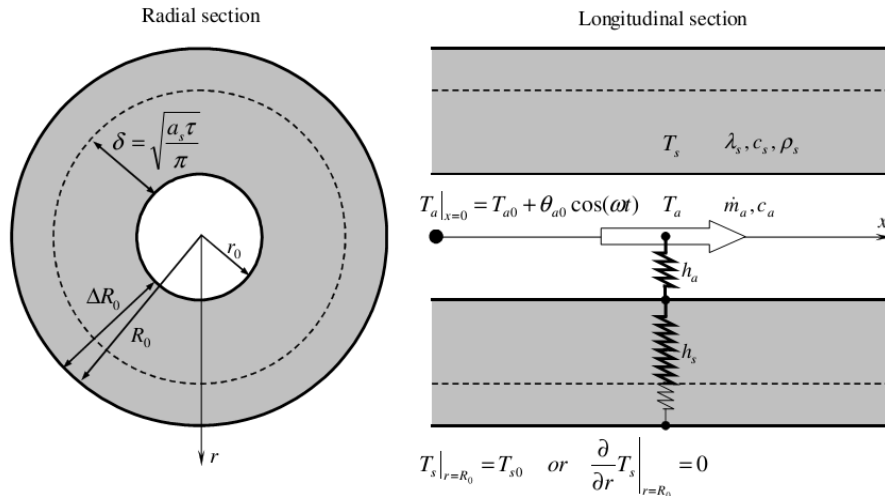


Figure 15: EAHE analytical model developed by Hollmuller (2002, 2003)

Furthermore, writing $h_\Gamma^* = h_g + ik_g$ one has $h = \frac{h_a h_g}{h_a + h_g} + \Delta h$ and $k = \frac{h_a k_g}{h_a + h_g} + \Delta k$. The terms Δh and Δk can be interpreted as an additional dampening and a shifting of the inlet thermal wave in the tube compared to the case of a constant condition. Hollmuller proved thanks to the study of the evolution of h_s that - for both isothermal and adiabatic boundary conditions on the outer soil surface - an increase of the soil thickness progressively isolates the pipe from the outside thermal load. For a soil thickness beyond δ , the soil is unaffected by the circulation of the air. The phase shifting coefficient k_s rises then stabilizes for soil thickness beyond δ . Contrary to the amplitude dampening which was independent of the pipe

radius for soil thickness beyond δ , the phase shifting stabilized value depends on it. These results from are consistent with the conclusions in section 2.1.2.1 and the work of (Yang et al., 2016). Finally Hollmuller generalized the solution (2.29) for any inlet air temperature using Fourier decomposition.

Yang et al. (2016) proposed a new analytical model based on those developed by Hollmuller. Their main difference lay on two points. First, the soil cylinder surrounding the pipe is assumed to have an infinite radius. The undisturbed ground temperature is applied here instead to at a finite distance of the pipe. Secondly, the interaction between the EAHE and the ground is taken into through an 'excess fluctuating temperature'. It mainly consists in solving the heat transfer equations for the normalized temperature $T = T^g(z, t) - T_{und.}^g(z, t)$. This analytical model was validated against a numerical CFD model.

2.2.2 NUMERICAL MODELLING

2.2.2.1. Simplest models: one- or two-dimensional heat transfers

Deglin et al. (1999) developed a model of EAHE based on one-dimensional heat transfer with cylindrical coordinates. The radial heat transfer within the soil cylinder – divided into several coaxial layers and sections along the airflow direction - around the pipe is taken into account. The model calculates the heat transferred from the air to the soil and deduces the air temperature at the outlet of the first cylinder and so on until the outlet of the last cylinder. Again, a validation is made against experimental measurements, led over two weeks. The maximal temperature differences were below 0.5 °C.

Lee and Strand (2008) implemented a module dedicated to the EAHE modelling for the EnergyPlus software. The heat transfer between the air and the earth is modelled as a heat flow through three thermal resistance: the first R_c representing the convective heat exchanges between the air and the pipe inner surface, the second R_p the conductive heat transfer between the inner and the outer pipe surfaces, and the third R_s the conductive heat transfer between the outer pipe surface and the undisturbed ground. Noting $U = \frac{1}{R_c + R_p + R_s}$, the heat balance equation for the flowing air is

$$\dot{m}_a c_a dT_a(y) + U(T_a(y) - T^g(z, t))dy \quad (2.30)$$

The authors solved analytically this equation; the solution has an exponential form. The boundary condition at the outer soil surface is the undisturbed ground temperature.

Niu et al. (2015) developed a numerical one-dimensional model for EAHE, based on the same principle than the numerical model in (Hollmuller, 2003) introduced in the next subsection. The evolution of the air in the duct has an exponential shape for each pipe section. If the air temperature of a pipe section drops to the dew point, the moisture condensation is considered, which is new compared to the two previous models. The governing equations for the air are

$$\dot{m}_a c_a (T_{a,j-1} - T_{a,j}) + \dot{m}_a L_v (\omega_{a,j-1} - \omega_{a,j}) = Afh_c (T_a - T_{pipe}) \quad (2.31)$$

$$\dot{m}_a(\omega_{a,j-1} - \omega_{a,j}) = A\rho_a h_v(\omega_a - \omega_{sat,pipe}) \quad (2.32)$$

This model was calibrated thanks to measurements data, including winter and summer mode (thus condensation and non-condensation mode) as well as natural (the fan is turned off) and forced ventilation. The mean relative error on the supplied air temperature and the humidity ratio are 1.6 % and 8.7 % respectively over the summer season.

Thiers and Peuportier (2008) studied the coupling of a double-flow air handling unit with a heat recovery system and an EAHE. The model was implemented in COMFIE, and is actually divided into two models: one for the soil and one for the EAHE. The soil was assumed homogeneous with constant thermal properties, dry, and was represented by a semi-infinite solid. It is subject to several thermal loads from the ambient air and the solar radiation, from the subground, and from the adjacent building. Compared to the previous numerical codes, the authors here proposed a modification of the classical undisturbed temperature (2.1) as detailed in

$$T^g(z, t) = geo \cdot z + \sigma_{bat}(r, z)\overline{T_{surf,bat}} + \overline{T^g(z_0)} + (1 - \sigma_{bat}(r, z)) \left[\sum_{n=1}^l A_n(z_0) e^{-\frac{z}{\delta(\omega_n)}} \sin\left(\omega_n t - \zeta_n - \frac{z}{\delta(\omega_n)}\right) \right] \quad (2.33)$$

$\sigma_{bat}(r, z)$ denotes the weight factor, i.e. the thermal influence of the building on the ground at depth z and from a distance r of the center of the slab and geo a thermal gradient representing the deep ground temperature variation. This temperature is applied as boundary condition of the EAHE model.

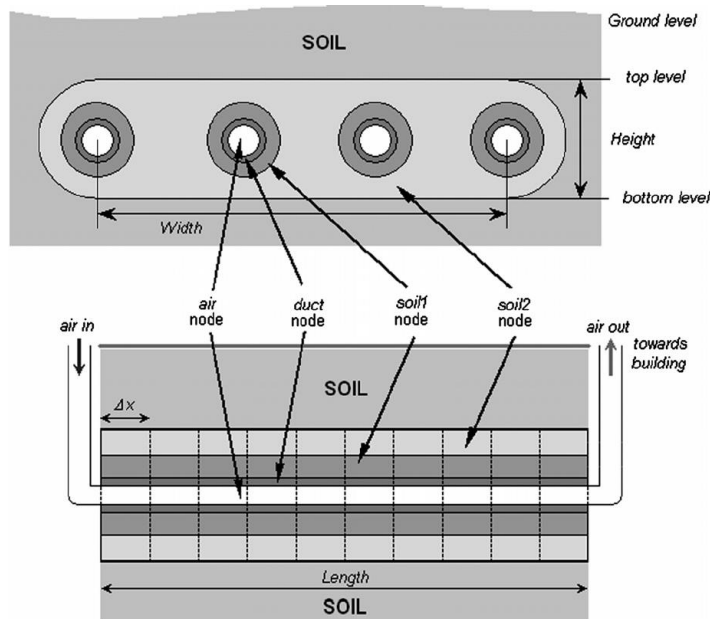


Figure 16: Cross and longitudinal section of the EAHE finite volume model (Thiers and Peuportier, 2008)

The EAHE is composed of several identical buried ducts in the same plane and equidistant. The air is supply at the entrance of the horizontal pipes and extracted at the outlet by vertical pipes, but their thermal impact is neglected. These pipes are embedded in a two soil layers assumed homogeneous, as illustrates on Figure 16. The discretization also operates along the flowing air axis. A heat balance enables to calculate the evolution of the temperature along the ducts, according to equation (2.34). The temperature is assumed uniform for each mesh. The radial conduction is only heat transfer taken into account. The axial conduction is neglected and the problem is further simplified considering only one pipe.

$$c_a \dot{m}_a (T_a(y + \delta y) - T_a(y)) = h_{c,EAHE} A_{air/pipe} (T_{pipe} - T_a) \quad (2.34)$$

The EAHE model is solved using a finite volume method with a 30min time step. A comparison of the simulation results with measurements of the outlet air temperature shows discrepancies below 2°C 98% of time. The temperature is overestimate during spring and autumn, which was explained by the authors as the consequence of neglecting the rainfall.

2.2.2.2. Two- or three-dimensional models with possibly latent heat transfer

The analytical EAHE models – introduced in the previous subsection – are useful for designing and to understand the global physical behaviour of the buried pipes but are nevertheless not adapted for the representation of realistic situations (Hollmuller, 2002; Hollmuller and Lachal, 2001, 2005). Therefore, the use of a numerical model was proposed, after having identified the limits of the existing ones:

- All used adiabatic boundary conditions for the vertical walls, which does not allow the consideration of edge effects,
- Only a few allow the consideration of inhomogeneous soils,
- The latent heat exchanges are usually neglected,
- The heat dissipated by the air friction on the pipe wall,
- The control of the direction of the airflow have never been taken into account,
- The validation is usually made against analytical or experimental results but only for short period, from some hours to some days.

They developed a finite element based model, considering both heat and latent flows between the air and the tube walls' – as illustrated on Figure 17 – and three-dimensional sensible heat transfers within the soil. The ground meshing is orthogonal with variable mesh sizes. The pipe circular section is approximated by a square section, and the convective heat coefficient is corrected by a factor $\frac{\sqrt{\pi}}{2}$. The heat properties of the soil are constant but non homogeneous and defined for each soil layer. Eventually water infiltrations can occur within the pipe. The sensible heat exchanges between the flowing air and the pipe are given by

$$P_{sens} = A_{EAHE} h_{c,EAHE} (T_a - T_{pipe}) \quad (2.35)$$

The latent exchanges are determinate through the Lewis approach

$$P_{lat} = L_v (\omega_a - \omega_{sat,pipe}) \cdot \frac{A_{EAHE} h_{c,EAHE}}{c_a} \quad (2.36)$$

The heat dissipation due to pressure losses is

$$P_{fric} = \dot{m}_a f \cdot \frac{L_{EAHE}}{D_{EAHE}} \cdot \frac{V_a^2}{2} \quad (2.37)$$

where f is the friction factor traditionally obtained from a Moody diagram.

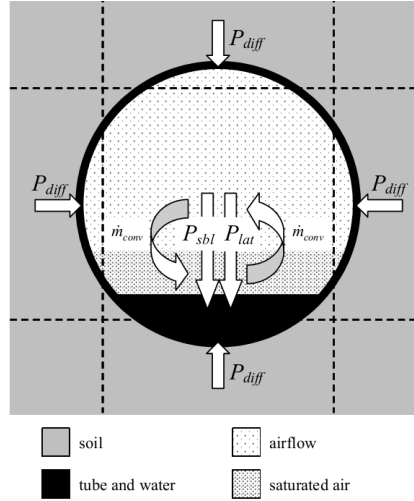


Figure 17: Modelling of the heat and mass flow within the buried pipe (Hollmuller, 2002)

The temperature and specific humidity evolution along the pipe are finally calculated according to

$$T_{a,j} = T_{a,j-1} + \frac{P_{fric} - P_{sens}}{(c_a + c_v \omega_a) \cdot \rho_a \Phi_a} \quad (2.38)$$

$$\omega_{a,j} = \omega_{a,j-1} + \frac{(\omega_a - \omega_{sat,pipe}) \cdot A_{EAHE} h_{c,EAHE}}{c_a \dot{m}_a \Delta t} \quad (2.39)$$

The model was validated against two set of experimental data. The first monitored building is the 'schwerzenbacherhof' commercial and administrative building of 8500 m^2 surface equipped with and EAHE of 43 pipes of 23 m length and 25 cm diameter buried 6 m beneath the ground surface. The comparison of the measurements with the numerical results is made over one year and presented for weekly and hourly dynamic. The sensible heat transfers are well reproduced: 4 % of over-estimation on summer charge, and 10% under-estimate on winter charge. The latent heat exchanges are absent if the water infiltration modelling is turned off. If it is turned on, there are 14 % of under-estimation on summer evaporation and 22 % of over-estimation on winter evaporation. The second monitored building is the 'Geoser' greenhouse, equipped with 24 pipes of 16 cm diameter, 11m length and buried 80cm below the surface. The monitoring is led over 17 months with 5 min time step. The results are similar as before.

Kopecky (2008) proposed in his thesis a similar method with nevertheless some modifications. The heat equation is solved in a two dimensional system of coordinates only (the axial heat diffusion is neglected). For the airflow, the pipe is divided into several sections and the evolution of the temperature and vapour density is described by

$$T_a(y + \delta y, t) = T_{pipe}(y + \delta y, t - \Delta t) + (T_a(y, t) - T_{pipe}(y, t - \Delta t)) e^{-\frac{h_c,EAHE 2\pi r}{m_a c_a} \Delta y} \quad (2.40)$$

$$\rho_{v,a}(y + \delta y, t) = \rho_{v,sat,pipe}(y + \delta y, t - \Delta t) + (\rho_{v,a}(y, t) - \rho_{v,sat,pipe}(y, t - \Delta t)) e^{-\frac{h_v,EAHE 2\pi r}{V_a} \Delta y} \quad (2.41)$$

The condensation is modelled only if $\rho_{v,a}(y, t) > \rho_{v,sat,pipe}(y, t - \Delta t)$, and the evaporation is and only if $\rho_v(y, t) > \rho_{v,sat,pipe}(y + \Delta y, t - \Delta t)$ liquid water was accumulated at the pipe surface at the previous time step. The liquid water does not move at the pipe inner surface.

The resolution of the final model is done by an explicit method which is, according to the author, not stable. The accuracy of the numerical model is evaluated over short and long term studies. The long term studies showed that the prediction accuracy is sometimes low (in terms of relative difference) which is according to Kopecky due to the fact that the soil/air heat exchange are low, and because of the intermittent operation. The accuracy depends strongly on the estimation of the initialization and the soil thermal characteristics. The heat balance at ground surface seems to govern the EAHE performance. Furthermore, the author noted that the air flow rate is unknown and has been used as adjustment parameter. The studies led on short term durations showed that correct reproduction of the moisture transfer is difficult.

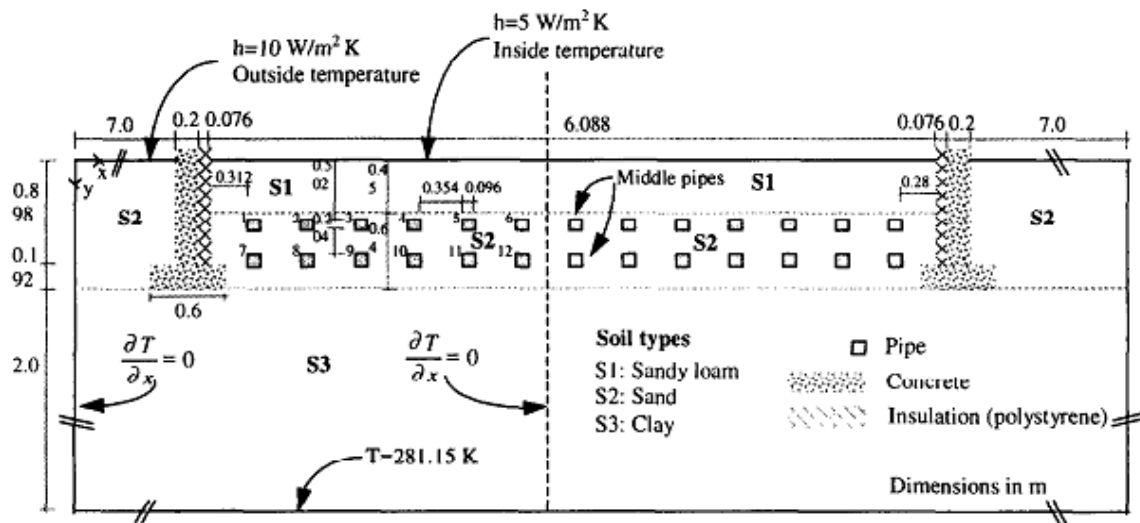


Figure 18 : Cross-sectional view of the EAHE installation modelled by Gauthier et al. (1997)

A three-dimensional model based on finite difference method is developed by Gauthier et al. (1997). It allows the modelling of several pipes, non homogeneous soils, the consideration of dynamics boundary conditions and condensation/evaporation within the tubes. The studied installation consists in dozens pipes buried underneath the building slab as illustrated on Figure 18. The impact of the insulation of the building basement is in particular analysed. The other assumptions of this model are the followings:

- The soil thermal properties are constant,

- The ground heat transfers due to a moisture gradient are neglected,
- The axial conductive heat exchanges in the pipes are neglected,
- As for the Hollmuller model's, the circular pipes are approximated by a square section.

The following equation is used to describe the energy balance within the pipes

$$\frac{\partial H_a}{\partial y} = \frac{\rho_a q_{EAHE}}{\dot{m}_a} - \frac{\partial \omega_a}{\partial y} \rho_a L_v \quad (2.42)$$

The predicted inlet/outlet temperature difference for two different pipes are compared to the measurements recorded over three days in April for a greenhouse located in Québec, Canada. The maximum relative discrepancy is 5.2 %. The authors considered this agreement as good given that the soil thermophysical properties 'can hardly be estimated within an accuracy ± 10 %'.

A quasi three-dimensional transient model is introduced by Badescu (2007). The soil, assumed homogeneous and isotropic, is divided into vertical sections. Contrary to most of the existing models, the axial heat conduction is not neglected. The model considers only the sensible heat transfers. The boundary conditions for the soil are of course the heat flow from the soil to the flowing air, and the heat flow at the ground surface. The latter is written as a sum of a convective heat flow, a short and long wave heat flow, and an evaporative heat flow. The monthly average thermal load supplied by the EAHE calculated with this model is compared against the results from a simpler numerical model. The agreements are good during summer and winter period, but large discrepancies are noted for mid-seasons.

A quasi three-dimensional transient model for EAHE is developed by Trzaski and Zawada (2011). The soil is divided into vertical sections. The (sensible) heat equation is solved for each of them thanks to the finite element method. The circular shape of the pipe section is approximated by the orthogonal meshing, and the convective heat transfer coefficient is corrected by a factor $\frac{\pi}{4}$. The authors used the 'Polish society of Soil Science' soil texture classification to create a set of 16 different soils: the soil density, specific heat and thermal conductivity are expressed as functions of textural parameters. The humidity ratio of the ground effect is only taken into account via the thermal conductivity. The airflow model simply consists in writing an enthalpy balance of the air for each section: the variation of the air enthalpy is due to the incoming/outgoing enthalpy (advection term) and to the convective heat exchange with the pipe wall. Since each mesh can be associated to one specific material and boundary condition, non homogeneous soil, different ground covers and shading can theoretically be modelled by this way. Each ground top surface mesh is tested to know whether it is shaded or not. The formulation of the ground upper surface boundary conditions is not explained, but one can assume that convection and short wave radiation are considered. The model was compared against experimental data, and was found to be accurate, except for special cases when the airflow is null or for meshes close to the ground surface.

Su et al. (2012) modelled a deeply buried (around 20 m) EAHE of 400 m long and section 8 m x 8 m. A one-dimensional implicit model is used to calculate the temperature and the humidity of the flowing air, according to (2.43) and (2.44) respectively.

$$\rho_a \frac{\partial \omega_a}{\partial t} = -\rho_a V_a \frac{\partial \omega_a}{\partial Z} - \frac{P_{EAHE}}{A_{EAHE}} h_v (\omega_a - \omega_{sat,pipe}) \quad (2.43)$$

$$\rho_a c_a \frac{\partial T_a}{\partial t} = -\rho_a c_a V_a \frac{\partial T_a}{\partial Z} + \frac{\partial}{\partial Z} \left(\lambda_a \frac{\partial T_a}{\partial Z} \right) - \frac{P}{A} h_c (T_a - T_{pipe}) \quad (2.44)$$

An implicit up-wind finite difference scheme is used to solve the two previous equations. Using a cylindrical system of coordinates, neglecting the angular variation of temperature and the axial heat conduction the soil modelling is treated as a quasi two-dimensional problem. Furthermore, since the soil top surface has almost no influence at such depth, and because of a high distance between the inner and the outer surface of the cylinder, a constant temperature is applied at the outer surface. The heat equation written in cylindrical coordinates is solved for each slice through a finite difference scheme. The performance of the resulting code with hourly time step was evaluated against experimental results over 130 hours. The maximum error is 1.4 °C for the temperature and 10 % for the relative humidity in most of the cases.

2.2.2.3. CFD based models

Wu et al. (2007) solved the three-dimensional heat equation for the soil and a two dimensional system of three equations - energy (2.45), mass (2.46) and turbulent kinetic energy (2.47) balances - for the air.

$$c_a \rho_a \frac{\partial T_a}{\partial t} + \nabla \cdot (c_a \rho_a \vec{V}_a T_a) = \nabla \cdot (\alpha_a \vec{\nabla} T_a) \quad (2.45)$$

$$\frac{\partial (\rho_a V_a)}{\partial t} + \nabla \cdot (\rho_a \vec{V}_a) = 0 \quad (2.46)$$

$$\frac{\partial (\rho_a k)}{\partial t} + \nabla \cdot (\rho_a \vec{V}_a k) = \nabla \cdot (\Gamma_k \cdot \vec{\nabla} k) - \rho_a \varepsilon \quad (2.47)$$

where k is the turbulent kinetic energy, ε and Γ_k are the dissipation rate and diffusion coefficient of k respectively. A Fourier condition - representing the convective heat transfer - is implemented for the ground surface. The heat convective coefficient also includes the radiation heat transfer coefficient. The undisturbed ground temperature is used as boundary condition for the ground base layer. The Phoenix software was used for the implementation and the resolution of this set of equations. It is based on the finite volume scheme. The agreement with the experimental measurements is good, as the maximal deviation is 0.8 °C.

Another 'CFD based' solution is proposed by Vaz et al. (2011). Here CFD is used for both the earth and the flowing air. The mass, momentum and energy conservation are more detailed than the system used by Wu et al. (2007), and implemented into the FLUENT-GAMBIT commercial software. The resolution is made through the finite volume method with tetrahedral volumes. The boundary conditions are isothermal (sinusoidal with annual fluctuation) on the ground surface, and constant air velocity at the pipe inlet. The problem is solved using the Reynolds Stress Model (RSM) as turbulence model, over one year with daily time step, and the accuracy of the results are evaluated thanks to measurements. The highest difference between the measure and simulated temperature did not exceed 15 %.

A CFD model was also used to model the flowing air within a two pipes EAHE and the soil around (Bansal et al., 2013a, 2013b; Misra et al., 2012). The main assumptions of the model are the following:

- The air is incompressible,
- The soil is homogeneous and its thermal properties are constant,
- The soil is not affected by the pipe presence beyond a distance equal to four times the pipe diameter,
- At such distance, a constant temperature of around 300 K is applied.

An experimental study of a 60 m long, 10 cm diameter pipe was carried out and enables the authors to verify the model accuracy. The maximum relative difference is 8 %. Nevertheless, it is important to note that the model validation is only based on one-off measurements, and that long period – monthly or yearly for example – are not studied. This is mainly due to the high computational time required by a CFD model.

Serageldin et al. (2016) led a study on a serpentine configuration of an EAHE, which is quite new, undertaken via experimental and two numerical models. Another specificity of this study is the fact that the inlet and the outlet vertical pipes are taken into account. The first is called ‘mathematical model’ and is implemented in the Matlab software. It considers transient one-dimensional heat transfers within the ground, and solved the equation thanks to a finite difference scheme. The other model is three-dimensional CFD based, solved with the commercial software Fluent. A comparison of these two numerical codes to the experimental results put in evidence that the CFD model reproduces clearly better the system behaviour than the mathematical model. Using the first one, the authors showed that the dominant heat transfer process mainly occurs via the horizontal pipes, the vertical ones do not play a significant role.

2.2.2.4. Other models

Mihalakakou et al. (1994b, 1994a, 1994c) and later Kumar et al. (2003) developed an EAHE model that takes into account the coupled heat and moisture transfer into both the flowing air and the soil was developed. The equations to solve for the soil are

$$\rho_s c_s \frac{\partial T^g}{\partial t} = \nabla \cdot (\lambda_s \vec{\nabla} T^g) - L_v \rho_s \nabla \cdot (D_v \vec{\nabla} w^g) \quad (2.48)$$

$$\frac{\partial w^g}{\partial t} = \nabla \cdot (D_{T_v} \vec{\nabla} T^g) + \nabla \cdot (D_u w^g) \quad (2.49)$$

where D_u ($m^2 \cdot s^{-1}$) is the isothermal moisture diffusivity, D_{T_v} ($m^2 \cdot s^{-1} \cdot K^{-1}$) the thermal moisture diffusivity and D_v ($m^2 \cdot s^{-1}$) the isothermal vapour diffusivity.

The equation describing the energy balance of the flowing air has a similar form to (2.30). Since the pipe is impervious, there is no moisture exchange between the air and the soil. The geometry of the soil domain is a 59 m radius cylinder. The boundary condition applied to this surface is isothermal, and its value is given by the undisturbed soil temperature at the corresponding depth and time. The model is solved thanks to a finite volume method – the soil cylinder is divided into concentric rings and several sections along the axis of the flow – and an implicit scheme and a Gauss-Seidel method. The resulting transient model was

implemented in TRNSYS. The validation against experimental measurements aggregated over fifteen days showed the maximum difference between the observed and the simulated outlet air temperatures were below 0.5 °C. Mihalakakou et al. (1994b, 1996) studied the influence of the ground cover on the heating and cooling potential of the EAHE. Nevertheless, their conclusion should be taken with caution as the ground cover is model in such a way that it only impacts the undisturbed ground temperature. Furthermore, the very simple boundary condition does not allow moisture exchanges at the ground surface, and the equation for the evolution of the air humidity is not given.

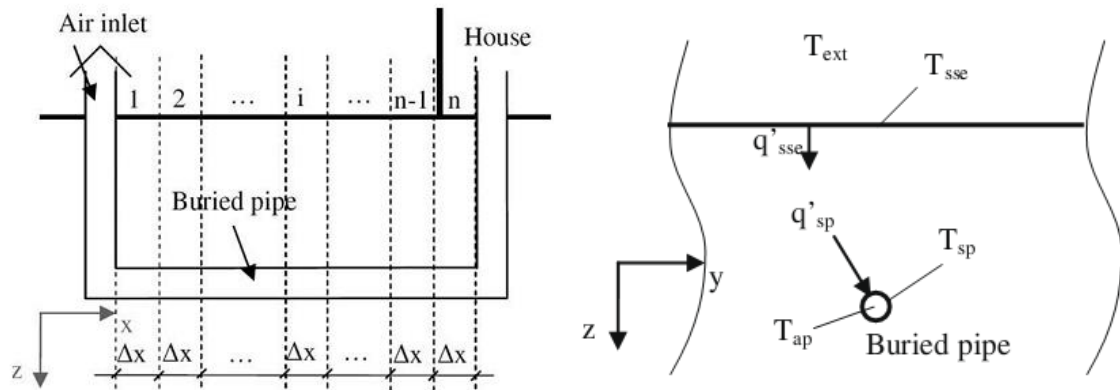


Figure 19: Principle of EAHE modelling with response factor method (Tittlein et al., 2009)

Tittlein et al. (2009) stated that the analytical methods are accurate but are limited by numerous restrictions. They only enable the modelling of very simple geometry and homogeneous soils. The numerical methods solve these problems, but require in return high computational time. They therefore proposed to use the factor response method as a relevant method to model EAHE. The system {soil + pipe} is divided into several cross-sections (see Figure 19) and the heat transferred to the circulating air is calculated for each of them. It is therefore a two-dimensional modelling. Convective, short and long wave radiation heat transfers are considered as boundary condition at the ground surface. The heat flow from the environment to the ground q'_{sse} and that from the ground to the pipe q'_{sp} are calculated thanks to the convolutive response factor method. A relation between the heat flow q'_{sse} and the ambient air temperature is obtained (2.50) for each section, where the numerical admittance X_i , the transmittance Y_i and the admittance Z_i are calculated thanks to a two-dimensional finite element model.

$$q'_{sse}(t) = \sum_{i=0}^{n_x} X_i T_{sse}(t - i\Delta t_x) + \overline{T_{sse}}(K - \sum_{i=0}^{n_x} X_i) - \sum_{i=0}^{n_x} Y_i T_{sp}(t - i\Delta t_y) - \overline{T_{sp}}(K - \sum_{i=0}^{n_y} Y_i) \quad (2.50)$$

The problem is then solved for the whole pipe length thanks to the equation

$$q'_{sse,i}\Delta x + m_a S c_a (T_{i-1/2} - T_{i+1/2}) = 0 \quad (2.51)$$

The results yield by this model are compared to the solution of both the analytical and the numerical model developed by Hollmuller (2002, 2003) and Hollmuller and Lachal (2001). The simulation of the response for both daily and annual load is accurate. According to the authors, the main advantages of this model are:

- The low computational time compared to other model of equivalent accuracy,
- The accurate simulation for both daily and annual load,
- The possible modelling of non homogeneous anisotropic soils,
- The possibility of the modelling of several pipes.

Nevertheless, the limits are:

- The neglecting of the axial heat conduction,
- The impossibility to model the shading from a building,
- The important computational time for several pipes.

Furthermore, one can note that this model requires the results of several numerical modelling to calculate the admittance and transmittance factors.

Finally, Gan (2014, 2015) was one of the first to use a three dimensional model considering a full coupling between heat and moisture transfer within the soil and the airflow. The set of conservation equations for the soil is

$$\frac{\partial(\rho_s c_s T^g)}{\partial t} = \nabla \cdot \left((\lambda + L_v \rho_l D_{Tv}) \vec{\nabla} T^g \right) + \nabla \cdot \left((L_v \rho_l D_{\theta,v}) \vec{\nabla} \theta^g \right) + \phi_h \quad (2.52)$$

$$\frac{\partial \theta^g}{\partial t} = \nabla \cdot \left((D_{Tl} + D_{Tv}) \vec{\nabla} T^g \right) + \nabla \cdot \left((D_{\theta l} + D_{\theta v}) \vec{\nabla} \theta^g \right) + \frac{\partial K_h}{\partial z} + \phi_m \quad (2.53)$$

Short and long wave radiations, convection as well as evaporation / condensation and precipitation are considered in the ground surface boundary condition. The ambient air temperature evolution is assumed sinusoidal with daily fluctuation. As no data are available for the rainfall, constant precipitation from 8:00 *pm* to 11:00 *pm* every third day are used. The vertical faces are assumed adiabatic and impermeable. The bottom face is isothermal, and the value of the temperature is equal to the undisturbed ground temperature. The heat and mass balance equation for the air are

$$\begin{aligned} \frac{\partial(\rho_a c_a T_a)}{\partial t} = & \nabla \cdot \left(-\rho_a c_a \vec{V}_a T_a + \lambda_a \vec{\nabla} T_a \right) + \frac{4}{D_{EAHE}} h_{c,EAHE} (T_a - T_{pipe}) \\ & + \frac{4}{D_{EAHE}} L_v h_{v,EAHE} (\rho_v - \rho_{v,pipe}) \end{aligned} \quad (2.54)$$

$$\frac{\partial \theta_a}{\partial t} = \nabla \cdot \left(-\vec{V}_a \theta_a + D_v \vec{\nabla} \theta_a \right) + \frac{4}{D_{EAHE}} h_{v,EAHE} \left(\theta_a - \frac{\rho_{v,pipe}}{\rho_l} \right) \quad (2.55)$$

A three-dimensional finite volume method enables the spatial discretisation. The integrated equations are then discretised into a set of algebraic equations, which are solved iteratively with under-relaxation method. The validation is made against the numerical results obtained from the software FLUENT. In the previous model, the soil properties, the

convective heat exchange coefficients, the temperature for the bottom boundary condition and the ambient air temperature are constant. The time step of the in-house program is set to 1s at the beginning of the simulation and progressively increased to 5 *min* after 10 days. The comparison over 30 days of the heat transfer rate per meter length of buried pipe showed good agreement with a maximum difference of 1 %. The authors concluded that neglecting the interactions between the soil and the atmosphere as well as the soil and the pipe, or the coupling between the heat and moisture transfer phenomena significantly over-predict the heat transfer rate. This over-prediction increases with the operating time.

2.2.2.5. Summary

Different models have been previously introduced and their main aspects are summed up in Table 10. According to the objectives, the levels of complexity are various. The need for a design tool requires fast models: analytical solutions are well suited. Such models however don't allow the modelling of complex (i.e realistic) geometries and boundary conditions. The numerical models are an alternative that are much more flexible. Their use is crucial if the buried depth is low – which mean a strong impact of the meteorological conditions – and for long term studies for example, i.e. when an accurate physical description is needed. One-, two- or three-dimensional heat transfers within the ground have been proposed for the last decades, solved most of the time thanks to finite element or volume scheme. CFD modelling of the flowing air has been sometimes implemented but this implies a high computational cost. The moisture transfer within the ground is rarely considered, and the condensation between the flowing air and the pipe inner surface is sometimes taken into account. The values used for the convection heat transfer coefficient that governs the heat transfer rate have been summed up in Table 9. The validation of the code has been often made against experimental results but only over short time periods. When complex boundary conditions are considered, the meteorological conditions are often simplified by sinusoidal evolution. As far as we know, the model integrating soil moisture transfers have never been validated against experimental results.

Table 9: Most common convective heat transfer coefficient

| Reference | Convective heat tf. coeff. ($\text{W} \cdot \text{m}^{-2} \cdot \text{K}^{-1}$) | Nusselt number (-) |
|---|--|--|
| (De Paepe and Janssens, 2003) Similar expression for (Al-Ajmi et al., 2006; Gan, 2014; Lee and Strand, 2008; Yang et al., 2016) | | $\mathcal{N}u = \begin{cases} 3.66 & \text{if } \text{Re} < 2300 \\ \frac{\xi/8(\text{Re}-1000)\mathcal{P}r}{1 + 12.7\sqrt{\xi/8}(\mathcal{P}r^{2/3} - 1)} & \text{if } 2300 < \text{Re} < 10^6 \end{cases}$ where $\xi = (1.82\log(\text{Re}) - 1.64)^{-2}$ |
| (Kopecky, 2008; Niu et al., 2015) | | $\mathcal{N}u = \begin{cases} 0.023\mathcal{R}e^{0.8}\mathcal{P}r^{0.4} & \text{in heating cases} \\ 0.023\mathcal{R}e^{0.8}\mathcal{P}r^{0.3} & \text{in cooling cases} \end{cases}$ |
| (Hollmuller, 2003) | $h_c = \frac{\mathcal{N}u\lambda_a}{D_h}$ with | $\mathcal{N}u = \begin{cases} 4.36 & \text{if } \text{Re}\mathcal{R}e < 2300 \\ 0.023\mathcal{R}e^{0.8}\mathcal{P}r^{0.33} & \text{if } 10^4 < \text{Re}\mathcal{R}e \end{cases}$ |
| (Badescu, 2007) | | $\mathcal{N}u = 0.021\mathcal{R}e^{0.8}\mathcal{P}r^{0.43}$ |
| (Tittlein et al., 2009) | | $\mathcal{N}u = 0.214(\mathcal{R}e^{0.8} - 100)\mathcal{P}r^{0.4}$ |
| (Trząski and Zawada, 2011) | | $\mathcal{N}u = \begin{cases} 0.17\mathcal{R}e^{0.33}\mathcal{G}r^{0.1}\mathcal{P}r^{0.43} & \text{if } \text{Re}\mathcal{R}e < 2400 \\ K_0\mathcal{P}r^{0.43} & \text{if } 2400 < \text{Re}\mathcal{R}e < 10^4 \\ 0.021\mathcal{R}e^{0.8}\mathcal{P}r^{0.43} & \text{if } 10^4 < \text{Re}\mathcal{R}e \end{cases}$ |
| (Gauthier et al., 1997) | $h_c = 23$ | |
| (Hollmuller, 2002) | $h_c = 3V_a + 3$ | |
| (Su et al., 2012) | $h_c = \begin{cases} 8.72 & \text{if } V_a < 1 \\ 0.045\frac{\lambda_a}{D_h}\mathcal{R}e^{0.8} & \text{if } V_a > 1 \end{cases}$ | |

Table 10: EAHE modelling: summary of the main existing models

| Method | References | Soil | | | | | Flowing air | | | | |
|-------------------------------------|-------------------------------|--|-------------|-----------------------------|------------|---|---|------|----------------------|------------|---|
| | | Resolution method | Dim. | Steady-st./Tran. | Moist. tf. | Boundary conditions | Resolution method | Dim. | Steady-st./Tran. | Moist. tf. | Boundary conditions |
| <i>Analytical / Semi-analytical</i> | (De Paepe and Janssens, 2003) | - | | | | | Logarithmic average temp. | 1D | Steady-st. | N | Constant pipe wall's temp. |
| | (Al-Ajmi et al., 2006) | Equivalent conductance | 1D | Trans. harmonic 1 pulsation | N | - | Cross-flow heat exchanger with one fluid unmixed | 1D | Steady-st. | N | Isothermal |
| | (Cucumo et al., 2008) | Green's function or superposition principle | 1D – radial | Trans. harm.2 pulsations | N | Isoth. harm. at ground upper surf. | Iterative method - Pre-supposed outlet air temp. – Quadratic evolution of air specific humidity | 1D | Trans. harm. 1 puls. | Y | Fourier condition with saturated air layer at pipe wall's temp. |
| | (Hollmuller, 2002, 2003) | Modified Bessel's functions + Fourier decomposition | 1D – radial | Trans. | N | Isoth const. Or diab. at ground upper surf. | Harm. exponentially dampened+ Fourier decomposition | 1D | Trans. | N | |
| | (Yang et al., 2016) | Modified Bessel's functions + 'excess fluctuating temp.' | 1D – radial | Trans. harm. 2 puls. | N | Isoth. harm. at ground upper surf. | Harm. exponentially dampened | 1D | Trans. harm. 2 puls. | N | Fourier condition with pipe wall's temp. = soil temp. at the same depth |

Table 10: EAHE modelling: summary of the main existing models (continuation)

| Method | References | Soil | | | | | Flowing air | | | | |
|-------------|-------------------------------|--------------------------|----------------------|------------------------------|--|--|--|--------|------------------|--------------------------------|--------------------------------|
| | | Resolution method | Dim. | Steady-st./Tran. | Moist. tf. | Boundary conditions | Resolution method | Dim. | Steady-st./Tran. | Moist. tf. | Boundary conditions |
| Numerical | (Lee and Strand, 2008) | Equivalent conductance | 1D | Steady-st. | N | Isoth. harm. (annual) at soil outer surf. | Heat balance for each section | 1D | Trans. | N | Fourier with pipe wall's temp. |
| | (Niu et al., 2015) | Undisturbed ground temp. | 1D | Stead-st. harm. annual puls. | N | - | Exponential evolution | 1D | Trans. | Y | Fourier |
| | (Thiers and Peuportier, 2008) | Finite volume | 1D | Trans. | N | Isoth. harm. (annual) at soil outer surf. + building influence correction | Heat balance for each section | 1D | Trans. | N | Fourier with pipe wall's temp. |
| | (Hollmuller, 2002) | Finite element | 3D | Trans. | N | Fourier with conv. and rad. heat flow | Heat and moisture balance for each section | 1D | Trans. | Y | Fourier |
| | (Gauthier et al., 1997) | Finite difference | 3D | Trans. | N | Fourier with conv. heat flow | Enthalpy balance | 1D | Trans. | Y | Fourier |
| | (Badescu, 2007) | Finite difference | Quasi-3D | Trans. | N | Fourier with conv. and rad. heat flow | Heat balance for each section | 1D | Trans. | N | Fourier with pipe wall's temp. |
| | (Trzaski and Zawada, 2011) | Finite element | Quasi 3D - Cartesian | Trans. | N | Fourier with conv. and rad. heat flow | Enthalpy balance | 1D | Trans. | N | Fourier with pipe wall's temp. |
| | (Su et al., 2012) | Finite difference | 1D | Trans. | N | Isoth. - constant at ground cylinder outer surface | implicit up-wind finite difference | 1D | Trans. | Y | Fourier |
| | (Wu et al., 2007) | Finite volume | 3D | Trans. | N | Fourier condition with convective and radiative heat flow for the ground surface - Undisturbed ground temps. for the ground bottom | CFD | 2D | Trans. | N | Fourier with pipe wall's temp. |
| | (Vaz et al., 2011) | CFD - Finite volume | 3D | Trans. | N | Isoth. harm. (annual) at ground upper surf. | CFD - Finite volume | 3D | Trans. | N | - |
| | (Bansal et al., 2013a) | CFD - Finite volume | 3D | Trans. | N | Isoth. constant temp. at ground cylinder outer surf. | CFD - Finite volume | 3D | Trans. | N | - |
| | (Serageldin et al., 2016) | CFD - Finite volume | 3D | Trans. | N | Isoth. constant temp. at ground upper and lower surf. | CFD - Finite volume | 3D | Trans. | N | - |
| | (Mihalakakou et al., 1994b) | Finite volume - implicit | 1D - radial | Trans. | Y | Isoth. harm. (annual) at ground cylinder outer surf. | Heat balance for each section | 1D | Trans. | N | Fourier with pipe wall's temp. |
| | (Tittlein et al., 2009) | Response factor method | 2D | Trans. | N | Complex meteo. | Heat balance for each section | 1D | Trans. | N | Fourier with pipe wall's temp. |
| (Gan, 2014) | Finite volume | 3D | Trans. | Y | Complex meteo. - Isoth. at ground bottom | Heat and moisture balance for each section | 1D | Trans. | Y | Fourier with pipe wall's temp. | |

2.3. FONDATHERM SPECIFICATIONS AND CONCLUSIONS

The operating principle of Fondatherm is similar to that of a traditional EAHE. The 'U' shape of the concrete prefabricated foundation creates a channel allowing the circulation of air as illustrated on Figure 20. Nevertheless, some major differences with EAHE have to be detailed as it potentially strongly influences the heat transfer rate.

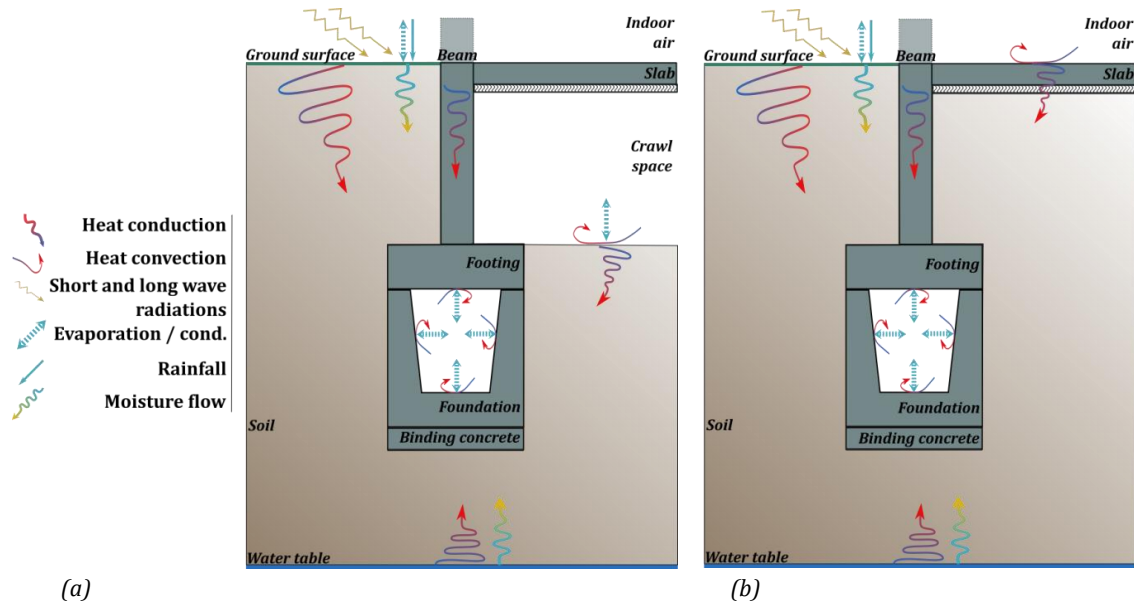


Figure 20: Fondatherm cross section with crawl space (a) or ground-on-slab (b) configuration: main physical phenomenon

2.3.1 DEPTH

The mean buried depth of the EAHE introduced in the section 2.1 is around 2.5 m. They are thus located in the 'shallow zone', where the meteorological factors still have an influence on the ground temperature field but only with a seasonal fluctuation. The depth of Fondatherm is imposed by structural issues, and is rather between 50 cm and 2 m. This position, closer to the 'surface zone', means a stronger influence of the weather. Convection, solar radiation, radiative exchanges with the sky and the buildings, evaporation and precipitation play a significant role in the distribution of the temperature field around the foundation. At such depth, the ground moisture content is also very variable, which of course influence the temperature field evolution.

2.3.2 CAVITY SIZE AND SHAPE

Contrary to almost all the EAHE of the literature review previously exposed, the cross-section of the Fondatherm duct is trapezoidal, but it can be easily approximated to a rectangular shape, of height and width respectively equal to 45cm and 35cm. As detailed in the subsection 2.1.2.3, this influences the heat transfer rate. Nevertheless, the models used for the calculation of the convective heat transfer coefficient are not adapted for such large sections. The alternatives are CFD models – but they require really high computational time – or suited correlations. The latter approach will be explored in the 4.5.2.1.

2.3.3 DUCT THICKNESS AND MATERIAL

The Fondatherm channel is composed of a 'U' shape concrete foundation of between 10 cm and 15 cm thickness, surmounted by a 20 cm thickness concrete footing as showed on Figure 20. Contrary to a plastic pipe, this cannot be considered as impermeable. Water infiltration from the ground surface or coming from the water table can thus penetrate into the concrete. It consequently affects the latent heat exchanges between the flowing air and the foundation inner walls'. Even though it is beyond the scope of this study, it can even favour the mould growth. An accurate reproduction of the moisture content field within the concrete can be useful for further studies.

2.3.4 POSITIONING IN RELATION TO THE BUILDING

The Fondatherm positioning with respect to building is unusual. It is simultaneously influenced by the climate, by the subground but also by the above building, which as far as we know has never been explored (the pipes are either beneath the building or next to the building). Indeed a part of the building heat loss through the slab or via the beam can be recovered by the foundation. The foundation outer surface is thus influenced by various conditions. All the models that set an isothermal temperature – equal to the undisturbed ground temperature – on the pipe surface or at a certain distance from the pipe are a priori inapplicable here.

2.3.5 CONCLUSIONS

The literature review as well as the highlighted Fondatherm characteristics put in evidence that:

- The development of at least a two dimensional model for the ground and for the concrete foundation is necessary in order to have a full understanding of this innovative EAHE,
- The consideration of coupled heat and moisture transfer within the ground but also within the foundation appeared as important, due to the position close to the ground surface, and possible influence of the water table,
- The latter implies to be able to take into account complex boundary conditions from the outdoor and from the underground,
- The building heat loss through the slab and recovered by the foundation walls' look determinant for the foundation performance, and thus have to be taken into account carefully.

All of these points motivated the next chapter, where the opportunities for the {ground+foundation} modelling are explored.

Chapter 3. GROUND HEAT TRANSFER PHENOMENA & COUPLED HEAT AND MOISTURE TRANSFER WITHIN POROUS MEDIA: MATHEMATICAL DESCRIPTION

3.1. BUILDINGS GROUND HEAT LOSS

Buildings ground heat loss accounts for up to one third of the whole heat loss in a cold climate. Accordingly to the reduction trend of building energy consumption, the study of this phenomenon has thus become a wide field of research since the 1940s. A full comprehension obviously implies modelling, which encounters difficulties mainly linked to:

- The three-dimensionality of the process,
- The variations of the geometry and the kind of basement floor,
- The wide temporal scale of the heat flow process below a building,
- The high thermal inertia of the ground, resulting in unsteady heat flow,
- The strong heterogeneity of the materials involved and
- The lack of knowledge about their heat and mass transfer characteristics.

This section provides an overview of the different kinds of modelling that have been developed during the past decades. They can be distinguished from each other by the method used – (semi) analytical, numerical, or design guide – and by the level of accuracy for the physical phenomena taken into account: one-, two- or three-dimensional heat transfers, material heterogeneity, complexity of the boundary conditions, complexity of the geometry of the building, moisture migration, freezing, ground water flow, etc.

Given the Fondatherm specifications described in section 2.3, it clearly seems that the two problems, the ground heat loss from a building via the slab one, and the modelling of a “new kind” of EAHE one, are similar. They indeed imply to have a full comprehension of heat transfer from the building interior to the ground below and around. This is the reason why attention to the past works on this topic must be paid.

3.1.1 DIFFERENT MODELLING LEVELS

The problem of buildings ground heat loss has first been solved under strong assumptions which enable to compute analytical or semi-analytic solutions. Authors who first carried on this way supposed that the heat transfer within the ground was only one- or two-dimensional, made a steady-state assumption or used periodic conditions, or even supposed a material homogeneity within the ground. But buildings ground heat loss via slabs is acknowledged as a three-dimensional process. They therefore began to include more and

more details in their model which could only be solved by numerical method. As the required time to obtain results using such models is too important in a designing process, other chose to stick with strong assumptions (one-dimensional heat transfer, climatic condition modelled by the outdoor air temperature only, building geometry simplified, etc.), and even tried to get simpler method than the analytical ones: the “manual” methods. Their objectives are to quickly produce an assessment of ground heat loss thanks to “rule of thumb” or abacus, for the most common basement cases. A relatively exhaustive overview of the work in this field is given by Zoras (2009), and the main results are presented below.

3.1.1.1. Analytical / semi-analytical methods

These techniques imply simplifications but are useful to predict the heat transfer rate in a fast and relatively accurate manner. Assuming harmonic time dependence for the ground temperature field, Delsante et al. (1983) used Fourier transforms to solve analytically this problem for rectangular or rectilinear slabs on ground. They proved that for daily-or less condition – a harmonic temperature – the heat flow into the ground is essentially one dimensional, perpendicular to the slab/ground surface. For annual-daily range conditions period, the flow is three dimensional and consists of curved-path around the edge of the slab plus the previous daily or less period conditions. Their innovation in their work compared to the former ones is based on the fact that they explicitly modelled the walls, assuming a linear variation of the temperature at the contact surface earth-walls. For a realistic separation between two outside opposite walls, and for condition periods’ up to one year, the effect of one wall on the opposite can be neglected with a high degree of accuracy. The work of Anderson (1991) is consistent with that of Delsante et al. (1983). Anderson proposed to introduce a shape factor L' of the building (3.1).

$$L' = \frac{2A}{P} \quad (3.1)$$

where A is the area of the floor, P is the exposed perimeter. Thanks to it, he could easily extend the previous method (Delsante et al., 1983) to three dimensional cases and other slab shapes by replacing the building width of the two-dimensional case by this value. He obtained a U factor given by (3.2) where w designate the wall thickness. He proved that the use of (3.2) is equivalent to the use of the same formula using the building width instead of L' .

$$U = \frac{2\lambda}{\pi L'} \ln \left(\frac{\pi L'}{w} \right) \quad (3.2)$$

He then treated the case of an insulated slab, from interior or exterior by introducing an equivalent length of insulation $d = \lambda R_{ins}$ where λ is its thermal conductivity and R_{ins} its thermal resistance. He also introduced the impact of the thermal resistance of the ground surface by introducing the length e . The final formulation he obtained was

$$U = \frac{2\lambda}{\pi L'} \frac{1}{1 + d/\pi L'} \ln \left(\frac{\pi L'}{w + d + e} + 1 \right) \quad (3.3)$$

This expression has been compared to the results of the numerical model developed by Hagentoft (1988). The agreement was good, the ability of the model to reproduce three-

dimensional problem with two-dimensional solution has therefore been proved. This was not true for heavy insulation; he thus proposed the formula (3.4) for these special cases:

$$U = \frac{\lambda}{d + 0.5L'} \quad (3.4)$$

Based on linearity properties of heat transfer equations, Claesson and Hagentoft (1991) proposed to sum the solutions for three different kinds of outdoor boundary conditions: steady-state, harmonic and Heaviside unit step (see Figure 21). Fourier transforms make it possible to solve more complex problem (real outdoor temperature) from the solutions of these three cases. They showed that the one- and two- dimensional transfers essentially result from transient transfer, while the three-dimensional heat losses are the consequence of

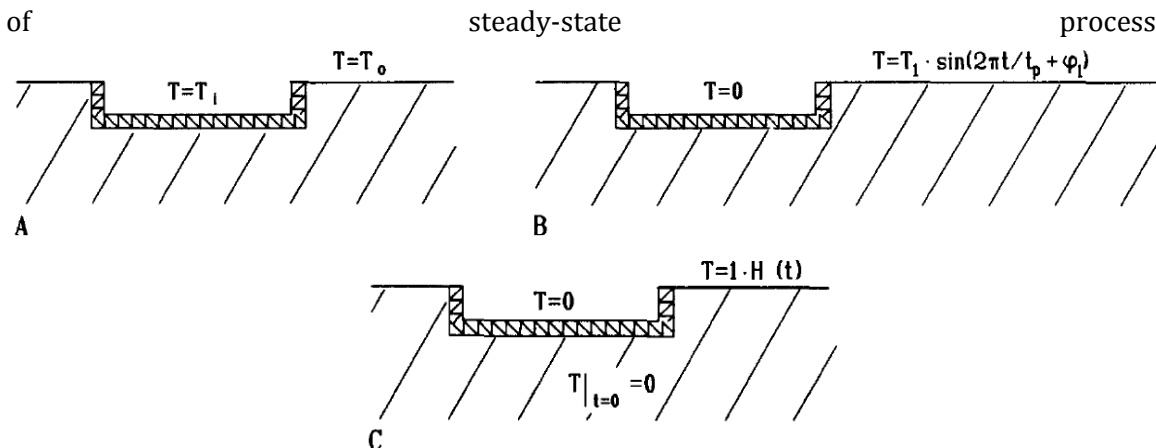


Figure 21: Fundamental thermal processes: steady-state (A), periodic (B) and outdoor temperature (C) (Claesson and Hagentoft, 1991)

In his PhD work, Hagentoft (1988) studied the effect of a ground water table, of frost, and of a snow cover on ground building heat loss. He demonstrated that for a common situation - soil for which hydraulic properties lie within those for clay and those for coarse sand, with a water table depth equal to the width of the building - the presence of the water table increase of about 5% the ground heat loss. He also studied the impact of frost using numerical modelling. Frost is simply taken into account by a modification of the ground thermal conductivity, specific heat and latent heat. The maximum difference induced by the frost modelling on heat loss was found to be around 5%, and its global effect is about 2%. Hagentoft concluded that the frost impact is negligible. He finally modelled a snow cover by the adding of a ground layer with a thickness that gives the thermal resistance of snow. He then modelled the snow cover as an average occurrence all over the year. The maximal difference observed on ground heat loss is around 10%, and the mean difference is of less than 2%. The snow cover can equally be neglected according to the author. Hagentoft (1996) set up an analytical solution for the building ground heat transfer problem. This solution is valid for two-dimensional steady-state problems. Based on that tool, an abacus gives the rate between building ground heat loss with and without ground water flow, as a function of the building dimensions, and the depth of the water table. The modelled case is the worst one for the heat flow: it assumes an infinite water flow, at the ambient air temperature. For uninsulated slabs, a common building shape and water table depth, this rate is around 2. For insulated basements, the rate is about 1.5, which cannot be considered as negligible.

All of the previously cited works focused on the ground building heat loss, without considering the whole building above. Chuangchid and Krarti (2001) made a step toward a full building modelling including ground heat loss. They studied the ground heat loss of a building equipped with a hydronic heating system. They determinate the temperature field within the ground underneath the building and within the heating system by the use of a transient periodic semi-analytical solution. Their study takes a water table into account. The heat flow derives directly from that, and they could obtain it for several configurations: insulation level, circulating water temperature, etc. Their solution is based on the « interzone temperature profile » technique, which consists in dividing each part of the domain in a homogeneous rectangular shape. The Fourier transforms method previously introduced can thus be applied for each zone. The major advantage of this technique is that it makes the modelling of complex geometry possible. The results obtained by this method are successfully validated against experimental data, for several configurations. The insulation reduces the spatial variation of the temperature of the floor surface. It has been proved to have a huge impact on the distribution of the isotherm within the ground.

Other authors made a physical analysis of the problem to propose a new kind of solution. Zhong and Braun (2007) developed a simple earth-contact model for different concrete slab configurations. Their goal was to build a simple ground-coupled heat flow model which doesn't need a high computational time and can be introduced in a whole building load simulation tool. They proposed to divide the heat flow from the building to the ground into two parts. First, the one dimensional heat flow from the centre of the slab to the ground beneath, which has been included in a three nodes model, taking into account soil properties. Secondly, the perimeter heat losses, depending on insulation level on the edge, soil properties and floor materials. For these two heat flow paths, correlations have been built thanks to the comparison against 2D finite element modelling. This has been made for two common floor geometries and soil materials, and enables to accurately predict the transient heat flow spatially averaged at the interior floor surface. Xiaona et al. (2008) followed the same idea: simplify the heat transfer through the slab by decomposing it. They chose to divide it into three parts:

1. Heat transfer between the indoor air and the subground
2. Heat transfer between the indoor air and the outdoor ground surface
3. Heat transfer between ground-coupled envelopes

For each process, they set a simplified one-dimensional model of a two layers “equivalent slab” under harmonic condition. This has been validated against the results obtained by a two-dimensional modelling with finite difference method. As previously, it supplies a relatively good approximation of building ground heat transfer, with a low computational effort, and can be easily implemented in a building load simulation tool.

3.1.1.2. Numerical methods

Fully numerical treatment of this problem appeared in the early 1980s, and has the interest to handle problem closer to the reality, giving the possibility to model complex geometry and boundary conditions. Davies et al. (1995) pointed out the importance of the use of a multi-dimensional model on the accuracy of the results. One-dimensional models systematically underestimate the building load and the ground heat loss compared to a two-dimensional model. Likewise, two-dimensional models underestimate the loads compared to a three-dimensional one.

Numerical models enable to easier couple different physical phenomenon or systems. For instance, Youcef (1991) developed a two-dimensional coupled model for a flat plate collector, a heating floor and the ground beneath. Although the model results are in relatively good accordance with experimental data (on hydronic water temperature, ground and indoor air temperature), some discrepancies call into question the choice that have been made for the boundary conditions. The author discusses the way to represent the water table, modelled by an isotherm at 17°C and 1.6m depth. This kind of assumption is well suited for deep ground water flow, but not for the shallow ones. He also highlighted the importance of the initial condition, for the water pipe temperature in his specific case.

Adjali et al. (2000a, 2000b) positioned their works in the same field: the experimental and numerical study of a building equipped with a hydronic heating system. The studied case is atypical, with a void in the middle of the slab which confirms the ability of the numerical model to adapt itself to complex geometry. The ground temperature is recorded at several depths in three different stacks, and the indoor air temperature at several place in the room. The water content of the ground is also recorded at several depths and in two different stacks. In parallel, they performed a two- and three-dimensional numerical study. They strive to embed a ground model into a full commercial building model (APACHE). They indeed noted that most of the time, both this models are stand-alone process. The ability of the coupled model “ground + slab + building” to accurately reproduce the experimental results is validated. The observed discrepancies mainly results from two parameters according to the authors: the thermal conductivity and the floor energy dissipated. A sensitivity analysis confirms this assumption. The limits of the model are also highlighted. Because of the high computational time induced, the studied domain has been reduced to a small portion of the building, which has been made possible by the symmetries. The opportunity of the use of a two-dimensional model instead of a three-dimensional one is assessed. This seems possible far from three-dimensional heat transfer sources –typically the corners.

Weitzmann et al. (2005) set up a numerical model achieving a full coupling between the ground and the building above, including a floor heating system. The authors chose to override the three-dimensional aspect of the physical phenomenon using the equation (3.1). Then, they made a two-dimensional finite control volume model based on this assumption and which has been validated against experimental measurements. One aspect of this model can explain the observed difference: the real building studied is narrow, such that the influence of the opposite wall should normally be taken into account.

In the trend of CPU time reduction, Al-Anzi and Krarti (2004) proposed a method called “local/global analysis” to evaluate the ground-coupled heat transfers. This method is

applicable for simplified foundation configurations but it presents the advantage to reduce the computational time compared to full numerical models. It nevertheless offers a relatively good insight of the involved phenomenon. The global domain forms a simple representation of the ground coupled heat transfer problem, sufficiently simple to be solved by an analytical method (in this paper, an ITPE technique like described by Chuangchid and Krarti (2001)). Then, a local domain is defined to model with a finite difference method all the details beneath the slab: insulation, gravel, foundation, etc. The boundary conditions of the local domain are those resulting from the simulation over the global domain. Consequently, the finite difference method is applied only on a reduced domain. The influence of the choice of the local domain, on the accuracy of the solution, and the saving computational time of the L-G method are analyzed. Compared to a full numerical solution, the L-G method is proved to be efficient from a computational point of view, and relatively accurate: 90% time reduction without loss of accuracy.

Thomas and Rees (2009) set up two experimental studies on two full scale buildings, in order to first assess heat flow from the slab to the ground, and secondly to validate their ground heat transfer numerical model. They gathered data recorded over one year every 30 min. They built a two-dimensional sensible heat transfer model, solved by a finite element method. The ability of this model to correctly reproduce ground temperature was successfully validated. The temperatures just beneath the slab are correctly reproduced, but the outside temperature at 25 cm depth shows some discrepancies, probably due to a too simple modelling of the top surface boundary conditions (the outdoor temperature was applied on the top nodes as a Dirichlet condition). They finally studied the influence of soil moisture content on heat transfer. For that purpose, they computed the steady-state ground water content profile (gravitational equilibrium) for several water table depths, between -10m and -0.5m below surface. This directly influences the ground thermal conductivity, which has been calculated by geometric mean of solids, water and gas conductivities (Rees et al., 2007). This is the only coupling between moisture and heat transfer that has been taken into account in their model. Using both one- and two-dimensional simulation, the water table depth has been proved to be an important factor that strongly influence heat losses. For the one-dimensional problem, a 60% heat flow increase has been computed between the deepest water table case and the highest one. This increase is reduced to 20% for the two-dimensional case, which is still significant.

All of the previous models didn't take into account the humidity – liquid or vapor – transfers into the ground, but only sensible heat transfers. In the rare cases where the ground water content was recognized like having an important effect on heat transfers, it was in a simple manner, without considering a full coupling. Other investigations focused on the impact of fully coupled heat and mass transfer equation onto building ground heat loss (Deru and Kirkpatrick, 2002a; Janssen et al., 2004; Mendes and Philippi, 2005; dos Santos and Mendes, 2006; Shen and Ramsey, 1988). Shen and Ramsey (1988) highlighted that “the analyses of earth-contact building problem [...] requires a two-dimensional numerical code that is capable of handling transient conditions for both saturated and unsaturated moisture flow and heterogeneous soil conditions”.

Thanks to a fully implicit finite difference method, recognized as well suited to model non linear coupled equations, they simulated coupled heat and moisture flow within the ground.

The model was validated against analytical solution for some one-dimensional cases and against experimental studied lead on a sand column of 1.38m high. Their study focused on a rather simple geometry: a basement wall in contact with a piece of ground (Figure 22). This element was exposed to fifteen days of summer climate, and fifteen day of a winter climate. In both cases, a rainy period was included. For each period, two simulations were run. The first one was based on fully coupled equations and the second one on decoupled equations. The temperature, the moisture content of ground and the wall heat loss is plotted, which clearly show:

- The wide effect of the moisture on foundation wall heat loss,
- The increasing of this phenomenon when using a coupled model.

These results can however not be generalized. In the case of a sandy ground, a 9% increase of the heat flow from the wall in the winter period and over 40% in the summer period arise from the fully coupled model instead of the decoupled one. But no difference for the clayey can be observed.

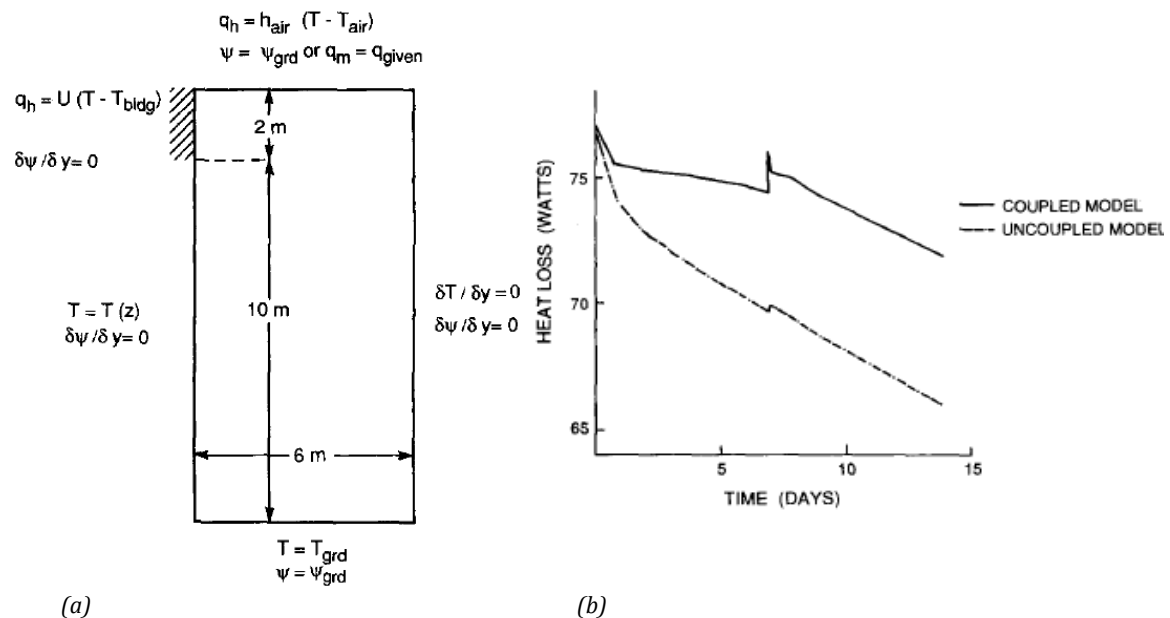


Figure 22: Boundary conditions for the numerical simulation of the soil surrounding a basement wall (a) and total wall heat loss values from day 85 to day 99 for a basement surrounded by a sandy soil (b) (Shen and Ramsey, 1988)

Janssen et al. (2004) pursued the studied building ground heat transfer via the slab, but extended it to more real applications. He integrated in his model more complex boundary conditions at ground surface, considering convection, evaporation / condensation, short- / long- wave radiation and sensible heat exchange by precipitation. He run his model over multiple years, which obviously gives more credit to the results. He analyzed the difference between the fully coupled model and the linear model. The comparison was led for several climate, precipitation amount, soil type, slab thermal resistance, foundation width and shape in order to generalize the previous results. The conclusion was that the coupling impact increases the building ground heat loss during the heating season of about 15%. He however explained that regarding the inaccuracy about the soil characteristics, the integration of the coupling effects into a standard calculation method is not relevant. Indeed, the inaccuracy on

thermal conductivity for example will lead on the same difference magnitude. He also recognized that some aspects have not been taken into account (three-dimensional heat and moisture transfer, complex soil surface, soil stratification, etc) which could change the previous conclusions.

3.1.1.3. Manual methods

A non negligible number of authors were interested by the development of tools to obtain simply and quickly the building ground heat loss without complex calculations. These manual methods take most of the time the form of abacus, tables or simple calculations. Mitalas (1983) for instance made a table to compute heat flow through the slab for a variety of configurations. These design rules result from 2D and 3D numerical simulation. One can question the accuracy of such tools. Adjali et al. (2004) made an evaluation of the ability of four simple design tools to correctly compute the heat loss through the ground from a building. The tools considered were those from ASHRAE, from BRE, from CIBSE and from AICVF, and have been compared to each other and when it was possible to the measured data. These simple calculations sometimes over- or under-estimate the actual value of heat losses up to 30%. This is logically the consequence of the high number of assumptions made to obtain quickly results. Furthermore, the authors proved that an improvement of some methods is sometimes affordable. For example the ASHRAE method uses a constant single value of soil conductivity. In some cases, the conductivity is known, and its value can be used instead of the default one, which gives back better results. Design tools are most of the time relevant to get good estimations, but the choice of the tool has to be made regarding the characteristics of the building studied. In the case where the building cannot be modeled by a manual method, the analytical and the numerical solutions can be used.

3.1.2 SUMMARY: USEFUL INFORMATION FOR FONDATHERM

All the previous works have been introduced because of the strong relation between the modelling of building ground heat loss and the objectives stated in this thesis. The results and methodologies presented can therefore be used as a good practices guide. The Table 11 provide a summary of the different kinds of building ground heat loss existing models. In addition to the models specifications, some physical considerations can be useful to guide the choice for the Fondatherm modelling.

Claesson and Hagentoft (1991) assessed the heat flow through a concrete slab on ground made of a material of diffusivity α . Considering a pure periodic thermal load of period t_p , the periodic penetration length is given by

$$\delta_p = \sqrt{\frac{\alpha t_p}{\pi}} \quad (3.5)$$

Foundation walls width's is at least of $12.5cm$. Assuming a diffusivity equal to $9 \cdot 10^{-8} m^2 s^{-1}$, $\delta_p \cong 5cm$ for a daily condition,. It's commonly accepted that beyond $3\delta_p$, the effect of the thermal wave is negligible. It entails that the conditions for which the period are lower than a day won't attain the near ground of the foundation. This may suggest the use of

two different time steps for the resolution of the heat transfer problem Fondatherm: one for the ground and another one, smaller, for the concrete foundation.

Delsante et al. (1983) showed the opposite walls influence on each other. He put in evidence that for the case of a two typical walls of thickness 20 cm with a 3 m separation, the influence of one wall on the other one can be considered as negligible. Extrapolating this result to the Fondatherm case, it means that it is unnecessary to model the whole ground domain under the building. Its width can be limited to some penetration depth corresponding to an annual period.

Janssen et al. (2004) showed that for a poorly insulated slab, the difference between a pure sensible transfer model and a coupled model is about 10 – 15%. Even though this difference is shrunk for a better insulated basement, it seems important to take moisture transfer into account regarding the objectives of the thesis, exposed in the section 1.3. He also pointed out that the influence of uncertainties on soil thermal and hydric characteristic leads to a similar order of magnitude that those due to the coupling effects. A good definition of the parameters used in the model appears as essential. One can also think to assess these uncertainty influences on the model output by a parametric study.

A lack of rigor on the way to treat the boundary conditions has been pointed out as leading to inaccurate results (Hagentoft, 1996; Janssen et al., 2004; Thomas and Rees, 2009; Weitzmann et al., 2005). This is valid for the ground outdoor surface as for the ground base layer and the coupling with the building. The drawbacks induced by such complex boundaries can be numerical (i.e. convergence) problem. A solution is proposed by Mendes et al. (2002) who overcomes this issue.

About the time step, Janssen showed that the use of daily and hourly averaged climate data have a limited impact on the results. A slight difference can be observed on temperature. The use of large time-step is possible, in order to reduce the computational time. It can however introduce errors in the heat and mass balance what Janssen solved by using the Celia and Bouloutas (1990) method.

One has to keep in mind that the choice of the best model to use, i.e. with respect to the objectives set, is a trade-off between accuracy and simulation time. In the Fondatherm case, the geometrical details are going to be analyzed. The objective is obviously also to obtain an accurate evaluation of the temperature and the humidity content of the air at the foundation's outlet. Furthermore, the position of the foundation and its relative low depth make it is presumably strongly influence by the outdoor conditions, among others, the precipitations. Consequently, an accurate modeling of these boundary conditions seems necessary. All of this implies to get the field of temperature and moisture level in the foundation and its vicinity as well as its evolution with time.

A numerical model can enable a good representation of all the geometrical and boundary conditions details. The choice of a 3D coupled heat and mass transfer ground and foundation model has thus been made and satisfy the other requirements previously explained. The construction of the system equations and the corresponding boundary conditions are developed in the section 3.2 and 4.5 respectively.

Table 11 : Building ground heat loss modelling: summary of the main existing methods

| Method | Authors | Resolution method | Dim. | Building geom. | Steady-st./Tran. | Soil char. | Boundary conditions | | | Coupling to building model | Moist. tf. |
|-------------------------------------|---|--------------------------------------|-----------------|---------------------------------|--|--|-------------------------------|--|-----------------------------|---|------------------------|
| | | | | | | | Out. surf. | Base | In. Surf. | | |
| <i>Analytical / Semi-analytical</i> | (Delsante et al., 1983) | Fourier transform | 2D 3D | Rect. Slab-on-grade | Steady-st. | Homog. Modelled Via diff. | Dirichlet Harm. temp. | Sem-inf. solid: adiab. | Dirichlet Harm. temp. | Via the build. indoor temp. and the wall thickness, No insulation | N |
| | (Anderson, 1991) | Green's theorem | 2D 3D | Rect. Slab-on-grade | Steady-st. | Homog. Modelled Via cond. | Dirichlet Const. temp. | Semi-inf. solid: adiab. | Dirichlet Const. temp. | Via the build. indoor temp. and the wall thickness, With insulation | N |
| | (Claesson and Hagentoft, 1991; Hagentoft, 1996) | Superposition Dimensional analysis | 3D | Rect. Slab-on-grade Cellar | Tran. | Homog. Modelled Via diff. | Dirichlet Real temp. | Dirichlet Wat. tab. isoth. | Dirichlet Real temp. | Via the build. indoor temp. With insulation | N |
| | (Chuangchid and Krarti, 2001) | ITPE technique | 2D | Various | Tran. | Homog. Modelled via diff. | Dirichlet Harm. temp. | Wat. tab.: isoth. | Dirichlet Const. temp. | Detailed : insulation, heating floor, floor covering | N |
| | (Zhong and Braun, 2007) | Correlations based on 2D FEM results | 1D | Rect. Slab-on-grade | Tran. | Homog. Modelled via diff. | Dirichlet Harm. temp. | Adiab. | Convection Harm. temp. | Via a three nodes resistance. model | N |
| | (Xiaona et al., 2008) | Equivalent slab | 1D | Rect. Slab-on-grade | Tran. | Homog. Modelled via diff. | Dirichlet Harm. temp. | Isoth. | Dirichlet Harm. temp. | Coupling between ground envelopes | N |
| <i>Numerical</i> | (Youcef, 1991) | Alternating direction implicit alg. | 2D | Rect. Slab-on-grade | Tran. | Homog. Modelled via diff. | Dirichlet Real temp. | Water table: isoth. | Convec.+radia. Const. temp. | Fully integrated into a build. model, incl. heating floor | N |
| | (Adjali et al., 2000a, 2000b) | FVM | 2D 3D | Various Slab-on-grade | Tran. | Homog. Modeled via diff. | Radia. Real temp. | Adiab. | Dirichlet Real temp. | Coupling with heating floor | N |
| | (Weitzmann et al., 2005) | FVM | 2D | Various Slab-on-grade | Tran. | Homog. Modelled via diff. | Convec. | Adiab. | Convec.+radia. | Fully integrated into a build. model, incl. heating floor | N |
| | (Al-Anzi and Krarti, 2004) | Local/Global analysis | 2D | Rect. Slab-on-grade | Tran. | Homog. Modeled as porous material (incl. water cont.) | Dirichlet Harm. temp. | Wat. tab.: isoth. | Dirichlet Harm. temp. | Via the build. indoor temp. | N |
| | (Thomas and Rees, 2009) | FEM | 2D | Various Slab-on-grade | Tran. | Homogeneous Modelled via diff. | Dirichlet Real temp. | Wat. tab.: isoth. | Dirichlet Real temp. | Via the build. indoor temp. | Via cond. & spec. heat |
| | (Shen and Ramsey, 1988) | FDM | 2D | Basem. wall | Tran. | Homog. Modelled as porous material (incl. water content) | Conv. Iso-matric head or rain | Wat. tab.: Iso temp. & matric head | Real temp. Imperm. | Via the build. indoor temp. | Y |
| | (Deru and Kirkpatrick, 2002b; Janssen et al., 2004) | FDM / FEM | 2D | Various Slab-on-grade Cellar | Tran. | Homog. Modelled as porous material (incl. water content) | Conv.+Radia. +Evap.+Rain | No heat tf by cond. | Dirichlet Const. temp. | Via the build. indoor temp. | Y |
| (dos Santos and Mendes, 2006) | FDM | 3D | Various No slab | Tran. | Homog. Modelled as porous material (incl. water content) | Conv.+Radia. +Evap.+Rain | Adiab. Imperm. | Conv.+ Evap. Indoor air temp. from buid. model | Full coupling | Y | |

3.2. COUPLED HEAT AND MASS TRANSFER WITHIN POROUS MEDIA: SPECIFIC CASE OF GROUNDS AND CONCRETE

The previous state of the art about building ground heat loss modelling showed that the most recent studies consider simultaneous heat and mass transfer in soils, and that latent heat exchanges might be an important part of the global building heat loss. This section attempts to give a good understanding of all the available opportunities to model grounds, and select the most appropriate for this work.

Several fields undertake detailed studies about the behaviour ground: thermal engineering, civil engineering, etc. Whether it is a thermal, a mechanic or hydraulic problem, most have the same approach, consisting in describing the soil as a porous media and then to switch from the conservation equations describing the fundamental phenomenon at a microscopic scale to a macroscopic modelling reproducing its global behaviour. This is for example at the origin of the Darcy law which gives the mean fluid velocity within porous material thanks to the hydraulic conductivity.

The first subsection endeavours to define and characterise a porous media and gives a brief explanation of methods for changing scales and the underlying assumptions to use it. The second gives a description of the available mathematical model for simultaneous heat and mass transfer within porous media, more particularly soils. These models necessitate knowing the thermal and hydric properties of the porous media and fluids involved. Measurements and modelling are the two possibilities to obtain them. As the measurement cannot be systematic for every kind of soils encountered in every Fondatherm project, the models used will be described in the third part of this section.

3.2.1 POROUS MEDIA: GENERALITIES ABOUT THEIR MATHEMATICAL MODELLING

3.2.1.1. Porous media: definition and characterisation

A porous media – as foams, leathers, tissues in the human body or still, our main field of interest, soils – is a three-dimensional arrangement of solid particles of different size and shape called matrix. Within this highly complex layout occurs storing, transportation and sometimes chemical reaction of a liquid and/or gaseous phase. These phenomena strongly depends on both the solid and the voids arrangement and the fluids storing and transfer properties. Due to the complexity of the solid matrix, a statistical approach is usually preferred to describe it, which implies to neglect some aspects of the microscopic details. Considering one sample, one can define for instance:

1. The porosity ε_t is the ratio of voids volume over the total sample volume. Since some pores are not connected to the other ones – they are called closed pores – it is also relevant to define the open porosity $\eta = \frac{\text{open pores volumes}}{\text{sample volume}}$,
2. The specific area $A_s = \frac{\text{solid/void interface area}}{\text{sample volume}}$,
3. The geometrical tortuosity $\tau = \frac{\text{mean length of a streamline}}{\text{length of the sample}}$,

4. The distribution of the size of the solid particles (or the pores), represented by a grading curve. The methods used to build such curves are based on geometrical arrangement of the solid mater and the voids. To give an idea, a macropore is a pore of which the equivalent diameter is more than $300 \mu m$, a micropore is within the range $[0.05 \mu m, 300 \mu m]$ diameter and a nanopore is less than $0.05 \mu m$ diameter.

All of these properties have been defined for a whole sample, but the writing of conservation equations for the modelling necessitates being able to define local properties, and consequently being able to define a local volume for their measurement. As illustrated on Figure 23, such a volume is called ‘elementary representative volume’ (ERV) and is defined so that it is small enough to conserve its local aspect, but large enough to ensure the needed characteristics can be defined over it. In summary, if l is the mean size of a pore, L the sample size, the characteristic length d of the ERV is such as $l \ll d \ll L$.

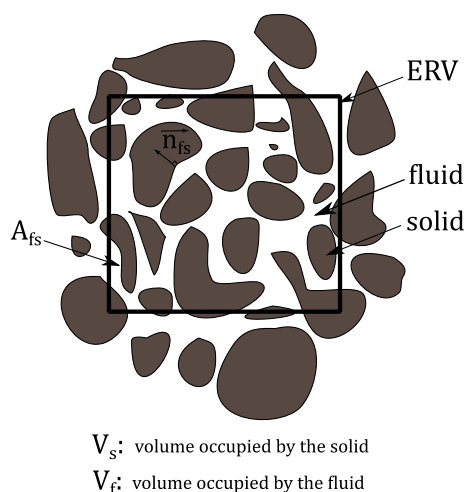


Figure 23: Porous media: definition of the Elementary Representative Volume

3.2.1.2. Porous media: modelling of a conductive thermal problem

Given the complexity of the pores structure at the scale of the ERV, a method for changing scale has to be applied in order to ignore the details of the microscopic geometry (Hassanizadeh and William G. Gray, 1979). For that purpose, this method first consists in building an equivalent (fictitious) media called ‘macroscopic’ as opposed to the real microscopic porous media. The process then consists in a rewriting of the conservation equations at the microscopic scale – derived from continuum mechanics or thermodynamics – for equations at the ‘macroscopic’ scale. Such transition can be done by several ways, like homogenization or volume average methods. Among the last ones, the most common method is to compute an average over the ERV previously defined. The following operation are thus applied to the conservation equation (Bories et al., 2008)

$$\langle \nabla \cdot \cdot \rangle = \nabla \langle \cdot \rangle + \frac{1}{V} \int_{A_{fs}} \cdot \vec{n}_{fs} dA \quad (3.6)$$

$$\left\langle \frac{\partial}{\partial t} \cdot \right\rangle = \frac{\partial}{\partial t} \langle \cdot \rangle - \frac{1}{V} \int_{A_{fs}} \cdot \vec{W} \cdot \vec{n}_{fs} dA \quad (3.7)$$

where $\langle \cdot \rangle = \frac{1}{V} \int_{V_e} \cdot dV_e$, is the average operator, A_{fs} the surface between the fluids and the solid, \vec{n}_{fs} the vector normal to A_{fs} oriented from the fluid to the solid, and \vec{W} the velocity vector for the points at the interface A_{fs} . $\vec{W} \neq \vec{0}$ for deformable medium.

Bories et al. (2008) gave an example for a heat conduction problem within a saturated porous medium by a non reactive single phase fluid. The porous sample is limited by a surface Σ and V_f denotes the fluid volume, and V_s the solid volume. At the microscopic scale, the equations to describe the heat transfers are:

$$(\rho c)_s \frac{\partial T_s}{\partial t} = \nabla \cdot (\lambda_s \vec{\nabla} T_s) \text{ in } V_s \quad (3.8)$$

$$(\rho c)_f \frac{\partial T_f}{\partial t} = \nabla \cdot (\lambda_f \vec{\nabla} T_f) \text{ in } V_f \quad (3.9)$$

$$T_s = T_f \text{ on } A_{fs} \quad (3.10)$$

$$\lambda_s \vec{\nabla} T_s \cdot \vec{n}_{fs} = \lambda_f \vec{\nabla} T_f \cdot \vec{n}_{fs} \text{ on } A_{fs} \quad (3.11)$$

plus eventually initial and boundary conditions on Σ . Assuming that the porous is non-deformable, one has $\vec{W} = \vec{0}$, and applying (3.6) and (3.7) on (3.8), (3.9), (3.10) and (3.11) the new system of equations – at the macroscopic scale – is:

$$\begin{aligned} (1 - \eta)(\rho c)_s \frac{\partial \langle T_s \rangle^s}{\partial t} \\ = \nabla \cdot \left[(1 - \eta) \lambda_s \vec{\nabla} \langle T_s \rangle^s + \frac{\lambda_s}{V} \int_{A_{fs}} (T_s - \langle T_s \rangle^s) \cdot \vec{n}_{fs} dA \right] \\ + \frac{1}{V} \int_{A_{fs}} \lambda_s \vec{\nabla} T_s \cdot \vec{n}_{fs} dA \end{aligned} \quad (3.12)$$

for the solid where $\langle T_s \rangle^s = \frac{1}{V_s} \int_{V_{es}} T_s dV_{es}$ and $\langle T_s \rangle = (1 - \eta) \langle T_s \rangle^s$ and

$$\begin{aligned} \eta(\rho c)_f \frac{\partial \langle T_f \rangle^f}{\partial t} = \nabla \cdot \left[\eta \lambda_f \vec{\nabla} \langle T_f \rangle^f + \frac{\lambda_f}{V} \int_{A_{fs}} (T_f - \langle T_f \rangle^f) \cdot \vec{n}_{fs} dA \right] \\ + \frac{1}{V} \int_{A_{fs}} \lambda_f \vec{\nabla} T_f \cdot \vec{n}_{fs} dA \end{aligned} \quad (3.13)$$

for the fluid where $\langle T_f \rangle^f = \frac{1}{V_f} \int_{V_{es}} T_f dV_{es}$ and $\langle T_f \rangle = \varepsilon \langle T_f \rangle^f$.

The second and third terms of the right hand side of these two equations respectively represent the structural effects and the conductive heat transfers between the two phases. It could be possible to stop the development at this stage: the resulting model would be a ‘two temperatures model’. But under additional assumptions it can be simplified. Indeed, assuming thermal local equilibrium i.e. $\langle T_f \rangle^f = \langle T_s \rangle^s = T$, and adding (3.12) and (3.13) the resulting equation is:

$$\begin{aligned}
 & (\eta(\rho c)_f + (1 - \eta)(\rho c)_s) \frac{\partial T}{\partial t} \\
 & = \nabla \cdot \left[(\eta\lambda_f + (1 - \eta)\lambda_s) \vec{\nabla} T \right. \\
 & \quad \left. + \frac{\lambda_f - \lambda_s}{V} \int_{A_{fs}} (T_f - T) \cdot \vec{n}_{fs} dA \right]
 \end{aligned} \tag{3.14}$$

The thermal local equilibrium is valid for a wide range of thermal diffusivities of fluid and solid, especially for ground materials. Furthermore, the term $\frac{\lambda_f - \lambda_s}{V} \int_{A_{fs}} (T_f - T) \cdot \vec{n}_{fs} dA$ can be rewritten under the form $\left(\frac{\lambda_f - \lambda_s}{V} \int_{A_{fs}} \vec{b}_{fs} \cdot \vec{n}_{fs} dA \right) \vec{\nabla} T$ and thus (3.14) becomes

$$(\rho c)^* \frac{\partial T}{\partial t} = \nabla \cdot [\lambda^* \vec{\nabla} T] \tag{3.15}$$

$(\rho c)^* = \eta(\rho c)_f + (1 - \eta)(\rho c)_s$ and $\lambda^* = (\eta\lambda_f + (1 - \eta)\lambda_s) + \frac{\lambda_f - \lambda_s}{V} \int_{A_{fs}} \vec{b}_{fs} \cdot \vec{n}_{fs} dA$ denotes respectively the equivalent specific heat and thermal conductivity of the porous media. The details of the geometry of the porous media disappear, and only one temperature is necessary to describe the heat transfers within the materials. It considerably simplifies the solution of the equations compared to the form (3.12) and (3.13).

3.2.1.3. Porous media: modelling of a conductive / convective thermal problem

In the case of a saturated media with a flowing fluid, the equations are usually modified by the adding of convection terms. Navier-Stokes, mass and energy conservation equations are needed to describe all the phenomena. Under the assumption of low velocity, the compressibility and the viscous dissipation terms are neglected. Using once again the averaging method the following two macroscopic equations can be obtained

$$\eta \frac{\partial \rho_f}{\partial t} + \nabla \cdot (\rho_f \vec{U}) = 0 \tag{3.16}$$

$$(\rho c)^* \frac{\partial T}{\partial t} + (\rho c)_f \vec{U} \cdot \vec{\nabla} T = \nabla \cdot [(\lambda^* + \lambda_d) \vec{\nabla} T] \tag{3.17}$$

where $\vec{U} = -\frac{K_p}{\rho_l} (\nabla P - \rho_f \vec{g})$ is the apparent velocity of the fluid, which corresponds to the Darcy law and λ_d is the effective thermal conductivity due to dispersion. These two last equations, which express the mass and the energy balance, are valid in the case where a local thermal equilibrium is verified. As previously (with the saturated stationary fluid) this is especially true when the rate $\left(\frac{l}{L}\right)^2$ is low. This ensures that if the two phases have close diffusivities values, the temperature variations won't be too high at the scale of the ERV. Otherwise the two phases have to be treated separately. This assumption is well accepted in

the considered cases throughout this work. It justifies the use of only one temperature for each ERV.

For our applications, the pores are simultaneously filled with liquid water and a mixing of dry air and water vapour. It considerably complicates the mathematical modelling because of the liquid and vapour movement, and the simultaneous sensible and latent heat exchange between the three phases. The details about the modelling of these couplings are exposed in the next paragraph.

3.2.2 COUPLED HEAT AND MASS TRANSFER EQUATIONS FOR POROUS MEDIA AND SOILS

The heat and mass transfer within a porous media filled with a two phase flow (Figure 24) necessitates the modelling of the complex interactions between the gas, the liquid and the solid. For our applications, the liquid is water, and the gas is a mixing of dry air and water vapour.

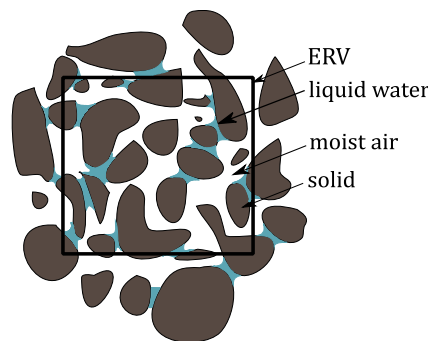


Figure 24: Partially saturated porous media

Most of the current studies about coupled heat and mass transfer in porous media are based on the work of Philip and De Vries (1957) and De Vries (1958). Their works have been carried out following the observation of discrepancies between previous theory predictions and experimental results. They extended the previous simple model of vapour transfer and proposed a new formulation that explicitly takes into account thermal and isothermal components. Since the results of the modelling were consistent with the experimental data, their new theory and all its underlying assumptions has been proved to be relevant.

From there, many authors built their own model to describe coupled heat and moisture transport within porous materials - using a 'one temperature model' based on what have been previously introduced. The construction of the heat and moisture transfer equations is going to be described in subsections 3.2.2.2 and 3.2.2.3. As the description of the moisture movements imply to carefully choose a driving potential, this will be carried out in the next subsection.

3.2.2.1. Moisture movement - driving potentials

Milly (1982) was one of the first to write a full model for coupled heat and moisture transfer within soil and to solve it with a finite difference method. The writing and the numerical resolution of combined heat and moisture transfer within building materials was also investigated (Künzel, 1995; Pedersen, 1990). The different transport modes of moisture (and thereafter heat) within a porous media were highlighted. According to the material considered, some of them can be neglected while others are predominant. This sometimes

leads to choose a moisture driving potential better suited, and thus to another formulation of the equations.

The migration of moisture occurs both in the gaseous phase and in the liquid phase. The calculation of the moisture transfers necessitates the knowledge of the storage and transfer properties of the porous media considered but before all, the description of the strengths that drive moisture movement.

Matric and gravitational strengths – storage functions

Considering an unsaturated porous media embedding liquid water, dry air and water vapour in its pores, several strengths coexist and are at the origin of moisture movement. The matrix strengths are the attractive strengths by the solid matrix on water. They include capillary strengths and adsorption strengths. The capillary strengths are due to the water surface tension at the interface water/solid/gas, and result in a pressure difference – the capillary pressure – between the liquid water (Figure 25) and the air given by:

$$P_c = P_l - P_a = -\frac{2\sigma\cos(\beta)}{r} \quad (3.18)$$

where σ is the water surface tension, β the contact angle between the liquid and solid phases, and r the pore radius in a cylindrical pore model. It is the leading strength for high relative humidity. The capillary pressure is negative and equal to zero at saturation. The adsorption strengths are due to intermolecular attraction between solid and air particles and are preponderant for low relative humidity. Adsorption and capillary strength are usually inseparable. The gravitational strength concerns mainly liquid water. Throughout this work, additional strengths like the osmotic strengths and the ground weight will be neglected.

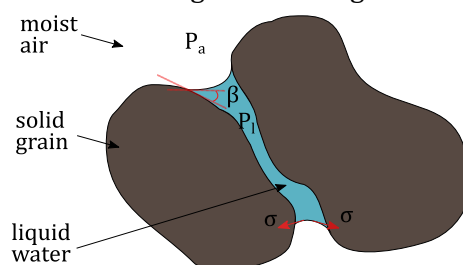


Figure 25: Definition of the capillary strengths within a porous unsaturated media

Still considering low water velocity within the pores, the heat dissipation by friction of water against the pore walls can be neglected. All the other strengths previously enumerated are conservative and consequently derive from a potential. The bulk potential energy of water can thus be written as a sum of the bulk potential energy of the matrix strengths and the bulk potential energy of the gravitational strengths. As with the gravitational potential z - the altitude of a given point - it is possible to define the matric head Ψ to describe the matric potential. Its link with the capillary pressure is given by $P_c = \rho_l g \Psi$ and the total water head is given by $\Phi = z + \Psi$. Usually, a thermodynamic equilibrium is assumed between the water vapour and the liquid water. Under this assumption, the Kelvin's law gives a link between the capillary pressure and the relative humidity φ in the gaseous phase:

$$\frac{P_v}{P_{v,sat}} = \varphi = \exp\left(\frac{P_c}{\rho_l R_v T}\right) = \exp\left(\frac{g\Psi}{R_v T}\right) \quad (3.19)$$

P_v and $P_{v,sat}$ respectively designates the partial vapour pressure of the air and the partial vapour pressure at saturation. The thermodynamic equilibrium is valid in similar conditions as previously: low velocities of liquid and gaseous phase, and low discrepancies between all the diffusivities involved. The volumetric water content θ that expresses the quantity of water per unit volume of porous media is related to the relative humidity by a function $\theta(\varphi)$ called 'moisture sorption isotherm curve' (Figure 26). The region of the lowest relative humidity is called 'hygroscopic region' where the water in the pores is mainly vapour. In such region the smallest pores are being filled. This region range from the dry state – where there is no humidity at all except chemically bounded water – to around $\varphi = 95\%$. For higher relative humidity, called 'capillary region', most of the water transport are due to the capillary strengths. When for example a porous material is in contact with liquid water, a 'free water saturation' state of equilibrium is then reached. For the highest relative humidity, all the pores are saturated. This region lies above the free water saturation and can only be reached by applying external pressure or only after a long time by dissolution of the encapsulated pore air in water (Künzel, 1995). This region is called 'supersaturated'. For both the capillary and the supersaturated region, since the pore diameter is large a slight variation of relative humidity induces a strong variation of water content (the smallest pores are now saturated and the biggest are being filled). For this reason, the relation $\theta(P_c)$ or $\theta(\Psi)$ called 'suction curve' is usually preferred to describe such conditions.

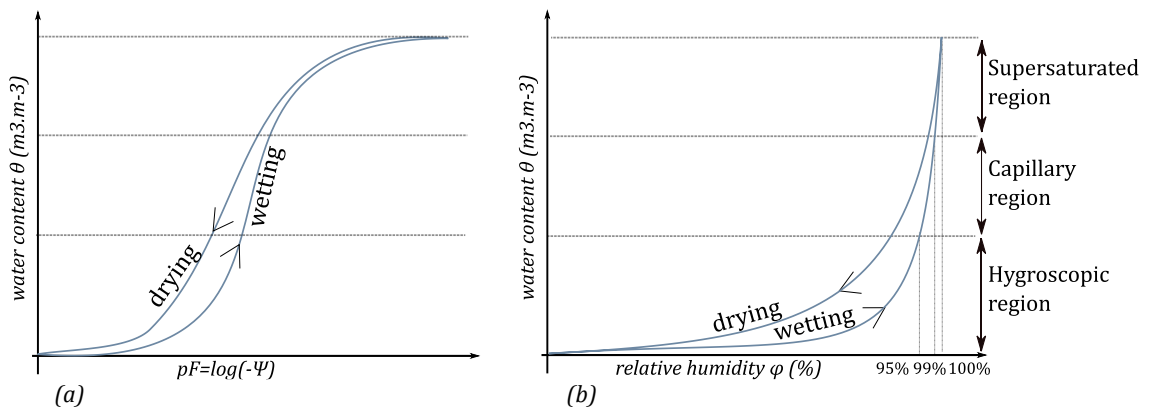


Figure 26: Isotherm suction (a) and corresponding sorption curves (b): classification of the regions

Vapour transfer and storage

The vapour storage is described by the isotherm sorption curve. The vapour migration has mainly two origins: convection and diffusion. The vapour can be transported by air movements. This transport mode is most of the time neglected, either because it is not predominant or because it is almost impossible to model. The vapour convection can be neglected if its partial pressure is lower than 10% of the total pressure, which is always the case if the temperature does not exceed 40°C. The second driving phenomenon is the diffusion. The vapour flow induces is proportional to the vapour pressure gradients, following a Fick's law. A porous media modifies the normal path of water vapour, and consequently the diffusion flow is also proportional to the 'vapour permeability' of the material, the latter

depending on the temperature and the water content. Indeed, (Philip and De Vries, 1957) were the first to understand the mechanism that, contrary to expectations, induces an elevation of the vapour permeability when the water content results is rising. They showed that the smallest capillaries filled with liquid water create 'bridges' between the biggest pores creating a vapour-liquid-vapour series water vapour flow.

Other mechanism can generate vapour movements. In the narrowest capillaries, the mean free path of the water molecule is larger than the pore radii. The molecules shock more often the capillaries' walls than the other molecules, which modifies the diffusion process. This phenomenon is called effusion. Furthermore, a temperature gradient leads to vapour pressure gradient and therefore induces vapour fluxes. Philip and De Vries (1957) noted that the coupling between moisture and heat transfers is also reinforced by the rising of the thermal conductivity where the pores are filled with liquid water.

Liquid transport and storage

The liquid storage is described by the suction curves, adapted to describe the capillary and the hypersaturated region. It turns out that the suction curves can also accurately represent the hygroscopic region (Figure 26). Since a ground is potentially saturated (after a rainy period or close to the water table) as well as very dry (in summer), the suction curves appears to be good candidates to model the moisture storage within grounds.

The liquid transfer is a consequence of two transport modes. The first is the capillary conduction the origin of which is a capillary pressure gradient and is proportional to the 'hydraulic conductivity' or the 'hydraulic permeability'. The latter are of course function of the water content. This flow model is very common and based on the Darcy's law. The dependence of this flux with temperature is almost all of the time neglected for temperature range close to normal air temperature. The second is the 'surface diffusion'. The liquid water adsorbed on the pore walls' move from the thickest layers to the thinnest. This process is always included in the capillary conduction.

The liquid and vapour transfers can be considered as independent in the hygroscopic region only. Table 12 gives a summary of the main moisture flows that usually occur in building material or soils. The high complexity of the real link between the water content of a given porous media and the matric head (or the relative humidity) is nearly impossible to capture by a mathematical expression. Indeed, this curve depends on the complex size distribution of the pores and their inter-connections. It is furthermore not a bijective function because of hysteresis: for a given Ψ , the water content is not the same in a wetting or in a drying process due to the 'ink bottle' effect. However, some good approximation models have been developed, and will be introduced in section 4.3.1.

The relation (3.19) and the water sorption / suction curves apparently gives an equivalence between all the moisture driving potentials – namely P_v , P_c , Ψ , φ , and the water content θ . But according to the problem studied, the use of one instead of one other can be preferred. As previously explained, the relative humidity and the partial vapour pressure are well suited to describe the hygroscopic domain. Consequently, the choice of using P_v or φ as variable to describe the moisture transfers within building materials is relatively common. Indeed, the building walls' are usually 'dry' and moisture transfers only occurs on vapour

form. On the contrary, other fields like geotechnical study materials that are most of the time saturated. For these cases, the capillary pressure, the water content or the matric head are well suited. As the water content is not continuous with a change of material, the capillary pressure P_c or the matric head Ψ are usually preferred. Both this variable will be used in what follows.

In the light of the foregoing and according to a sum up of numerous works, the moisture and the heat equation for the ground and for the concrete foundation have been chosen and are introduced in the next two sub-sections (Berger, 2014; De Vries, 1958; Deru and Kirkpatrick, 2002a; Janssen, 2002; Janssen et al., 2004, 2007; Künzel, 1995; Labat, 2012; Milly, 1982; Pedersen, 1990; Philip and De Vries, 1957; Rouchier, 2012; dos Santos and Mendes, 2006; Woloszyn, 1999).

Table 12 : Main moisture movements within porous media

| | Vapour | | | Liquid | | |
|--|-------------------------------------|------------------|-----------------------|--------------------|--|-----------------------|
| | Hygroscopic region | Capillary region | Supersaturated region | Hygroscopic region | Capillary region | Supersaturated region |
| <i>Storage</i> | Isotherm sorption curve | | | - | Suction curve | |
| <i>Transfer mode / Driving potential</i> | Convection / Total air pressure | | - | - | Convection / Total water pressure | |
| | Diffusion / Partial vapour pressure | | - | - | Capillary conduction / Capillary pressure (Suction stress) | |
| | Effusion / Partial vapour pressure | | - | - | Gravitational flow / Altitude | |
| | Thermodiffusion / Temperature | | - | - | Surface diffusion / Relative humidity | |

3.2.2.2. Mass conservation: moisture equation

The soil is often saturated, mainly on its top layer – because of rainfall – and on its base layer – due to the presence of water table - while the building material constructions are most of the time kept in the hygroscopic region. A matric-head based system of equations is therefore relevant to describe the moisture flows within the soil, while a capillary pressure formulation is well suited to describe concrete. Furthermore, the soil and the concrete foundation modelling requires a large computational domain i.e. a high computational level. A domain decomposition method can be used to avoid this problem (see Chapter 4). A natural decomposition corresponds to the soil and the foundation domains distinction. Consequently, having two systems of equations with different variables is not detrimental.

Ground moisture equation

The general equation for mass conservation is given by

$$\frac{\partial w}{\partial t} = -\nabla \cdot (\vec{\phi}_m) \quad (3.20)$$

w is the mass moisture content given by the sum of the humidity contained in the air and the liquid water

$$w = \rho_v \theta_a + \rho_l \theta \quad (3.21)$$

in which ρ_v is the vapour density and θ_a is the bulk air content of the soil. $\overrightarrow{\phi_m}$ is the moisture flow and can be written as a sum of a vapour transfer $\overrightarrow{\phi_{m,v}}$ vector and a liquid transfer vector $\overrightarrow{\phi_{m,l}}$. According to the widely used Darcy's law, $\overrightarrow{\phi_{m,l}}$ can be written

$$\overrightarrow{\phi_{m,l}} = -\rho_l K_h \vec{\nabla} \Phi = -\rho_l K_h (\vec{\nabla} \Psi + \vec{u}_z) \quad (3.22)$$

where K_h is the hydraulic conductivity. Its shape will be discussed in the next section. As we can observe, the influence of the temperature gradient on the liquid flow is assumed negligible. The term $-\rho_l K_h \vec{u}_z$ corresponds to the liquid flow driven by the gravity, and is consequently only oriented along the vertical axis. Similarly, the Fick's law gives the vapour flow as being proportional to the vapour density ρ_v gradient

$$\overrightarrow{\phi_{m,v}} = -D_v \vec{\nabla} \rho_v \quad (3.23)$$

with D_v the effective vapour diffusivity. Since we are considering the porous media is a soil, the matric head Ψ has been assumed to be the more relevant variable to use. Thus, using the chain rule $\vec{\nabla} \rho_v$ can be expressed as

$$\vec{\nabla} \rho_v = \left(\frac{d\rho_{v,sat}}{dT} \varphi - \frac{g\Psi\rho_v}{R_v T^2} \right) \vec{\nabla} T + \frac{g\rho_v}{R_v T} \vec{\nabla} \Psi \quad (3.24)$$

And therefore

$$\overrightarrow{\phi_m} = -\rho_l (D_{Tv} \vec{\nabla} T + (D_{\Psi v} + K_h) \vec{\nabla} \Psi) - \rho_l K_h \vec{u}_z \quad (3.25)$$

where $D_{Tv} = D_v \left(\frac{1}{\rho_l} \frac{d\rho_{v,sat}}{dT} \varphi - \frac{g\Psi\rho_v}{\rho_l R_v T^2} \right)$ is the thermal vapour diffusivity and $D_{\Psi v} = D_v \frac{g\rho_v}{\rho_l R_v T}$ the hydraulic vapour diffusivity. Using the same derivation method to the mass moisture content derivative relative to time, considering that the moisture content is a function of temperature and matric head, and using the relation $\frac{\partial \theta_a}{\partial t} = -\frac{\partial \theta}{\partial t}$ we obtain

$$\frac{\partial w}{\partial t} = \rho_l \left(\frac{\theta_a}{\rho_l} \frac{\partial \rho_v}{\partial T} + \left(1 - \frac{\rho_v}{\rho_l} \right) \frac{\partial \theta}{\partial T} \right) \frac{\partial T}{\partial t} + \rho_l \left(\frac{\theta_a}{\rho_l} \frac{\partial \rho_v}{\partial \Psi} + \left(1 - \frac{\rho_v}{\rho_l} \right) \frac{\partial \theta}{\partial \Psi} \right) \frac{\partial \Psi}{\partial t} \quad (3.26)$$

Combined with (3.20), (3.25) and (3.26) we have:

$$\begin{aligned} & \left(\frac{\theta_a}{\rho_l} \frac{\partial \rho_v}{\partial T} + \left(1 - \frac{\rho_v}{\rho_l} \right) \frac{\partial \theta}{\partial T} \right) \frac{\partial T}{\partial t} + \left(\frac{\theta_a}{\rho_l} \frac{\partial \rho_v}{\partial \Psi} + \left(1 - \frac{\rho_v}{\rho_l} \right) \frac{\partial \theta}{\partial \Psi} \right) \frac{\partial \Psi}{\partial t} \\ & = \nabla \cdot [D_{Tv} \vec{\nabla} T + (D_{\Psi v} + K_h) \vec{\nabla} \Psi] + \frac{\partial K_h}{\partial z} \end{aligned} \quad (3.27)$$

Concrete moisture equation

The capillary pressure formulation usually involves vapour and liquid permeability instead of the diffusivities previously introduced. Furthermore, it is commonly accepted to neglect the gravitational liquid flow. Starting from the same general mass conservation equation, the term $\overrightarrow{\phi_m} = \overrightarrow{\phi_{m,l}} + \overrightarrow{\phi_{m,v}}$ is this time developed as follow

$$\overrightarrow{\phi_{m,l}} = -K_p \vec{\nabla} P_c \quad (3.28)$$

$$\overrightarrow{\phi_{m,v}} = -\delta_v \vec{\nabla} P_v \quad (3.29)$$

where K_p and δ_v are the liquid and the vapour permeabilities. As the liquid flow is already expressed in terms of capillary pressure gradient, the vapour flow $\overrightarrow{\phi_{m,v}}$ only is going to be developed. Using once again the chain rule, the Kelvin's law and the Clausius Clapeyron law $\frac{\partial P_{v,sat}}{\partial T} = \frac{L_v}{R_v T^2} P_{v,sat}$, we obtain

$$\overrightarrow{\phi_{m,v}} = -\frac{\delta_v P_v}{\rho_l R_v T^2} (\rho_l L_v + P_c (T\gamma - 1)) \vec{\nabla} T - \frac{\delta_v P_v}{\rho_l R_v T} \vec{\nabla} P_c \quad (3.30)$$

with $\gamma = \frac{1}{\sigma} \frac{\partial \sigma}{\partial T}$ where σ is the water surface tension. Neglecting the influence of the temperature on the sorption curve (expressed under the form $w(P_c)$), the term $\frac{\partial w}{\partial t}$ is equal to $\frac{\partial w}{\partial P_c} \frac{\partial P_c}{\partial t}$. Thus, the final mass balance equation is

$$\frac{\partial w}{\partial P_c} \frac{\partial P_c}{\partial t} = -\frac{\delta_v P_v}{\rho_l R_v T^2} (\rho_l L_v + P_c (T\gamma - 1)) \vec{\nabla} T - \left(K_p + \frac{\delta_v P_v}{\rho_l R_v T} \right) \vec{\nabla} P_c \quad (3.31)$$

3.2.2.3. Heat conservation: heat equation

Ground heat equation

The general equation for heat conservation is given by

$$\frac{\partial e}{\partial t} = -\nabla \cdot (\overrightarrow{\phi_h}) \quad (3.32)$$

where e is the volumetric energy of the soil, and $\overrightarrow{\phi_h}$ the total heat flow within a control volume. Neglecting the advective fluxes due to the air movements within the pores, $\overrightarrow{\phi_h}$ is a sum of a conductive $\overrightarrow{\phi_{h,cond}}$ and an convective term $\overrightarrow{\phi_{h,conv}}$. Following what have been explained, the convective term is the sum of the heat flow due to liquid convection and the heat flow due to the vapour convection flux.

$$\overrightarrow{\phi_{h,cond}} = -\lambda \vec{\nabla} T \quad (3.33)$$

$$\overrightarrow{\phi_{h,conv}} = c_l (T - T_0) \overrightarrow{\phi_{m,l}} + (c_v (T - T_0) + L_0) \overrightarrow{\phi_{m,v}} \quad (3.34)$$

According to Janssen (2002) λ 'stands for the thermal conductivity of the soil medium in the hypothetical case that no moisture movement occurs'. Using the relation $c_v (T - T_0) + L_0 = c_l (T - T_0) + L_v$ and the equations (3.22), (3.23) and (3.24) we obtain

$$\begin{aligned} \overrightarrow{\phi_h} = & -[\lambda + \rho_l (c_l (T - T_0) + L_v) D_{T_v}] \vec{\nabla} T \\ & - \rho_l [c_l (T - T_0) K_h + (c_l (T - T_0) + L_v) D_{\psi_v}] \vec{\nabla} \Psi \\ & + \rho_l c_l (T - T_0) K_h \vec{u}_z \end{aligned} \quad (3.35)$$

The energy storage within a soil control volume can be expressed by

$$e = c_s + \rho_l c_l (T - T_0) \theta + \rho_v (c_v (T - T_0) + L_0) \theta_a + \rho_a c_a (T - T_0) \theta_a \quad (3.36)$$

This formulation neglects the heat of wetting corresponding to the energy stored or released during the adsorption or desorption of water molecule on the pore walls, but this is commonly accepted in most of the publications about ground modelling. Again, using the chain rule, we obtain

$$\begin{aligned} \frac{\partial e}{\partial t} = & \left[c_s + \theta_a (L_0 + c_v (T - T_0)) \right] \frac{\partial \rho_v}{\partial T} \\ & + (c_l \rho_l (T - T_0) - c_v \rho_v (T - T_0) - \rho_v L_0) \frac{\partial \theta}{\partial T} \frac{\partial T}{\partial t} \\ & + \left[\theta_a (L_0 + c_v (T - T_0)) \right] \frac{\partial \rho_v}{\partial \Psi} \\ & + (c_l \rho_l (T - T_0) - c_v \rho_v (T - T_0) - \rho_v L_0) \frac{\partial \theta}{\partial \Psi} \frac{\partial \Psi}{\partial t} \end{aligned} \quad (3.37)$$

Concrete heat equation

Similarly to what have been written for the ground, the heat equation for the concrete is derived from the moisture equation, the general heat equation is similar to (3.32) and the total heat flow is still $\vec{\phi}_h$ is a sum of a conductive $\vec{\phi}_{h,cond}$ and an convective term $\vec{\phi}_{h,conv}$.

$$\begin{aligned} \vec{\phi}_{h,conv} = & - \left[c_l T K_p + (c_v T + L_v) \frac{\delta_v P_v}{\rho_l R_v T} g \right] \vec{\nabla} P_c \\ & - \left[(c_v T + L_v) \frac{\delta_v P_v}{\rho_l R_v T^2} (\rho_l L_v + P_c (T \gamma - 1)) \right] \vec{\nabla} T \end{aligned} \quad (3.38)$$

The energy stored and its variation with time can be expressed as follows

$$e = c_b + c_l (T - T_0) w \quad (3.39)$$

$$\frac{\partial e}{\partial t} = [c_b + c_l w] \frac{\partial T}{\partial t} + T \frac{\partial w}{\partial P_c} \frac{\partial P_c}{\partial t} \quad (3.40)$$

3.3. CONCLUSIONS

The brief literature review about the building ground heat loss highlighted that ignoring the presence of humidity and its variation with time induces inaccurate estimation of the heat flow through the slab, especially in the case without insulation. Considering these conclusions and both the objective of this work introduced in the Chapter 1 – be able to reproduce the dynamic of the foundation outlet air characteristics for summer, winter and mid-season – and the features of the foundation detailed in the section 2.3 – the low depth and the simultaneous influence of the climate and the building – it seems clear that the modelling of coupled heat and mass transfer within the ground and the foundation is necessary.

The formulation of the coupled equations to describe these flows for soils and building materials such as concrete are widespread. Among all the existing models, the adopted has been made according to three main reasons:

- The accuracy of the modelling with an (almost) exhaustive consideration of the physical phenomena
- The ease of the coupling between the soil and the concrete foundation models
- The (relatively) low number of parameters.

The first and the last points are of course antagonist. The extra difficulty lies on the fact that the thermal and the hydric properties of the soil remain very often unknown. The solution proposed by Janssen, introduced in the current chapter has been adopted in this work. The materials description as well as the numerical resolution of the resulting equations is going to be further detailed in the next chapter.

Chapter 4. OBJECTIVES AND

DEVELOPMENT OF THE COUPLED HEAT AND MASS TRANSFER MODEL

4.1. OBJECTIVES

The conclusions of Chapter 2 and Chapter 3 gave the main constraints for the Fondatherm model development. A strong influence of the meteorological conditions and the potential water infiltration through the concrete require the modelling of coupled heat and moisture transfer in the soil and the concrete domains with complex boundary conditions. The EAHE former modelling highlighted that the resolution via finite volume method with at least two dimensions seems well suited.

Regarding the ventilated cavity domain, given the high computational time required by CFD models, the resolution of the Navier-Stokes associated to the energy equations is excluded. However, an accurate representation of the complex evolution of the flowing air temperature and humidity has to be made. Since the foundation is strictly linear with a simple rectangular cross-section and the flow is forced and turbulent, the airflow velocity profile can be assumed uniform. The use of an averaged air velocity over the cross-section is therefore relevant and leads to opt for a one-dimensional finite volume model for the airflow domain.

A three-dimensional finite volume model for coupled heat and mass transfer is going to be developed. The first subsection is concerning the system of conservation law equations. These equations require the description of the thermal and hydraulic properties of porous media that will be introduced in the subsection 4.3 and 4.4 for soil and concrete respectively. Then the boundary conditions closing the set of equations are presented in the subsection 4.5. The methods that are implemented for the resolution of this set of equations are exposed in the section 0. Conclusions and limitations of the obtained model are finally discussed in the last section of this chapter.

4.2. SYSTEM OF CONSERVATION LAW EQUATIONS

The complete systems of equations to describe heat and moisture movement within the soil and the foundation are respectively given by

$$\begin{cases} c_{TT}^g \frac{\partial T^g}{\partial t} + c_{T\psi}^g \frac{\partial \psi^g}{\partial t} = \nabla \cdot (k_{TT}^g \vec{\nabla} T^g + k_{T\psi}^g \vec{\nabla} \psi^g + \vec{g}_T^g) \\ c_{\psi T}^g \frac{\partial T^g}{\partial t} + c_{\psi\psi}^g \frac{\partial \psi^g}{\partial t} = \nabla \cdot (k_{\psi T}^g \vec{\nabla} T^g + k_{\psi\psi}^g \vec{\nabla} \psi^g + \vec{g}_\psi^g) \end{cases} \quad (4.1)$$

$$\begin{cases} c_{TT}^f \frac{\partial T^f}{\partial t} + c_{TP_c}^f \frac{\partial P_c^f}{\partial t} = \nabla \cdot (k_{TT}^f \vec{\nabla} T^f + k_{TP_c}^f \vec{\nabla} P_c^f) \\ c_{P_c T}^f \frac{\partial T^f}{\partial t} + c_{P_c P_c}^f \frac{\partial P_c^f}{\partial t} = \nabla \cdot (k_{P_c T}^f \vec{\nabla} T^f + k_{P_c P_c}^f \vec{\nabla} P_c^f) \end{cases} \quad (4.2)$$

All the coefficients involved are function of the state variables: $c_{TT}^g = c_{TT}^g(T^g, \Psi^g)$, etc. For the sake of simplicity, this is not specified in the following. Their explicit description is given in Appendix A. These equations take into account:

- Liquid transfer due to matric potential / capillary pressure gradient i.e. suction,
- Liquid transfer due to gravity, except for the concrete foundation model,
- Vapour transfer due to hydraulic and thermal diffusion,
- Conductive heat transfer within the solid matrix, the water and the moist air,
- Advection heat transfer produce by liquid or vapour movement,
- Latent heat transfer by evaporation and condensation between the water and the moist air filled pores.

These equations are not considering:

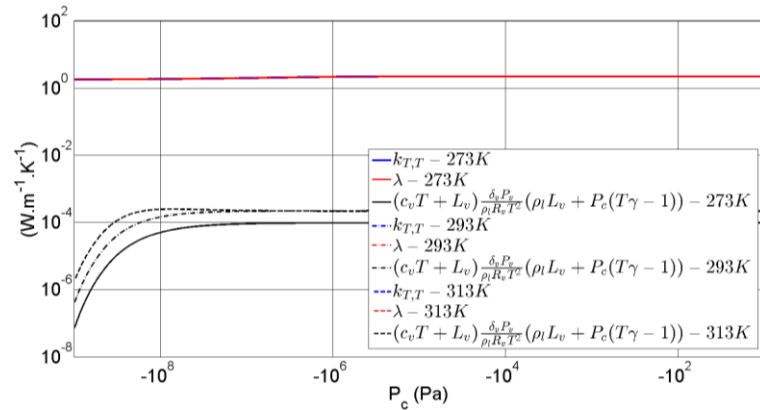
- Air movement: air filled pores is supposed to be everywhere at atmospheric pressure,
- Liquid transfer due to temperature gradient,
- Contribution of water contained in the vapour phase on the total quantity of moisture.

Within his thesis, Janssen (2002) proposed and justified a simplification of the system of equations (4.1). Analysing the relative weight of the different terms involved in the storage and the transfer coefficients, he showed that:

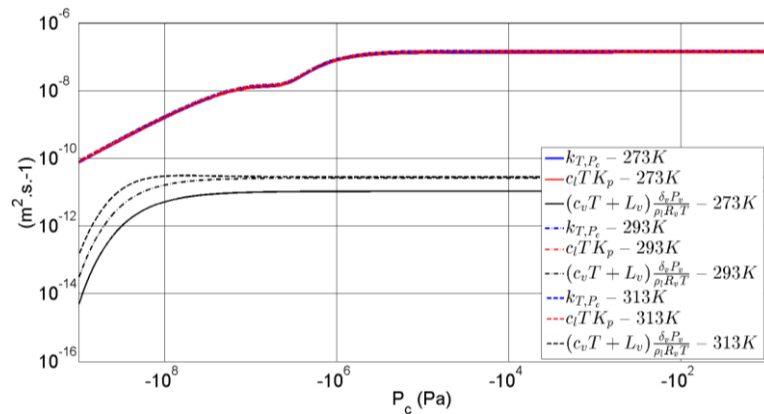
- The moisture storage in the vapour phase is negligible compared to that in the liquid phase. Moreover, the influence of a change in temperature on the liquid storage is negligible compared to the influence of a change in the matric head, except for very dry soil which leads to $c_{\Psi T}^g = 0$ and $c_{\Psi \Psi}^g = \frac{\partial \theta}{\partial \Psi}$,
- The thermal vapour diffusivity has a very low impact on the moisture transfers and thus $k_{\Psi T}^g = 0$,
- The transfer of sensible heat by thermal vapour transfer, the transfer of latent heat by hydraulic gradient, and the transfer of sensible heat by hydraulic vapour transfer are negligible. Consequently $k_{TT}^g = \lambda^*$ and $k_{T\Psi}^g = c_l \rho_l (T^g - T_0) K_h$,
- The latent heat of vaporization, and the sensible heat contained in the gaseous phase are negligible so $c_{TT}^g = C + c_l \rho_l \theta$ and $c_{T\Psi}^g = c_l \rho_l (T^g - T_0) \frac{\partial \theta}{\partial \Psi}$.

Complex equations could be at the origin of numerical instability during the resolution process. In order to anticipate such problems, the potential unnecessary terms have to be identified and removed: the same work of simplification has thus been done here for the capillary pressure based equations for the concrete foundation. Figure 27 shows that the transfer of sensible and latent heat by thermal vapour transfer can be neglected. Indeed, the

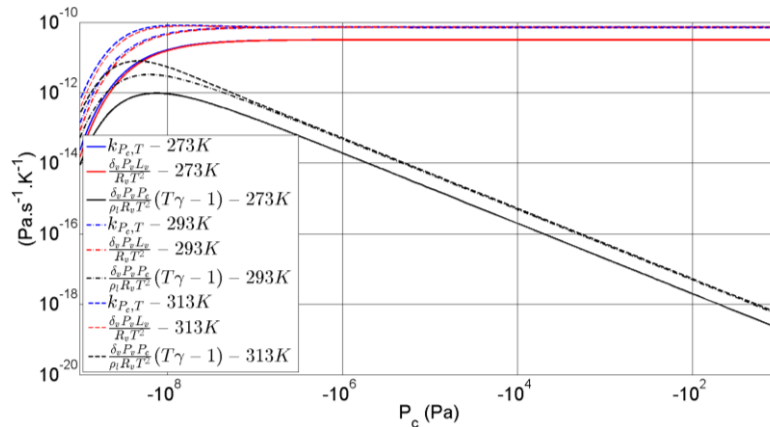
term $(c_v T^f + L_v) \frac{\delta_v P_v}{\rho_l R_v T^2} (\rho_l L_v + P_c^f (T^f \gamma - 1))$ is at least four orders of magnitude below the thermal conductivity over a wide range of capillary pressure and temperature. This term can consequently be discarded without any loss of accuracy. For the three other transfer coefficients, some terms appear to be of secondary order. The hydraulic vapour diffusion term $\frac{\delta_v P_v}{\rho_l R_v T^2}$ for example seems low compared to the liquid permeability K_p . But for the lowest capillary pressure, the hydraulic vapour diffusion term rises with temperature, and the difference between the two terms is reduced to less than two orders of magnitude. In order to stay consistent with the physics, and to avoid approximation that could introduce an important bias for simulation over a time period of several months, the coefficients $k_{TP_c}^f$, $k_{P_c T}^f$ and $k_{P_c P_c}^f$ will be keep unchanged thereafter.



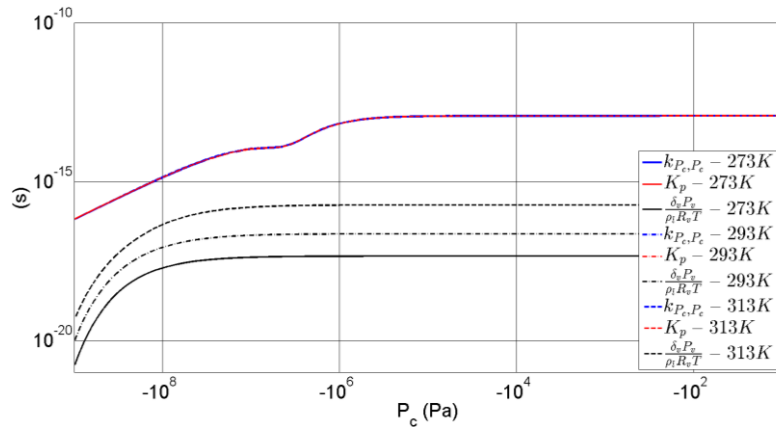
(a)



(b)



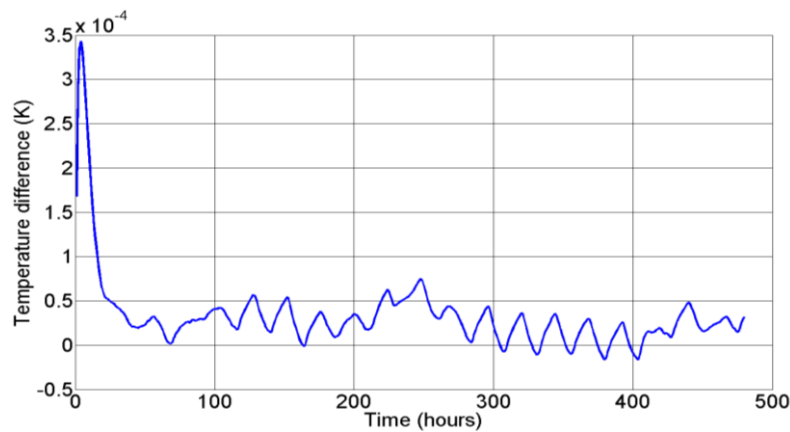
(c)



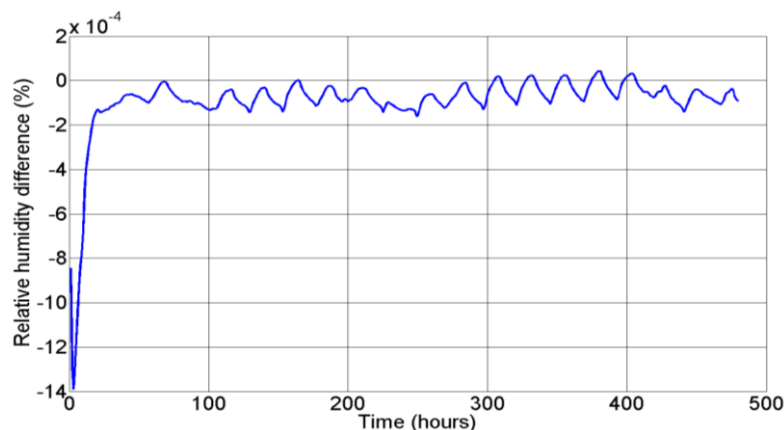
(d)

Figure 27: Hydraulic (a) and heat (b) transfer coefficients for the moisture equation, and thermal (c) and hydraulic (d) heat (d) transfer coefficient for the heat equation

The difference between the foundation model (described in the next chapter) integrating the simplification described above and the full model on the outlet air temperature and relative humidity is plotted on Figure 28. The temperature and the relative humidity difference don't exceed $3.5 \cdot 10^{-4}$ and $1.4 \cdot 10^{-3}$ respectively. This simplification is therefore reasonable.



(a)



(b)

Figure 28: Difference between the complete equation and the simplified one for the term k_{TT}^f : impact on the outlet air temperature and relative humidity

4.3. THERMAL AND HYDRAULIC PROPERTIES OF UNSATURATED SOILS

A lot of work has been done on the formulation of the heat and mass transfer equations within porous media and soils. As it has been previously described, these equations involve many parameters or functions. Nevertheless, the appropriate approach to compute the parameters remains a subject of active discussion. The main discussions are on:

1. The water retention curve model,
2. The way to compute the ground thermal conductivity,
3. The ground hydraulic conductivity model,
4. The hydraulic vapour diffusivity calculation.

The objective is to develop an accurate ground model, flexible enough to tackle different kinds of grounds, different geometry and boundary conditions, and which is adapted to the coupling with a ventilated foundation model. Nonetheless, we have to keep in mind that we usually have very few information about the soil properties. Consequently, a trade-off has to be made between very accurate models and high number of parameters involved.

4.3.1 WATER RETENTION CURVE

Several models exist for the suction curves. Van Genuchten and Nielsen (1985) studied the Brooks and Corey formulation and found that it led to poor fit near saturation, especially for fine textured soils. After a brief overview of all the existing alternatives to correct that issue, they proposed the use of the Van Genuchten-Mualem (VGM) (Mualem, 1976; Van Genuchten, 1980) model given by

$$\theta(\Psi) = \theta_r + (\theta_s - \theta_r)(1 - (-\alpha\Psi)^n)^{-m} \quad (4.3)$$

They then studied the influence of the choice of the parameters n and m on the accuracy of the prediction. Naturally, allowing n and m independent leads to the best fitting with the experimental data, but the restriction $m = 1 - \frac{1}{n}$ does not induce a high deviation and eliminate one parameter from the equations. Vogel et al. (2001) then proposed to modify the latter VGM model. They proved that taking into account a very small but not null matric head Ψ_{sat} and a parameter θ_m such as $\theta(\Psi \geq \Psi_{sat}) = \theta_m$, the fitting with experimental data was improved and the simulation code was more stable. Ψ_{sat} is defined such as $S(\Psi_{sat}) = 99.9\%$ where $S = \frac{\theta - \theta_r}{\theta_s - \theta_r}$ is the saturation level. Although this study was undertaken mainly for non-swelling soils, the final model given by (4.4) was successfully used by Janssen (2002). An example for soils of type sand, silt and clay is plotted on Figure 29. In this study the dependence of the water content with the temperature is neglected.

$$\theta(\Psi) = \theta_r + (\theta_m - \theta_r)(1 - (-\alpha\Psi)^n)^{\frac{1}{n}-1} \quad (4.4)$$

Furthermore, some authors like Janssen (2002) and Mualem (1974) chose to include a hysteresis model into the water retention curve, but it will not be considered in this work.

Such choice has been made firstly because a hysteresis model can lead to serious numerical difficulties, and secondly because its influence on the temperature and moisture field is limited compared to the impact of a bad evaluation of the soil parameters.

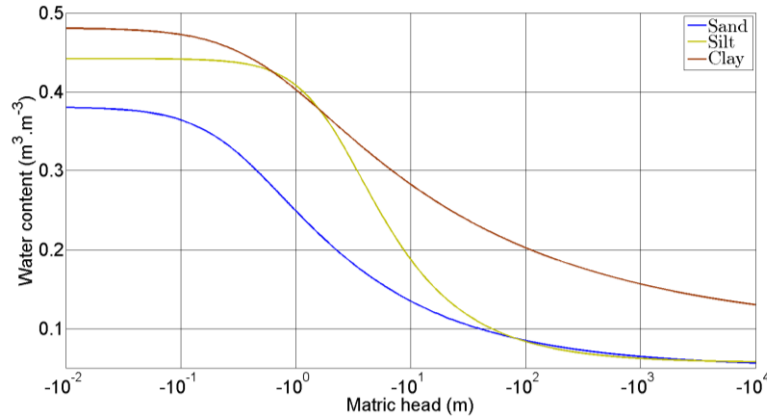


Figure 29: Suction curve for three different soils with the Janssen-VGM model

4.3.2 HYDRAULIC CONDUCTIVITY

Most of the existing models to calculate the hydraulic conductivity of porous materials are based on the retention curve formulation. Van Genuchten (1980) and Van Genuchten and Nielsen (1985) compared the Mualem's (Mualem, 1976) and the Burdine's formulation, both consisting in the modulation of the hydraulic conductivity at saturation K_{sat} by a function depending on the matric head. The Mualem's equation (4.5) appeared to be slightly better, with $S = \frac{\theta - \theta_r}{\theta_s - \theta_r}$ the saturation level

$$K_h(\theta) = K_{sat} S^{1/2} \frac{\int_0^S \Psi(\theta)^{-1} d\theta}{\int_0^1 \Psi(\theta)^{-1} d\theta} \quad (4.5)$$

Another formulation of (4.5) is given by

$$K_h(\theta) = K_{sat} S^{1/2} \left[1 - (1 - S^{1/m})^m \right]^2 \quad (4.6)$$

As for the suction curve, Vogel et al. (2001) proposed to use the matric head Ψ_{sat} previously defined for the hydraulic conductivity calculation too. Schaap and Leij (2000) also improved the VGM model. Instead of K_{sat} , they showed thanks to neural networks that the use of K_0 as a matching point enhanced the fitting with the experimental data on 235 soil samples representative of the textural distribution. Similarly, a best fitting is also possible by taking an exponent τ of S different from $1/2$. Using the models previously exposed, Janssen proposed the model given by (4.7) and illustrated on Figure 30 for three soils and three temperatures.

$$K_h(\theta) = K_0 S^\tau \left(\frac{1 - (1 - S_0^{1/m})^m}{1 - (1 - S_{0,sat}^{1/m})^m} \right)^2 K_T \quad (4.7)$$

where $K_T = 1.12 \cdot 10^{-4} T^2 - 4.12 \cdot 10^{-2} T + 3.46$ (–) is a viscosity dependent temperature correction, and $S_0 = \frac{\theta - \theta_r}{\theta_m - \theta_r}$.

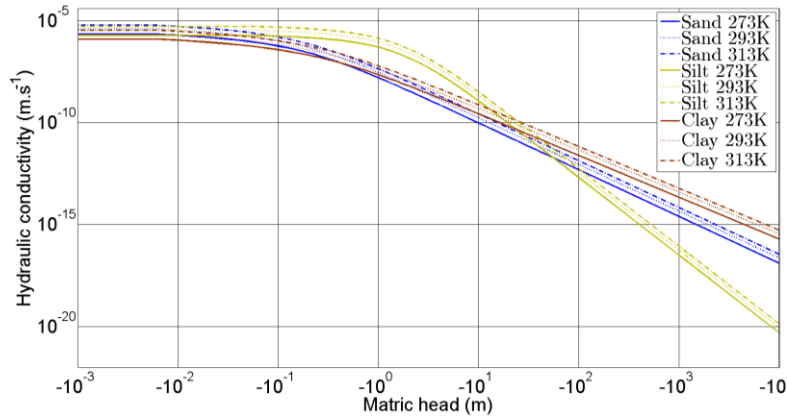


Figure 30: Hydraulic conductivity for three different soils with the Janssen-VGM model

4.3.3 THERMAL CONDUCTIVITY

The calculation of an equivalent thermal conductivity of a multiphase media from the thermal conductivities of its basic constituents was a topic of active research in the past. It is a function of the size, the shape, the orientation of the grains of the solid matrix and of the fluids. Even for a pure conductive problem of a saturated porous media with only one fluid, its expression $\lambda = \eta\lambda_f + (1 - \eta)\lambda_s + \frac{\lambda_f - \lambda_s}{V} \int_{A_{fs}} \vec{b}_{fs} \cdot \vec{n}_{fs} dA$ (see 3.2.1.2) is complex, due to the difficulty in characterising the geometry of the solid matrix. A number of models have been developed to overcome the difficulty of the previous formula. (Farouki, 1981) made an extensive study on the existing models and their comparison with the available measurements. Among them, the upper and lower bounds are respectively given by the parallel and the series models: $\lambda^* = \eta\lambda_f + (1 - \eta)\lambda_s$ and $\lambda = \frac{\lambda_f\lambda_s}{\eta\lambda_f + (1-\eta)\lambda_s}$. The geometric mean given by $\lambda = \lambda_f^\eta \lambda_s^{1-\eta}$ can be seen as an average between these limits. Other authors proposed more complex formulas for dry soils (solid matrix and air), empirical relation for frozen soils, or even for partially saturated soils. Gori and Corasaniti (2013) developed a purely geometric model to calculate the thermal conductivity of an unsaturated soil. Their formulation does not require other parameters than the porosity. Nevertheless, its complexity makes its integration difficult into a numerical code in which it will be evaluated iteratively. Zhang et al. (2007) proposed a randomly mixed model to simulate the spatial structure of the multi phase media, and to solve the three-dimensional heat equation to deduce the effective thermal conductivity. As for the model of Gori and Corasaniti, even if its relevance has been proved against experimental data, using it in a numerical code seems difficult. Indeed, for every control volume, the heat equation should be solved for every time step. This would be time consuming.

Philip and De Vries (1957) proposed a relatively simple model for a partially saturated soil, considering the solid matrix, the liquid water and the moist air, specified by the equation (4.8), where i corresponds successively to water, air, quartz and non quartz elements, ξ_i the ratio of the thermal gradient in the phase i and the thermal gradient in the material, θ_i and λ_i their volumetric content and pure conductivity. A distinction between quartz and non-quartz elements of the solid matrix has been proposed because of the high conductivity of the quartz.

$$\lambda = \frac{\sum_{i=1}^4 \xi_i \theta_i \lambda_i}{\sum_{i=1}^4 \xi_i \theta_i} \quad (4.8)$$

The thermal conductivity for the moist air λ_2 must integrate the vapour-liquid-vapour series moisture flow induced by a thermal gradient. Indeed imposing a thermal gradient on a soil sample, the conductive heat flow cannot be dissociated of this process. We thus have

$$\lambda_2 = \lambda_a + L_v D_{v,a} \frac{\partial \rho_v}{\partial T} \quad (4.9)$$

An adaptation of equation (4.8) has been proposed by Campbell et al. (1994), and implemented by Janssen (2002). First, the effect of the thermal vapour diffusion of the moist air is added in λ_2 , following the observation of Philip and De Vries (1957). Secondly, this formula is valid as long as the liquid water can be considered as a continuous media, which is wrong for a dry soil. Instead, the dry air can be considered as the continuous fluid. Consequently, Campbell proposed to use an equivalent thermal conductivity λ_f for a continuous fluid, defined by (4.10). This ensures a transition between the cases when the liquid water is the continuous fluid. The function f_w and the parameter q define the shape and the rapidity of this transition. θ_k is the water content from which the liquid water phase is not continuous anymore.

$$\lambda_f = \lambda_2 + f_w(\lambda_1 - \lambda_2) \quad (4.10)$$

$$f_w = \left(1 + \left(\frac{\theta}{\theta_k}\right)^{-q}\right)^{-1} \quad (4.11)$$

$$q = q_0 \left(\frac{T}{303}\right)^2 \quad (4.12)$$

Integrating this modification, the expression for ξ_i is

$$\xi_i = \frac{2}{3} \left(1 + \left(\frac{\lambda_i}{\lambda_f} - 1\right) g_i\right)^{-1} + \frac{1}{3} \left(1 + \left(\frac{\lambda_i}{\lambda_f} - 1\right) (1 - 2g_i)\right)^{-1} \quad (4.13)$$

θ_k , q_0 and g_i are thus fitting parameters of the thermal conductivity. Janssen (2002) identified 14 soils representative for 554 samples defined by textural characterization (sand, clay and silt fraction on the textural triangle) in the Rosetta software (Schaap et al., 2001). Linear regressions for these 14 soils enable to relate these three parameters to the sand fraction Sa only, given by (4.14), (4.15) and (4.16). Adding the silt fraction in the relations does not reduce the dispersion of the values. Furthermore, it does not appear as a serious problem regarding the relatively good accuracy of the predictions of the thermal conductivity for these 'average soils'. Examples of thermal conductivities calculated according to this model are depicted on Figure 31.

$$\theta_k = 0.21 - 0.16Sa \quad (4.14)$$

$$q_0 = 4 - Sa \quad (4.15)$$

$$g_i = 0.0675 + 0.074Sa \quad (4.16)$$

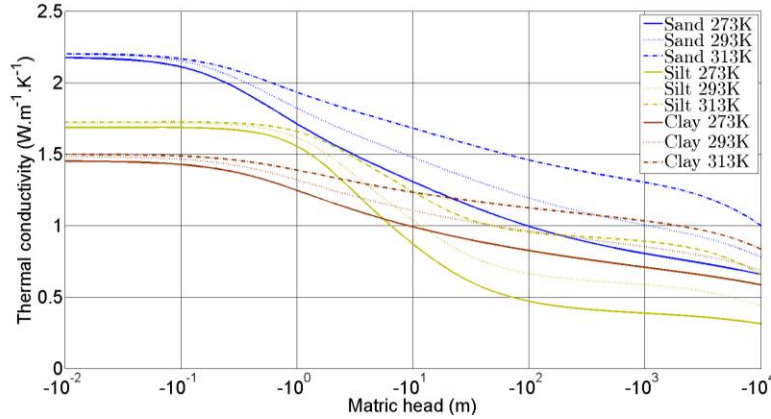


Figure 31: Thermal conductivity for three different soils with the de Vries - Janssen model

4.3.4 VAPOUR DIFFUSIVITY

One of the first vapour diffusion model was given by the equation (3.23), where the vapour diffusivity could be written under the form (4.17) with $D_{v,a}$ the water vapour diffusivity in the air, ν a mass flow factor assumed equal to unity given the conditions of this study, and v the tortuosity factor.

$$D_v = D_{v,a} \nu v \theta_a \quad (4.17)$$

However, Philip and De Vries (1957) noted a large difference between the calculated thermal vapour flow with this model, and the experimental data available. They made two changes that have proven to be reliable after comparison with the experimental data.

Firstly, they highlighted that a correction was required due to the large difference between the temperature gradient in the air and in the liquid. Since the thermal diffusion of water vapour has been neglected in the simplified system of equation for the ground, this will not be detailed further.

Secondly, they put in evidence the vapour-liquid-vapour series moisture flow, not taken into account in the original model. Therefore, they proposed to modulate the available cross section thanks to a factor f in order to enhance the vapour flow.

$$f = \begin{cases} \theta_s & \text{if } \theta \leq \theta_k \\ \theta_a \left(1 + \frac{\theta}{\theta_s - \theta_k} \right) & \text{if } \theta > \theta_k \end{cases} \quad (4.18)$$

Assuming the expression for the tortuosity is $\nu = \theta_a^{2/3}$ we obtain

$$D_{\Psi v} = \frac{D_{v,a}}{\rho_l} f \theta_a^{5/3} \frac{\partial \rho_v}{\partial \Psi} \quad (4.19)$$

The shape of the hydraulic vapour diffusivity $D_{\Psi v}$ for three different soils and temperature is given on Figure 32.

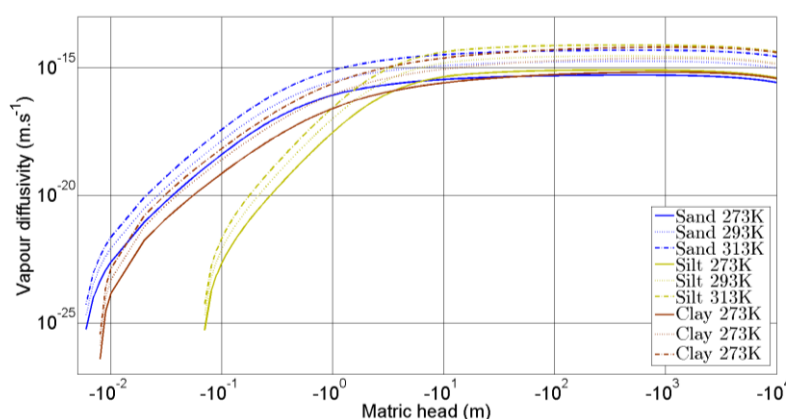


Figure 32: Hydraulic vapour diffusivity for three different soils according to the Philipp & de Vries model

4.3.5 PARAMETER VALUES

The soil on the site of the studied building (see Chapter 6) is very complex, made of several layer of various materials and is a mixing of natural materials and construction wastes. Consequently, it would be rather difficult to characterise each components of the soil to evaluate all its thermo-hygric characteristics. Furthermore, the sampling and the measurements campaign should be repeated for each new project integrating Fondatherm which would be costly.

Instead, the solution adopted by Janssen has been adopted in this work. All the physical quantities discussed above and developed above offer the great advantages of being accurate whilst depending only on a limited number of parameters. A set of parameters for seven kinds of soils got from statistics fitting with experimental data and representative of most of the traditional soils has been given in the Janssen's thesis, and is reproduced in Appendix B. The estimation of the soil classification may be sufficient to choose the set of parameter that better characterise it. For the considered soil (see Chapter 6), it has been estimated that the silt class was the closer to the real nature of the ground.

4.4. THERMAL AND HYDRAULIC PROPERTIES OF CONCRETE

Janssen et al. (2007) proposed a formulation for heat and mass transfer equations within building materials, that have been used by Rouchier (2012) to study the heat and moisture transfer within damaged building construction materials, especially concrete. In this latter study, the concrete hydraulic characteristics have been measured. Berger (2014) who also developed numerical model for similar applications used the material data base available with the software Delphin (Bauklimatik-Dresden, 2017). Baroghel-Bouny (2007a) made an extensive experimental study to measure the sorption-desorption isotherm for a set of seven normal and high performance concrete and four cement paste, and related it with their composition. Baroghel-Bouny (2007b) also measured and analysed their moisture transport properties. However, since the experimental results are discrete data, the choice has been made to stick to the explicit formulas given in the works cited above. Nevertheless, the studies carried out by Baroghel-Bouny enable to have a point of comparison for the analytical models. Table 13 gives the main characteristics of the concrete used in Fondatherm. A comparison to

the studied concrete by Baroghel-Bouny (2007a) put in evidence similarities with the material references under 'BO' and 'B30-A'.

Table 13: Concrete composition and main characteristics for the foundation in Val-de-Mercy

| | |
|---|-----------------------|
| <i>Gravel content (kg.m⁻³)</i> | 1050 |
| <i>Sand(kg.m⁻³)</i> | 800 |
| <i>Cement (kg.m⁻³)</i> | 350 |
| <i>Water content (kg.m⁻³)</i> | 160-175 |
| <i>Superplasticizer</i> | Grace - Adva Cast 596 |
| <i>Water-to-cement ratio (-)</i> | 0.48 |
| <i>Gravel-to-sand ratio (-)</i> | 1.3 |
| <i>28-day cylinder average compressive strength (MPa)</i> | 32.5 |

4.4.1 WATER RETENTION CURVE

Rouchier (2012) and Berger (2014) opted for the use of the original VGM model introduced in the previous section, with adapted parameters for the concrete. This function appeared to correctly reproduces the measurements taking $w_{sat} = 101.44$, $\alpha_p = 6.165 \cdot 10^{-7}$, $n = 1.2566$ and $m = 0.2191$.

$$w = w_{sat} \left(1 + (-\alpha_p P_c)^n \right)^{-m} \quad (4.20)$$

4.4.2 LIQUID PERMEABILITY

Rouchier (2012) then Berger (2014) chose to use a bi-modal expression for the liquid unsaturated conductivity of the concrete. Based on the VGM model and considering a two pore size Priesack and Durner (2006) showed that a really good representation of the real relative conductivity can be reached using the expression (4.21). Although their conclusions was mainly for soil materials, Rouchier (2012) applied successfully the same expression for concrete and got good fitting with his measurements.

$$K_p = K_{p,sat} (l_1 S_1 + l_2 S_2)^\tau \frac{K_1 + K_2}{l_1 \alpha_{p,1} + l_2 \alpha_{p,2}} \quad (4.21)$$

where $S_i = \left(1 + (-\alpha_{p,i} P_c)^{n_i} \right)^{-m_i}$ and $K_i = l_i \alpha_{p,i} \left(1 - \left(1 - S_i^{1/m_i} \right)^{m_i} \right)^2$ are respectively the saturation level and the relative hydraulic conductivity of the pore size subsystem i . All the fitting parameters are given in Table 14.

Table 14: Moisture suction curve: parameters for a bi-modal representation of concrete

| | $K_{p,sat}$ | τ | l | α | m | n |
|-----------------|-------------------------|---------|--------|-----------------------|--------|--------|
| Pore size $i=1$ | $2.2182 \cdot 10^{-13}$ | -4.6975 | 0.5062 | $5.533 \cdot 10^{-7}$ | 0.618 | 2.5963 |
| Pore size $i=2$ | | | 0.4938 | | 0.1913 | 1.2366 |

4.4.3 VAPOUR PERMEABILITY

(Rouchier, 2012) measured a value for (non-damaged) concrete water vapour permeability equal to $8.46 \cdot 10^{-13}$. Berger (2014) used a similar value for the relative permeability and modulated it with an exponential term, as written in equation (4.22), with $\delta_r = 8 \cdot 10^{-13}$ and $\delta_e = -2 \cdot 10^{-4}$.

$$\delta_v = \delta_r \exp(\delta_e P_v) \quad (4.22)$$

The order of magnitude of this model is in agreement with the measurements of the effective water vapour diffusion coefficient made by Baroghel-Bouny for both the 'BO' and 'B30-A' concrete.

4.4.4 THERMAL CONDUCTIVITY

The formulation for the thermal conductivity is here simpler than for the soil. The expression in DELPHIN and used by Berger assumes a linear evolution between a dry state where $\lambda = \lambda_0 = 1.75$ and a saturated state where $\lambda_w = 4.5 \cdot 10^{-3}$ is the slope of the function (4.23).

$$\lambda = \lambda_0 + \lambda_w w \quad (4.23)$$

4.5. BOUNDARY CONDITIONS DESCRIPTION

4.5.1 BOUNDARY CONDITIONS FOR THE GROUND

4.5.1.1. Ground top surface

Main equations

Considering short and long wave radiation onto the ground ($\phi_{h,sw}$ and $\phi_{h,lw}$ respectively), convection due to wind and surface/air temperature differences ($\phi_{h,conv}$), evaporation ($\phi_{h,evap}$) and precipitation ($\phi_{h,prec}$), the general equations describing the energy and mass balance at ground top surface can be written (Deru and Kirkpatrick, 2002a; Janssen, 2002; dos Santos and Mendes, 2006)

$$\phi_{h,surf} = \phi_{h,sw} + \phi_{h,lw} + \phi_{h,conv} + \phi_{h,evap} + \phi_{h,prec} \quad (4.24)$$

$$\phi_{m,surf} = \frac{1}{\rho_l} (\phi_{m,evap} + \phi_{m,prec}) \quad (4.25)$$

The corresponding heat and moisture flow are given by

$$\phi_{h,sw} = G \left(1 - a \left(1 - \frac{\theta_{surf}}{2\theta_s} \right) \right) \quad (4.26)$$

$$\phi_{h,lw} = \sigma \varepsilon (T_{sky}^4 - T_{surf}^4) \quad (4.27)$$

$$\phi_{h,conv} = h_{c,surf} (T_a^{ext} - T_{surf}) \quad (4.28)$$

$$\phi_{h,evap} = L_{v,surf} h_{v,surf} (\rho_{v,a}^{ext} - \rho_{v,surf}) \quad (4.29)$$

$$\phi_{h,prec} = c_l (T_a^{ext} - T_0) Prec \quad (4.30)$$

$$\phi_{m,evap} = h_{v,surf} (\rho_{v,a}^{ext} - \rho_{v,surf}) \quad (4.31)$$

$$\phi_{m,prec} = Prec \quad (4.32)$$

As illustrated on Figure 33, the 'half control volume' method is applied as described by Patankar (1980). Instead of solving the heat and mass balances to compute the temperature and the matric head at the ground top surface, the heat and moisture flow are treated as if they were a source term at the ground top meshes. The meshes at the surface have a thickness halved, in such a way that the thermal and hygric capacities of these meshes are low. Consequently, the heat and moisture fluxes exchanged with the surroundings can be assumed equal to exchanges between the ground top surface and the central nodes of the ground top meshes. This approximation is assumed to have a negligible impact on the ground temperature and water content evaluation close to the foundation. The main objective of this choice is to reduce the number of equations to solve and thus the computational time. The use of this method is justified by the fact that the ground top surface is complex – this is all the more true considering the grass - and it is not reasonable to consider it as a theoretical perfect surface. Actually, its coarseness can be seen as the introduction of an additional storage property.

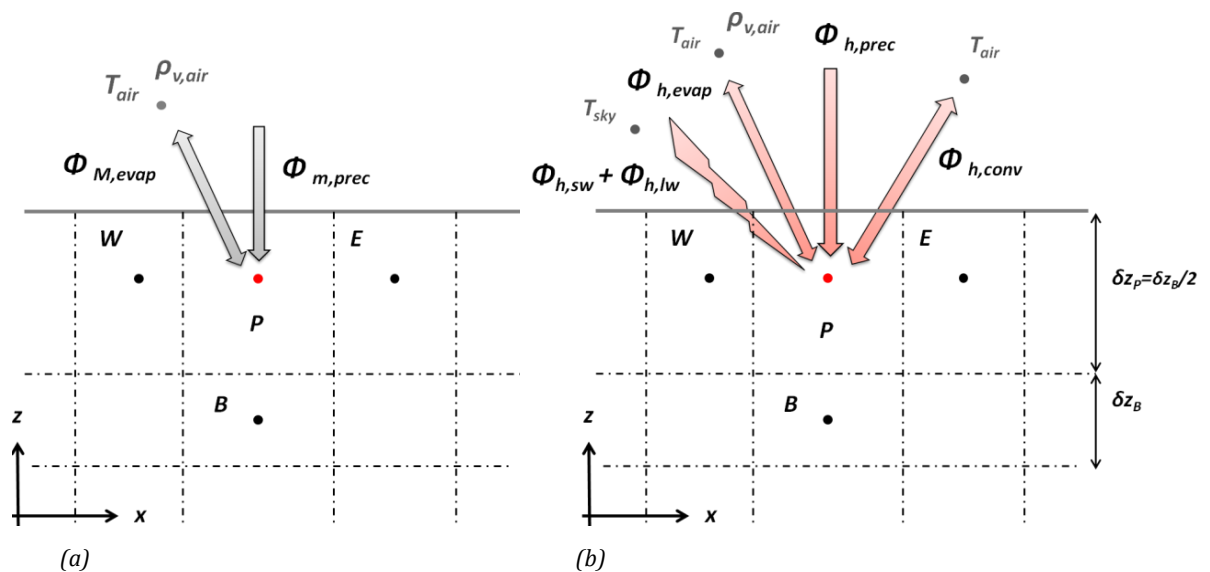


Figure 33 : Ground top surface boundary conditions: (a) moisture and (b) heat transfers

Exchange coefficients' evaluation

Attention must be paid to the evaluation of the thermal and vapour transfer coefficients and the sky temperature. They are necessary but not sufficient conditions of the model consistency with the experimental data. The models developed by Deru (2003) and Janssen (2002) have been widely used to build this one.

The convection heat transfer coefficient h_c is the product of the mass specific heat of air and the aerodynamic conductance $h_c = \rho_a C_a U_e$. The conductance depends on the air layer stability above the ground and is given by

$$U_e = \frac{\kappa^2 W}{\ln\left(\frac{Z_e}{Z_0}\right)^2} \varphi \quad (4.33)$$

where φ is a correction coefficient taking into account the air layer stability above the ground, and W the wind speed measured at the altitude Z_e . The stability can be quantified by the Richardson number given by

$$R_i = \frac{g(T_a^{ext} - T_{surf})(Z_e - Z_0)}{T_a^{ext} W^2} \quad (4.34)$$

This dimensionless number is negative when the air layer is unstable and is in the range $]0,0.2]$ for the stable cases. Several models exist to calculate the correction coefficient, but one of the more relevant according to (Janssen, 2002) is given by

$$\varphi = \begin{cases} (AB)^{-1} & \text{if } R_i \leq 0 \\ (1 - 5R_i)^2 & \text{if } 0 \leq R_i \leq 0.2 \end{cases} \quad (4.35)$$

where all the needed variables are calculated according to

$$A = 1 - \frac{\ln\left(\frac{1+X^2}{2}\right) + 2\ln\left(\frac{1+X}{2}\right) - 2\tan^{-1}(X) + \frac{\pi}{2}}{\ln\left(\frac{Z_e}{Z_0}\right)} \quad (4.36)$$

$$B = 1 - \frac{\ln\left(\frac{1+X^2}{2}\right)}{\ln\left(\frac{Z_e}{Z_0}\right)} \quad (4.37)$$

$$X = \left(1 - 16\frac{Z_e}{L_{MO}}\right)^{0.25} \quad (4.38)$$

$$\frac{Z_e}{L_{MO}} = A^2 B^{-1} \ln\left(\frac{Z_e}{L_{MO}}\right) R_i \quad (4.39)$$

Z_e and Z_0 are respectively the altitude of the wind speed measurement and the roughness length of the surface. L_{MO} is the Monin-Obukhov instability length. These relations give a non linear dependence between the correction coefficient φ and the Richardson number R_i that

should be solved by an iterative procedure. Since such methods reduce the numerical efficiency of the modelling, Janssen proposed to modify the previous relations to obtain a direct relationship between φ and R_i . This last method has been used in our model. As we can observe, this model does not include natural convection, which is negligible compared to forced convection due to the wind. However, natural convection phenomena still exist especially governed by thermal effects when there is no wind. In order to avoid null convective heat exchanges during such period, the aerodynamic correction coefficient has been limited to a minimum of 0.2.

The vapour diffusivity coefficient is assumed to be equal to the aerodynamic conductance. According to Deru (2003), a resistance is added in series to reduce the value of the vapour exchange coefficient that has been experimentally proved to be too high. The modulation is made by the water content of the ground top surface mesh according to (4.40), and the total vapour exchange coefficient is given by (4.41).

$$r_s = \max(410 - 8140\theta_{surf}, 0) \quad (4.40)$$

$$h_v = \left(\frac{1}{U_e} + r_s \right)^{-1} \quad (4.41)$$

Regarding radiation transfer, several sky temperature models exist, but one of the most relevant appeared to be that used by Janssen, see equation (4.42). Indeed, the model proposed by Deru does not enable to reproduce well the experimental soil surface temperature measured. Indeed, difference of up to 10 °C can be observed, especially in summer (Deru, 2003; Deru and Kirkpatrick, 2002a).

$$T_{sky} = T_a^{ext} - (23.8 - 0.2025(T_a^{ext} - 273.15))(1 - 0.87 \cdot cf) \quad (4.42)$$

A 'cloud factor' cf emerges to modulate the sky temperature as a function of the cloudiness. Janssen set it at a mean value of 0.6, corresponding to the mean cloud cover of the place he was considering over one year. In our case, the ground top surface in contact with the ambient air doesn't exchange long wave radiations with the whole sky half-sphere. Indeed, the buildings walls intercept an important part of this radiation. Their radiant temperature is almost all the time higher than that of the sky. The cloud factor has thus been used to take into account in a simple manner the influence of the buildings walls. It has been set at 1.1, which doesn't have a physical meaning anymore, but enable to build artificially a temperature of an equivalent surface ('sky + building') exchanging radiation with the ground top surface.

Finally, the ground emissivity ε and albedo a has been taken equal to 0.75 and 0.15 respectively, which is representative for grass and soil. This choice has been made after several tries and comparisons with the experimental data (see section 7.2).

All of these were the equations to model a bare ground, typically the lawn of the EHPAD retirement home (see Chapter 6). But the main part of the ground top surface is covered with deactivated concrete, thus allowing simplifications of the previous equations. The concrete

layer can be considered impermeable. Therefore, all the moisture flows, and the associated heat fluxes are ignored. Figure 34 shows the remaining heat flows considered in the case of a deactivated concrete cover on the ground top surface. These fluxes are calculated in the same way as previously. The resolution of the energy balance at the deactivated concrete surface yields the surface temperature, and afterward the heat flux crossing the meshes at the ground top surface.

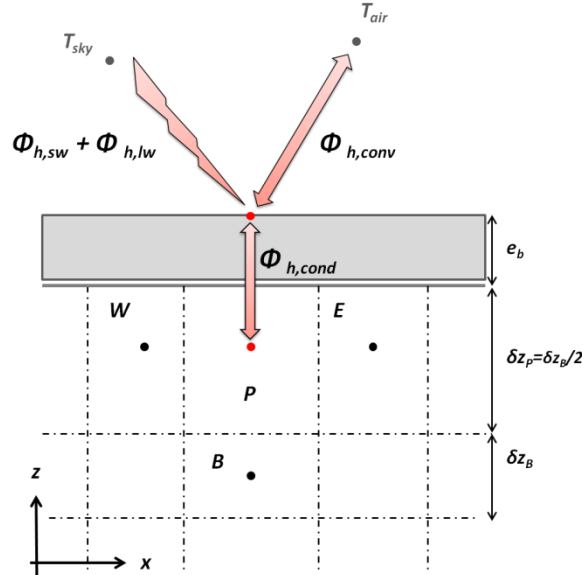


Figure 34: Boundary heat flows on the ground top surface with deactivated concrete cover

4.5.1.2. Water table

The ground base layer is assumed to be a water table. Naturally, the matric head at the ground bottom is thus equal to Ψ_{sat} . For the thermal boundary equation, Janssen (2002) proposed, instead of an adiabatic or an isotherm condition, to impose a null conductive heat flow, i.e. a null gradient of temperature. According to him, this is the best way to model a low ground water flow: the moisture drainage still enables sensible and latent heat transfers to the water table. The heat boundary equation is thus:

$$\phi_{h,base} = \rho_l c_l (T_{base} - T_0) K_h \left(\frac{2}{\delta z_{base}} (\Psi_{sat} - \Psi_{base}) - 1 \right) \quad (4.43)$$

4.5.1.3. Ground – crawl space interface

The evaluation of heat and moisture transfer between the ground beneath the building slab and the crawl space air require knowing the temperature and the humidity of the latter. A very strong assumption would consist in considering a constant temperature and relative humidity. This leads to poor fitting with the real ground temperature measurements (see Chapter 7). This model has to be grounded on a satisfying compromise between more realistic boundary condition and relative simplicity in order to avoid considering much more new parameters. For that purpose, the experimental work of Kurnitski (2000) is used. The main assumptions of our model are:

1. no moisture production within the air volume
2. no condensation within the air volume

3. the inlet airflow is equal to the outlet airflow
4. no radiative flux.

Under these circumstances, the moisture and heat balance equation for the crawl space air volume are respectively given by (4.44) and (4.45) where V_{CS} designates the volume of the crawl space, A_{CS} the ground-crawl space interface area, U_{slab} the heat loss coefficient of the slab, T_{int} the indoor air temperature and ACR the air change rate. $h_v^{g,CS}$ and $h_c^{g,CS}$ are respectively the mass and heat convective exchange coefficients between the crawl space air and the soil. Similarly, $h_v^{f,CS}$ and $h_c^{f,CS}$ are the mass and heat convective coefficients for the foundation external walls exchanging with the crawl space air.

$$V_{CS} \frac{\partial \rho_v^{CS}}{\partial t} = ACR \frac{V_{CS}}{3600} (\rho_{v,a}^{ext} - \rho_{v,a}^{CS}) + \sum_{i,j} \delta S_{i,j}^{g,CS} h_v^{g,CS} (P_{v,i,j}^g - P_{v,a}^{CS}) + \sum_{i,j} \delta S_{i,j}^{f,CS} h_v^{f,CS} (P_{v,i,j}^f - P_{v,a}^{CS}) \quad (4.44)$$

$$V_{CS} \rho_v^{CS} c_a \frac{\partial T_a^{CS}}{\partial t} = U_{slab} A_{CS} (T_{in} - T_a^{CS}) + c_a ACR \frac{V_{CS}}{3600} (\rho_{v,a}^{ext} T_a^{ext} - \rho_{v,a}^{CS} T_a^{CS}) + \sum_{i,j} \delta S_{i,j}^{g,CS} [h_c^{g,CS} (T_{i,j}^{g,CS} - T_a^{CS}) + (c_v T_a^{CS} + L_{v,i,j}^g) h_v^{g,CS} (P_{v,i,j}^{g,CS} - P_{v,a}^{CS})] + \sum_{i,j} \delta S_{i,j}^{f,CS} [h_c^{f,CS} (T_{i,j}^{f,CS} - T_a^{CS}) + (c_v T_a^{CS} + L_{v,i,j}^f) h_v^{f,CS} (P_{v,i,j}^{f,CS} - P_{v,a}^{CS})] \quad (4.45)$$

The last equations imply new variables and parameters that could not be measured in this work. Nevertheless, the work of Kurnitski has been carried out for a naturally ventilated crawl space with similar dimensions. It allowed to reasonably thinking that some of the descriptive variables of the present crawl space are similar to his. Consequently, we assumed that the air change rate is constant and equal to the mean air change rate measurement over one year for the 'naturally ventilated crawl space', namely $1.7 h^{-1}$ (Kurnitski, 2000). The indoor air temperature is assumed constant and equal to $293 K$, and the heat loss coefficient is equal to $0.31 W \cdot m^{-2} K^{-1}$.

The heat and moisture transfer convective coefficients at the ground top surface and at the external horizontal wall of the foundation are calculated according to (4.46). The Nusselt number Nu_{CS} is given by (4.47) if the temperature of the surface is lower than the crawl space air temperature, and by (4.48) otherwise (Incropera and DeWitt, 1990).

$$h_c^{CS} = \frac{Nu_{CS} \lambda_a^{CS}}{L_{CS}} \quad (4.46)$$

$$Nu_{CS} = 0.27 Ra_{CS}^{1/4} \quad (4.47)$$

$$Nu_{CS} = 0.54 Ra_{CS}^{1/4} \quad (4.48)$$

L_{CS} is the characteristic length of the ground crawl space top surface or of the external horizontal top surface of the foundation, and \mathcal{Ra}_{CS} is the Rayleigh number of the air. For the beam vertical wall facing the crawl space air, the correlation to calculate the Nusselt number is the Churchill and Chu equation (Incropera and DeWitt, 1990)

$$\mathcal{Nu}_{CS} = \left(0.825 + 0.387 \frac{\mathcal{Ra}_{CS}^{1/6}}{\left(1 + \left(\frac{0.492}{\mathcal{Pr}} \right)^{9/16} \right)^{8/27}} \right)^2 \quad (4.49)$$

The resolution of (4.44) and (4.45) is realised with a Newton-Raphson method and yields the values of T_a^{CS} and Ψ_a^{CS} . Finally, the heat flux and the moisture flow at the ground top surface beneath the slab are given by (4.53) and (4.55) where the summation signs have been removed for the sake of simplicity.

$$\phi_h^{g,CS} = [h_c^{g,CS}(T_{CS}^g - T_a^{CS}) + (c_v T_{CS}^g + L_v^g)\phi_m^{g,CS}] \quad (4.50)$$

$$\phi_m^{g,CS} = \frac{h_v^{g,CS}}{\rho_l} (P_v^g - P_{v,a}^{CS}) \quad (4.51)$$

Similar equations are used for the boundary condition between the concrete beam and the crawl space air.

4.5.2 BOUNDARY CONDITIONS FOR THE CONCRETE FOUNDATION

4.5.2.1. Cavity walls – circulating air

The model to compute the temperature and the relative humidity evolution of the circulating air along the foundation is widely reported in the section 5.3.1.1. We focus here only on the heat and moisture exchanges between the air and the cavity walls.

Each section of the circulating air along the y axis corresponds to one air volume and is represented by one air node. The moisture and the heat exchanged between the air node and a mesh in the cavity wall are respectively calculated according to (4.52) and (4.53).

$$\phi_m^{f,cav} = h_v^{f,cav}(P_{v,a}^f - P_{v,cav}^f) \quad (4.52)$$

$$\phi_h^{f,cav} = h_c^{f,cav}(T_a^f - T_{cav}^f) + (c_v T_a^f + L_v)\phi_m^{f,cav} \quad (4.53)$$

The convective coefficient $h_{c,cav}$ is calculated thanks to the relation (4.54) where the Nusselt number is given by the Colburn equation (4.55) (Incropera and DeWitt, 1990). $D_{h,cav}$ is the hydraulic diameter of the foundation cavity's.

$$h_c^{f,cav} = \frac{\mathcal{Nu}_{cav}\lambda_a^{cav}}{D_{h,cav}} \quad (4.54)$$

$$\mathcal{Nu} = 0.023\mathcal{Re}_{cav}^{4/5}\mathcal{Pr}_{cav}^{1/3} \quad (4.55)$$

According to the heat and mass transfer analogy (Incropera and DeWitt, 1990), the moisture transfer coefficient is related to the convective heat transfer coefficient by

$$h_v^{f,cav} = \frac{h_c^{f,cav}}{\rho_a^f R_v T_a^f C_a} \cong 6.1 \cdot 10^{-9} h_c^{f,cav} \quad (4.56)$$

4.5.2.2. Foundation – ground interface

The foundation external walls are partially covered with a bituminous coating, in order to inhibit all the vapour and the liquid transfers from the ground that could thus damage the building materials. However, this treatment enables sensible heat transfers. This bituminous coating is applied on the outside faces only. The inside walls are left without treatment, which allows moisture transfers. Two kinds of boundary conditions will be thus taken into account for the foundation-ground interface modelling: interface with and without bituminous coating.

Interface with bituminous coating

Three sensible heat transfers take place at this interface (Figure 35):

1. The sensible heat transfer between the ground central node of the mesh facing the concrete wall's foundation and its surface,
2. The sensible heat transfer between the foundation central node of the mesh facing the ground and its surface,
3. A sensible heat flow between the ground surface and the foundation wall surface due to the imperfections of the contact between the two materials.

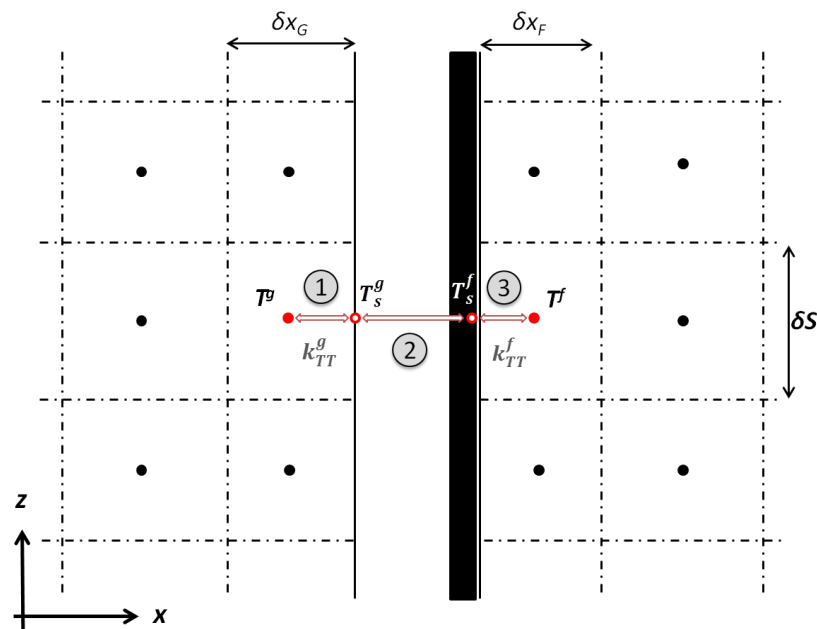


Figure 35: Modelling the heat and mass transfer through the interface soil / bituminous coating / foundation (not in scale)

Let k_{TT}^g the thermal conductance in heat transfer equation for the ground, k_{TT}^f the thermal conductance in the heat transfer equation for the concrete and $R_{TT,ctct}$ the thermal contact resistance between the soil and the concrete. The global thermal resistance is the sum of three

resistances. Facing the complexity of the modelling of the thermal and hydric contact between two materials, and the lack of information about the real implementation, all kind of contact resistance will be ignore thereafter. The equivalent thermal conductance is thus given by

$$k_{TT}^{eq} = \frac{(\delta x_G + \delta x_F)k_{TT}^g k_{TT}^f}{\delta x_G k_{TT}^f + \delta x_F k_{TT}^g} \quad (4.57)$$

Finally, the boundary condition for the ground meshes in contact with the foundation in the zone with bituminous coating is

$$\varphi_{H, fnd \rightarrow grd} = \delta S \cdot k_{TT}^{eq} \cdot \frac{2}{(\delta x_G + \delta x_F)} (T^f - T^g) \quad (4.58)$$

Interface without bituminous coating

As previously exposed, we can define equivalent heat and moisture conductance for both heat and mass transfer equations (Figure 36), still neglecting the contact resistances. One example is given with the moisture equivalent conductance for the heat equation, considering a heat flow from the foundation to the soil

$$k_{T\psi}^{eq} = \frac{(\delta x_G + \delta x_F)k_{T\psi}^g k_{T\psi}^f}{\delta x_G k_{T\psi}^f + \delta x_F k_{T\psi}^g} \quad (4.59)$$

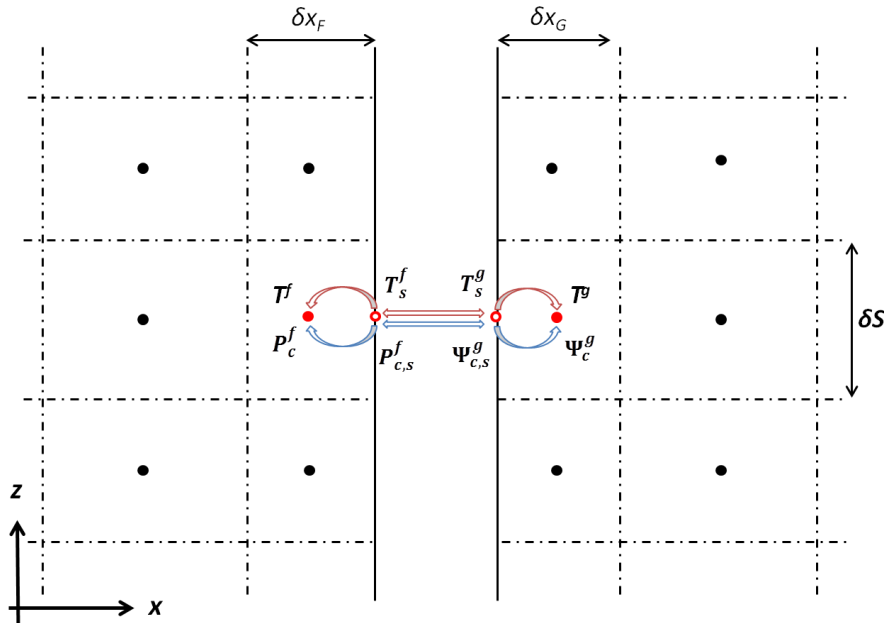


Figure 36: Modelling the heat and mass transfer through the interface soil / foundation (not in scale)

Since the ground and the foundation system of equations use respectively the matric head and the capillary pressure as potential to describe the moisture movement, the mass conductance for the heat equation in the foundation is not expressed with the same unit. The linear relation between these two variables gives a simple equation to write the conversion

$$k_{T\Psi}^f = \frac{1}{\rho_l g} k_{TP_c}^f \quad (4.60)$$

Therefore,

$$k_{T\Psi}^{eq} = \frac{(\delta x_G + \delta x_F) k_{T\Psi}^g k_{TP_c}^f}{\delta x_G k_{TP_c}^f + \delta x_F \frac{k_{T\Psi}^g}{\rho_l g}} \quad (4.61)$$

And as $k_{\Psi T}^g$ is assumed negligible, the same holds for $k_{\Psi T}^{eq}$

$$k_{\Psi T}^{eq} = 0 \quad (4.62)$$

The same procedure is applied to calculate the equivalent heat and moisture transfer coefficients for the heat and the mass transfer equations. The results are summed up in Table 15.

Table 15: Boundary conditions at ground-foundation interface

| | Foundation → Ground | Ground → Foundation |
|--------------------------------------|---|--|
| <i>Heat transfer coefficient</i> | $k_{TT}^{eq} = \frac{(\delta x_G + \delta x_F) k_{TT}^g k_{TT}^f}{\delta x_G k_{TT}^f + \delta x_F k_{TT}^g}$ | |
| <i>Moisture transfer coefficient</i> | $k_{T\Psi}^{eq} = \frac{(\delta x_G + \delta x_F) k_{T\Psi}^g k_{TP_c}^f}{\delta x_G k_{TP_c}^f + \delta x_F \frac{k_{T\Psi}^g}{\rho_l g}}$ | $k_{TP_c}^{eq} = \frac{(\delta x_G + \delta x_F) k_{T\Psi}^g k_{TP_c}^f}{\delta x_G \rho_l g k_{TP_c}^f + \delta x_F k_{T\Psi}^g}$ |
| <i>Heat equation</i> | $\phi_h^{f \rightarrow g} = \frac{2\delta S}{(\delta x_G + \delta x_F)}$ | |
| <i>Full equation</i> | $\cdot \left(k_{TT}^{eq} \cdot (T^f - T^g) \right.$ $\left. + k_{T\Psi}^{eq} \cdot \left(\frac{P_c^f}{\rho_l g} - \Psi^g \right) \right)$ | $\phi_h^{g \rightarrow f} = \frac{2\delta S}{(\delta x_G + \delta x_F)}$ $\cdot \left(k_{TT,eq} \cdot (T^g - T^f) \right.$ $\left. + k_{TP_c,eq} \cdot (\rho_l g \Psi^g - P_c^f) \right)$ |
| <i>Heat transfer coefficient</i> | 0 | |
| <i>Moisture transfer coefficient</i> | $k_{\Psi\Psi}^{eq} = \frac{(\delta x_G + \delta x_F) k_{\Psi\Psi}^g k_{P_c P_c}^f}{\delta x_G k_{P_c P_c}^f + \delta x_F \frac{k_{\Psi\Psi}^g}{g}}$ | $k_{P_c P_c}^{eq} = \frac{(\delta x_G + \delta x_F) k_{\Psi\Psi}^g k_{P_c P_c}^f}{g \delta x_G k_{P_c P_c}^f + \delta x_F k_{\Psi\Psi}^g}$ |
| <i>Moisture equation</i> | $\phi_m^{f \rightarrow g} = \frac{2\delta S}{(\delta x_G + \delta x_F)} \cdot k_{P_c P_c,eq} \cdot (\rho_l g \Psi^g - P_c^f)$ | |
| <i>Full equation</i> | $\phi_m^{g \rightarrow f} = \frac{2\delta S}{(\delta x_G + \delta x_F)} \cdot k_{\Psi\Psi}^{eq} \cdot \left(\frac{P_c^f}{\rho_l g} - \Psi^g \right)$ | |

4.6. NUMERICAL RESOLUTION

4.6.1 PROJECTION OF THE CONSERVATION EQUATIONS

4.6.1.1. Spatial discretization: a finite volume method

Finite volume method consists in integration of the conservation equations on a control volume. All the details of the calculation are available in Appendix C, and the resulting matrix system of equation is given by

$$\begin{aligned} \mathbf{C}_{TT} \frac{\partial T}{\partial t} + \mathbf{C}_{T\Psi} \frac{\partial \Psi}{\partial t} &= \mathbf{K}_{TT} T + \mathbf{K}_{T\Psi} \Psi + \mathbf{G}_T + \mathbf{B}_T \\ \mathbf{C}_{\Psi T} \frac{\partial T}{\partial t} + \mathbf{C}_{\Psi\Psi} \frac{\partial \Psi}{\partial t} &= \mathbf{K}_{\Psi T} T + \mathbf{K}_{\Psi\Psi} \Psi + \mathbf{G}_\Psi + \mathbf{B}_\Psi \end{aligned} \quad (4.63)$$

where \mathbf{C}_{TT} , $\mathbf{C}_{T\Psi}$, $\mathbf{C}_{\Psi T}$ and $\mathbf{C}_{\Psi\Psi}$ are diagonal heat capacity matrix, \mathbf{K}_{TT} , $\mathbf{K}_{T\Psi}$, $\mathbf{K}_{\Psi T}$ and $\mathbf{K}_{\Psi\Psi}$ are tridiagonal by bloc conductance matrixes, \mathbf{G}_T and \mathbf{G}_Ψ are load vectors and \mathbf{B}_T and \mathbf{B}_Ψ are boundary vectors. A similar system can also be developed for the foundation model. The spatial derivatives are differenced which is a considerable simplification of the problem. Nevertheless all of these matrixes still depend on the variables T and Ψ (P_c for the concrete) and on time. An efficient programme is thus required to compute fast enough the solution for each iteration and time step.

4.6.1.2. Temporal discretization: a Newton-Raphson method

Once the spatial derivatives have been removed from the conservation equation, we need to evaluate the temporal derivatives. This has been done using an implicit forward Euler method. An example for the heat equation is given in the following equation (4.64) where Δt denotes the time step, eventually variable.

$$\begin{aligned} \mathbf{C}_{TT}^{t+\Delta t} (T^{t+\Delta t} - T^t) + \mathbf{C}_{T\Psi}^{t+\Delta t} (\Psi^{t+\Delta t} - \Psi^t) \\ = \Delta t \mathbf{K}_{TT}^{t+\Delta t} T^{t+\Delta t} + \Delta t \mathbf{K}_{T\Psi}^{t+\Delta t} \Psi^{t+\Delta t} \\ + \Delta t (\mathbf{G}_T^{t+\Delta t} + \mathbf{B}_T^{t+\Delta t}) \end{aligned} \quad (4.64)$$

The Newton-Raphson method was chosen to solve this matrix system as it is relatively stable and robust compared to other method such Picard method for example. The details of the method are given in Appendix D. The final matrix system equation to solve – either for the soil or the concrete domain - is given by

$$\begin{aligned} [\mathbf{C}^{t+\Delta t, m} - \Delta t \mathbf{K}^{t+\Delta t, m} \\ - \Delta t (\partial \mathbf{K}^{t+\Delta t, m} + \partial \mathbf{G}^{t+\Delta t, m} + \partial \mathbf{B}^{t+\Delta t, m})] \Delta U^{t+\Delta t, m+1} \\ = \Delta t (\mathbf{K}^{t+\Delta t, m} U^{t+\Delta t, m} + \mathbf{G}^{t+\Delta t, m} + \mathbf{B}^{t+\Delta t, m}) \end{aligned} \quad (4.65)$$

As one can note, only one equation allows the representation of both the heat fluxes and the moisture flows. Indeed, instead of solving two systems of equations, one for the heat conservation and one for the moisture conservation, it has been decided to gathered in one matrix system – the size of which is double – alternating one row for the heat equation of one mesh and one row for the moisture equation which allow a better balance of the matrixes. For example, the ground state vector that gathers temperature and matric head is written

$$U^g = \begin{pmatrix} \vdots \\ T_i^g \\ \Psi_i \\ T_{i+1}^g \\ \Psi_{i+1} \\ \vdots \end{pmatrix} \quad (4.66)$$

where i is the mesh number.

Such temporal discretization scheme is not mass conservative. As first introduced in Celia and Bouloutas (1990) and then used by Janssen et al. (2007) and Miller et al. (1998), a mass-conserving procedure has been proposed to solve this issue. It consists in adding in the balance equation (4.67) the variation of a corrective term S between two consecutive time steps.

$$\begin{aligned} & [\mathbf{C}^{t+\Delta t, m} - \Delta t \mathbf{K}^{t+\Delta t, m} \\ & - \Delta t (\partial \mathbf{K}^{t+\Delta t, m} + \partial \mathbf{G}^{t+\Delta t, m} + \partial \mathbf{B}^{t+\Delta t, m})] \Delta U^{t+\Delta t, m+1} \\ & = \Delta t (\mathbf{K}^{t+\Delta t, m} U^{t+\Delta t, m} + \mathbf{G}^{t+\Delta t, m} + \mathbf{B}^{t+\Delta t, m}) \\ & - (S^{t+\Delta t} - S^t) \end{aligned} \quad (4.67)$$

where the corrective term is given by for the foundation equation and for the soil equation.

$$\begin{aligned} S_T^g &= C(T^g - T_0) \delta V \\ S_\Psi^g &= \theta \delta V \end{aligned} \quad (4.68)$$

$$\begin{aligned} S_T^f &= c_{TT}^f T^f \delta V \\ S_{P_c}^f &= \delta V w \end{aligned} \quad (4.69)$$

4.6.2 ALGORITHM PROCEDURE, MESHING AND TIME STEP DEFINITION

4.6.2.1. Algorithm procedure - a variable time step method

The algorithm for the resolution of the equation (4.67) for both the soil and the foundation domain is described on Figure 37. This procedure has been widely inspired from the work of Janssen (2002). The resolution is governed by a global time step Δt , and two independent time steps: one for the soil model Δt^g and one for the foundation model Δt^f .

For a given time t , the ground model is first solved, using all the equations and the numerical method described from section 4.2 to sub-section 4.6.1.2. The equation (4.67) yields the state of the ground at the current time t and the next iteration $m + 1$. If the convergence condition given by equation (4.70) is true, then the calculation starts for the next time $t + \Delta t^g$.

$$\begin{aligned} & COND^g \\ & = \frac{\max |[\mathbf{C}^{t, m} - \Delta t^g \mathbf{K}^{t, m}] U^{g, t, m+1} - [\Delta t^g (\mathbf{G}^{t, m} + \mathbf{B}^{t, m}) + \mathbf{C}^{t, m} U^{g, t-\Delta t, m} - (S^t - S^{t-\Delta t})]}{\max |\Delta t^g (\mathbf{G}^{t, m} + \mathbf{B}^{t, m}) + \mathbf{C}^{t, m} U^{g, t-\Delta t, m} - (S^t - S^{t-\Delta t})|} \quad (4.70) \\ & < 10^{-6} \end{aligned}$$

At that stage, a variable time step procedure has been adopted. The value of the next time step Δt^g depends on the convergence speed of the previous time t , measured by the number

of iteration required to satisfy the convergence condition. If the iteration number is low, then the time step can be increased. On the contrary if it is high, the risk of divergence for the next time increases and the time step has to be decreased. This is mathematically reflected in the equations (4.71). As one can notice, the time step increasing is limited by a factor 2 since a too high time step would automatically lead to divergence. Furthermore, its value is limited in such a way it does not exceed the global time step: the two models merge at every Δt .

$$\begin{aligned}\Delta t^g &= \Delta t^g \cdot \min\left(\frac{m}{30}, 2\right) \\ \Delta t^g &= \min(\Delta t^g, (t + \Delta t) - (t^g + \Delta t^g))\end{aligned}\tag{4.71}$$

In the cases where:

The temperature is out of the interval [243,343] K,

The matric head exceed 2 cm,

The iteration m exceed the maximum allowed value of 30,

the time step is halved and the calculation start again from the time $t^g - \frac{\Delta t^g}{2}$. This is often the case when the outdoor conditions vary sharply, especially during rainfall or in summer when the soil surface is wet and the evaporation rate is high.

Unfortunately, as noted by Janssen (2002) there still remains times for which the convergence is impossible. The identification of such cases is done according to the values of the time steps (of the soil and the foundation) and their mean values over the 30 last computations. If their value is under 10^{-4} s or if the average of latest 30 values is under 60 s, it is considered as a sign of divergence. For such cases, the current time t^g is skipped, and the calculation starts again from $t + \Delta t$.

The procedure above is repeated until the ground solution is computed for the time t . The state of the soil at the time t enables the calculation of the foundation loads, and thus the computation of the foundation solution at the time t , also according to the procedure described above. The calculation of the state of the foundation is then repeated to reach the time $t + \Delta t$, while the soil state is assumed unchanged. This solution in turn enables the calculation of the soil conditions and consequently the resolution of the soil model at the time $t + \Delta t$. The soil state at time $t + 2\Delta t$ is once again computed while the state of the foundation remains unchanged. This is repeated until the final time of the simulation.

4.6.2.2. Verification tests

Given the complexity of the coupled system of equations and their numerical resolution, it is common to do some verification on reference cases (Deru, 2003; Janssen, 2002). This is realized in order to evaluate the correctness of the computation compared to analytical solutions for several simple cases or against others numerical results. Two one-dimensional configurations have been used here to cover the main difficulties of such coupled heat and moisture transfer model.

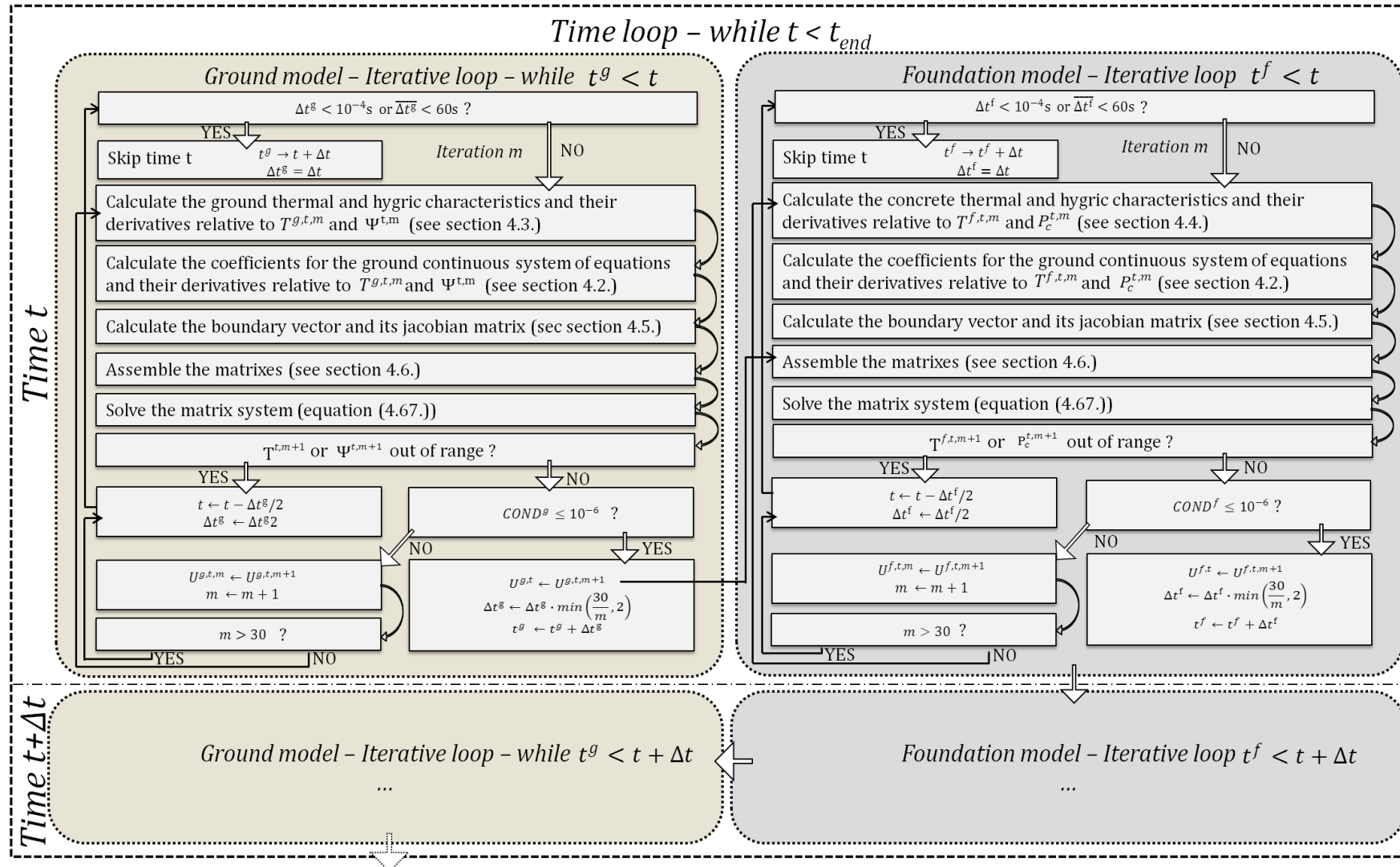
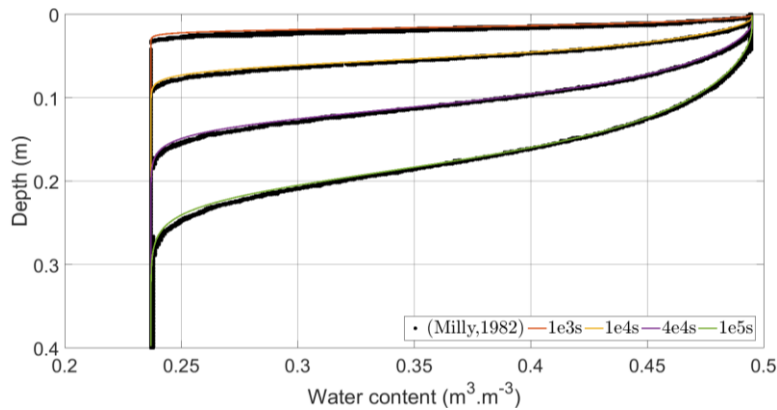


Figure 37: Algorithm of the 3D finite volume model for the resolution of the coupled heat and moisture equations within the soil and the concrete foundation

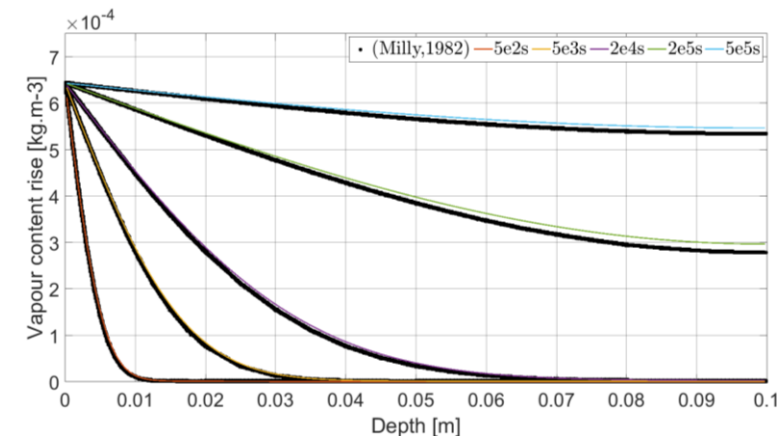
The first one has been introduced by Milly (1982) is a try to evaluate the ability of the code to reproduce an isothermal liquid transfer within a soil column. A 40 cm depth Yolo light clay column is firstly assumed to be dry ($\Psi = -6 \text{ m}$). Then it is subject to a sudden change in the matric head at the top - assumed at saturation ($\Psi = 0 \text{ m}$) while the other end is subject to a matric head unchanged of -6 m . Neglecting the heat and moisture transfer, only one equation is required to describe the water flow. Equation (4.1) is thus reduced to

$$c_{\Psi\Psi}^g \frac{\partial \Psi^g}{\partial t} = \nabla \cdot (k_{\Psi\Psi}^g \vec{\nabla} \Psi^g + \vec{g}_{\Psi}) \tag{4.72}$$

with $c_{\Psi\Psi}^g = \frac{\partial \theta}{\partial \Psi}$, $k_{\Psi\Psi}^g = K_h$ and $\vec{g}_{\Psi} = K_h \vec{u}_z$. The expression for the water retention curve and the hydraulic conductivity can be found in (Milly, 1982). The numerical procedure described above is applied to solve this problem. The solution has been plotted over the figure in (Milly, 1982) representing both the analytical and the numerical solution - calculated via finite element method. The comparison presented on Figure 38 (a) shows a good agreement.



(a)



(b)

Figure 38: Validation of the numerical code over test exercises: (a) infiltration - results from (Milly, 1982) (b) heat and vapour transfer - results from (Janssen, 2002)

The second case deals with the vapour transfer within a 10 cm high dry soil column. This study was first introduced by Milly (1982) and re-used by Janssen (2002) with other soil thermo-hygric parameters. Indeed, the characteristics of loam in Table 24 were used for the calculation of the water retention curve. At $t = 0$ s, the matric head at soil surface is changed from $-2 \cdot 10^4$ to $-1.8 \cdot 10^4$ which induces an increase of the water vapour density, thus a vapour flow toward the bottom of the column, then condensation against the pore walls and temperature rising. The results superimposed to the calculation of Janssen (2002) show good agreement with both finite element numerical results and analytical results, as can be observed on Figure 38 (b).

4.6.2.3. 3D finite volume meshing definition

The objective of this part is to identify the best meshing for the foundation and the beam above, i.e. the best trade-off between accuracy and computational time. The foundation is 60cm width by 1m high with a 35 cm width by 45 cm high cavity. The beam is 20 cm width by 1.2 m high. In order to raise the number of meshes that can be tested, and since the heat and mass transfer are mainly two-dimensional, the simulation will be led with two-dimensional grid first. Then, the third axis will be added to the 2D optimal grid, and the study of the full 3D grid will focus on this axis only.

The criterion for the accuracy of a grid is defined as the root mean square error between the outlet air temperature yield by the model using this grid, and the outlet air temperature of the same model using a reference grid. The reference is built with 2493 nodes, which the maximum size is 2cm x 2cm. Several meshing have been modelled and compared to this reference. The simulation is run over ten days in August with a ten minutes time-step.

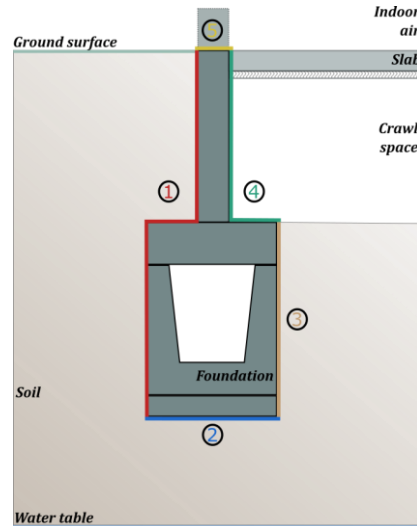


Figure 39: Domain studied and its limits

As this study is only led on the foundation model, attention has to be paid to the boundary conditions. Indeed, the grid has to be optimized as if it was embedded in ground. The boundaries thus have to correctly represent the real conditions. Five kinds of boundary of the studied domain are distinguished and seem to be relevant to takes into account the full complexity of the problem (Figure 39):

1. The first condition is the limit between the foundation and the beam left walls, in contact with ground exposed to outdoor. A Dirichlet condition is applied on this edge, and the temperature is supposed to be equal to $T(z, t)$ calculated according to the equation (2.1) where z is the depth from the ground surface,
2. The second limit is the foundation base, in contact with the sub-ground. For the sake of continuity, it is supposed to evolve linearly between the left and the right base corner of the foundation,
3. The third boundary is the right edge of the foundation, in contact with the ground below the building. As the ground below the building is supposed to be cooler than the ground directly exposed to the weather, and its amplitude lower, the temperature imposed over this limit is $T(z_b, t)$ calculated according to the equation (2.1) where z_b the depth of the base of the foundation,
4. The fourth boundary is the limit between the beam and the crawl-space air. The slab presence is ignored. As previously, a Dirichlet condition is considered here, and the temperature is equal to $T_{crawl-space}(t) = (1 - \beta)T(z_{crawl-space}, t) + \beta T_{air}$ i.e. a weighted average between the crawl-space ground surface and the ambient air, with $\beta = 0.3$,
5. The fifth and last boundary is the top of the beam exposed on the left side to the outdoor air and on the right side to the building. The temperature impose on this surface is a linear evolution between this two extreme. It assumes that the temperature on the right side is equal to the air temperature of the crawl space, which still neglects the presence of the slab, and the presence of insulation of all kind.

Nine grids are successively used for the simulation. They are all compared to the reference grid called '47x123' for '47 meshes along the x axis and 123 meshes along the z axis'. The outlet air temperature and relative humidity difference with the reference are plotted on the Figure 40 (a) and (b) respectively.

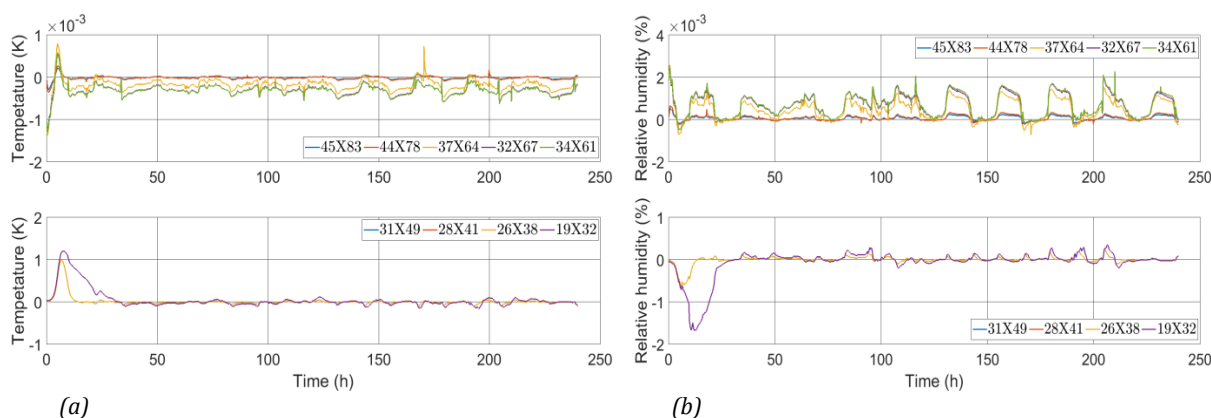


Figure 40: Comparison of the outlet temperature (a) and relative humidity (b) to the 2D reference case

The coarser mesh sizes lead to unacceptably large errors, but the first five grids seem to be relevant. A more careful analysis is provided on the Figure 41. It sums up the accuracy by using the root mean square error. It although takes into account a crucial factor: the simulation time. It clearly shows that some grids are not relevant, as the accuracy does not improve when the computational time keep rising. The grid '34x61' corresponding to 1270 nodes is the best one according to this analysis and taking into account all the assumptions

made. Indeed it provides results in 300 s for the exercise considered, and the difference between the outlet air temperatures and relative humidity with the reference model is lower than $10^{-3} K$ and $10^{-3} \%$.

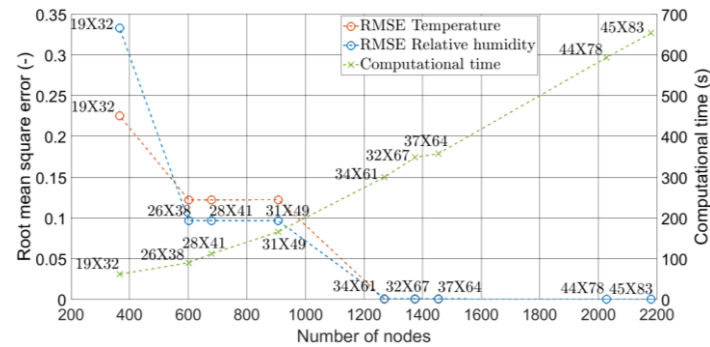


Figure 41: Trade-off simulation time / Accuracy as a function of the number of nodes for a 2D simulation

The impact of spatial discretization along the y axis is then studied. Figure 42 shows the trade-off between the RMSE and the computational time resulting from the meshings, while Figure 43 details the differences between the outlet air state with the reference case. First, simulations with uniform meshings with 4, then 5, 8, 10, 15 and 20 meshes along the y axis - which correspond respectively to 5080, 6350, 10160, 12700 and 19050 meshes - are carried out. The simulation is this time restrained to one day, and the reference case is the grid with 19050 meshes. Even for the coarser grid, the results are not so different from the reference case. The difference between the finest grid and the grid $34 \times 15 \times 61$ is around $10^{-3} K$. It confirms the fact that the heat and moisture transfer are mainly two-dimensional. It also shows that the use of more than 15 meshes along the y axis is unnecessary. The grid $34 \times 10 \times 61$ and $34 \times 8 \times 61$ give differences lower than $10^{-2} K$ and allow a considerable reduction of the simulation time.

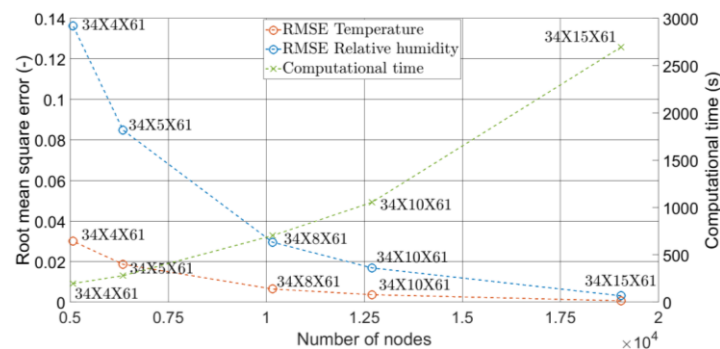


Figure 42: Trade-off simulation time / Accuracy as a function of the number of nodes for a 3D simulation

As illustrated on Figure 44 (a) and (d), the maximal temperature gradient along the y axis is $1.4 K$, and the maximal water content gradient is $11 kg.m^{-3}$ close to the cavity edges. This is quite low and suggests that a grid with high number of meshes along the y axis is unnecessary. As can be seen on Figure 44 (b) and (c), the strongest thermal and moisture gradient are at the foundation entrance but range in moderate values. Consequently, refine the grid at the entrance also appears as unnecessary. A uniform meshing with 5 meshes along the y axis is thus justified. The final foundation mesh $34 \times 5 \times 61$ will be used for further considerations.

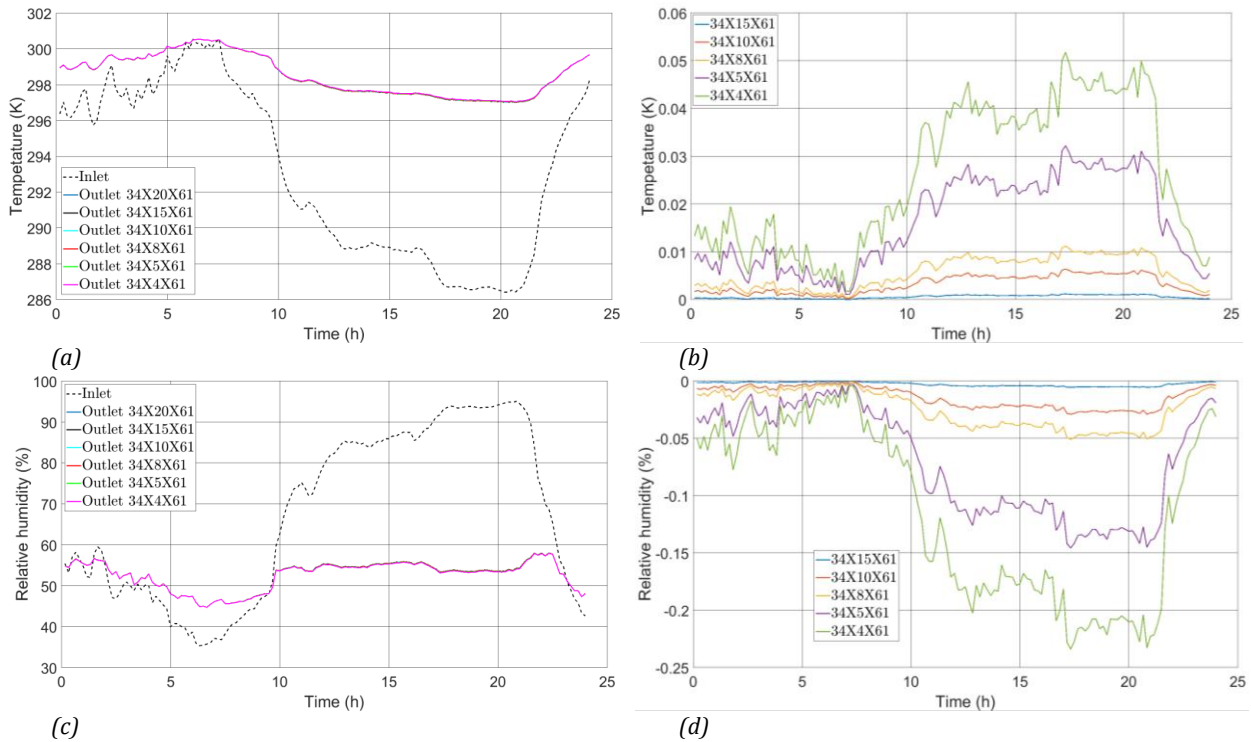


Figure 43: Comparison of the circulating air outlet temperature (a) and (b) and relative humidity (c) and (d) to the 3D reference case

The upper and the central part of the ground meshing stem from the foundation meshing. As illustrated on Figure 45, the remaining part of the ground meshing has been set in harmony with it, progressively rising the size of the meshes toward the subground and far from the foundation outer edges.

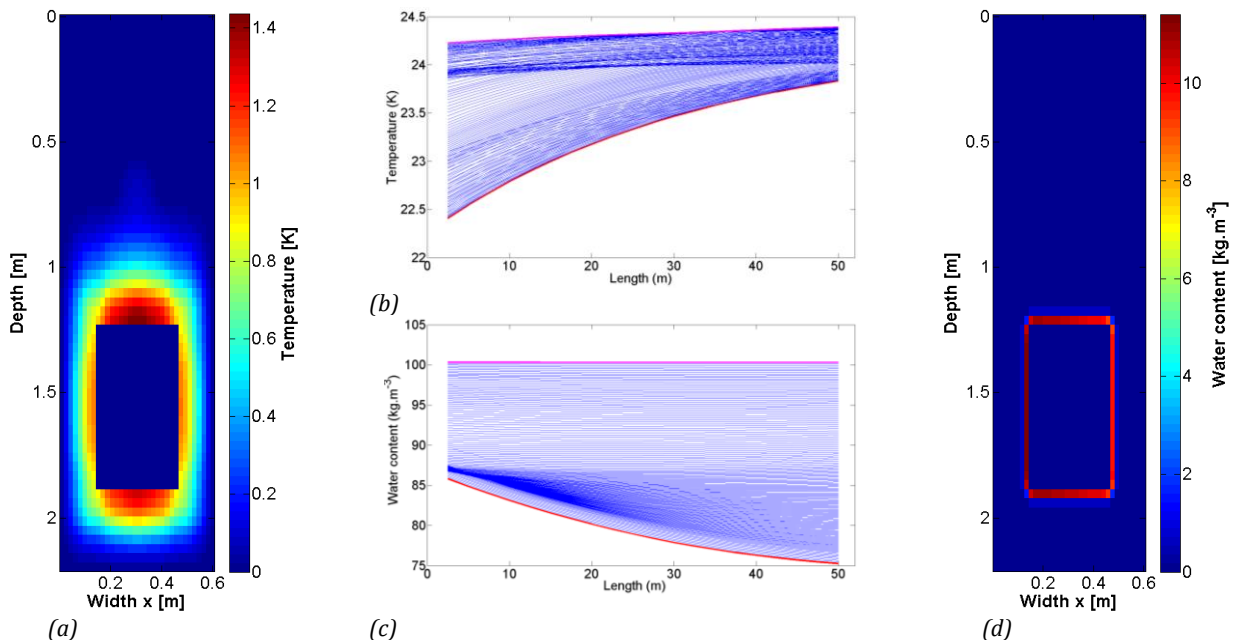


Figure 44: Maximum temperature (a) and water content (d) gradient along the y axis - Temperature (b) and water content (c) evolution through the concrete foundation for the finest grid 34X20X61

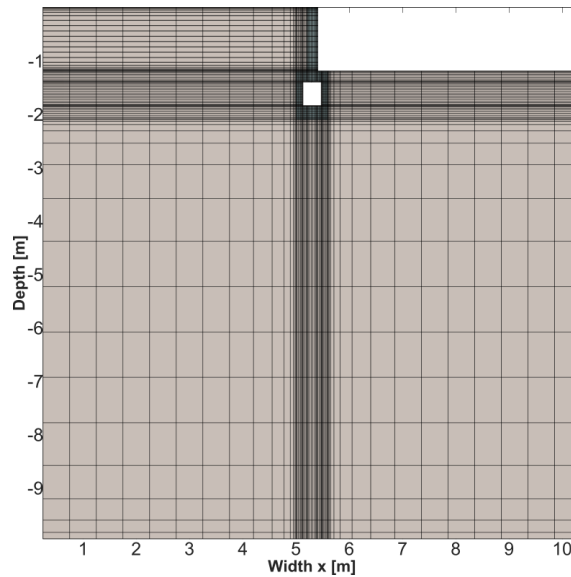


Figure 45: Global meshing a cross-section of the system {soil+foundation}

4.6.3 IMPLEMENTATION OF BOUNDARY CONDITIONS

4.6.3.1. Ground top surface

Sometimes the formulation (4.26) - (4.32) of the ground top surface boundary conditions cannot be applied, more specifically the moisture transfer due to evaporation ((4.29) and (4.31)). Indeed they result in convergence problems that are linked to specific weather conditions. Some of them have been identified like for example:

- A heavy rainfall on a dry soil,
- A sunny and hot weather after a rainy period.

The following numerical methods have been implemented to get around these problems. It was inspired by that proposed by van Dam and Feddes (2000) who studied the modelling of a moisture flow into a soil. He proposed to split the problem into simpler cases that can be easily solved from a numerical point of view. More precisely, the method consists in changing the previous general flow -based formulation (Figure 46 (a)) into a potential/Dirichlet-based formulation (Figure 46 (b)).

The first case identified is when the ground top surface meshes are saturated, in the middle of just after a rain period. Two sub-cases are possible:

- 1.a. A flow is entering the meshes. It most of the time correspond to a period of heavy rainfall, when the soil is not able to drain enough water. Consequently, water is stored at the ground top surface: this will be called 'stacking' in what follows.
- 1.b. A flow is going out of the meshes. Most of the time, this situation appears at the end of a rainfall.

By opposition, the second case corresponds to unsaturated ground top surface meshes. Three sub-cases have been distinguished:

- 2.a. A moisture flow is entering the meshes, and the air volumes in the pores are not large enough to contain it. This will lead again to water stacking at the ground top surface.
- 2.b. A moisture flow is entering the meshes, but the air volumes in the pores are large enough to contain it. This generally occurs just after a rain period.
- 2.c. A moisture flow is going out of the meshes. From a numerical point of view, this sometimes induces an important evaporative flow that cannot be supplied by the ground. Indeed the hydraulic and vapour transfer coefficient are too low.

All of these specific cases are treated by the same manner. As previously explained, a matric-head controlled is set instead of a flux-controlled boundary flow. This involves defining and calculating a set of new variables at ground top surface (Ψ_{surf} and T_{surf}) and a set of new liquid and vapour transfer coefficients ($K_{h,surf}$ and $D_{\Psi v,surf}$). The new values for the moisture flow added in the system of equations, and the values of the liquid and vapour transfer coefficients are listed in Table 16.

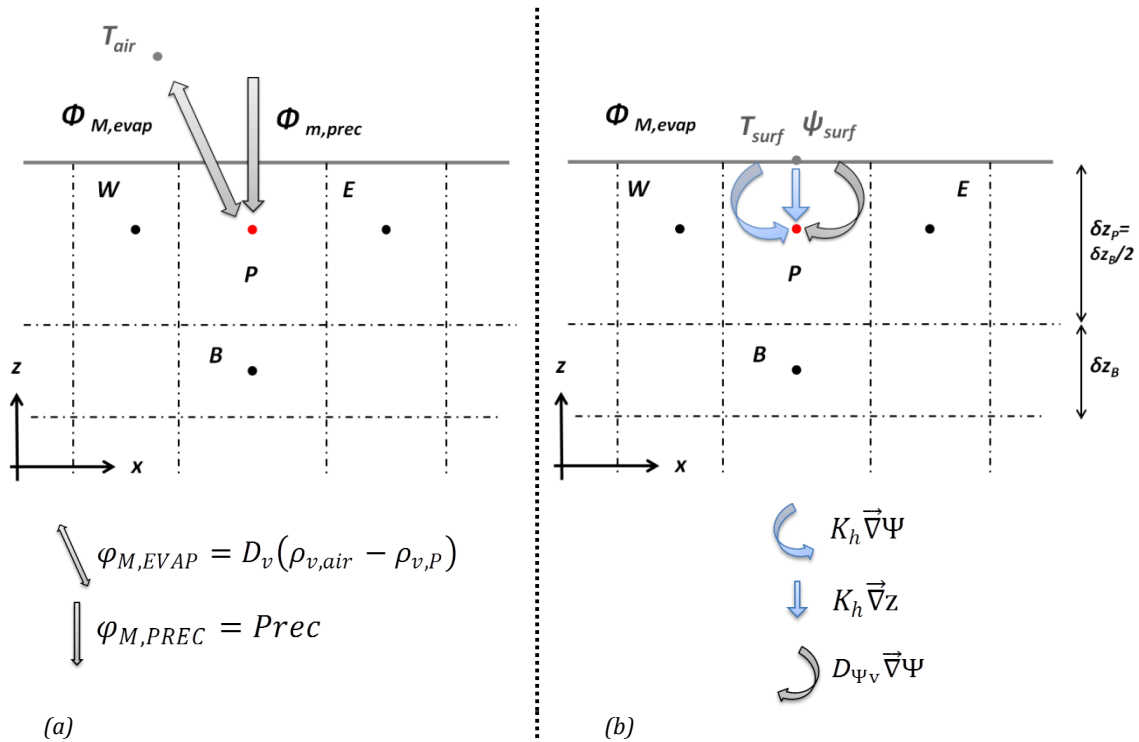


Figure 46: Description of the moisture flow in the flux-controlled (a) and the matric-head controlled case (b)

For the cases where the moisture inflow exceeds the ground capacity:

$$\Psi_{surf} = \Psi_{pond} \tag{4.73}$$

$$\Psi_{pond} = \min\left(\frac{INFLOW}{\delta S_p}, 0.01\right) \tag{4.74}$$

$$INFLOW = \begin{cases} \Delta t \cdot \phi_m & \text{for case 1.a} \\ \Delta t \cdot \phi_m - \delta V_{P, free} & \text{for case 2.a} \end{cases}$$

The formula that gives the quantity of pounded water at the ground top surface express that for quantities over 1cm, the rain is supposed to be evacuated. For the outflow cases, the driving potential is assumed to be the atmosphere humidity. For that purpose, a matric head is artificially associated to the outdoor air, thanks to the Kelvin's law:

$$\Psi_a^{ext} = \frac{R_v T_a^{ext}}{g} \ln(\varphi_a^{ext}) \quad (4.75)$$

More specifically, the case 2.a. occurs at the beginning of a rainy period, followed by the case 1.a. Most of the time when the rain stop, pound water is still left at the ground top surface. As the soil has begun to drain the excess, such situation generally corresponds to cases 2.b. Then and finally, sun and wind dry the surface, but the quantity involved - due to the high moisture content of the ground top surface - prevent the convergence of the code. This is the need for the case 2.c.

Table 16: Matric head-controlled boundary conditions at ground top surface: moisture equations and transfer coefficients

| | Ψ_{surf} | $K_{h,surf}$ | $D_{\psi_v,surf}$ | τ | Moisture flow ϕ_m |
|------|----------------------------|---|---|-------------------|---|
| 1.a. | Ψ_{pond}^t | $K_h(\Psi_{sat})$ | 0 | - | $\phi_m = \delta S_p \left(K_{h,surf} + k_{\psi\psi,surf} \left(\frac{2}{dz} \right) (\Psi_{pond}^t - \Psi_p) \right)$ |
| 1.b. | $\Psi_a^{ext,t}$ | | | $5 \cdot 10^{-9}$ | $\phi_m = \delta S_p \left(K_{h,surf} + k_{\psi\psi,surf} \left(\frac{2}{dz} \right) (\Psi_a^{ext,t} - \Psi_p) + \frac{\Psi_{pond}^{t-\Delta t}}{\Delta t} \right)$ |
| 2.a. | Ψ_{pond}^t | $\tau K_h(\Psi_p) + (1 - \tau) K_h(\Psi_a^{ext,t})$ | $\tau D_{\psi_v}(\Psi_p) + (1 - \tau) D_{\psi_v}(\Psi_a^{ext,t})$ | $5 \cdot 10^{-3}$ | $\phi_m = \delta S_p \left(K_{h,surf} + k_{\psi\psi,surf} \left(\frac{2}{dz} \right) (\Psi_{pond}^t - \Psi_p) \right)$ |
| 2.b. | $\Psi_{pond}^{t-\Delta t}$ | | | $5 \cdot 10^{-3}$ | $\phi_m = \delta S_p \left(K_{h,surf} + k_{\psi\psi,surf} \left(\frac{2}{dz} \right) (\Psi_{pond}^{t-\Delta t} - \Psi_p) \right)$ |
| 2.c. | $\Psi_a^{ext,t}$ | | | $5 \cdot 10^{-9}$ | $\phi_m = \delta S_p \left(K_{h,surf} + k_{\psi\psi,surf} \left(\frac{2}{dz} \right) (\Psi_a^{ext,t} - \Psi_p) \right)$ |

This procedure modifies the original moisture boundary condition formulation, and rigorously the heat equation should be adjusted accordingly. But the difference between the original heat equation and the adjusted one is assumed to be negligible. It has a low impact over the temperature and water contents fields close to the foundation.

Close to the ground top surface, where the conditions are fast and of large amplitude:

- the variation of the vapour density, the water content, the liquid and vapour transfer coefficients are strong - of several orders of magnitude over a few millimetres;
- the local thermal equilibrium - reflected in the Lewis' law - is not valid anymore.

The need for the boundary equations change described in the previous section actually results from these physical aspects of the problem. The physical properties modelling at the ground top surface cannot consider the whole complexity of the physics. It generates numerical difficulties and of course a bad estimation of the real moisture and heat flow through the ground top surface. The method previously detailed has been developed to enable (in almost all cases encountered) the convergence of the code and of course to stay as far as possible consistent with physical laws.

4.6.3.2. Foundation inner surface

Zhang and Haghghat (2005, 2009) studied an EAHE with a large rectangular cross-sectional area, similar to the Fondatherm duct. Compared to conventional EAHE, this system is said to have a lower airflow resistance and is more energy efficient than conventional small ones. They noticed that most of the studies about EAHE focused on the heat conduction within the ground, while the evolution of the air temperature along the channel is calculated using various correlations (exposed in Table 9) with large discrepancies between each other. A lack of accuracy regarding the heat convection at the duct / air surface is thus pointed out and they proposed to use a CFD model to improve on that issue.

Once validated against results from the literature, the CFD model enables the authors to calculate the heat flow between the flowing air and the walls. The local area-weighted Nusselt number is thus deduced from (4.76).

$$\mathcal{N}u_{cav} = \frac{D_{h,cav}}{\lambda_a^{cav}} \frac{\phi_h^{f,cav}}{T_a^f - T_{cav}^f} \quad (4.76)$$

Because of entrance effects, the complexity and the non uniformity of the boundary conditions on each end of the foundation, the heat transfer are anisotropic, therefore delicate to evaluate. Accordingly, the usual correlations to calculate the convective heat transfer coefficient for large cross sectional areas are not adapted.

The evolution of the Nusselt numbers along the duct is very important. Strong differences are also observed between the orientations of the different walls. The Nusselt is higher for the floor than for the ceiling. A strong decreasing is observable along the cavity length. A strong variation also exists between heating and cooling modes.

The equations (4.54) and (4.55) have thus been adapted to take into account the previous observations. From the evolution of the Nusselt number along the rectangular duct and for the four walls given by the results of the work of Zhang and Haghghat, multiplicative corrective factors have been applied to the heat transfer coefficient. Their values are listed in Table 17 for a given wall (upper, lower or vertical) and a given meshes along the airflow direction.

Table 17: Multiplicative corrective factor for the convective heat transfer coefficient of the foundation cavity

| | Segment (along the airflow dir.) | 1 st | 2 nd | 3 rd | 4 th | 5 th |
|------------------------------|----------------------------------|-----------------|-----------------|-----------------|-----------------|-----------------|
| Foundation inner wall | X | 1.3 | 1.2 | 1.2 | 1.1 | 1 |
| <i>Upper</i> | 1.3 | 1.69 | 1.56 | 1.56 | 1.43 | 1.3 |
| <i>Verticals</i> | 1.2 | 1.56 | 1.44 | 1.44 | 1.32 | 1.2 |
| <i>Lower</i> | 1.1 | 1.43 | 1.32 | 1.32 | 1.21 | 1.1 |

4.7. CONCLUSIONS

The set of conservation equations that describes the heat and moisture transfer within soil and concrete have been introduced in the previous chapter. Some terms have been proved to be negligible in section 4.2.

The thermo-hygric characteristics of both media have been exposed in the two next sections. Seven soils have been identified and assumed representative for most of the common grounds encountered. For each of these soils, a compilation of experimental data enables to link its thermal and hygric properties with the textural properties.

Finally, a limited set of parameters was built for representing seven soils. About the foundation, the parameters are not specifically known for the concrete used, but this material is quite common and a lot of studies characterized it. A set of thermo-hygric parameters has been built thanks to data available in the literature.

A mathematical formulation of the complex boundary conditions of the problem has also been proposed for:

- The boundaries at ground top surface,
- The coupling between the ground and the concrete foundation,
- The heat and moisture transfer between the foundation and the flowing air,
- The coupling with the crawl space.

A direct implementation of the boundaries at ground top surface sometimes leads to divergence problems and unphysical situations. A solution has been proposed to solve those issues, consisting in dividing the moisture evaporation / infiltration into several cases and switching from the initial flow formulation of the equation to a potential formulation.

The resolution of the problem is made through a finite volume method for the spatial discretization of the non linear conservation equations, and a Newton-Raphson method for the temporal discretization. The choice of the three-dimensional meshing has been justified according to accuracy and computational time criteria. Finally, the validity of the whole numerical model will be evaluated thanks to the collected experimental data over several months in Chapter 7.

Chapter 5. OBJECTIVES AND DEVELOPMENT OF THE SENSIBLE HEAT TRANSFER MODEL

5.1. OBJECTIVES

The general objective of the previous detailed model is to understand through a dynamic approach the functioning of the ventilated foundation, the nature and the role of the processes involved and their relative importance in relation to the phenomenon studied.

The objective of the model presented in this chapter is quite different and complements the previous approach. Indeed, the aim of this second model is to create a design tool that yields the evolution with time of air temperature and relative humidity along the foundation. This model will also complement both the detailed and experimental approach. The comparison of both the sensible and the coupled models to the experimental results will allow identifying the degree of relevance of the adopted hypotheses as well as the limits of use of each model.

Several constraints motivate the development of a specific model. Contrary to the model introduced in the previous chapter, for which the objectives were only related to science (accurately represent the physical phenomenon), a design brief here sets out the objectives. The main aspects of the requirement specifications are described and explained in the seven subsections below.

5.1.1 GEOMETRY

The present model has to be able to give to the user the possibility to evaluate the impact of a change in the foundation geometry on the output of the model such as width, and height of the cavity, width and height of the outside walls of the foundation, etc. The literature review established in section 2.1 showed that these characteristics can strongly modify the heat transfer within the EAHE. From that conclusion, it appears that the explicit modelling of the foundation is a mandatory requirement. Regarding this, it clearly means that models based on transfer functions are not good candidates.

5.1.2 THERMAL CHARACTERISTIC

The model should enable the assessment of the impact of the properties of the ground and the concrete on the foundation performance. Therefore, the ground and the foundation thermal characteristics such as thermal conductivity, density and specific heat should be taken into account.

5.1.3 GROUND STRATIFICATION

In real cases, the ground is rarely a homogeneous and continuous medium, but more a stacking of different layers. A change in the thermal characteristic with depth implies a modification of propagation of heat within the ground. The penetration depth, the thermal wave dampening and phase shifting are affected. The stacking of ground layers is a discontinuous variation of the thermal characteristic of ground with depth, but it's also possible to find cases where the variation occurs along the two other axes, with the same consequences. It therefore appears as important to first, be able to use several materials, and secondly to be able to place them in different locations to model ground heterogeneities.

5.1.4 AIR FLOW

As explained in section 2.1, the air speed within the pipes of an EAHE affects the heat transfer between the air and the wall. This is usually taken into account via the convective heat transfer coefficient and the advection term. Furthermore, the air flow i.e. the air renewal is imposed by the health standard, depending on the building typology (commercial, residential, etc.). The air flow / air speed is therefore an important design parameter that has to be incorporated in the model.

5.1.5 CLIMATE

The EAHE behaviour has been proved to strongly depend on climate conditions. In a designing process, the heat that is possible to recover from the ground and to release to the ground via the EAHE will change the building heating and cooling loads, and as a result the sizing of the heating and cooling systems. It seems therefore natural to take into consideration the climate while implementing the model.

5.1.6 BUILDING BASEMENT CONFIGURATION

Hollmuller and Lachal (2014) highlighted the fact that in the case of an EAHE placed below the building, some part of the heat loss by the building via the slab is recovered by the heat exchanger. Even if the efficiency of such process has however been proved to be low - the global balance for the building is negative - the building influence is of course an important factor of the EAHE thermal behaviour. The constructional type of the building basement - slab-on-ground or cellar, with or without insulation beneath the slab and over the foundation - has to be considered in the intended model. Throughout this work, the most complicated configuration - with cellar - will be modelled only, but the model could be easily adapted to the slab-on-ground case.

5.1.7 SIMULATION TIME AND ACCURACY

A design tool allowing dimensioning a foundation element and coupled HVAC systems can be useful only if it is fast enough to give the user the possibility to carry out a parametric study. However the computation speed cannot represent the main objective at the detriment of accurate results. A trade-off between these two criteria has to be found. Model reduction techniques, formerly developed in the field of automation and control, can enable to reach a

good compromise. In this regard, the model will be compared on experimental results as described in Chapter 7.

5.2. STATE MODEL DEVELOPMENT AND REDUCTION

5.2.1 STATE MODEL FOR CONDUCTION WITHIN THE SOLIDS

In this section the operation of the sensible heat transfer model, developed to fill the requirements previously exposed, is detailed. The conservation equation to describe the conductive heat transfers within a material with thermal conductivity λ , specific heat C , density ρ and a source term S is then resolved

$$\rho c \frac{\partial T}{\partial t} = \nabla \cdot (\lambda \vec{\nabla} T) + S \quad (5.1)$$

As highlighted in the literature survey in sections 2.1 and 2.2, the heat transfers within the vicinity ground of an EAHE is mainly two-dimensional in a section perpendicular to the direction of the airflow. Most of the time, the heat transfers along the third dimension is neglected, the modelling is restrain to a two-dimensional study. Indeed in most cases, the conditions and the soil properties vary two-dimensionally, and the temperature gradient along the EAHE pipes are low. However, as explained in the previous section, the ground nature can vary along the three axes, so as the geometry of the building basement. Furthermore, considering the features of Fondatherm, the effect of the flowing air on the ground could lead to higher thermal gradient along this third axes. It is therefore reasonable to first consider a three-dimensional model.

Except for one- and two-dimensional with simple geometry and boundary condition, it's not possible to find an analytical solution of (5.1). As previously, a finite volume method has been chosen to spatially discretize the studied domain, as it has been recognized as robust and easy to implement. Assuming that the source term is null, and that some of the meshes at the boundaries of the domain are exposed to a thermal flow from the outside, the integration of (5.1) leads to (5.2), where the index E, W, N, S, T, B designate the east, west, north, south top and bottom meshes adjacent to the mesh P . K_O is the semi-conductance for the meshes in contact with the outside, T_O the outside temperature V_P the mesh volume, $\delta x, \delta y$ and δz the meshes width, length and height, $K_P = K_E + \dots + K_B + K_O$. The evaluation of all the conductive coefficients K has been done according to Patankar (1980). The nodes are set in the middle of a mesh, and the values for the conductivities at the interfaces between two meshes are computed as a geometric mean of the values at the adjacent nodes. Finally, the conductances are of the form $K_E = \frac{2\lambda_P\lambda_E\delta y_P\delta z_P}{\lambda_E\delta x_P + \lambda_P\delta x_E}$ - and so on for the other indexes.

$$\rho_P c_P V_P \frac{\partial T_P}{\partial t} = K_E T_E + K_W T_W + K_N T_N + K_S T_S + K_T T_T + K_B T_B - K_P T_P + K_O T_O \quad (5.2)$$

Considering N nodes, the system of N equations can be written in a matrix form (5.3), where \mathbf{C} is a diagonal matrix (the capacitance matrix, with non zero elements), \mathbf{K} is square

tridiagonal by bloc (the conductance matrix), \mathbf{B} a N by l matrix and $T = \begin{pmatrix} T_1 \\ \vdots \\ T_N \end{pmatrix}$ and $U = \begin{pmatrix} T_{O1} \\ \vdots \\ T_{Ol} \end{pmatrix}$ are vectors where l is the number of meshes on the boundaries.

$$C\dot{T} = \mathbf{K}T + \mathbf{B}U \quad (5.3)$$

Diagonalizing $C^{-1}\mathbf{K}$ and writing $X = \mathbf{P}^{-1}T$ with \mathbf{P} the transfer matrix, the equation becomes

$$\dot{X} = \mathbf{W}X + \mathbf{Q}U \quad (5.4)$$

where $\mathbf{W} = \mathbf{P}^{-1}\mathbf{C}^{-1}\mathbf{K}\mathbf{P}$ is diagonal and $\mathbf{Q} = \mathbf{P}^{-1}\mathbf{C}^{-1}\mathbf{B}$. Assuming that U evolve linearly between two consecutive time step t and $t + \Delta t$, i.e. that for $t < \tau < t + \Delta t$ U^τ is given by $U^\tau = U^t + (\tau - t) \frac{U^{t+\Delta t} - U^t}{\Delta t}$, the equation has an analytical solution

$$X^{t+\Delta t} = \mathbf{E}X^t + \mathbf{F}_1U^t + \mathbf{F}_2U^{t+\Delta t} \quad (5.5)$$

where $\mathbf{E} = e^{\mathbf{W}\Delta t}$, $\mathbf{F}_1 = \left(\mathbf{I} - \mathbf{W}^{-1} \left(\frac{1}{\Delta t} \mathbf{I} + \mathbf{Q} \right) \right)$, $\mathbf{F}_2 = \mathbf{W}^{-1} \left(\frac{1}{\Delta t} \mathbf{I} + \mathbf{Q} \right)$ and $\mathbf{I} = \mathbf{W}^{-1}(\mathbf{E} - \mathbf{I})\mathbf{Q}$

The strength of the formulation (5.5) is that it explicitly yields the temperature field of the whole domain. For a constant time-step, the matrixes \mathbf{E} , \mathbf{F} , and \mathbf{G} are constant for the whole simulation. Usually, to analyse the evolution of a few value nodes' is sufficient to fulfil the objectives of the study. These are generally the temperature or the heat flow on the boundary nodes. Therefore, an observation equation can be defined to focus on these values.

$$Y = \mathbf{J}T + \mathbf{D}U \quad (5.6)$$

The Y vector, of dimension $(d, 1)$ is given by a linear operation of the concerned outputs T , the observation matrix \mathbf{J} (dimension (d, N)), the direct transmission matrix \mathbf{D} (dimension (d, l)) and the excitation vector U . The problem to solve is therefore given by the system (5.7) where $\mathbf{H} = \mathbf{J}\mathbf{P}$.

$$\begin{cases} \dot{X} = \mathbf{W}X + \mathbf{Q}U \\ Y = \mathbf{H}X + \mathbf{D}U \end{cases} \quad (5.7)$$

The thermal characteristics of the materials used for the simulations are given in Table 18.

Table 18: Thermal characteristics values for the sensible heat transfer model

| | Thermal conductivity ($W.m^{-1}.K^{-1}$) | Specific heat ($J.kg^{-1}.K^{-1}$) | Density ($kg.m^{-3}$) |
|----------|--|--------------------------------------|-------------------------|
| Soil | 1.97 | 800 | 1650 |
| Concrete | 2.9 | 880 | 1650 |

5.2.2 STATE REDUCED ORDER MODEL: BALANCED REALIZATION (MOORE) METHOD

Given the high number of nodes involved – three-dimensional modelling and large dimensions of the ground and foundation model – this model can be slow to solve with regard to the objectives of this model. It is nevertheless possible to reduce the order of the model without accuracy loss. A lot of methods to reduce linear models exist and have been successfully applied (Kim, 2011; Kim et al., 2014; Ménézo, 1999). One of the most efficient for building simulation studies appears to be the inner symmetrisation method, also called Moore method. The main idea is to change the basis of the state model (5.7) for an r order basis with $r \ll N$ and with $\|Y - \tilde{Y}\| \ll 1$ where \tilde{Y} is the observed variables yield by the reduced model.

This method is based on the concept of the controllability and the observability of the state variable. The controllability is the capacity of the state variables of the model to be influenced by the inputs with a change in the external excitations. The observability is the capacity of the state variables to contribute to the observed outputs evolution. The more the outputs Y_j are changed by a state variable, the more the state variable is said observable. The more the inputs U_i are impacting the state variable, the more the state variable is said controllable. This notion can be quantified by imposing a Dirac impulse or a Heaviside function for inertial stable systems on each input U_i ($i \in \llbracket 1, l \rrbracket$) and observe the effect on the state variables and then on the outputs Y_j for each $j \in \llbracket 1, d \rrbracket$. The strength (represented by level of energy) of the impacts of inputs on state variables are stored in a square matrix called grammian controllability $W_c \in \mathcal{M}_N(\mathbb{R})$. Through the same way, the observability is related to the effect of the state variables on the observed variables. As previously, it is possible to quantify this link by imposing a Heaviside impulse on each state variable X_i ($i \in \llbracket 1, N \rrbracket$) and observe the effect on the observed variables Y_j for each $j \in \llbracket 1, d \rrbracket$. The data (energy level of contribution to the output) are similarly stored in a matrix called grammian observability $W_o \in \mathcal{M}_N(\mathbb{R})$. The grammians are solutions of the Lyapunov system of equations.

$$\begin{cases} C^{-1}KW_c + W_c(C^{-1}K)^T = -BB^T \\ C^{-1}KW_o + W_o(C^{-1}K)^T = -H^T H \end{cases} \quad (5.8)$$

Expressed in the basis that transforms (5.3) into (5.4) the grammians are equal and diagonal. The objective is then to build a basis in which the variables are either controllable and observable or non controllable and non observable. Based on a criterion relative to the eigen values of the grammians, this last group of variables can be eliminated of the system (5.7), while passing on their contribution to steady state of the system. This technique induces a considerable reduction of state variable number and thus system equations. More details of the construction of this basis and of the grammians are given by Kim (2011) and Ménézo (1999). The final system of equation is given by (5.9) and solved similarly to the original system using the equation (5.5) in which E , F_1 and F_2 are calculated using the reduced matrixes W_r , Q_r and H_r .

$$\begin{cases} \dot{Z} = W_r Z + Q_r U \\ \tilde{Y} = H_r Z + D_r U \end{cases} \quad (5.9)$$

This method has been used in the frame of this study. The results in terms of accuracy – thanks to comparison with the experimental data as well as the full linear model – and in terms of computational time will be introduced in Chapter 7.

5.3. BOUNDARY CONDITIONS

Six boundary conditions have been modelled in the sensible heat transfer model and are successively presented in this section and illustrated on Figure 47:

1. The first one is the core of the problem: the interface between the circulating air within the foundation and the cavity walls,
2. The second is the part of the ground exposed to the atmosphere,
3. The third is the part of the ground or the beam exposed to the crawl-space air,
4. The fourth is the link between the beam and the slab,
5. The fifth is the ground base layer,
6. The sixth are the vertical walls and the beam top surface.

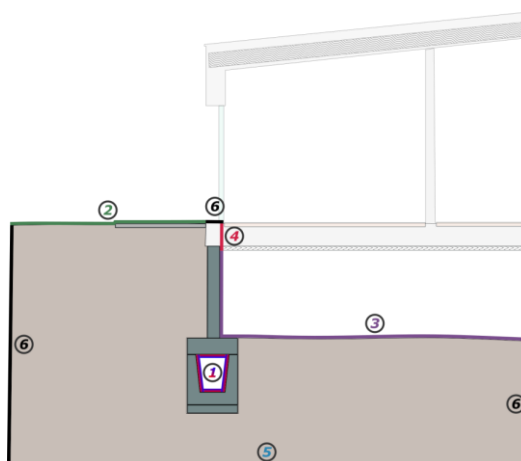


Figure 47: Boundary conditions for the crawl-space case

5.3.1.1. Circulating air / Cavity walls

The heat transfer model within the foundation have been adapted from Hollmuller (2002). In his work, the EAHE is divided into several sections. For each segment, the heat and moisture quantities exchanged between the pipe wall and the air flow are computed, and enable to determinate the temperature and the relative humidity of the next segment. Both mass and heat exchanged are computed thanks to a convective coefficient that depends on the air velocity. The air is considered as incompressible and the relation between the volumetric and the mass air flow is considered constant along the pipe. The last main aspect of his model is that liquid water can appear on the pipe wall, due to condensation. In this case, the water temperature is supposed to be equal to the pipe temperature. The long-wave radiation heat transfers are neglected.

Hollmuller (2002) worked on a traditional EAHE model. The channel is thus a pipe of which the radius range is between 6 cm and 13 cm. This enabled him to consider that the temperature of the pipe wall was homogeneous in a cross-section. This is not a priori the case anymore for the foundation. The cavity section, 35 cm x 45 cm and its position with multiple

interfaces make it impossible to assume that the temperature is homogeneous all around the cavity wall. The details of the air flow model are explained below.

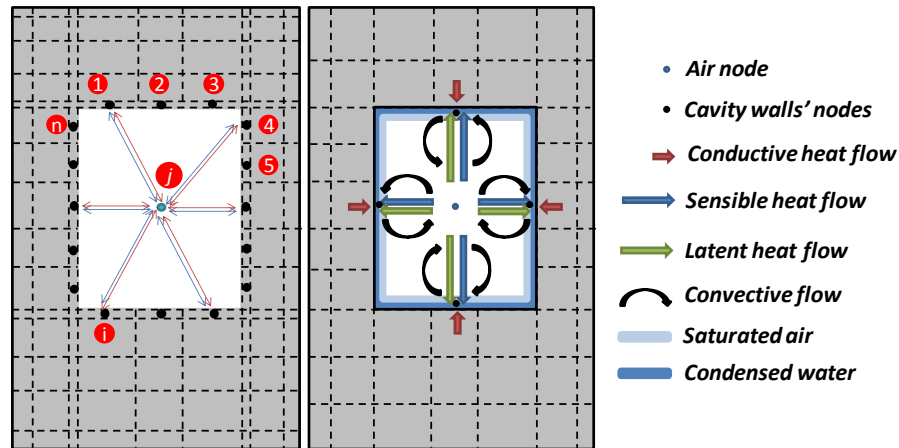


Figure 48: Cavity section: j^{th} air node exchanging heat and moisture with n cavity wall surfaces

The foundation cavity is divided into several sections. Each segment is characterised by one and only one node for both the air temperature and relative humidity. The air node exchanges heat and moisture with several cavity small surfaces at the same time. These surfaces result from the spatial discretization of the foundation. The volumetric airflow is assumed to be constant along the foundation which implies to neglect the pressure drop. This is quite reasonable according to the measurements that have been made and presented in section 6.2.1.

- The sensible heat transfer between one air node and one cavity wall mesh is given by (5.10) where j denotes the j^{th} foundation section, and i the i^{th} mesh of the cavity wall for this section. The Figure 48 gives a better understanding of this.

$$\phi_{h,sens}^{f,cav}(i,j) = h_c^{f,cav} (T_{a,j}^f - T_{cav}^f(i,j)) \quad (5.10)$$

$T_{scav}(i,j)$ is the temperature of the i^{th} mesh of the cavity wall for the j^{th} section. $T_{air}(j)$ is the j^{th} air node temperature.

- The previous sensible heat transfer is actually assumed to result from a mass transfer between the air flow and a thin air layer at the cavity wall. This layer is supposed to be saturated in humidity and its temperature equal to the wall temperature. According to the heat and mass transfer analogy this sensible heat transfer determinate the moisture flow (Incropera and DeWitt, 1990). The moisture flow is given by (5.11), and the latent heat transfer that directly results from it by (5.12).

$$\phi_m^{f,cav}(i,j) = (\omega_{a,j}^f - \omega_{sat,cav}(i,j)) \frac{h_c^{f,cav}}{C_a} \quad (5.11)$$

$$\phi_{h,lat}^{f,cav}(i,j) = (c_v T_{a,j}^f + L_v) \phi_m^{f,cav}(i,j) \quad (5.12)$$

This is consistent with the theory developed in the subsection 4.5.2.1. Nevertheless, three problems can be raised by the mass flow modelling according to (5.11). First, for the cavity

meshes where the mass flow is toward the cavity wall – for every i such as $\omega_a(j) > \omega_{sat,cav}(i,j)$ which corresponds to condensation – the air might not contain enough humidity to satisfy (5.11). In these cases, a correction factor $F_{cond} \in [0,1]$ expressed in (5.13) is applied to (5.11) aiming at avoiding unphysical situation. i_{cond} denotes the indexes for which $\omega_a(j) > \omega_{sat,cav}(i_{cond},j)$.

$$F_{cond,j} = \frac{\rho_{v,a,j}V_{a,j}}{\Delta t \sum_{i_{cond}} A_{cav}(i,j)\phi_m^{f,cav}(i,j)} \quad (5.13)$$

The final moisture flow for the cavity meshes concerned by condensation is given by

$$\phi_m^{f,cav}(i_{cond},j) = \left(\omega_{a,j}^f - \omega_{sat,cav}(i,j)\right) \frac{h_c^{f,cav}}{C_a} F_{cond,j} \quad (5.14)$$

Secondly, for the cavity meshes where the mass flow is toward the air node – for every i such as $\omega_a(j) < \omega_{sat,cav}(i,j)$ which corresponds to evaporation – the air might be saturated and does not satisfy (5.11). As previously presented, a correction factor $F_{evap} \in [0,1]$ has been set up. The factor $\rho_{v,a}(j)V_a(j)(1 - RH_a(j))$ represents the quantity of humidity that the air can still contain.

$$F_{evap,j} = \frac{\rho_{v,a,j}V_{a,j}(1 - RH_{a,j})}{\Delta t \sum_{i_{evap}} A_{cav}(i,j)\phi_m^{f,cav}(i,j)} \quad (5.15)$$

The final moisture flow for the cavity meshes concerned by evaporation is given by

$$\phi_m^{f,cav}(i_{evap},j) = \left(\omega_{a,j}^f - \omega_{sat,cav}(i_{evap},j)\right) \frac{h_c^{f,cav}}{C_a} F_{evap,j} \quad (5.16)$$

Thirdly, the quantity of water evaporated cannot exceed the available condensed water on the walls. This is reflected in the following condition

$$\phi_m^{f,cav}(i_{evap},j) = \max\left(A_{cav}(i,j)\phi_m^{f,cav}(i_{evap},j), -\frac{m_w^t(i,j)}{\Delta t}\right) \quad (5.17)$$

The energy balance (5.18) is solved iteratively to determinate the cavity wall temperatures.

$$\begin{aligned} & \frac{C_l m_w^{t-\Delta t}(i,j)(T_{cav}^t(i,j) - T_{cav}^{t-\Delta t}(i,j))}{\Delta t} \\ & = A_{cav}(i,j) \left(\phi_{h,sens}^{f,cav}(i,j) + \phi_{h,lat}^{f,cav}(i,j) \right. \\ & \quad \left. + \phi_{h,cond}^{f,cav}(i,j) \right) \end{aligned} \quad (5.18)$$

where $\phi_{h,cond}^{f,cav}$ the conductive heat flow that comes from the foundation. The new water content of the cavity walls meshes' is given by

$$m_w^t(i,j) = m_{w,i}^{t-\Delta t}(i,j) + \Delta t A_{cav}(i,j)\phi_m^{f,cav}(i,j) \quad (5.19)$$

Finally, the heat and moisture balances on the flowing air provide the evolution of the characteristics along the foundation according to (5.20) and (5.21). At the foundation entrance, the temperature and the relative humidity of the air are given by the recorded data (see section 6.1).

$$T_{a,j+1}^f = T_{a,j}^f - \frac{\sum_i A_{cav}(i,j) \phi_{h,sens}^{f,cav}(i,j)}{(C_a + L_v \omega_{a,j}^f) \rho_{a,j} \phi_a} \quad (5.20)$$

$$\omega_{a,j+1}^f = \omega_{a,j}^f - \frac{\sum_i A_{cav}(i,j) \phi_m^{f,cav}(i,j)}{\rho_{a,j} \phi_a} \quad (5.21)$$

5.3.1.2. Weather-related loads: ground top surface

In order to be able to compare the results from the detailed heat and moisture transfer model and from the present model, similar boundary conditions at ground top surface has been considered. As this model take only sensible heat transfers into account, the short and long wave radiation as well as convection have only been modelled according to equation (4.26), (4.27) and (4.28) respectively. Equations (4.33)-(4.39) again allowed the calculation of the convective heat transfer coefficient, and equation (4.42) gave the sky temperature.

As a reminder, all of this doesn't take into account latent heat transfer due to evaporation and condensation at the ground surface. The presence or absence of vegetation only influences the albedo, which is an extreme simplification but allowed the construction of a simple and fast model.

5.3.1.3. Ground below the building: crawl-space case

The equations proposed in the subsection 4.5.1.3 to calculate iteratively the crawl space air temperature is reused, removing the terms representing the latent heat flows. Consequently the heat equation becomes

$$\begin{aligned} V_{CS} \rho_v^{CS} c_a \frac{\partial T_a^{CS}}{\partial t} &= U_{slab} A_{CS} (T_{in} - T_a^{CS}) \\ &+ c_a ACR \frac{V_{CS}}{3600} (\rho_{v,a}^{ext} T_a^{ext} - \rho_{v,a}^{CS} T_a^{CS}) \\ &+ \sum_{i,j} \delta S_{i,j}^{g,CS} [h_c^{g,CS} (T_{i,j}^{g,CS} - T_a^{CS})] \\ &+ \sum_{i,j} \delta S_{i,j}^{f,CS} [h_c^{f,CS} (T_{i,j}^{f,CS} - T_a^{CS})] \end{aligned} \quad (5.22)$$

in which the required heat transfer convective coefficients for the calculation of the heat flows are computed according to the equation introduced in this subsection.

5.3.1.4. Link beam / slab

The building slab is assumed to be made of 36 cm of concrete –representing the floor cover, the concrete screed, the concrete compression slab and the concrete beam – plus 4 cm of insulation. Knowing the building indoor temperature and the crawl-space air temperature, the heat flux and as a result the temperature evolution along the slab can be determinate. All

the values used for the coupled model and given in the subsection 4.5.1.3 are reused. The corresponding temperatures are applied for each mesh between the beam top and the slab lower surface.

5.3.1.5. Base layer

An isothermal condition is applied on the base layer. The imposed temperature is given by (2.1), where the coefficient have been obtained via a curve fitting with the recorded soil temperature at different depth (see Figure 5) and are listed in Table 19.

Table 19: Coefficient for the one dimensional ground temperature model

| | Yearly oscillation | Daily oscillation |
|-------------------------|---|---|
| Yearly mean temperature | $\overline{T_{und}^g} = 11.5$ | |
| Thermal diffusivity | $\alpha_s = 1.01 \cdot 10^{-6}$ | |
| Pulsation | $\omega_1 = 1.99 \cdot 10^{-7}$ | $\omega_1 = 1.99 \cdot 10^{-7}$ |
| Penetration depth | $\delta(\omega_1) = \sqrt{\frac{2\alpha_s}{\omega_1}} = 3.18$ | $\delta(\omega_1) = \sqrt{\frac{2\alpha_s}{\omega_1}} = 3.18$ |
| Amplitude | $A_1 = 8.28$ | $A_1 = 8.28$ |

5.3.1.6. Vertical walls – Beam top surface

The vertical walls are usually considered adiabatic. This assumption is reasonable if the ground element modelled is wide enough so that the isotherm can be considered perpendicular to these walls. The wider it is, the more accurate this assumption will be. This is obviously also a trade-off with the simulation time. It also depends on the size of the building. 5 m by each side of the foundation will be assumed as sufficient. Furthermore, it is assumed that there is no thermal gradient perpendicularly to the beam top surface. This boundary is therefore considered as adiabatic.

5.4. NUMERICAL RESOLUTION

As for the detailed hygrothermal model, the calculation model is divided into two parts: the soil and the foundation. Contrary to the detailed model – the form of the equations to describe the soil and the concrete were similar but not rigorously equal – the computational time is here the only motivation of such decomposition domain. Consequently, two set of equations (5.5) and (5.9) are built and solved. The iterative procedure is described on Figure 49. Once the ground model is run for a given time step, the observed variables allow the calculation of the foundation external factors. Then, the foundation model resolution could be run. Reversely, the observed variables enable the computation of the soil domain loads. The link between the ground and the foundation domains is made in the same manner as described in the subsection 4.5.2.2. This procedure is repeated until convergence – of the soil and foundation observed variables and the flowing air temperature and absolute humidity – is reached.

The convergence threshold is arbitrarily fixed at 10^{-2} . A maximum number of iteration of 30 was set for each time step of the simulation. If the convergence condition is still false, the

current time step is considered divergent. The simulation goes on taking the last values for the variables as if the convergence was reached. Over one year of simulation time with a hourly time step, this happened less than 2 % of time. It is therefore considered that it has a limited impact on the results.

The meshing of a cross section of the domain is pictured on Figure 50. The wider meshes are 1 m x 1 m close to the soil base, far from the foundation. The thinner are 3 cm x 3 cm and positioned in the foundation; close to the inner walls. In the third dimension – along the flowing air direction – the computational domain is divided into five equal meshes of 9.1 m long each.

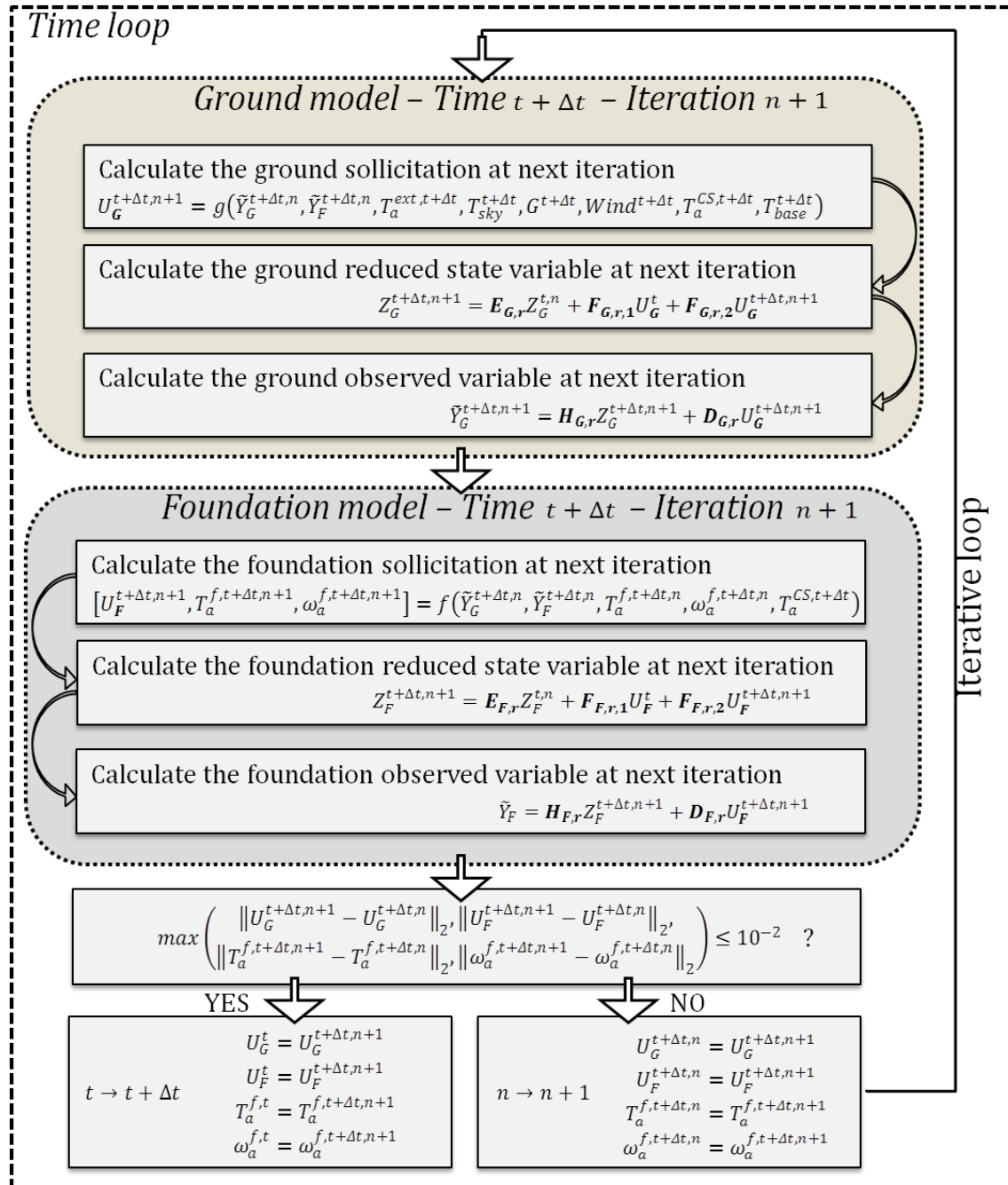


Figure 49: Fondatherm sensible heat transfer model: numerical resolution general procedure

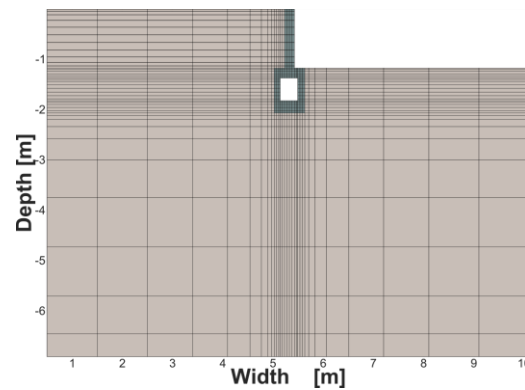


Figure 50: Cross-sectional meshing

5.5. CONCLUSIONS

A model based on sensible heat transfers within the soil and the foundation has been introduced in this chapter. The objectives were to develop a design tool allowing a fast nonetheless accurate computation of the airflow temperature variations throughout the year. It enables the evaluation of the impact of geometry, basement configuration, climate and soil specifications modifications on the results. The computational time was minimized reducing the obtained model thanks to a balanced realization method. Generally speaking, the boundary conditions involved in this model have been built to be as similar as possible to those used in the detailed model without considering the moisture transfers. This would indeed allow a clear comparison between the two models against the measurements introduced in Chapter 7.

Chapter 6. FONDATHERM FULL SCALE MONITORING

A full scale experiment of an occupied building has been realised. This building is equipped with two 45 m long geothermal foundations. The first section 6.1 accurately describes the facilities, the building location and its main characteristics as well as the sensor positions. The objective of such experimental study is triple. It is first to evaluate the opportunities of energy savings of Fondatherm standing alone or coupled with an air handling unit with a heat recovery system, the coupling being studied in the next chapter. The energy performance is calculated both for heating and cooling purposes throughout various indicators generally used for thermal systems especially EAHE – as exposed in the subsection 2.1.3. Secondly, the objective is the improvement of the understanding of the Fondatherm thermal behaviour, of the coupling in one side with the ground and the other side with the buildings. Given all the characteristics evoked in the subsection 2.3, it means to assess the heat flow from the four foundation walls, to be able to foresee their evolution along the airflow direction and with time, and to identify their contribution to the global performance. Thirdly, a monitoring has to yield enough data to be able to validate the models developed in Chapter 4 & 5 and to identify the limits of the simplified approach of Chapter 5. The two first points are exposed in the subsections 6.2.1 and 6.2.2 respectively, and the last one in Chapter 7.

6.1. FACILITIES PRESENTATION

The studied building is an EHPAD⁷, i.e. a long-term care for elderly people. This unit is a specialized centre for the Alzheimer Disease, located⁸ 10 km far from Auxerre city in France. The building is divided into two wings (East and West) - each constituted of twelve bedrooms for the patients and one living room - plus the north part of the building for the technical installations, the meeting rooms and the kitchen. The study will only focus on the East and West wings since they are equipped with the Fondatherm system down under.

Overviews of the building are depicted on Figure 51. Two dual-flow air-handling units (AHU) with heat recovery system of 90 % efficiency – without cooling/heating/humidification systems - are supplying fresh air for the two wings. According to the construction specifications, the airflow supplied by the AHU is around 450 $m^3.h^{-1}$. The wings area (rooms only) is around 200 m^2 , and the air change air rate is thus roughly equal to 0.9 h^{-1} . Nevertheless, the air speed measurement within the cavity was around 0.5 $m.s^{-1}$, which mean the airflow rate is around 290 $m^3.h^{-1}$. As the simulation studies (see Chapter 7) yields results in relative agreement with 0.5 $m.s^{-1}$, this value was retained in all the following. The huge difference between the airflow specification and the measure can be explained by the fact that the AHU was originally designed to stand alone. The coupling

⁷ In french an 'Etablissement d'Hébergement pour Personnes Agées Dépendantes'.

⁸ GPS coordinates : 47°40'18.8"N 3°35'26.0"E

with the foundation added pressure losses and thus reduced the air speed. The foundation air exhaust is connected to the AHU inlet fresh air (usually connected to the outdoor air). The building wings shapes, Fondatherm and the AHU positioning are schemed on Figure 52.

A comprehensive measurement instrumentation has been set up. The foundations but also their near environments are studied. The sensors location and data acquisition system have been designed in order to evaluate the foundation specifications against a traditional EAHE, namely the simultaneous influence from the meteorological, the sub-ground and the building loads, the low burying depth and the high cross-sectional area of the cavity inside the concrete foundation. For all these reasons, a follow-up of the ground temperature but also its moisture content has been implemented for several depths and cross-sections along the foundation axis, both for the free field soil and the terrain underneath the building. Three inspection manholes – at the inlet, the middle and the outlet sections – have been built to easily access the foundation channel. Thanks to them a follow-up of the foundation inner walls temperature has been realised. The flowing air temperature and relative humidity evolutions along the foundation then through the AHU have also been recorded as well as the AHU electric consumption and the main meteorological data. The recording is done every minute. The number, reference and accuracy of the sensors used are listed in Table 20. Their positions are shown section by section on Figure 53 and that of the corresponding cross-sections on the ground plane Figure 52.

Table 20: Sensors characteristics

| Environment | | Quantity measured | Sensors number, type and ref. | Accuracy ⁹ |
|----------------------------------|-----------------------|------------------------|--|------------------------|
| <i>Meteorological conditions</i> | | Temp. & Relative hum. | 1 thermo-hygrometer <i>Sensirion SHT-75</i> | |
| | | Solar radiation | 3 pyranometers <i>Hukseflux LP02</i> | ±8 % |
| | | Wind speed & direction | 1 anemometer and vane <i>Young Wind Sentry</i> | ±0.5 m.s ⁻¹ |
| | | Rainfall | 1 rain gauge <i>Young 52202</i> | ±3 % |
| <i>Soil (East wing only)</i> | Outdoor field | Temp. & water content | 12 RTDs + <i>time domain reflectometer Delta-T SM300</i> | Temp.: ±0.5 °C |
| | Beneath build. | Temp. & water content | 6 RTDs + <i>time domain reflectometer Delta-T SM300</i> | Water cont.: ±2.5 % |
| <i>Foundations</i> | Inner walls | Surface temp. | 24 RTDs Pt-100 <i>Prosensor SPCT</i> | ±0.1 °C |
| | Flowing air | Temp. & Relative hum. | 8 thermo-hygrometers <i>Sensirion SHT-75</i> | |
| | | Pressure losses | 1 differential pressure gauge <i>Testo 512</i> | ±0.5 % |
| <i>Air handling units</i> | Fresh air from found. | Temp. & Relative hum. | 2 thermo-hygrometers <i>Sensirion SHT-75</i> | |
| | Fresh air to room | Temp. & Relative hum. | 2 thermo-hygrometers <i>Sensirion SHT-75</i> | Temp.: ±0.5 °C |
| | Exhaust air from room | Temp. & Relative hum. | 2 thermo-hygrometers <i>Sensirion SHT-75</i> | Rel. hum.: ±4 % |
| | Electric consumption | | 2 electric meters <i>MCI Contax</i> | |

The denominated ‘SM300’ sensors measure at the same time the temperature and the moisture content of a ground. Three of them (called SM6, SM12 and SM15) are placed at the ground surface of the lawn, close to the east wing. Three others (SM5, SM11 and SM14) are buried 80 cm below the previous one, and three more (SM4, SM10 and SM13) at 1.6 m depth below the ground surface. All are situated 2 m away from the foundation.

⁹ According to the sensors’ datasheets. Unfortunately, calibration of the whole data acquisition system (sensors + wires + data loggers) has not been done because of the complex setting up.

They thus yield the temperature and humidity of the ground at several depths. The soil nature is unknown and we have not at our disposal experimental means to characterize it. Furthermore at the depth concerning the foundation, it is probably partially made of construction wastes. Therefore the presence of three sensors for each depth instead of only one ensures a better representation of the ground. Six more 'SM300' (SM2, SM3, SM8, SM9, SM17 and SM18) are placed on both sides of Fondatherm along the airflow direction, close to its outer walls. The objective was to obtain information at the interface between the concrete and the soil (which is numerically a boundary condition). Finally, sensors SM1, SM7 and SM16 yield information about the ground on beneath the building, at the same depth as the foundation and 2 m away from the foundation.

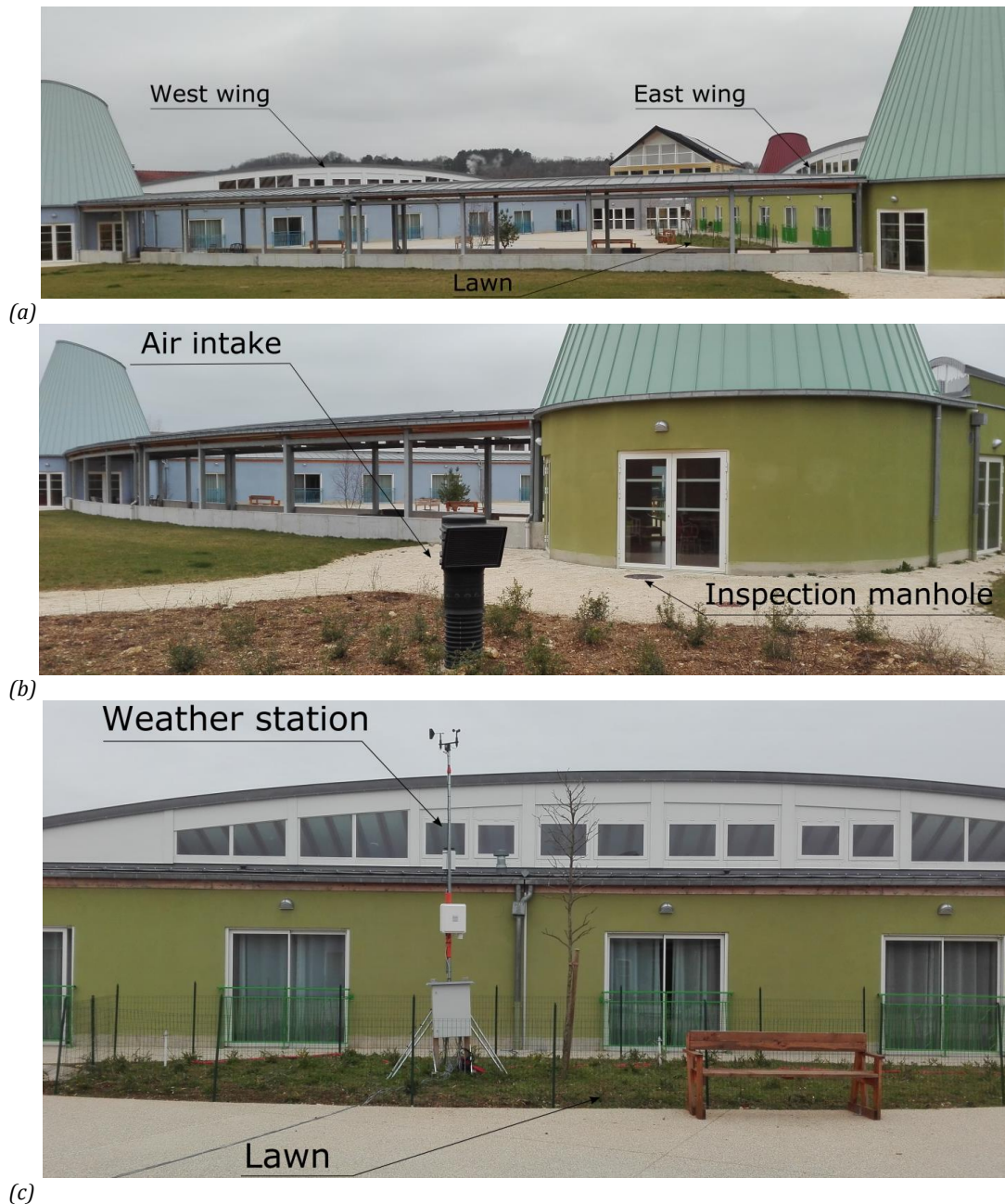
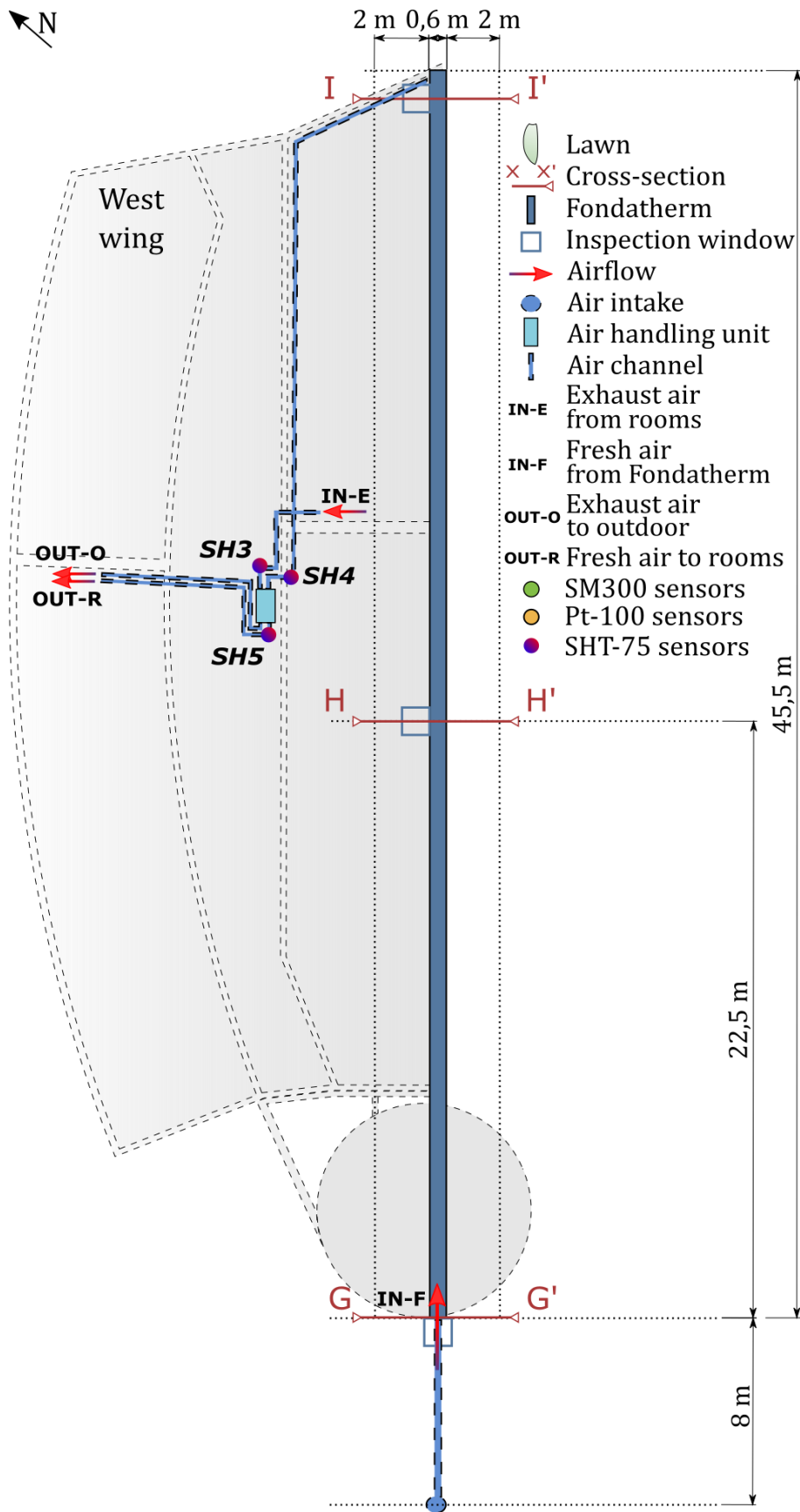


Figure 51: Overview of the monitored building: (a) general view of the west and east wings, (b) position of the east air intake and inspection window at the foundation inlet and (c) weather station installation



(a) West wing

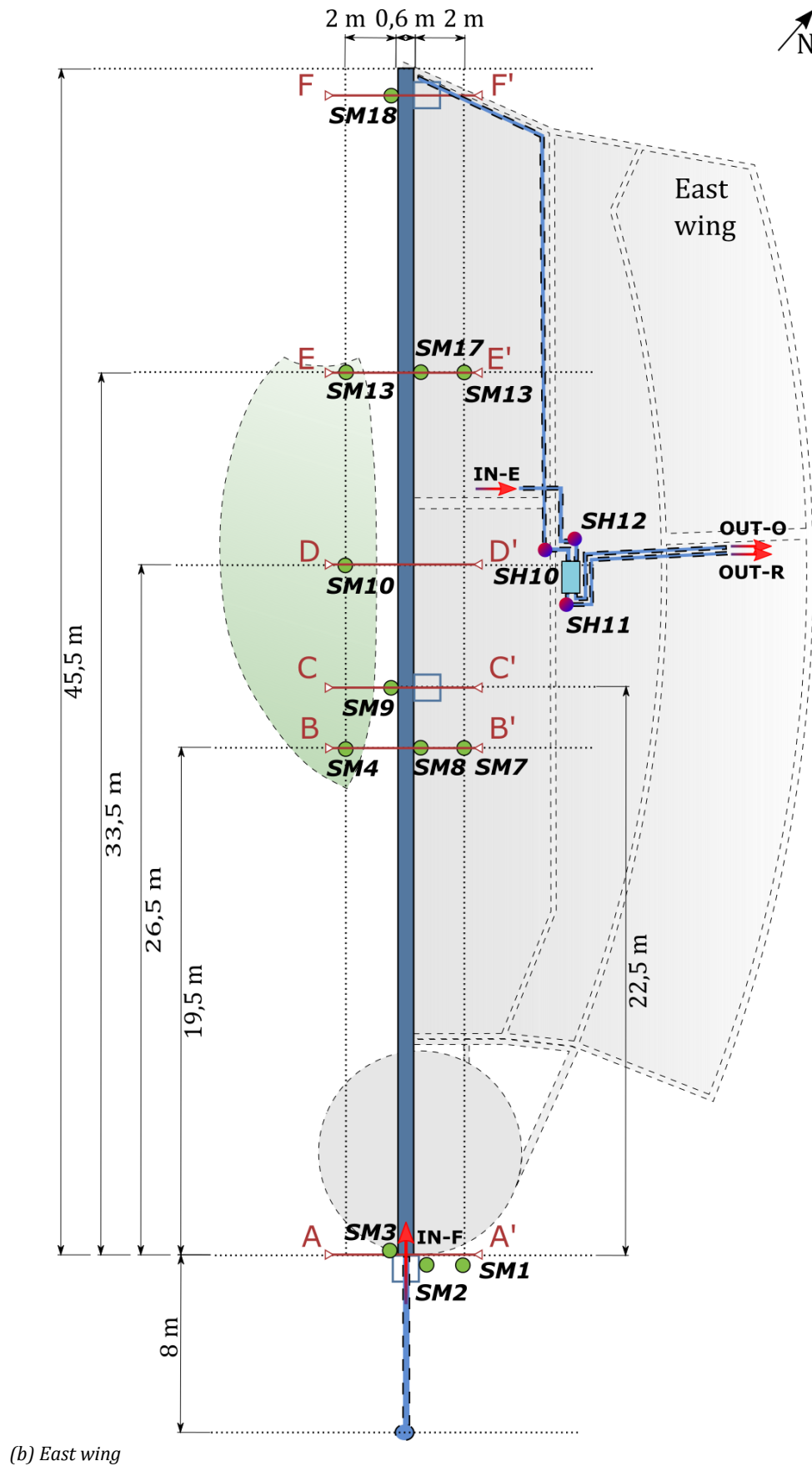
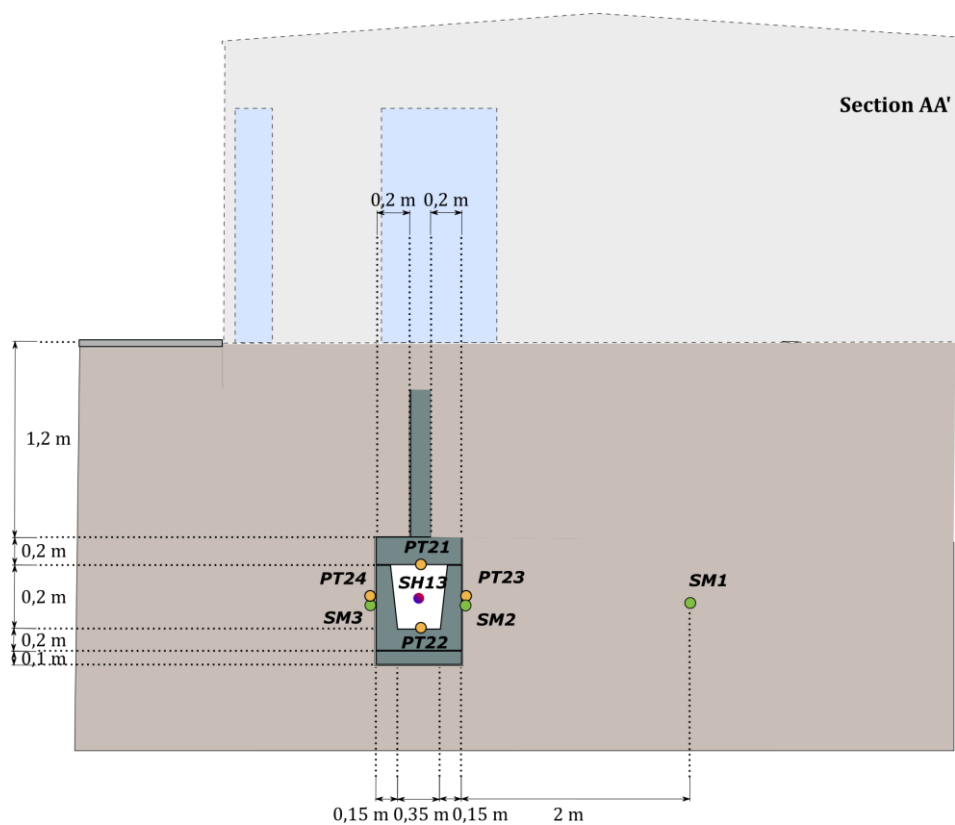
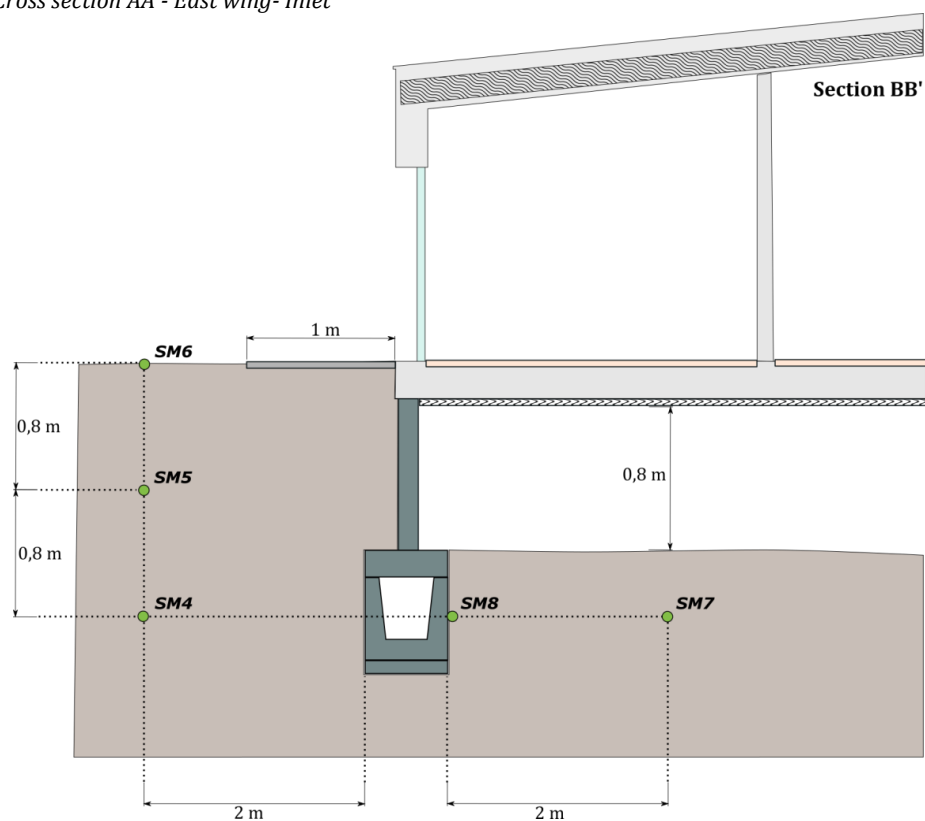


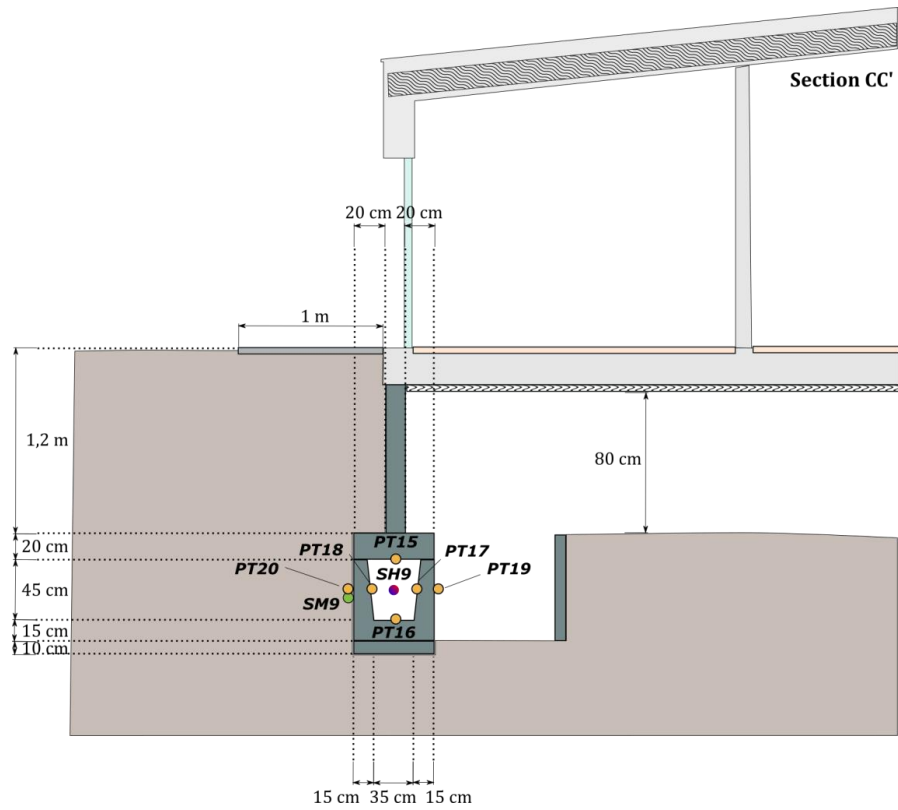
Figure 52 : Ground plan of the monitored building: (a) west wing and (b) east wing



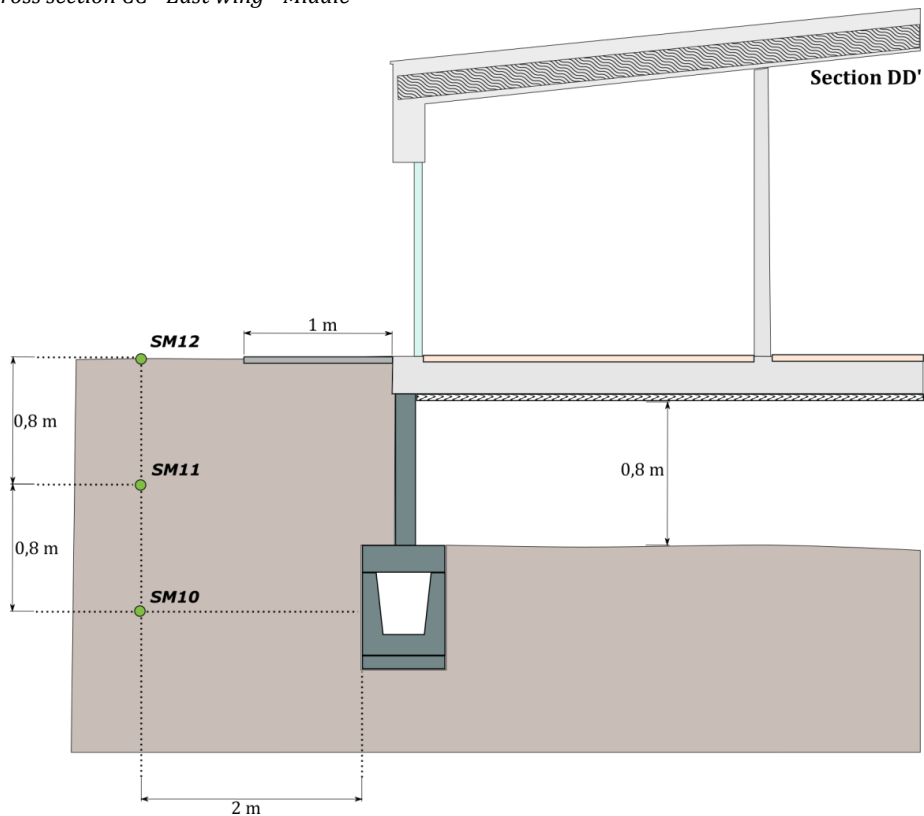
(a) Cross section AA'- East wing- Inlet



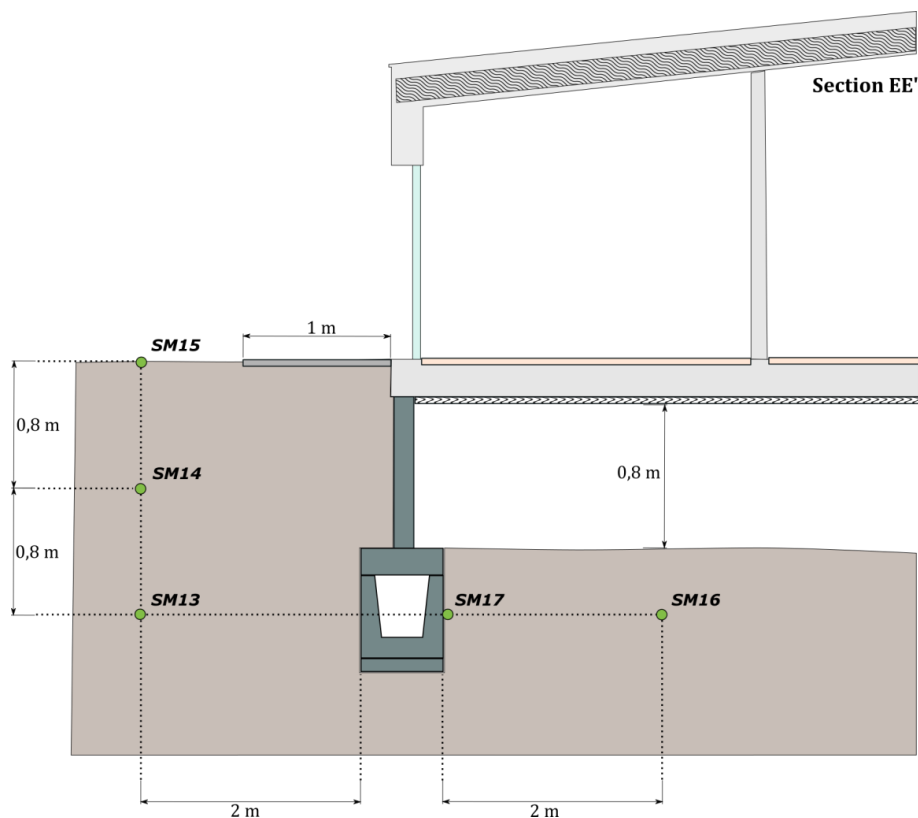
(b) Cross section BB'- East wing



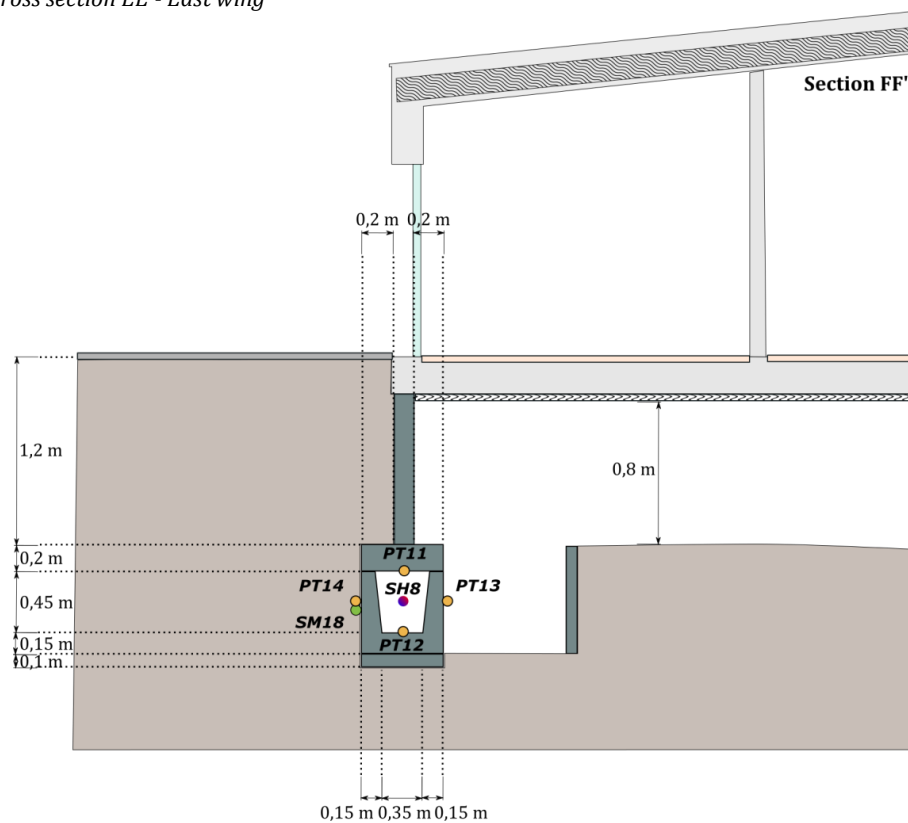
(c) Cross section CC'- East wing - Middle



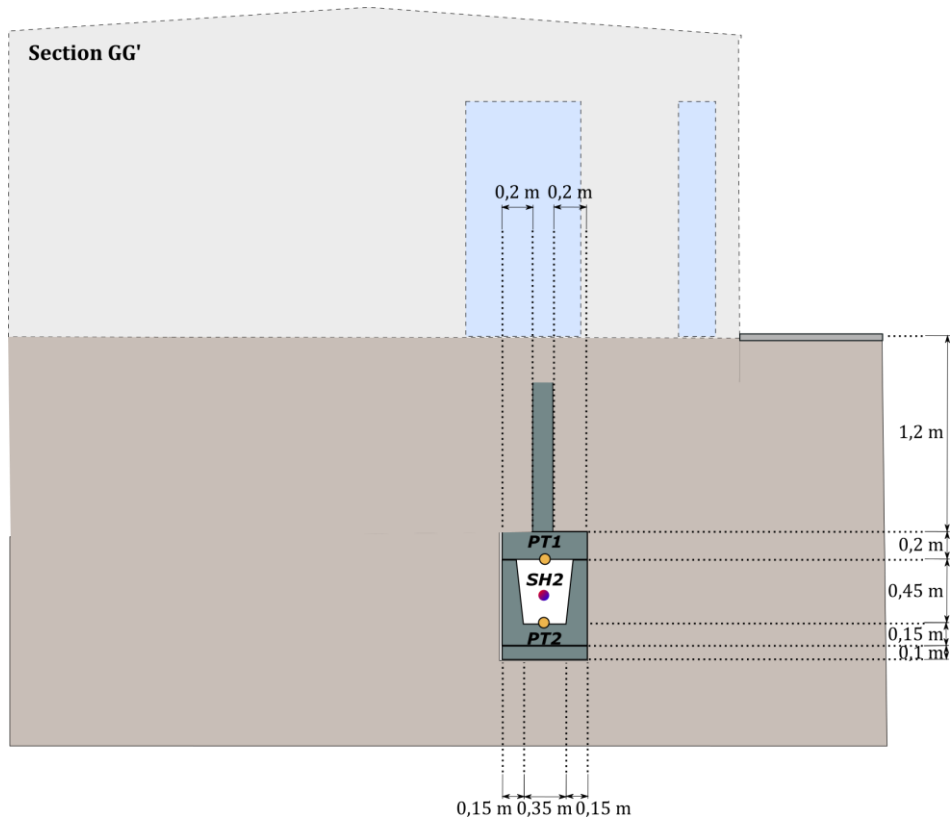
(d) Cross section DD'- East wing



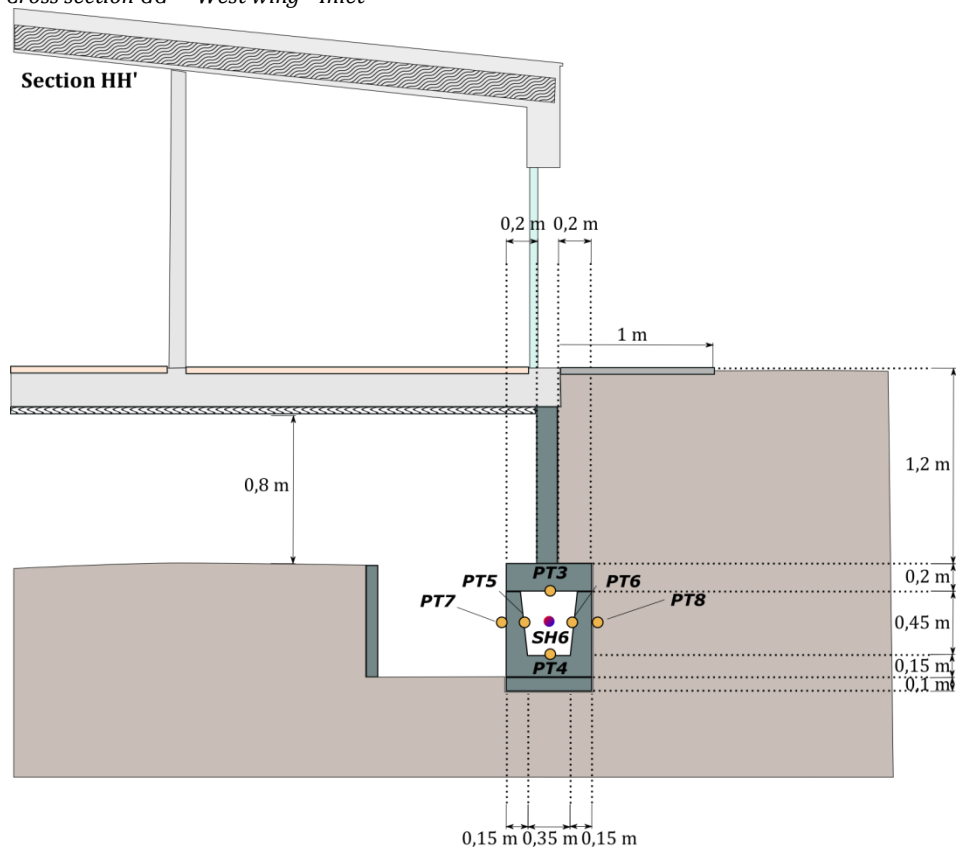
(e) Cross section EE' - East wing



(f) Cross section FF' - East wing - Outlet



(g) Cross section GG' – West wing - Inlet



(h) Cross section HH' – West wing - Middle

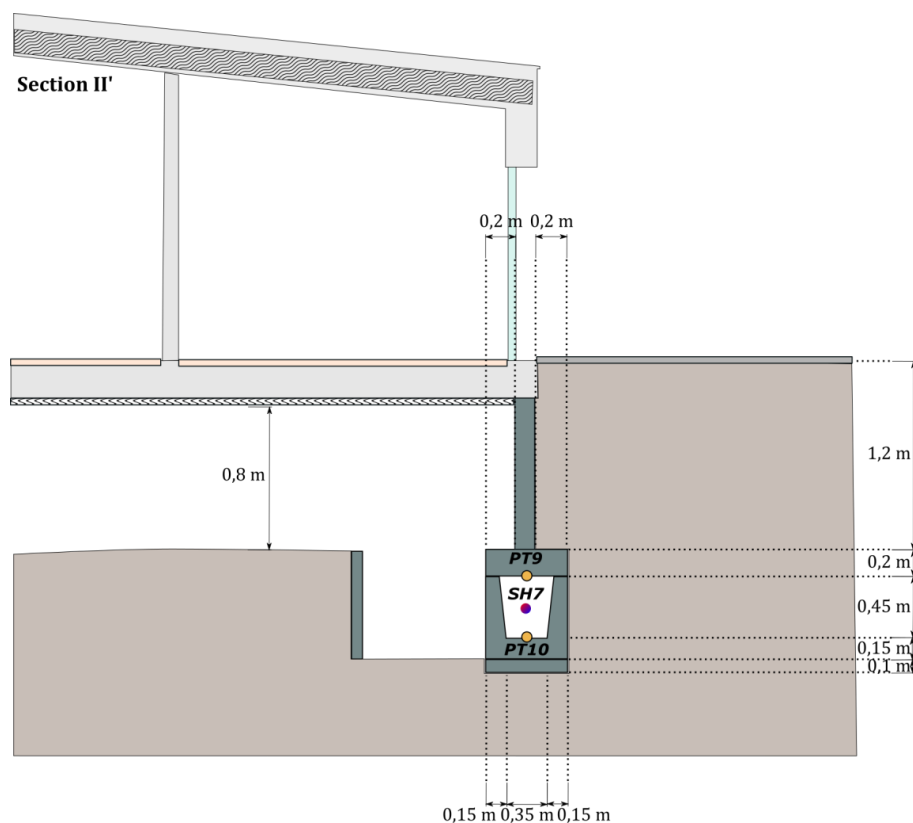


Figure 53: Cross-sectional views of the monitored building: sensors positioning

Furthermore, the inspection manholes allowed setting up Pt-100 RTD on the inner walls of the foundations (East and West) at the inlet, middle and outlet sections, as illustrated on Figure 54. At the inlet as well as the outlet section, the surface temperature of the upper wall and the lower wall are recorded. In the middle section, four sensors give the surface temperature of the upper, lower, and vertical walls. When it was possible, additional Pt-100 have been set-up on both sides of the vertical outer walls of the east foundation, which for several cases duplicates the measurements yield by the SM300 located at the same place.

The data acquisition system is accurately described in Appendix E.

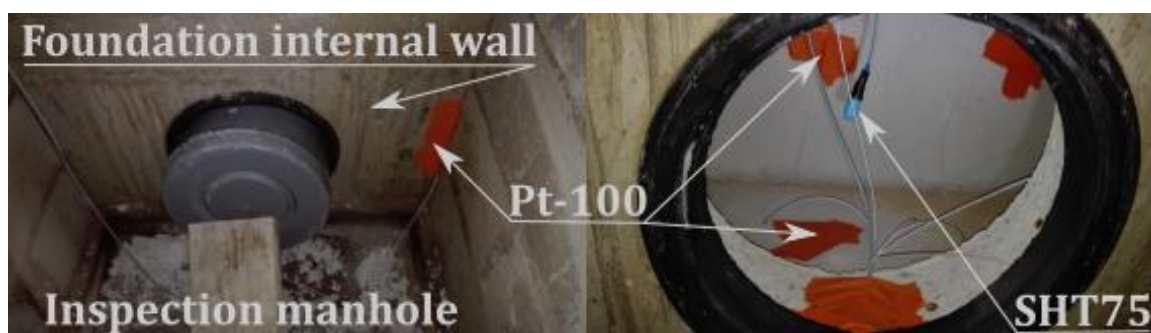


Figure 54: Inspection manhole: access to the foundation cavity

6.2. EXPERIMENTAL RESULTS ANALYSIS

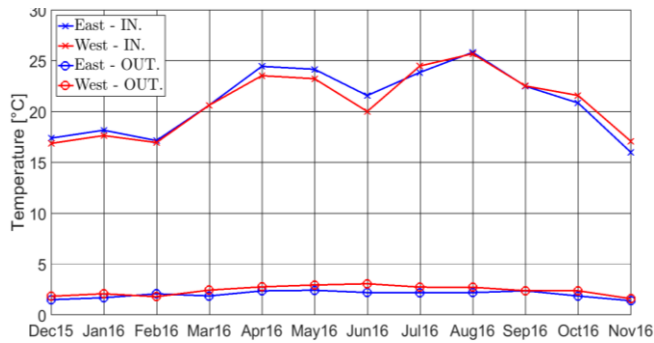
The measurement campaign was realized from December 2015 to November 2016. The acquisition time step is one minute, but the data has been averaged over half an hour in the following. Two levels of analysis are presented in the next two subsections. First an energy analysis provides information about the energy savings opportunities for the heating as well as for the cooling of a building. The foundation performance is evaluated in terms of amplitude dampening of the outdoor thermal wave, heating / cooling power and energy gains, operation time and COP. Secondly, the details of the heat transfers for each of the four walls of the foundation inner surface are analysed in order to provide a better understanding of the Fondatherm component.

6.2.1 ENERGY BEHAVIOUR UNDERSTANDING

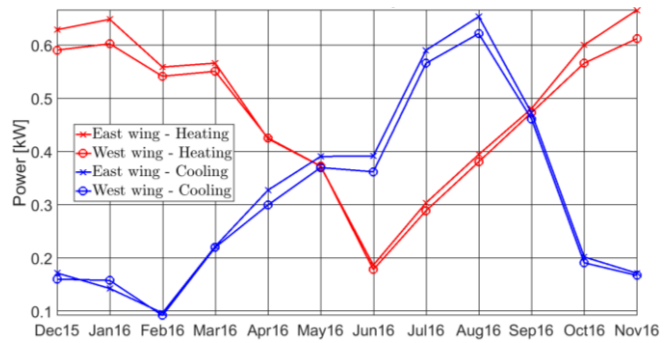
The indicators of the energy performance of Fondatherm are calculated thanks to the measurements provided by the SHT-75 sensors and the AHU electric-meters. The monthly maximum daily amplitude of the ambient and of the outlet foundation air temperature are shown on Figure 55 (a). While the daily ambient air temperature amplitude varies between 15 °C and 25 °C over the year, it is reduced to between 2 and 4 °C at the foundation outlet. This will ensure a stability of the fresh air supplied to the building and thus improves the thermal comfort conditions of it.

The heating and cooling power are calculated according to the equation (2.8) then monthly averaged and plotted on Figure 55 (b). The monthly maximum power ranges between 0.6 and 1.8 kW for heating and between 0.5 and 1.7 kW for cooling. The obtained mean powers may appear low when compared to the data gathered in Table 7 and Table 8 given in 2.1.4. Nevertheless, the airflow rate within the foundation is much lower than most of the cases exposed in these tables. When compared to the study in (Burton, 2004), where the airflow is 290 m³.h⁻¹ for a maximum cooling power of 2.5kW, it reveals that the performance of the foundation is actually of the same order of magnitude.

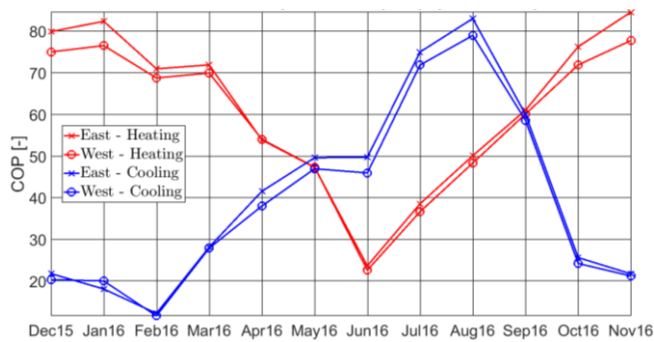
The COP is calculated by two different ways, and monthly averaged as previously. The first calculation considers that the energy consumption of the system corresponds to the energy dissipated by the pressure drops. Thus, the formula (2.7) was used to plot the COP_{pl} on Figure 55 (c). The pressure losses were measured only for the foundation channel: they are approximately equal to 10 Pa. Though additional pressure drops have to be taken into account due to the pipe that drains air from the intake to the foundation inlet and the pipe from the foundation outlet to the AHU inlet. Because of all the elbows, these two pipes are of course at the origin of the main part of the total pressure losses. The total pressure losses have been estimated around 100 Pa (see Appendix F for the calculation details). The resulting heating and cooling COP_{pl} vary from 10 to 90 which is very high compared to usual values for an EAHE. As for the monthly mean power, there is an asymmetry between the heating and the cooling values. Indeed, the minimum values for the heating are reached in June and the maximum in November, while for the cooling, the minimum is reached in February and the maximum in August. The second calculation of the COP_{pl} replaces the term $\Delta p \Phi_a$ of the previous formulation (2.7) by the electric consumption of the AHU.



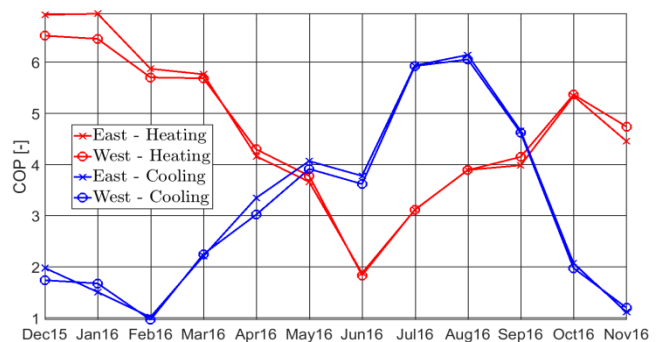
(a) Intake vs. AHU outlet air temperature amplitude



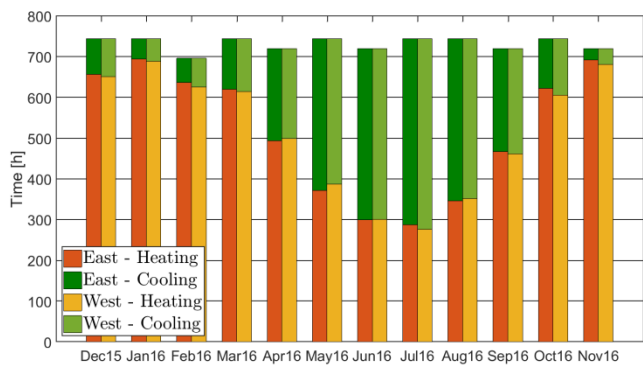
(b) Monthly mean power



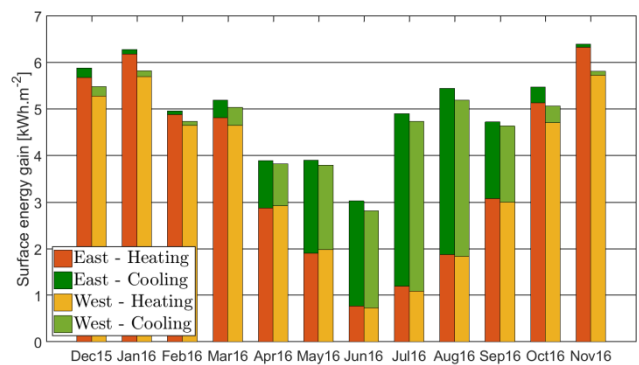
(c) COP_{pl} - calculation based on pressure drop



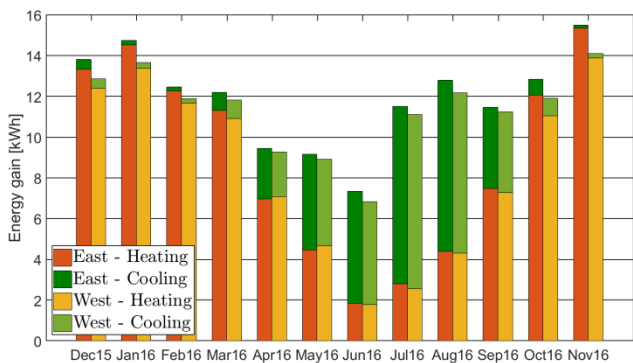
(d) COP - calculation based on AHU elec. cons.



(e) Cumulated heating and cooling operation time



(f) Heating and cooling monthly surface energy gains



(g) Heating and cooling mean daily energy gains

| | Heating | | Cooling | |
|---|---------|------|---------|------|
| | West | East | West | East |
| Operation time (h) | 6141 | 6187 | 2644 | 2598 |
| Total energy gain (kWh.m ⁻²) | 42,3 | 44,7 | 14,7 | 15,4 |
| Mean daily energy gain (kWh.day ⁻¹) | 8,4 | 8,9 | 2,9 | 3,0 |
| Annual mean power (kW) | 0,5 | 0,5 | 0,3 | 0,3 |
| Annual max. power (kW) | 1,7 | 1,8 | 1,7 | 1,7 |
| COP _{pl} - pressure drop based (-) | 59,1 | 61,7 | 38,8 | 40,5 |
| COP - AHU elec. cons. based (-) | 4,6 | 4,7 | 3,1 | 3,2 |

(h) Annual summary

Figure 55 : Energy experimental analysis of Fondatherm

The heating and cooling COPs thus range between 1 and 7 (see Figure 55 (d)) – with monthly maximum ranging between 6.9 and 18.1 for the heating, and between 0 and 17.2 for the cooling - which is fully consistent with the performance of a traditional EAHE.

The distribution of the time when the foundation is used for heating ($T_{outlet} > T_{ext}$) and when it is used for cooling ($T_{outlet} \leq T_{ext}$) is given on Figure 55 (e). During winter time (December to February), the foundation is used more than 80% of time for heating. However during summer time (June to August), the cooling operation time represent only 50 to 65 % of the total operation time. This illustrates the asymmetry between heating and cooling for mid-European climates evoked by Hollmuller and Lachal (2014). Furthermore, in winter the 20% of time when the foundation is used for cooling are of course undesirable. In such cases a by-pass should be used to optimise the energy storage energy from the environment. In mid-European climates, the cooling is only needed occasionally to dampen the ambient air peak temperatures especially during summer.

The Figure 55 (f) depicts the heating and the cooling energy gains normalized by the exchanging surface area of the foundation for each month, calculated according to

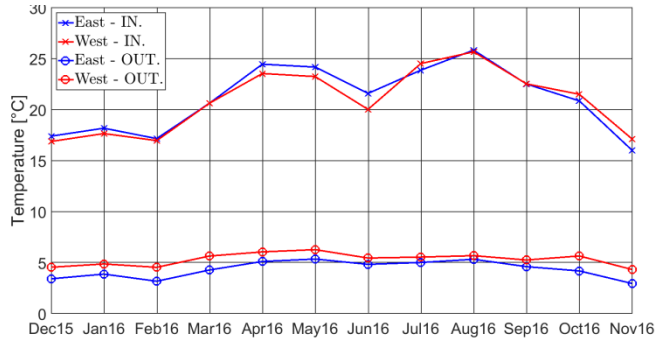
$$E_{found,surf} = \frac{1}{3.6 \cdot 10^6 A_{EAHE}} \int_{1\ month} \dot{m}_a c_a (T_{outlet} - T_{inlet}) dt \quad (6.1)$$

Figure 55 (g) shows the daily energy gains - averaged over each month - calculated according to (6.2). The monthly maximum of the daily energy gains ranges between 6.3 and 31.6 kWh for heating and between 2 and 18.8 kWh for cooling. The orders of magnitudes of the obtained values are in agreement with that for traditional EAHE and even slightly better in what concerns the heating with total energy gains higher than 43 kWh.m⁻².y⁻¹. The cooling energy gains of almost 15 kWh.m⁻².y⁻¹ falls in the middle range of the performances announced in the literature survey (see 2.1 especially Table 7 and Table 8).

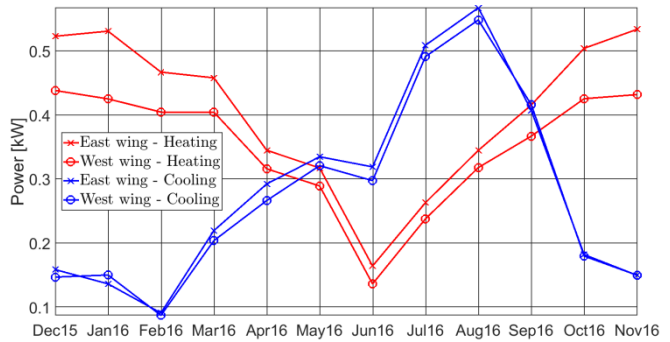
$$E_{found,daily} = \frac{1}{3.6 \cdot 10^6} \frac{1}{N} \sum_{i=day\ 1}^{i=day\ N} \int_{day\ i} \dot{m}_a c_a (T_{outlet} - T_{inlet}) dt \quad (6.2)$$

The same study is carried out for a Fondatherm ‘half-length’ (about 23 m) and the results gathered in Figure 56. The comparison of the annual summary data of the half-length (Figure 56 (h)) with the annual summary of the total length (Figure 55 (h)) show that the cooling performances are almost unchanged between the half and the full length. The mean daily energy gain is reduced by only 8 %, the maximal power is diminished by 12 % and the COP with a pressure based and an electric consumption based calculation are respectively decreased by 7 and 3 %. The total surface energy gain for cooling is logically raised by 84 %. It confirms the fact that the heat transfer power comes from the first meters of the exchanger. Surprisingly, the operation time is raised by 10 %, which means that there exist times for which the air is cooled down by the first half of the foundation, and heated up by the second half. The thermal study of the next subsection should be able to highlight this phenomenon.

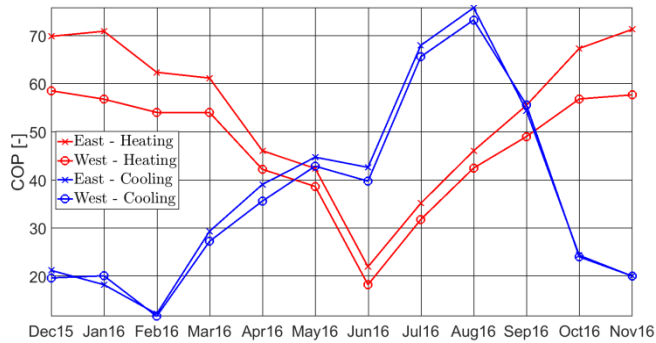
However, the heating mean daily energy gain is reduced by 24 %, the annual mean power by 30 %, the maximum power by 20 %, and the COPs by 16 and 19 %.



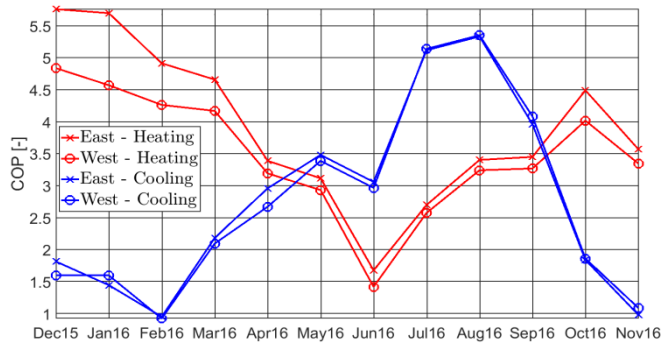
(a) Intake vs. AHU outlet air temperature amplitude



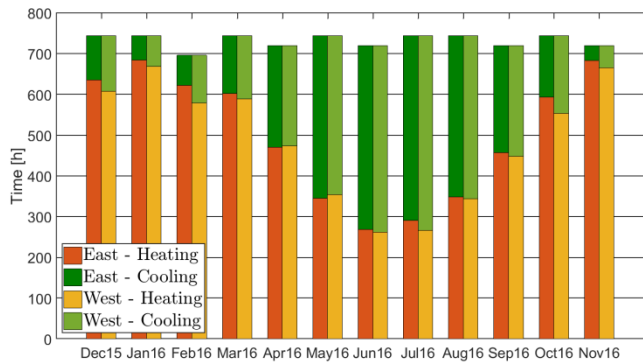
(b) Monthly mean power



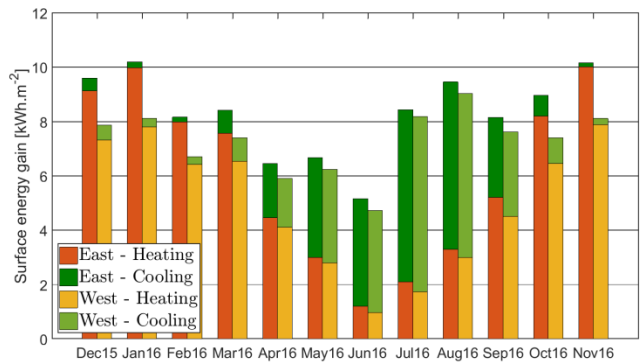
(c) COP_{pl} - calculation based on pressure drop



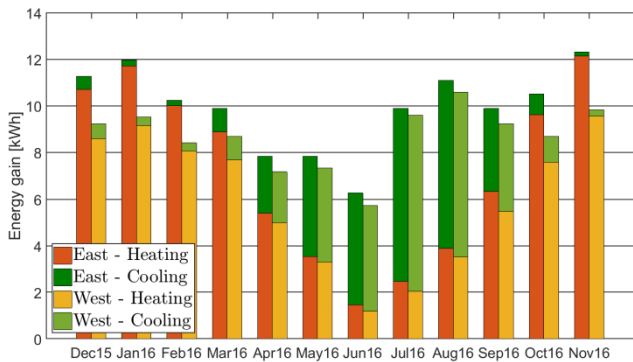
(d) COP - calculation based on AHU elec. cons.



(e) Cumulated heating and cooling operation time



(f) Heating and cooling monthly surface energy gains



(g) Heating and cooling mean daily energy gains

| | Heating | | Cooling | |
|---|---------|------|---------|------|
| | West | East | West | East |
| Operation time (h) | 5811 | 6002 | 2973 | 2782 |
| Total energy gain (kWh.m ⁻²) | 59,6 | 72,2 | 27,7 | 27,7 |
| Mean daily energy gain (kWh.day ⁻¹) | 5,9 | 7,2 | 2,7 | 2,7 |
| Annual mean power (kW) | 0,3 | 0,4 | 0,3 | 0,3 |
| Annual max. power (kW) | 1,3 | 1,5 | 1,5 | 1,5 |
| COP _{pl} - pressure drop based (-) | 46,7 | 54,2 | 36,3 | 37,5 |
| COP - AHU elec. cons. based (-) | 3,5 | 4,0 | 2,9 | 3,2 |

(h) Annual summary

Figure 56: Energy experimental analysis of the half length of Fondatherm

This also confirms the design rules for mid-European climates evoked by Hollmuller and Lachal (2014): for cooling purposes, one or two dozen meters of heat exchanger are enough to dampen the daily oscillations, but for heating purposes it necessitates longer exchanger to dampen the annual oscillation.

Furthermore, it is interesting to compare the discrepancies between the east and west foundations in the case of the Fondatherm ‘full length’ and ‘half length’. The differences between east and west wings for all the cooling performance calculated for the ‘full length’ are less than 5%. For the heating, it is less than 6 %. These low discrepancies can reasonably be explained by the measurements uncertainties. However, in the case of the ‘half length Fondatherm’:

- the heating surface energy gain and the heating mean daily energy gain are respectively 21 % and 22 % higher for the east wing,
- the annual mean power is 33 % higher for the east wing,
- the heating COPs pressure drop based and AHU electric consumption based are respectively 16 % and 14 % higher for the east wing,
- the differences between east and west wings for all the cooling performances are less than 6 %, except for the cooling COP AHU electric consumption based (10 %).

A clear behaviour difference in the first half of the two foundations has been highlighted. It is nevertheless difficult to explain but the local ground properties and the orientation can definitely play an important role. Although there is no more precision, one has to keep in mind that the soil, the foundation and the boundary condition characterization is an important step especially for the modelling.

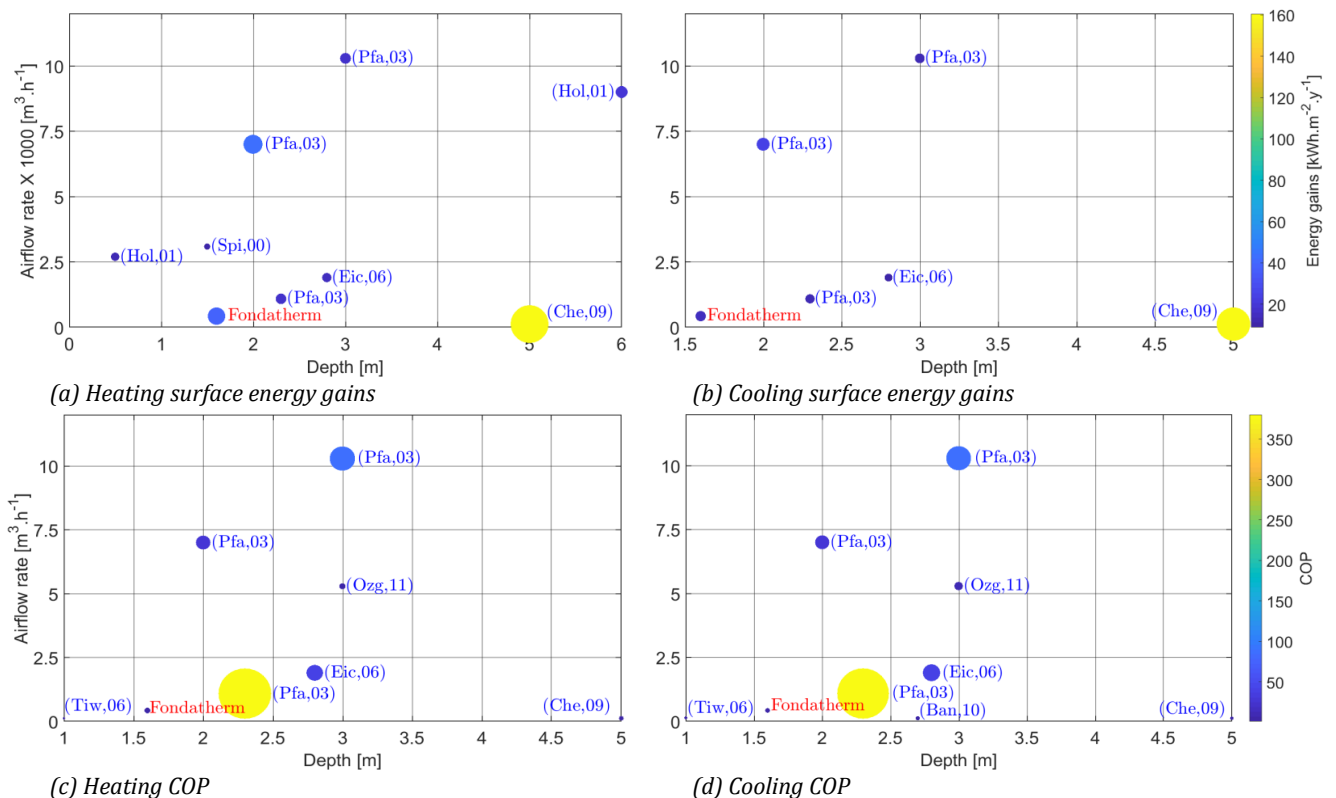


Figure 57: Comparison of the energy performance of Fondatherm technology against traditional EAHE

Finally, the Fondatherm technology is compared against the performance of the traditional EAHE obtained from the literature survey (see 2.1.4). To this end, bubble charts enable to visually identify the differences between all the available data. The Figure 57 represents on the abscissa axis the depth of the EAHE and on the ordinate axis the airflow rate. The size and the colour of the bubble are then proportional to the considered physical quantity. The Figure 57 (a) and (b) are for example the surface energy gains respectively for heating and cooling. The Figure 57 (c) and (d) are the coefficient of performance respectively for heating and cooling.

The Figure 57 (a) and (b) clearly put in evidence that given the relatively low depth and airflow rate compared to the other elements, the Fondatherm technology is efficient. Considering heating, it is equal or better than almost all the others elements for the lowest airflow rate and one of the lowest buried depths. Considering cooling, Fondatherm performance is in the average, but for both the lowest airflow rate and buried depth. According to the Figure 57 (c) and (d), the COP – based on AHU electric consumption – of Fondatherm is one of the lowest both for heating and cooling. It has nevertheless similar COP than EAHE buried deeper or with higher airflow rate. Furthermore, this result has to be treated with caution for many reasons:

- Some points actually represent the global COP and not the heating or cooling COP,
- Some points are obtained by modelling extrapolations, sometimes with steady-state calculation,
- The results don't always result from simulation over a full year but sometimes only over a couple of days,
- The way to calculate the COPs may differ from an author to another (see 2.1.3).

6.2.2 THERMAL BEHAVIOUR UNDERSTANDING

An analysis of the foundation behaviour in summer, winter, and during the two mid-seasons is carried out here. The objective is to get a better understanding of the energy results previously exposed. Furthermore, the Fondatherm specifications presented in section 2.3, especially its position relatively to the building and the cavity size lead to specific thermal mechanisms that it is important to identify and explain. The vocabulary and the acronyms conventions used in what follows are explained on Figure 58 and Table 21.

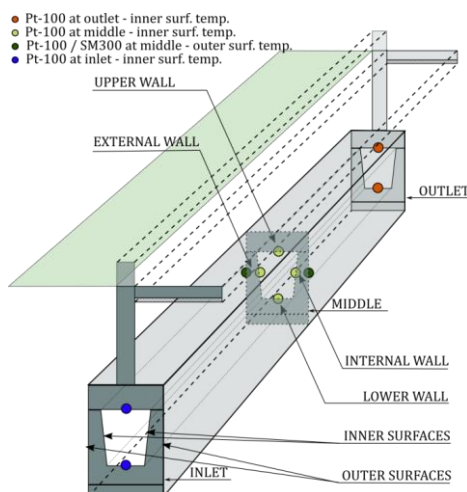


Figure 58: Vocabulary used - Main sensors positions

Table 21: Acronyms used definitions

| Acronym | Location | | | Corresponding sensors | | |
|-----------------------------|----------|---------|--|-----------------------|---------------|------------------|
| | Wing | Section | Wall | Air temp. | Surface temp. | Temp. difference |
| <i>W.IN.Up.</i> | West | Inlet | Upper | <i>SH2</i> | <i>PT1</i> | <i>PT1-SH2</i> |
| <i>E.IN.Up.</i> | East | Inlet | Upper | <i>SH13</i> | <i>PT21</i> | <i>PT21-SH13</i> |
| <i>W.IN.Low.</i> | West | Inlet | Lower | <i>SH2</i> | <i>PT2</i> | <i>PT2-SH2</i> |
| <i>E.IN.Low.</i> | East | Inlet | Lower | <i>SH13</i> | <i>PT22</i> | <i>PT22-SH13</i> |
| <i>W.MID.Up.</i> | West | Middle | Upper | <i>SH6</i> | <i>PT3</i> | <i>PT3-SH6</i> |
| <i>E.MID.Up.</i> | East | Middle | Upper | <i>SH9</i> | <i>PT15</i> | <i>PT15-SH9</i> |
| <i>W.MID.Low.</i> | West | Middle | Lower | <i>SH6</i> | <i>PT4</i> | <i>PT4-SH6</i> |
| <i>E.MID.Low.</i> | East | Middle | Lower | <i>SH9</i> | <i>PT16</i> | <i>PT16-SH9</i> |
| <i>W.MID.Ext.</i> | West | Middle | External (facing the ground outside) | <i>SH6</i> | <i>PT6</i> | <i>PT6-SH6</i> |
| <i>E.MID.Ext.</i> | East | Middle | External (facing the ground outside) | <i>SH9</i> | <i>PT18</i> | <i>PT18-SH9</i> |
| <i>W.MID.Int.</i> | West | Middle | Internal (facing the ground beneath the bldg.) | <i>SH6</i> | <i>PT5</i> | <i>PT5-SH6</i> |
| <i>E.MID.Int.</i> | East | Middle | Internal (facing the ground beneath the bldg.) | <i>SH9</i> | <i>PT17</i> | <i>PT17-SH9</i> |
| <i>W.OUT.Up.</i> | West | Outlet | Upper | <i>SH7</i> | <i>PT9</i> | <i>PT9-SH7</i> |
| <i>E.OUT.Up.</i> | East | Outlet | Upper | <i>SH8</i> | <i>PT11</i> | <i>PT11-SH8</i> |
| <i>W.OUT.Low.</i> | West | Outlet | Lower | <i>SH7</i> | <i>PT10</i> | <i>PT10-SH7</i> |
| <i>E.OUT.Low.</i> | East | Outlet | Lower | <i>SH8</i> | <i>PT12</i> | <i>PT12-SH8</i> |
| <i>E.MID.Ext.Soil.SM300</i> | East | Middle | Inner / Outer External wall | - | - | <i>SM9-PT18</i> |
| <i>E.MID.Ext.Soil</i> | East | Middle | Inner / Outer External wall | - | - | <i>PT20-PT18</i> |
| <i>W.MID.Ext.Soil</i> | West | Middle | Inner / Outer External wall | - | - | <i>PT8-PT6</i> |
| <i>E.MID.Int.Soil.SM300</i> | East | Middle | Inner / Outer Internal wall | - | - | <i>SM8-PT17</i> |
| <i>E.MID.Int.Soil</i> | East | Middle | Inner / Outer Internal wall | - | - | <i>PT19-PT17</i> |
| <i>W.MID.Int.Soil</i> | West | Middle | Inner / Outer Internal wall | - | - | <i>PT7-PT5</i> |

6.2.2.1. Summer period

The focus is first on five of the hottest days during the summer period from 16 to 21 July. First of all, it is important to note that the behaviour of the East and the West foundation are similar since Figure 59 shows similar trends for both foundations. The observed disparity between the flowing air temperatures of the two wings are under the accuracy threshold of the SHT-75 sensors. This confirms the agreement between all the cooling indicators calculated in the previous section for the east and the west wing.

Figure 59 (a) shows that while the daily ambient air temperature amplitude is around 25 °C, it is reduced to maximum 3°C at the foundation outlet. The maximum ambient air temperature over this period is 37.5 °C – but only 31 °C at the foundation inlet – and 20 °C at the foundation outlet, even after five hot days. During the hottest hours, the temperature reduction between the intake and the foundation inlet is between -8 and -5 °C. It ranges between -9 and -5 °C between the foundation inlet and the middle section and is only of -2 °C between the middle and the outlet section. The cooling occurs during the daytime, but the air

is heated up by the foundation at night (roughly from 10pm to 10am). Indeed, the outdoor air temperature falls below 15 °C at night which is lower than the concrete temperature. Since it is cooled down, the flowing air relative humidity rises and is very often over 80 % at the foundation outlet. Nevertheless, the risk of condensation seems limited: the highest temperature difference between the air and the wall surface is 5 °C at the inlet section but there the air relative humidity is only about 50 %

Figure 59 (c) and (d) highlighted that the evolution of the surface temperature of the walls follows that of the flowing air temperature. High amplitudes are observable at the entrance and are lower at the outlet. Discrepancies between the upper and the lower surface wall temperatures can be noticed. For the outlet and the middle section, the upper wall is around 1 °C hotter than the lower wall. This can be simply explained by the height difference between these walls (1.4m depth for the upper wall and 1.85m depth for the lower wall) which lead – according to the equation (2.1) – to +1 °C for the upper wall during summer and -1°C in winter. At the inlet section, the upper surface is also hotter, up to +1 °C difference during the night and up to 5 °C during the daily peak temperature. This is partially explained as previously by the elevation difference but probably also by the local perturbation due to the manhole that drains outdoor air directly to the foundation inlet section. This has to be kept in mind for the validation of the code, in which the presence of the manhole is not considered.

The objective is to have a better understanding of the role played by each wall and the evolution along the airflow direction. It is thus proposed to evaluate the ‘thermal potentials’ of the different parts of the foundation. ‘Thermal potential’ designates in this document the temperature difference between the circulating air and one of the four surface walls in the same cross-section (inlet / middle / outlet), and is plotted on Figure 59 (e) and (f) for the east and west wing respectively. In practical terms, it corresponds to the heat flow from the foundation walls toward the flowing air normalized by the convective heat transfer coefficient. Its sign informs about the heating or the cooling impact of one wall on the air. Its amplitude has to be considered carefully. Indeed the heat flow is the product of the temperature difference by the convective heat transfer coefficient; the latter varies from a wall to another and along the airflow direction.

Figure 59 (e) and (f) show that all the studied walls heat the air at night. During the daytime, all the walls cool the air except the upper wall at the outlet, the contribution of which is almost negligible. The heating but especially the cooling potential is clearly lower at the middle and the outlet section than at the inlet section. Furthermore, the upper wall provides higher heating potential while the lower wall provides higher cooling potential, which is perfectly logical considering the temperature evolution with depth.

At the middle section, the heat flux through the concrete is evaluated by the same way. The difference between the surface temperature of the inner and the outer wall is calculated for the two vertical walls (the one facing outside, and the one facing the ground beneath the building) and plotted on Figure 59 (g). The thermal potentials are identical and synchronized with the flow from the lower wall. No distinction appears between the two vertical walls. The heating potential (through the concrete) is decreased and the cooling potential is unchanged with the air temperature raising. As the inner surface wall temperature is also rising it means

that the foundation outer walls i.e. the soil is gradually heated up and its cooling potential less efficient.

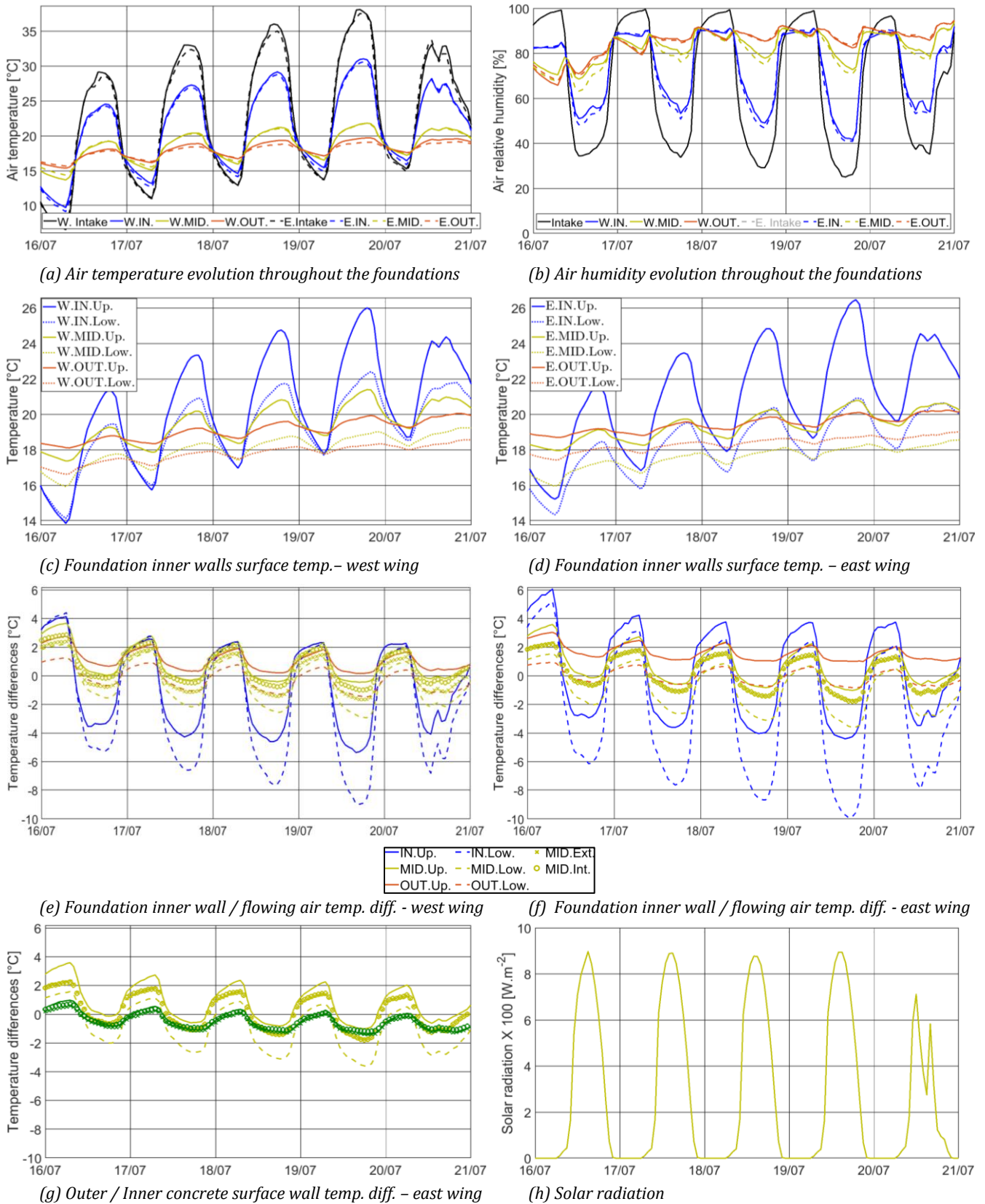


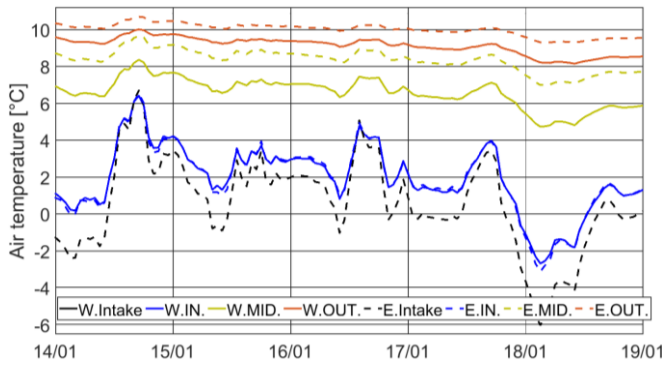
Figure 59: Fondatherm thermal performance analysis over five typical summer days

6.2.2.2. Winter period

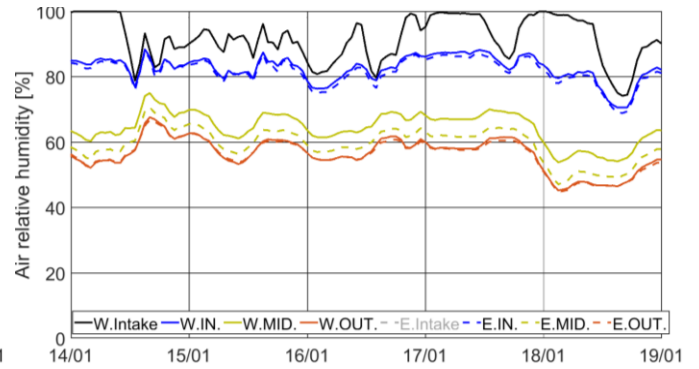
As for the summer period, a similar analysis is carried out for five typical winter days from 14 to 19 January. The Figure 60 (a) shows that while the daily ambient air temperature amplitude is between 4 and 8 °C, it is only about 1 °C at the outlet. The minimum ambient and outlet air temperature are respectively -6 °C and 8 °C. Even after five cold days, the outlet air temperature is in the interval 8 °C – 10 °C, which means that the temperature elevations are between 4 and 14 °C. Unlike the previous summer case, there is no alternation between heating and cooling period, but only heating. Although no difference can be observed on the inlet air temperature between both foundations, the middle and the outlet air temperature are higher – respectively around +2 °C and +1 °C - for the east than for the west foundation. This is in agreement with the differences observed in the previous section: the east foundation (especially the first half) has better heating performance than the west foundation.

The Figure 60 (c) and (d) can partially explain the difference. As one can observe, the lower and the upper wall surface temperatures of the east foundation are more or less equal. Furthermore, these temperatures are almost equal to the lower wall surface temperature of the west foundation. On the contrary, the upper wall surface temperature of the west foundation is around 2 °C lower than the lower one. So all in all, the heat flow from the foundation inner walls to the air is higher for the east foundation. At the middle and the outlet sections of the two foundations, the upper wall surface temperature is higher than the lower one and globally the temperatures of the east foundation are higher.

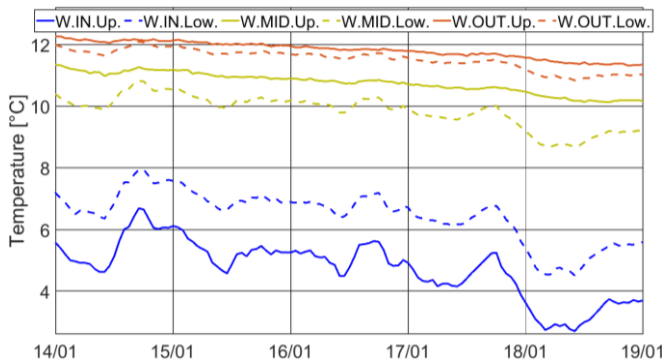
More details can be obtained from the analysis of the thermal potentials plotted on Figure 60 (e) and (f). They show that all the foundation inner walls heat the air. A differentiation between the walls however appears contrary to the summer case. The heat flow from the upper wall is notably higher than the heat flow from the vertical wall facing the crawl space, which is in turn higher than the heat flow from the lower wall and the vertical wall facing outside. This can be seen for the two foundations. This is not consistent with the fact that the lower wall is supposed to be hotter than the upper wall (about 1 °C more) in winter. A possible explanation is that an additional heat flux comes from the building via the beam and heat the upper wall surface up. A part of the building heat loss through the slab would thus be recovered by the airflow. Hollmuller already put in evidence a similar phenomenon in (Hollmuller and Lachal, 2014). The heat flow from the soil beneath the building to the foundation is slightly higher than the heat flow from the outside soil (Figure 60 (e), (f) and (g)). This is of course in agreement with the fact that in winter the soil temperature beneath the building is higher than the free-field soil.



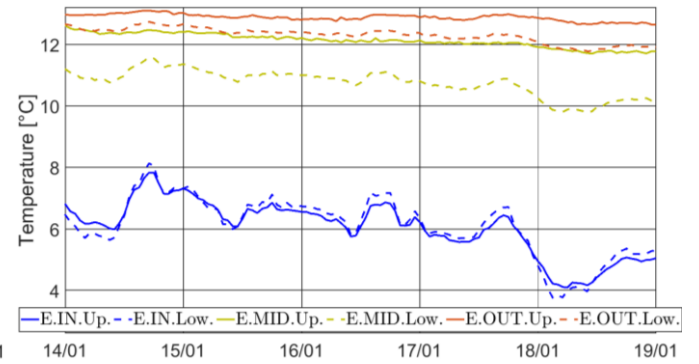
(a) Air temperature evolution throughout the foundations



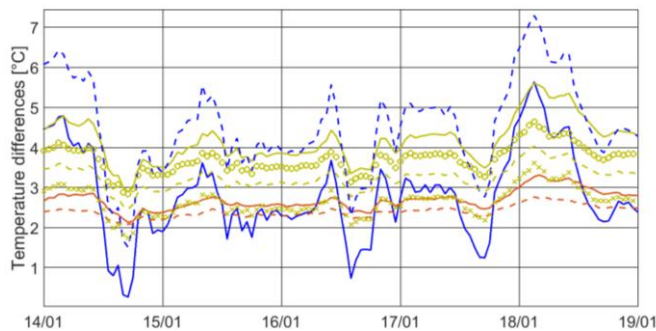
(b) Air humidity evolution throughout the foundations



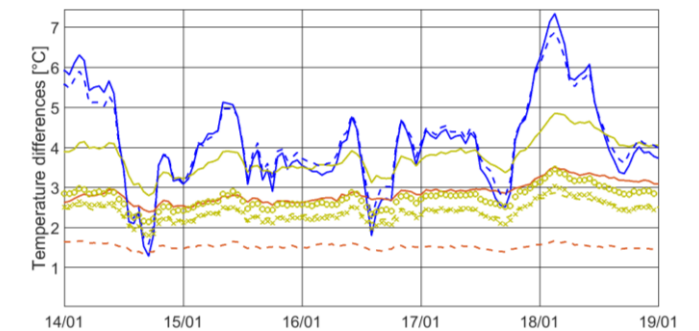
(c) Foundation inner walls surface temp. - west wing



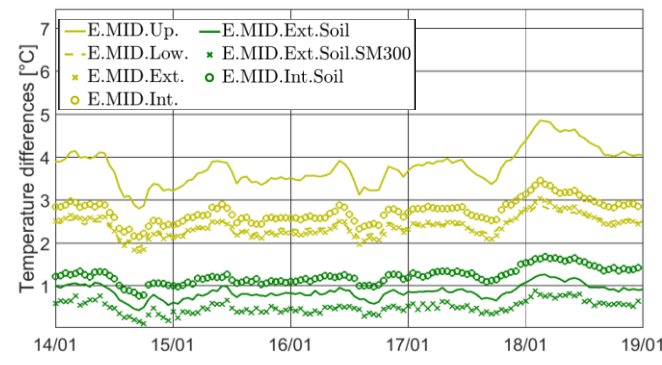
(d) Foundation inner walls surface temp. - east wing



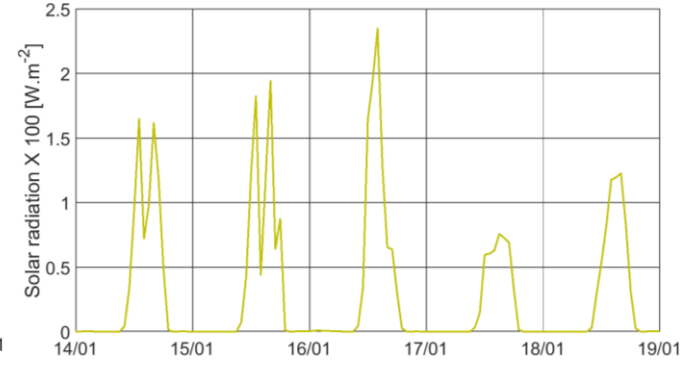
(e) Foundation inner wall / flowing air temp. diff. - west wing



(f) Foundation inner wall / flowing air temp. diff. - east wing



(g) Outer / Inner concrete surface wall temp. diff. - east wing



(h) Solar radiation

Figure 60: Fondatherm thermal performance analysis over five typical winter days

6.2.2.3. Mid-seasons

Spring period

Contrary to the summer and the winter cases, the heating and cooling periods are not well demarcated. The alternation requires to use a by-pass. However the irregularities at the entrance completely disappeared at the outlet. A relative stability is indeed observable (Figure 61 (a)) since the outlet air temperature ranges from 10 to 13 °C although the ambient air temperature varies between -1°C to 21°C.

The surface temperature of the upper wall is 0.5 °C higher than the lower wall surface temperature (significant compared to the Pt-100 sensors accuracy) at the outlet and 1 °C at the middle section (Figure 61 (c) and (d)). No conclusion can be easily made at the inlet. Thanks to the study of the thermal potentials (Figure 61 (e) and (f)) it can be said that:

- The upper as well as the lower wall heat the air at the outlet section, slightly more for the upper wall,
- At the middle section, the upper wall has a faintly higher contribution to heat the air up during the heating periods, while the lower wall has a slightly higher contribution to cool the air down during the cooling period,

At the inlet, the lower wall has also a higher contribution to cool the air down during the cooling period.

The thermal potential through the concrete is almost nil the first days and becomes negative during the last days with the hottest ambient air temperature: the soil recovers energy from the flowing air.

Autumn period

In autumn like in spring the heating and cooling periods are not well demarcated but the variations at the entrance are smoothed by the foundation. A relative stability is indeed observable since the outlet air temperature ranges from 13 to 15 °C although the ambient air temperature ranges from 0°C to 20°C (Figure 62 (a)).

The surface temperature of the upper wall at the middle and at the outlet section are also higher than the surface temperature of the lower walls (Figure 62 (c) and (d)). No general conclusion can be made at the inlet section as different behaviours are observables for the two foundations.

Figure 62 (e) and (f) put in evidence that all the walls of the middle and the outlet sections contribute to heat the air almost all the time. The walls of the inlet section occasionally cool the air. The upper wall contributes slightly more than the other to heat the air. The thermal potential through the concrete shows that the foundation mainly contributes to the heating of the air. This is consistent with the fact that the soil was heated up by the flowing air during summer, and that it is hotter than air during autumn as temperatures begin to decrease.

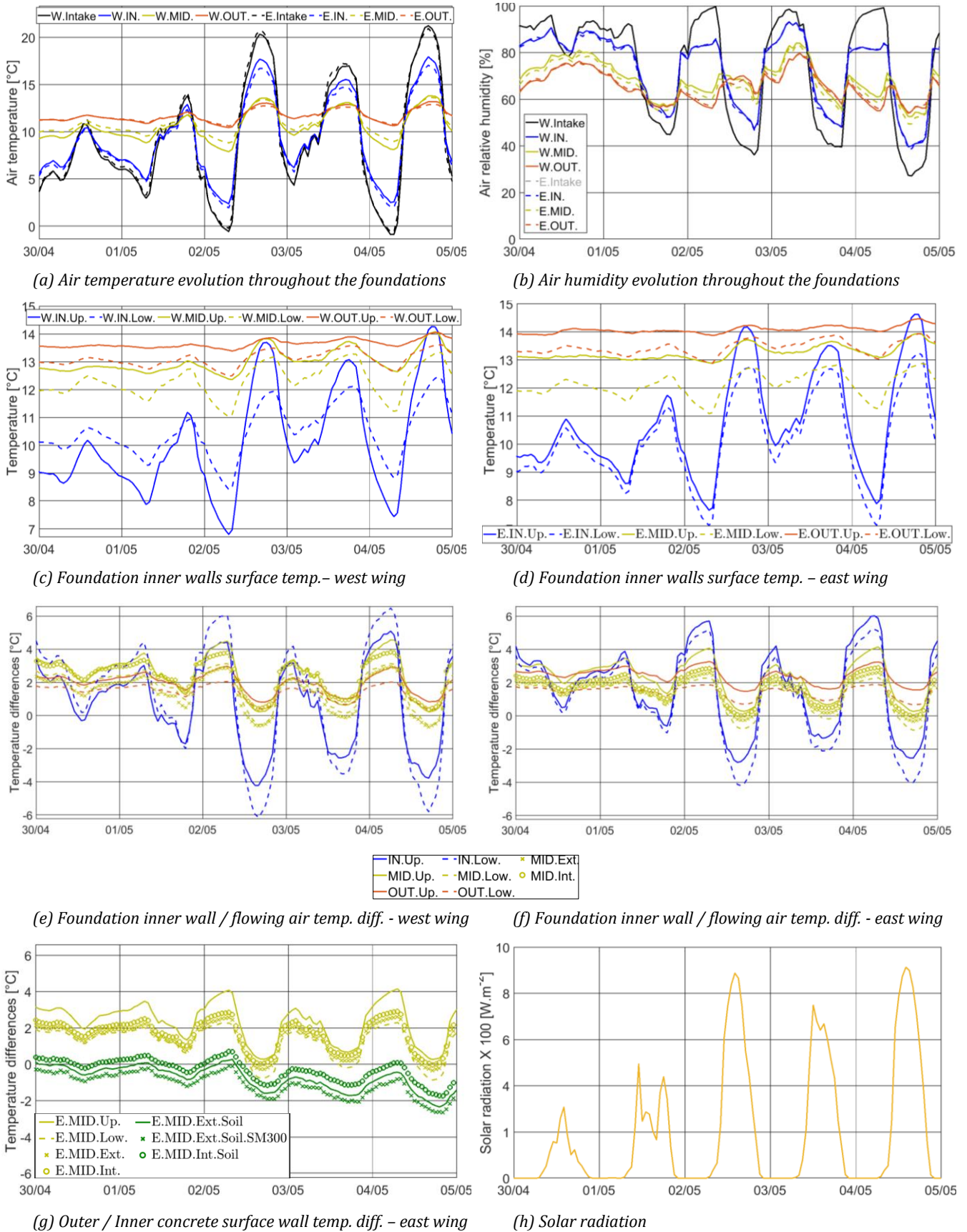
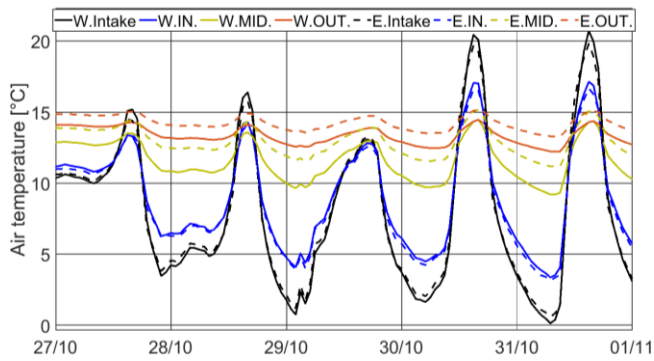
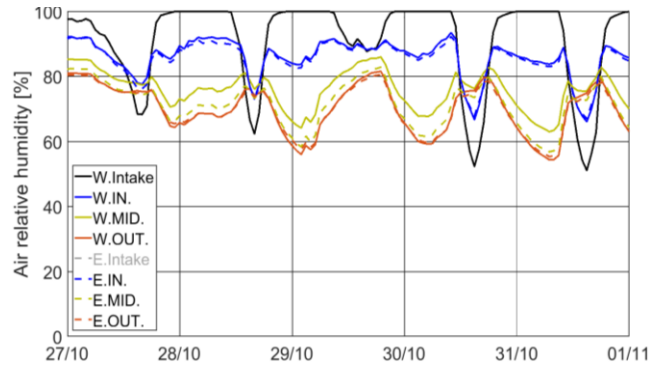


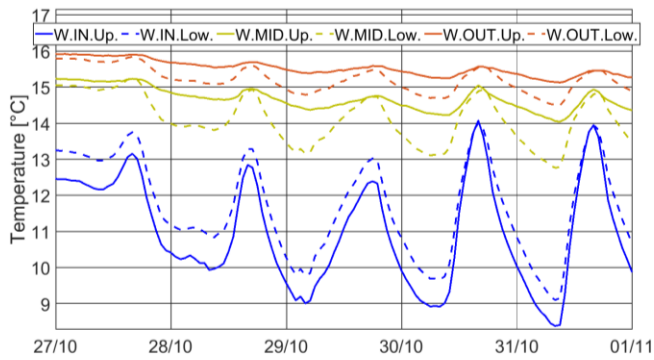
Figure 61: Fondatherm thermal performance analysis over five typical spring days



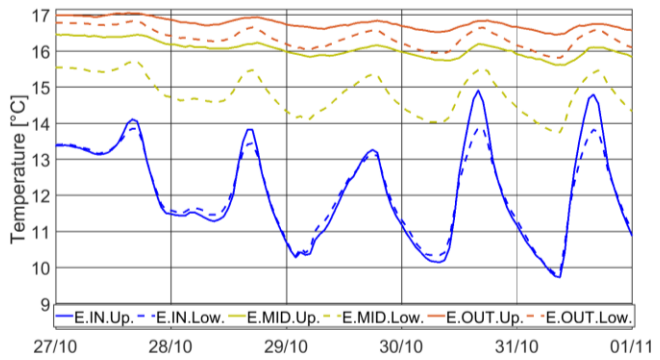
(a) Air temperature evolution throughout the foundations



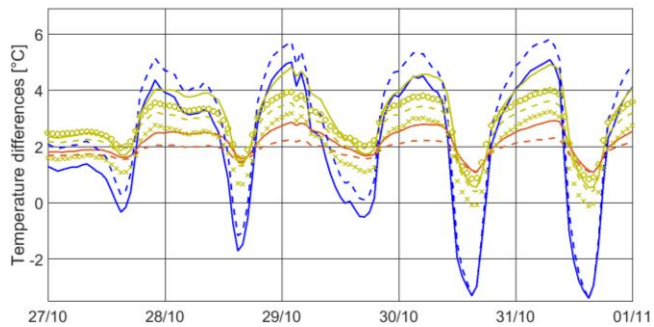
(b) Air humidity evolution throughout the foundations



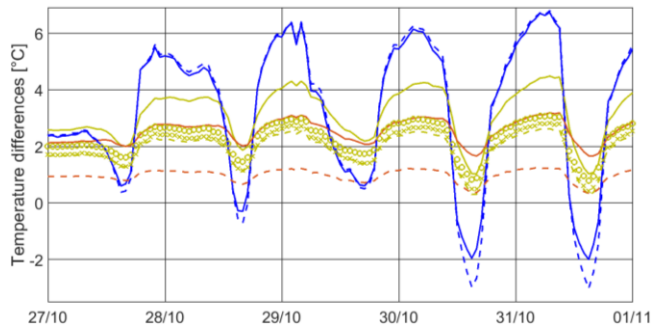
(c) Foundation inner walls surface temp. - west wing



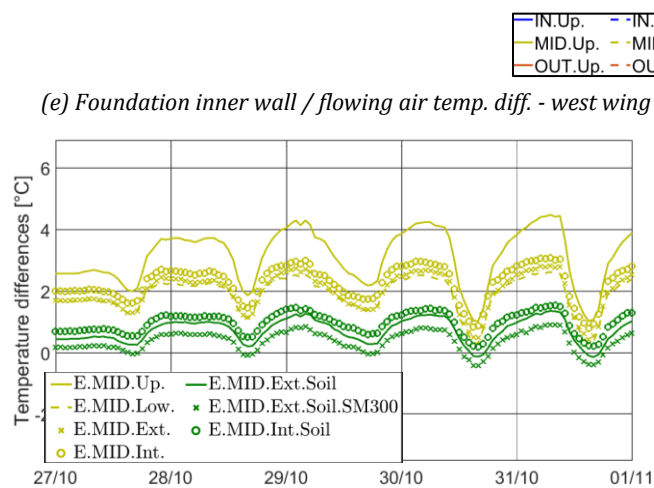
(d) Foundation inner walls surface temp. - east wing



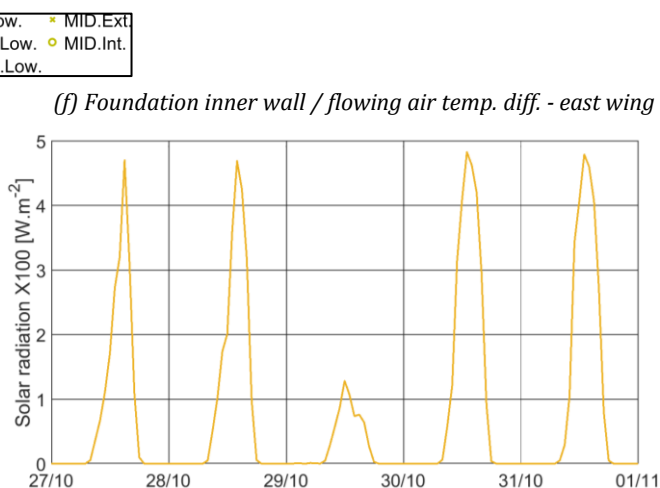
(e) Foundation inner wall / flowing air temp. diff. - west wing



(f) Foundation inner wall / flowing air temp. diff. - east wing



(g) Outer / Inner concrete surface wall temp. diff. - east wing



(h) Solar radiation

Figure 62: Fondatherm thermal performance analysis over five typical autumn days

6.2.2.4. Behaviour over the whole year

In order to generalize the observations previously made, boxplots for every thermal potential are represented for each month and for both foundations on Figure 63.

At the inlet section, the heating duration from the upper wall is over 75 % of the operation time from October to March. It is only over 50 % of the time from April to September. The maximal thermal potential ranges between about 4 °C and 7 °C, and the minimum between -5 and -2 °C. The heating duration from the lower wall is also over 75 % from October to March. It is over 50 % of the time in April and September. In May, June and August, the operation time of this wall is half devoted to cooling, half to heating. In July, the cooling time is even over 50% of the time. The maximum thermal potential is between 3 and 7 °C, while the minimum is between -10 and -2 °C.

At the middle section, the boxplots show that:

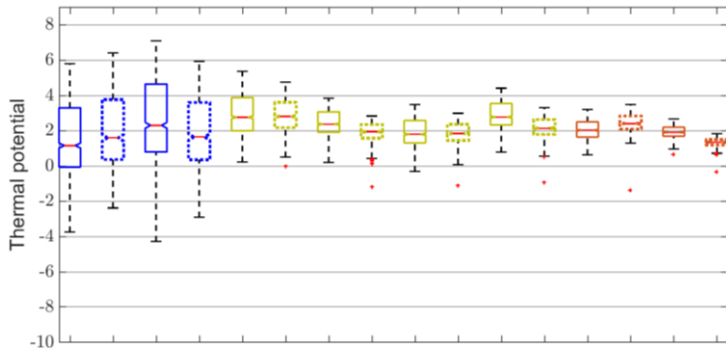
- The upper and the internal walls only contribute to the heating of the air from October to May. They occasionally contribute to cooling from June to September, but less than 25 % of the operation time. The maximum thermal potentials range between 3.5 and 5 °C for the upper wall, and between 2 and 4 °C for the internal wall. The minimum range between -1 and 1 °C and between -1.5 and 1 °C for the upper and the internal walls respectively.
- The lower and the external walls contribute to the heating of the air from October to March. In April and September this contribution is reduced, but is still over 75 % of the operation time. The lower wall is in cooling mode from May to August. In May and June, the cooling time is equal or more than 25 % of the operation time. In July and August, it is even over 50 %. For the external wall, over three quarter of the time of May is operating in heating mode. From June to August, the cooling time is equal or more than 25 % of time. The maximum thermal potentials range between 2 and 3.5 °C for the lower wall, and between 2 and 3.5 °C for the external wall. The minimum range between -3 and 1 °C and between -2 and 0.5 °C for the lower and the external walls respectively.

It thus appears that for the middle section the lower wall is the one which is the most efficient for cooling the air. The external wall is in the second position. On the contrary the upper wall is definitely the one which provides the more energy for heating, logically followed by the internal wall. The contribution of the two other walls is similar for the heating.

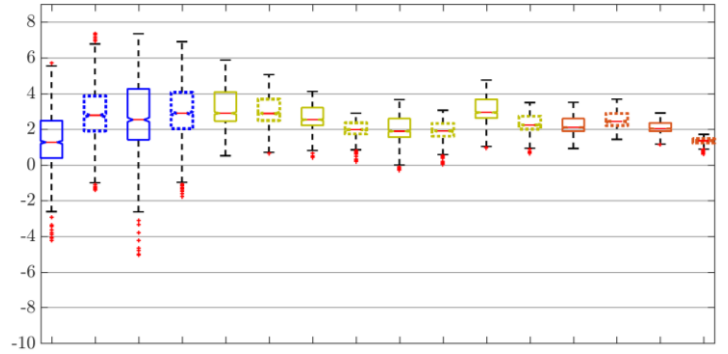
It is easily observable that at the outlet section, the main contribution of the upper and the lower wall is for heating. The lower wall has a cooling effect 25 % of time in June, 50 % of time in July, 25 % of time in August, and punctually in September. However, the upper wall function is only heating. It is also clear that the thermal potential of the lower wall is under that of the upper wall. This difference is increasing from January to July and decreasing from August to December.

To sum up, the upper wall mainly 'provides heat' throughout the year while the lower wall mainly 'supply cold' during the cooling season. The external wall has a slight better performance than the upper and the internal wall to cool the air in summer. On the contrary,

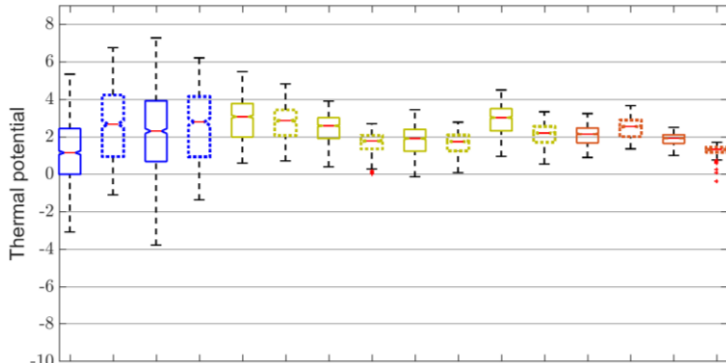
the internal wall has slightly a better potential than the lower and the external walls to heat the air in throughout the year.



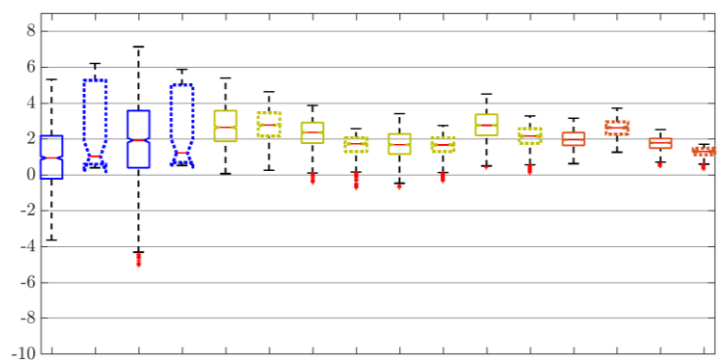
December 2015



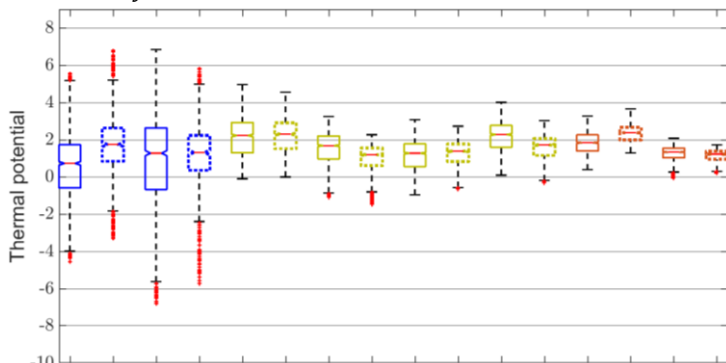
January 2016



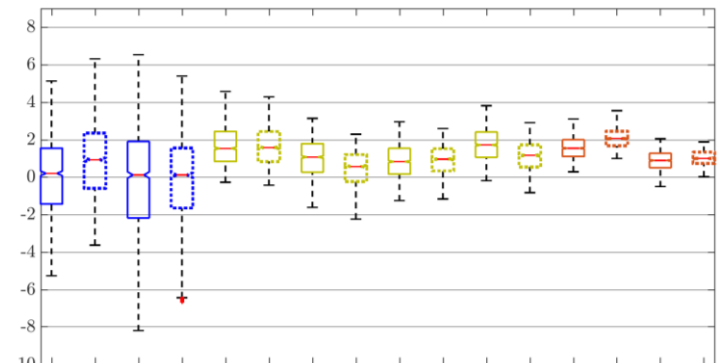
February 2016



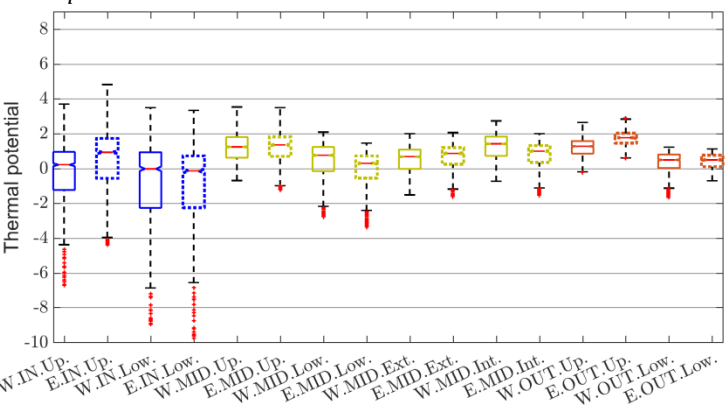
March 2016



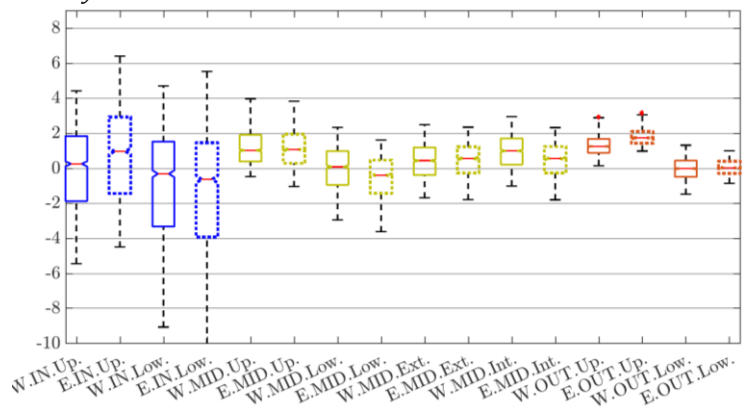
April 2016



May 2016



June 2016



July 2016

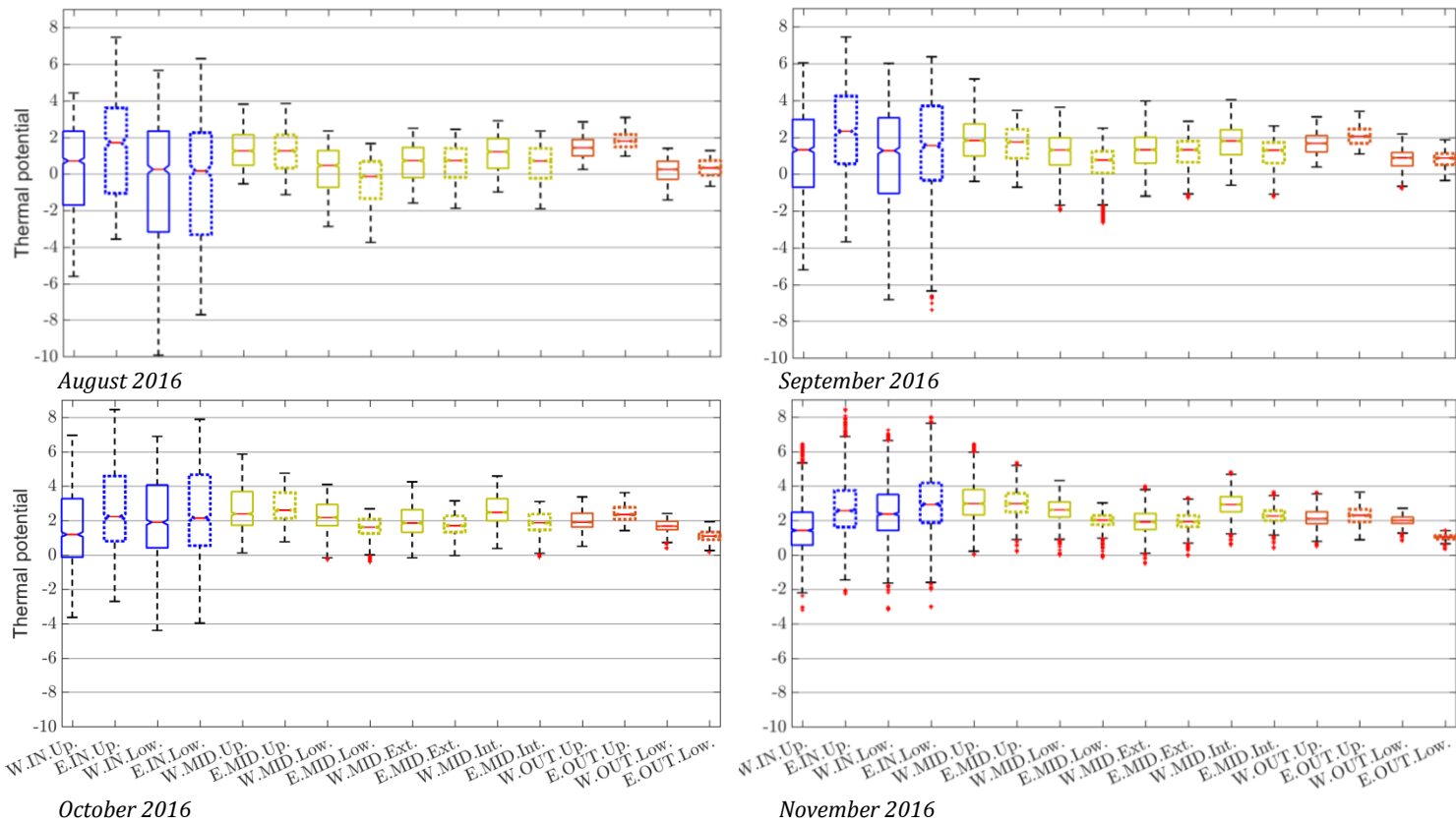


Figure 63: Monthly boxplot diagram of the thermal potentials within the foundations (full line: west wing, dashed line: east wing, blue line: inlet section, green line: middle, red line: outlet)

What has been previously exposed is concerning the contribution of each wall (upper, lower and verticals) for the heating and the cooling of the flowing air over short periods. However it is necessary to understand the dependencies of these fluxes to parameters such as soil temperature and moisture content. Facing that end, the thermal potential of the internal (respectively external) wall at the middle section is plotted on Figure 64 (c) (respectively (a)) as a function of the undisturbed¹⁰ soil temperature of the soil beneath the building (respectively the free-field soil) measured by the sensor SM7 (respectively SM4). The colour scale indicates the heating (or cooling) of the air through the foundation.

The heating of the circulating air seems to be well correlated to the thermal potential of the vertical walls of the middle section. For example, if the thermal potential ranges between 2 and 3 °C, the heating is around 5 and 10 °C. The air is cooled down if the thermal potential is less than 1 °C. These tendencies are true for all undisturbed soil temperatures. One can observe a slight global decreasing of the thermal potential with the soil temperature. However, this can be hardly interpreted. Indeed, the highest soil temperature are reached in mid-September, but this does not correspond to the highest ambient air temperature and consequently to the highest temperature decreasing by the foundation. Furthermore, the standard deviation of the regression curve indicated on Figure 64 (a) and (c) are relatively high (3.5 and 1.5 respectively), which means that the values are widely

¹⁰ The ground is assumed to be undisturbed at 2 m far from the foundation

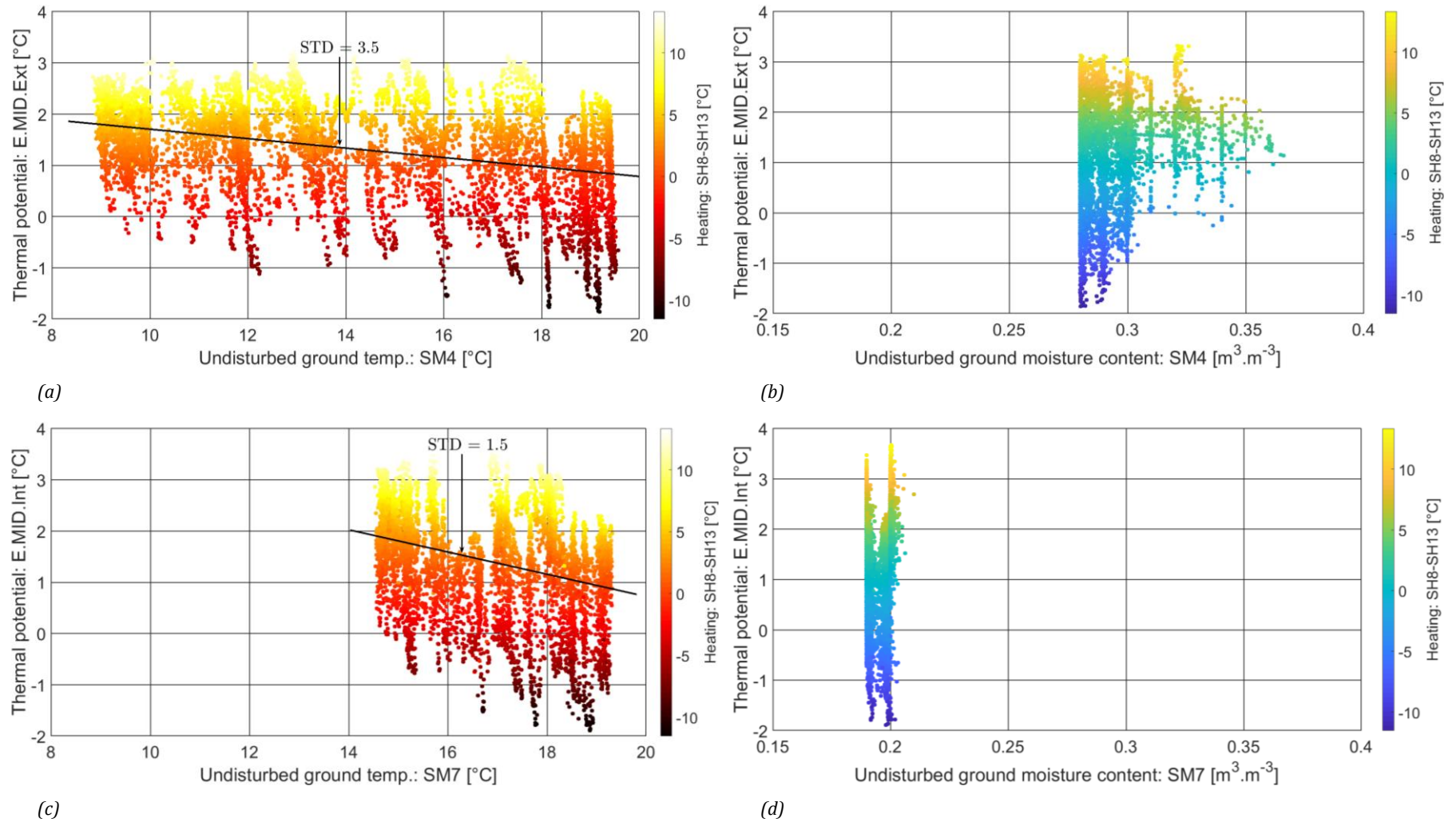


Figure 64: Impact of the ground temperature and water content on the flowing air heating / cooling

spread. The same work has been done with the ground moisture content as parameter instead of the ground temperature. The soil humidity of the crawl space soil does not vary a lot as can be seen on Figure 64 (d). No clear conclusions can be done. The humidity of the free-field soil varies more, but again no clear tendencies can be observed on Figure 64 (b).

6.3. CONCLUSIONS

In this chapter, an extensive instrumentation of the geothermal ventilated foundation and its surrounding soil as well as a weather monitoring have been carried out. Since numerous differences between a traditional EAHE and Fondatherm have been introduced in Chapter 1 – as for instance the low buried depth and the cross-section width which results in complex heat and moisture flow within the foundation - the position of the probes in both domains has been chosen in order to capture as far as possible the thermal and moisture gradient in the three dimensions.

The results concerning the airflow have shown that the ambient air temperature amplitude is strongly dampened, which increases the thermal comfort and in cases of a coupling with heat pump is intended, it can prevent frost formation and supply more stable cold source. The maximal heating and cooling power over one year is between 0.5 and 1.8 kW, in the average of EAHE power. Likewise the COP ranges between 1 and 7 throughout the year both for heating and cooling, which is consistent with the literature data available about EAHE. The mean daily energy gain is around 8.7 kWh for heating which is slightly better than traditional EAHE for similar airflow and buried depth. It is only around 3 kWh for cooling, which is consistent with the literature data available about EAHE. The strong asymmetry between heating and cooling time repartition can be found in the study of the half-sized Fondatherm. It reveals that the cooling performances are almost unchanged compared to the full length Fondatherm. Nevertheless, the heating performances are reduced by between 15 and 30% - which is still lower than 50%. This is consistent with the fact that first, a longer exchanger is required for heating purpose. Secondly, most of the thermal transfers occur over the first meter of the air-soil exchangers. Furthermore, these results should be taken with caution, as non negligible difference has been observed between the two first half (East and West) instrumented foundations.

The detailed study section by section and wall by wall of the thermal transfers confirmed that most of the heating and cooling potentials result from transfers in the first part of the exchanger. It also confirmed that there exists significant difference between Fondatherm and traditional EAHE. Indeed, the cooling power is mainly driven by exchanges with the lower wall, and second with the external wall. Given the usual size of the pipes, the heat flow through their surface is considered homogeneous. On the contrary, for Fondatherm, the heating power is mainly driven by the upper wall, and second by the internal wall. While the inlet section alternates throughout the year heating and cooling mode, the outlet section is mainly devoted to heating.

The next chapter will reveal the potential of the previously introduced models to reproduce this complex behaviour, by a careful comparison of the simulation results to the recorded experimental data.

Chapter 7. SIMULATION RESULTS - COMPARISON WITH THE MEASUREMENTS

7.1. INTRODUCTION

7.1.1 OBJECTIVES

The objectives of this part are related to the comparison between the models previously introduced and experimental data. Our analysis consists to identify the time range for which the agreement with the experimental data – widely introduced in Chapter 6 - is satisfying, and those for which the numerical models prediction are too far from experiments.

The reasons of these discrepancies would be analysed as they could be explained either by physics related to the conservation equations detailed in Chapter 3 that could be not fully representative of the reality in some specific cases. The reasons could also be numerical. It is possible that for the algorithm of resolution and the implementation of the conservation equations as exposed in Chapter 4 & 5 could appear to be badly adapted to the physical problem. Moreover, in order to identify the relative advantages and drawbacks of each model, and their potential to fulfil their own objectives (design tool for one, analysis tool for the other) an analysis to identify their limits of use is carried out. In order to carry out all of these cross-analyses, we suggest developing them in two stages.

The first step consists in analyzing the comparison of both models with the experimental results over short periods of fifteen days is well suited. It is indeed not too long to be able to visualize the whole simulation period, and long enough to be sure of the code stability and to be able to draw some relevant conclusions. This step will be used to answer the first objective. If the physics is the cause of the deviation of the model, this step could also enable to partially fulfil the second objective. All these points will be discussed in subsection 7.2.

The second step deals with the verification of the ability of the code to reproduce correctly the physics over long time periods. The validity of the code over short periods that will be analysed in the first step has to be extended. Furthermore, the global deviation or agreement of the codes with the measurements will be discussed. This will be made in the subsection 7.3.

7.1.2 PARAMETERS OF THE MODELS, SIMULATION PERIOD, AND DIVERGENCE PROBLEMS

The initial objective of the running of the model was to simulate the foundation over the experimental monitoring period (more than one year).

Measurements were gathered successfully from mid November 2015 to April 2017. The only blemish was that the rain gauge didn't work over a long period at the beginning of the measurement campaign. Indeed, the tipping bucket movement was limited for mechanical reasons, and the yielded rainfall were too low. This failure period lasted until mid July 2016. From the beginning of the measurement campaign to the end of this period, the rainfall data were replaced by the hourly data from the website infoclimat.fr¹¹. The data are for the Auxerre city, which is about 15 km away from the building location. This has to be kept in mind when comparing the soil surface water content yielded by the model and those obtained from the measurements.

Concerning the coupled heat and mass transfer model, some numerical divergence problems have failed the resolution of the equation over the whole period and still remain. Indeed, after simulation of several month, the time step for which the calculation is impossible (the 'skipped time step', see sub-section 4.6.2.1) multiply, sometimes consecutively such that the computation has to be stopped. For those cases, two solutions have been tried:

- The first consisting in restarting the computation with initial condition equals to the output of the code several hours or days before the latest calculated time step. This sometimes enables to continue the simulation for several hours or days, but the problem always repeat soon or later.
- Analysing the evolution of the convergence threshold (see equation (4.70)) the problem often appeared to come from the complex interface of the soil surface. Indeed, while the convergence condition is respected for all other meshes, the value of the convergence threshold for several meshes in a few centimetres below the ground top surface is at best steady but beyond the condition 10^{-6} , and sometimes continuously increasing. This seemed particularly true for summer conditions. However none clear correlations allowed us to prove this assertion. Following these observation, the boundary conditions has been identified as potentially tricky. The second solution consisted in slightly modifying the weather data to get around the problematic time step. In rare cases it allowed the computation to continue but the same problem reappeared several time steps later.

Neither efficient solution has been found to solve this problem, the origin of which seemed to be purely numerical. Nevertheless, in order to maximize the simulation period, the first solution has been used several times in May and June 2016 as the previously cited problem especially occurred from the end of April. This could be attributed to a greater variability of climatic conditions (especially regarding rainfall) during spring time. Even

¹¹ <http://www.infoclimat.fr/observations-meteo/temps-reel/auxerre-perrigny/07266.html?metar> (accessed September 2017)

though the total simulation period was limited, several months could still be successfully studied. The period retained in what follows extend from December 1, 2015 to June 22, 2016.

As explained in the section 6.1, even though the airflow rate is $435 \text{ m}^3 \cdot \text{h}^{-1}$ (which corresponds to an average cross-sectional air speed of $0.77 \text{ m} \cdot \text{s}^{-1}$ within the foundation cavity) according to the construction specifications, the measured air speed ($0.5 \text{ m} \cdot \text{s}^{-1}$) yields a much lower value around $290 \text{ m}^3 \cdot \text{h}^{-1}$. This latter value has been retained in what follows, and allow – in the view of the results introduced in the next sections – good agreement with the experimental data.

About the value initialisation, the soil temperature field has been determinate for both models according to equation (2.1). The exception is for the ground located below the building. From the water table to the base level of the foundation this temperature is incremented by $2 \text{ }^\circ\text{C}$. From the base level of the foundation to the soil top surface on the crawl space side, it is incremented by $+3.5^\circ\text{C}$. This was chosen in compliance with the SM300 measurements. The foundation temperature has been set in compliance with the Pt-100 measurements. The temperatures of the five sections have been set to 11, 13.5, 14.25, 14.5 and $14.5 \text{ }^\circ\text{C}$ in the direction of the flowing air respectively.

Similarly to (2.1) for the soil temperature evolution with depth and time, the initialisation of the soil matric head has been made using the following formula (7.1), the parameter has been set to fit with the water content measurements. The foundation capillary pressure is assumed to be homogeneous and equal to $-2.5 \cdot 10^6 \text{ Pa}$.

$$\Psi(z, t) = -2.5 - 10e^{-\frac{z}{3}} \cdot \sin\left(\pi \frac{z}{10}\right) \quad (7.1)$$

It is important to note that the skipped time steps - according to the algorithm description Figure 37 for the detailed hygrothermal model, Figure 49 for the sensible heat transfer model - is low, especially for the linear model (both for the full and the reduced model). Indeed, 19 divergence has been recorded for the full linear model, 29 for the reduced model, and 47 for the coupled heat and mass transfer model (including 37 for the soil model and 10 for the foundation model), which is respectively equal to 0.6 %, 0.4 % and 0.8 % of the total number of time steps. Therefore it can reasonably be assumed that the results are not affected by these steps.

Throughout this chapter, the simplified model taking into account only sensible heat transfers – introduced in Chapter 5 - will be designates by the term ‘linear model’. The detailed hygrothermal model will be designated by the term ‘coupled model’.

7.1.3 COMPUTATIONAL TIME

As introduced in Chapter 5, the linear model has been reduced in order to reduce the computational time. This has been done at the expense of the information yielded by the model. Indeed, the model returns only the values for the observed vector (defined by the equation (5.6)). The longer this vector is, the less efficient the reduction is. Consequently, the observed vector has been limited to the minimum required for the simulation. For the soil domain, these nodes are:

- At the interface soil / foundation,
- At the soil surface,
- At the soil surface facing the crawl-space.

For the foundation domain, these are:

- At the interface foundation / soil,
- At the interface foundation / crawl-space air.

The size of the full and the reduced models are given in Table 22. The reduction is not as efficient as might be expected, especially for the foundation domain, for which only 35% of the state variables are removed, while usually it is closer to 90 %. The soil domain reduction is closer to the usual performance with around 81% of nodes removed. This relatively modest reduction can be explained by the fact that the percentage of the nodes at the edges of the domain is really high, especially for the foundation. An important part of the system is therefore subject to external loads. Since the observed variables are given at the same nodes, they are very likely at the origin of observable and controllable modes. By comparison, the volume of the soil is much more important which means that the fraction of the nodes subjected to external loads is lower. Indeed, the size reduction of the soil domain is much higher than the foundation domain.

Table 22: Node number used for the reduced and the full linear model

| <i>Node number</i> | Reduced model | Full model | Reduction % |
|--------------------------|----------------------|-------------------|--------------------|
| <i>Ground domain</i> | 783 | 4060 | 80.7 % |
| <i>Foundation domain</i> | 769 | 1180 | 34.8 % |

Obviously the limited reduction of the system size restricts the computational time reduction between the full and the reduced model. With a Core i7 processor 2.7 GHz under Window 7, the computation time for the three models are given in Table 23.

Table 23: Computational time of the full and reduced linear model, and of the coupled model

| <i>Computation time (s / h)</i> | Linear reduced model | Linear full model | Coupled model |
|---|-----------------------------|--------------------------|----------------------|
| <i>Weather data assembling on a readable format</i> | | 2048 / 0.57 | |
| <i>Assembling the matrix system of equation</i> | 422 / 0.12 | 82 / 0.02 | 7 / 0.002 |
| <i>Resolution of the system</i> | 862 / 0.24 | 1630 / 0.45 | 62013 / 17 |
| <i>Total</i> | 3332 / 0.93 | 3760 / 1.04 | 64068 / 17.8 |

The computational time for the resolution of the equations of the reduced linear model is reduced by almost 50 % compared to the full model. Nevertheless, the assembling of the matrix system of equation is 6 times longer for the reduced model than for the full model, due to the reduction procedure. Considering both this CPU time (that for the assembling of the matrix system and that for its resolution), the reduction model is interesting. Nevertheless, the required procedure – that could be probably improved – to built the weather data file is long. Considering this time, the gain between the total computational time for the reduced and for the full linear model is negligible. Nevertheless, the reduction might be interesting for a multiple years simulation. The computational time of the coupled model is logically much higher given the complexity of the equations. It has to be noted that an important part of this time is attributed to the numerical problem cited above, mainly starting from May. To give an

idea, the required time to compute the solution from December 1 to April 30 is 27534 s or 7.6 h, corresponding to less than half of the total time.

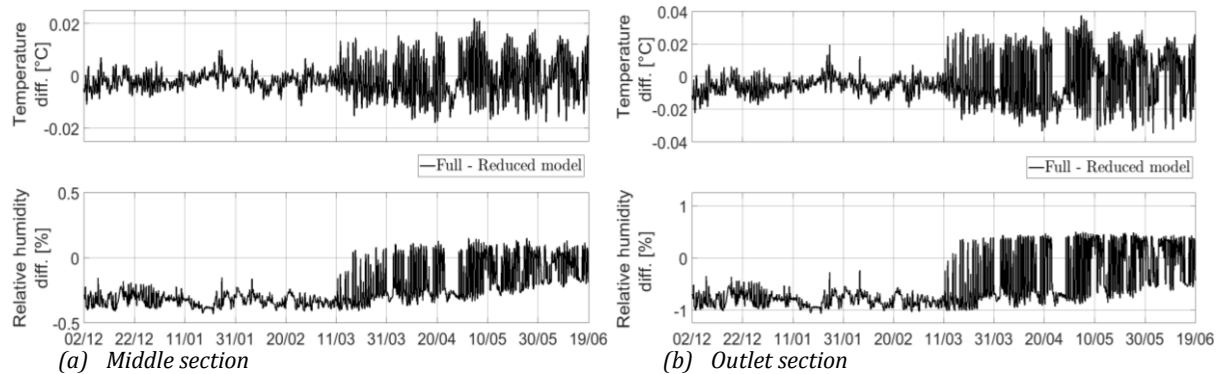


Figure 65: Comparison of the calculation from the full and from the reduced linear model: temperature and relative humidity differences at the foundation (a) middle section (b) outlet section

The comparison of the reduced and the full model is shown on Figure 65. Figure 65 (a) shows the airflow temperature and relative humidity differences observed between both models at the foundation middle section. Figure 65 (b) shows the same information at the foundation outlet section. In both cases, the agreement between both models is good: the absolute temperature difference does not exceed 0.04 °C and the absolute relative humidity difference 1%. Since the reduction is done at the detriment of information – the soil temperature field is not yield by the reduced model – the full model will be used in the following.

7.2. FOCUS OVER SHORT PERIODS

7.2.1 GLOBAL ANALYSIS OF THE COUPLED MODEL BEHAVIOUR

In order to ensure the global consistency of the complex coupled model, Figure 66 shows cross-sectional (a and b) and longitudinal (c and d) view of the temperature and the saturation level fields obtained from the models in winter conditions.

The deep ground is saturated and at around 14 °C. In keeping with the boundary conditions imposed, the soil below the building is hotter and dryer than the soil directly subjected to the weather loads. The soil surface is logically colder, around 5 °C. Surprisingly, it is dryer than what could be expected. This can be explained by the fact that first the December month was not rainy compared to the normal rainfall, and second, the considered day is probably still affected by the initial conditions.

Concerning the foundation, a heat flux coming from the building slab toward the concrete beam is highlighted by Figure 66 (a and c). The lower and the internal part of the foundation are close to saturation. This is the consequence of the change of material. Even if the soil is not saturated, the matric head potential leads to concrete water content values close to saturation. The external and the top walls are drier: their outer surfaces are indeed covered with an impervious bituminous coating. The airflow is logically heated up throughout the foundation cavity from about 5 to more than 10 °C. One can note that at the foundation outlet,

the air temperature is still colder than the ground (around 3 °C difference). The efficiency of the heat exchanger in heating mode is therefore not maximal.

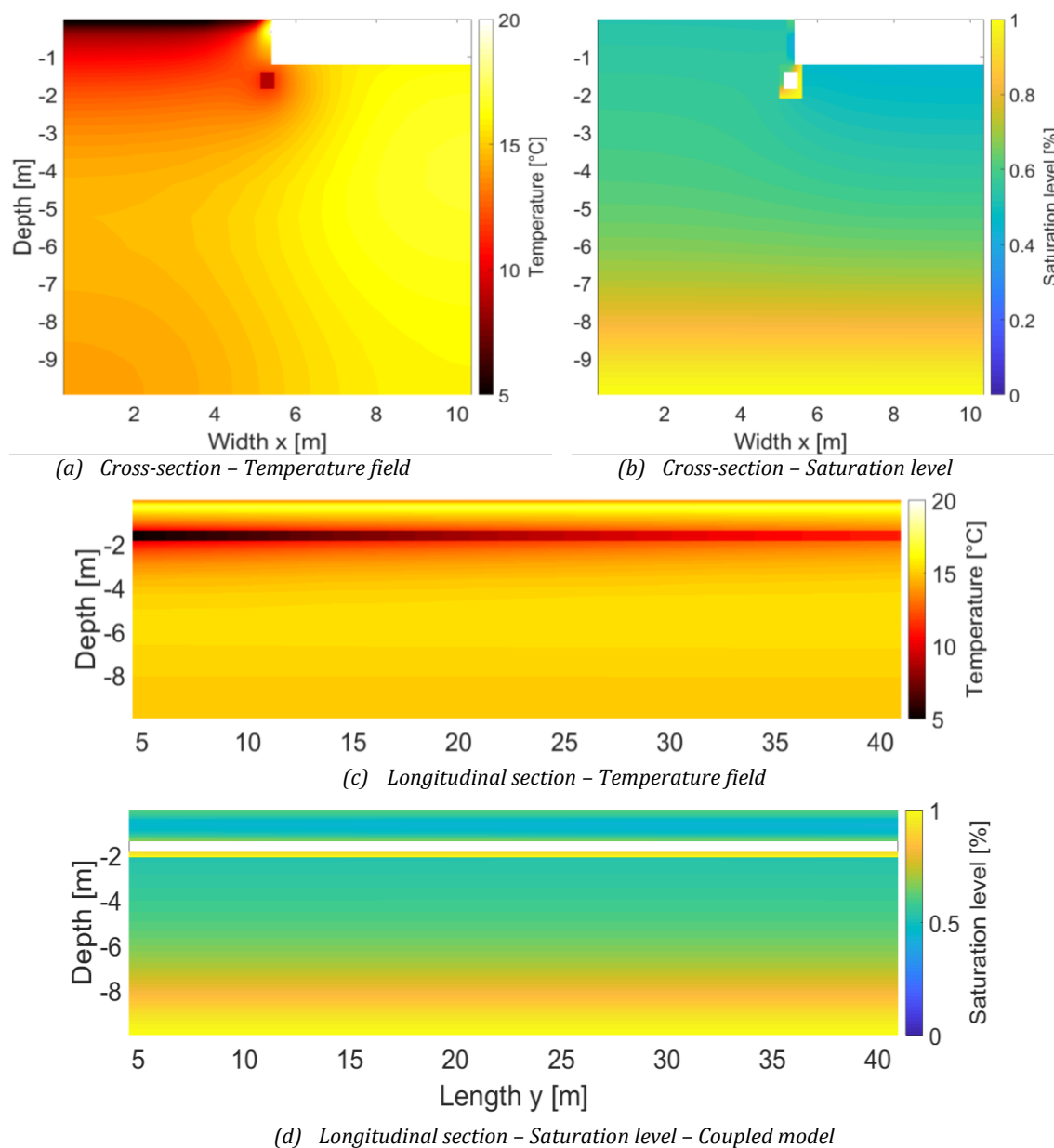


Figure 66: Temperature and water saturation level fields obtained from the coupled model - cross and longitudinal sections - 12 January 2016, 12h

A similar analysis but for spring conditions is done on Figure 67. The top left corner on the cross-sectional view of the saturation level (Figure 67 (b)) confirms that the global functioning of the model is good. Indeed, after a rainy period, the saturation level is higher than the soil above the building: the first two meters from the soil surface are at about 60 % of saturation. The soil beneath the concrete cover (next to the concrete beam) is dryer. The influence of this concrete layer is also easily identifiable on Figure 67 (a): since the albedo of this surface has been set lower than that of the lawn, it is much hotter. On the longitudinal view Figure 67 (c) one can see that the air is correctly cooled down by the foundation. It goes out at the ground temperature.

From a general point of view, one can note that both temperature and water content gradients are really low along the airflow direction. This is less obvious in the vicinity of the foundation. The choice of setting only 5 meshes along this direction thus appears as reasonable.

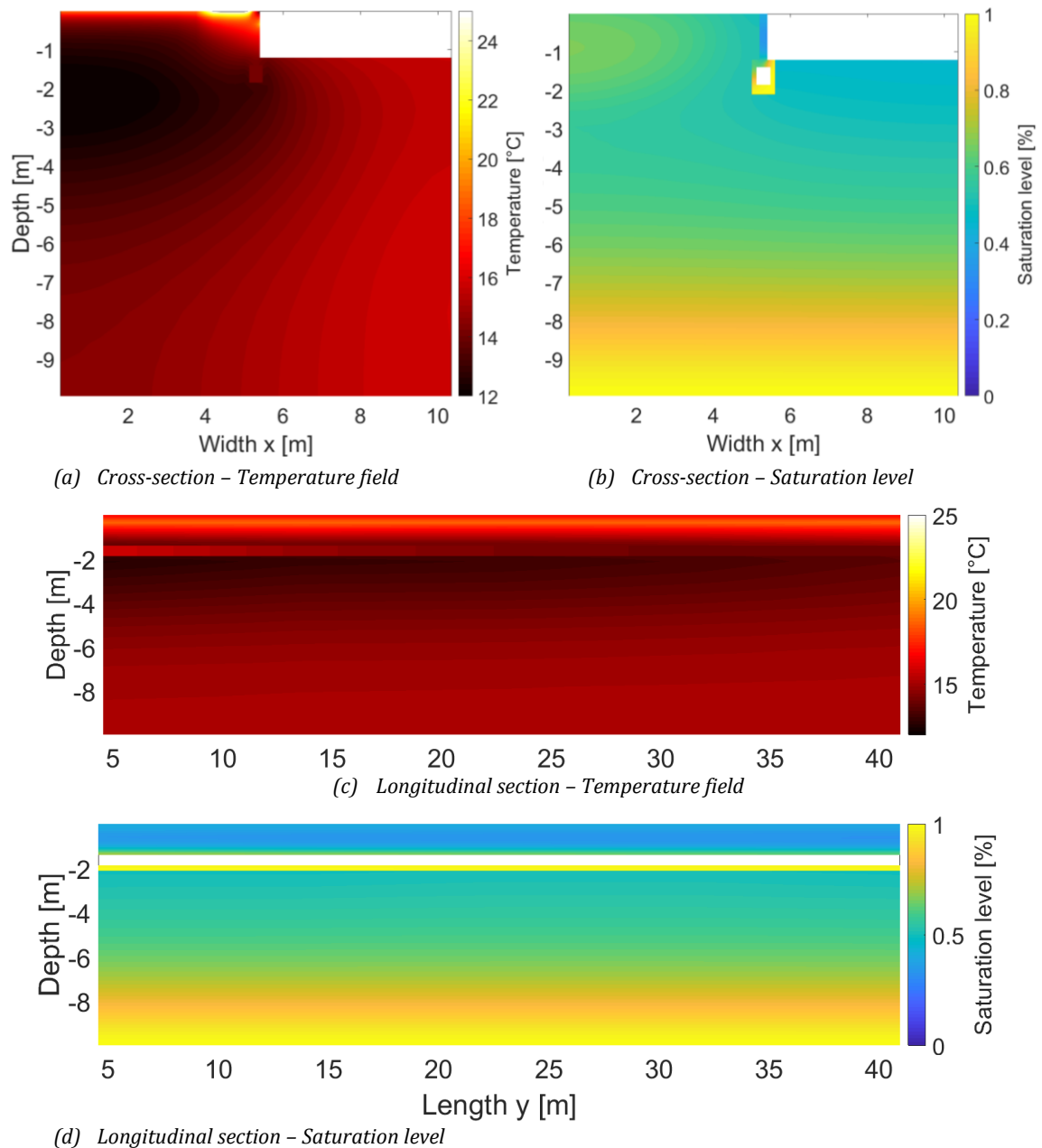


Figure 67: Temperature and water saturation level fields obtained from the coupled model - cross and longitudinal sections - 17 May 2016, 16h

7.2.2 TWO WINTER WEEKS

7.2.2.1. Focus on the soil domain

Figure 68 shows the results yield by the models concerning the soil beneath the building. First Figure 68 (a) shows the air temperature of the crawl-space calculated by the linear as

well as the coupled model. The tendencies are similar for both: the air temperature is almost constant around 18 °C. In addition, the air relative humidity is calculated by the coupled model, varying between 35 % and 70 %. As no measure has been done within the crawl space, the relevance of these values can hardly be discussed.

The study of the ground beneath the building at 40 *cm* depth gives more information. Figure 68 (b) shows that the soil temperature is really well reproduced by the coupled model, and slightly overestimated (about 2 °C) by the linear model. As in the observation made at the outdoor ground surface, the latter difference can potentially be explained by the absence of latent heat transfers.

With all the previous observation, one can consider that the ground model yields correct boundary values (both for the temperature and the humidity) to the foundation domain studied in the next subsection.

Figure 69 enables the comparison of the results obtained by the linear and the coupled model with the experimental measurements of the soil subjected to the outdoor loads. The studied period is from 5 to 20 January 2016. Figure 69 (a) shows the measured environment conditions, namely the air temperature, the total horizontal radiation and the rainfall. For the three other graphs ((b), (c) and (d)), the orange lines are the measurements returned by the SM6, 12 and 15 sensors, while the black full and dashed line are respectively the coupled and the linear model results. The yellow spindle represents the SM300 sensor uncertainties.

Figure 69 (b) focuses on the soil surface temperature and water content. The temperature is really well reproduced by the coupled model. The dark line is indeed most of the time within the uncertainty spindle. However, over or under-prediction appears very often for the linear model. This is apparently true when the temperature is maximal. The absence of the latent heat transfers in this model can be pointed out as a possible explanation for these discrepancies. Regarding the coupled mode, the moisture content is badly reproduced. However, the study of this short period cannot allow concluding about a poor performance of the code to reproduce the moisture transfers. The problem cited above (sub-section 7.1.) about the rain gauge means that perhaps the local rainfall are very different to the data in Auxerre taken from infoclimat.fr. The rainfall used for the model (Figure 69 (a)) are actually really low, and one can observe a slight increasing of the water content corresponding to the 0.5mm rainfall which means that the model response to the moisture load could be correct.

Figure 69 (c) shows the temperature and moisture content values of the soil at 80 *cm* depth. The trend and the values – in the upper limit of the uncertainties bounds – of the coupled model are in a good agreement with the measurements. The values returned by the linear model are also in agreement. Nevertheless, the variation seems too fast compared to the relative stability of the measurements. This could be explained by two reasons. The first is directly linked to what has been highlighted at the soil surface: the amplitude temperature returned by the linear model is too strong. The incoming flux is thus too high, and this potentially modifies the daily behaviour at 80 *cm* depth. The second valuable explanation is a bad estimation of the thermal properties – thermal conductivity, specific heat and density - of the soil. Regarding the water content, it is difficult to make conclusions since the values yield by the sensors are very different from one another. It is nevertheless possible to say that the moisture content returned by the coupled model is almost constant, compared to the

measurements. However, the default cannot be fully attributed to the model. Indeed, the SM300 sensors are screw at the end of a PCV tube, which - even though a great attention has been paid to the instrumentation - in some cases could drain water from the soil surface. This assumption is plausible since the water content (and temperatures) variations of SM5 sensor follows in synchrony that of the soil surface. This does not seem realistic as the water can hardly go through 80 cm of soil only in maximum tens of minutes.

Figure 69 (d) focus on the soil at 1.6 m depth. The linear model reproduces well both the values and the slow decreasing of the temperature. The coupled model follows the tendency of the measure relatively well, but the temperature is slightly overestimated by about 1.5 °C. Regarding the water content, the infiltration problem discussed above is removed at that depth. The values are almost constant for both the model and the measurements. The water content is a little bit under estimated. Both the discrepancies observed between the coupled model and the measurements may at that stage be partially explained by the choice of the hygrothermal properties of the soil. Since no information is available about the ground, it is almost impossible to choose the good retention curve, vapour diffusivity, etc. Regarding the little information we have, one can considers that the coupled model response is satisfactory, especially at ground surface.

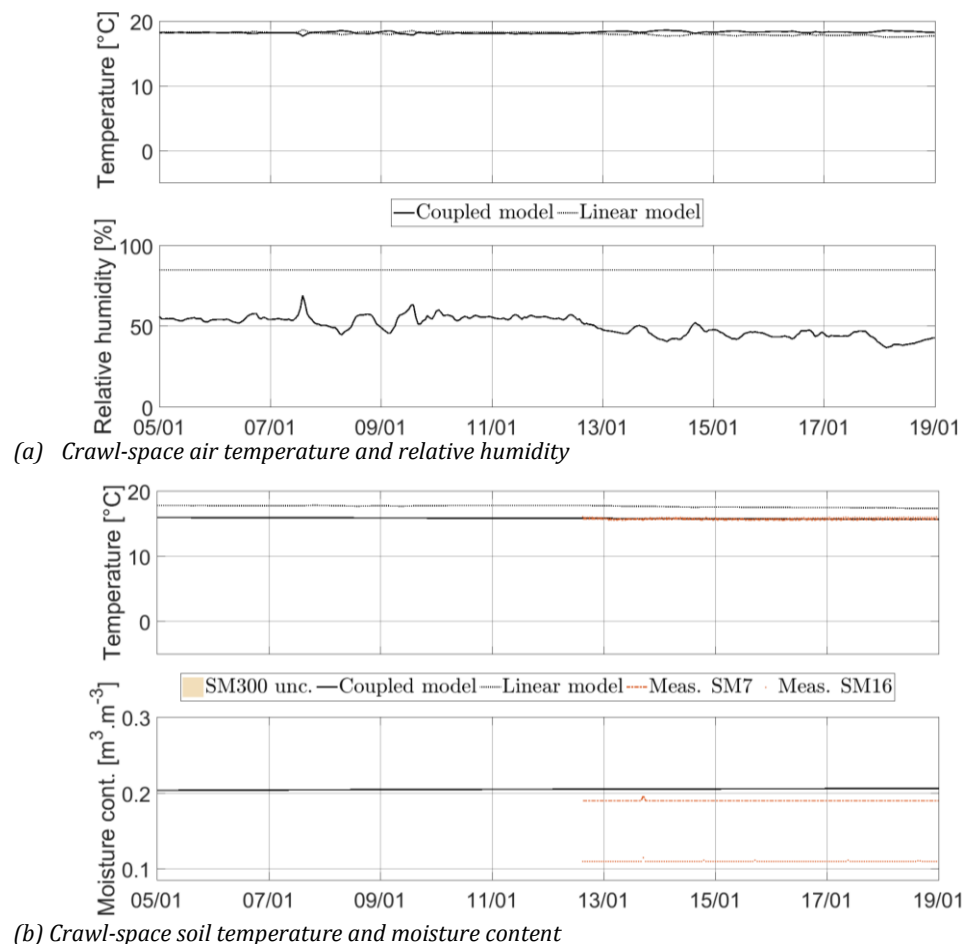


Figure 68: Crawl-space modelling results: (a) Air volume (b) Soil 42cm depth

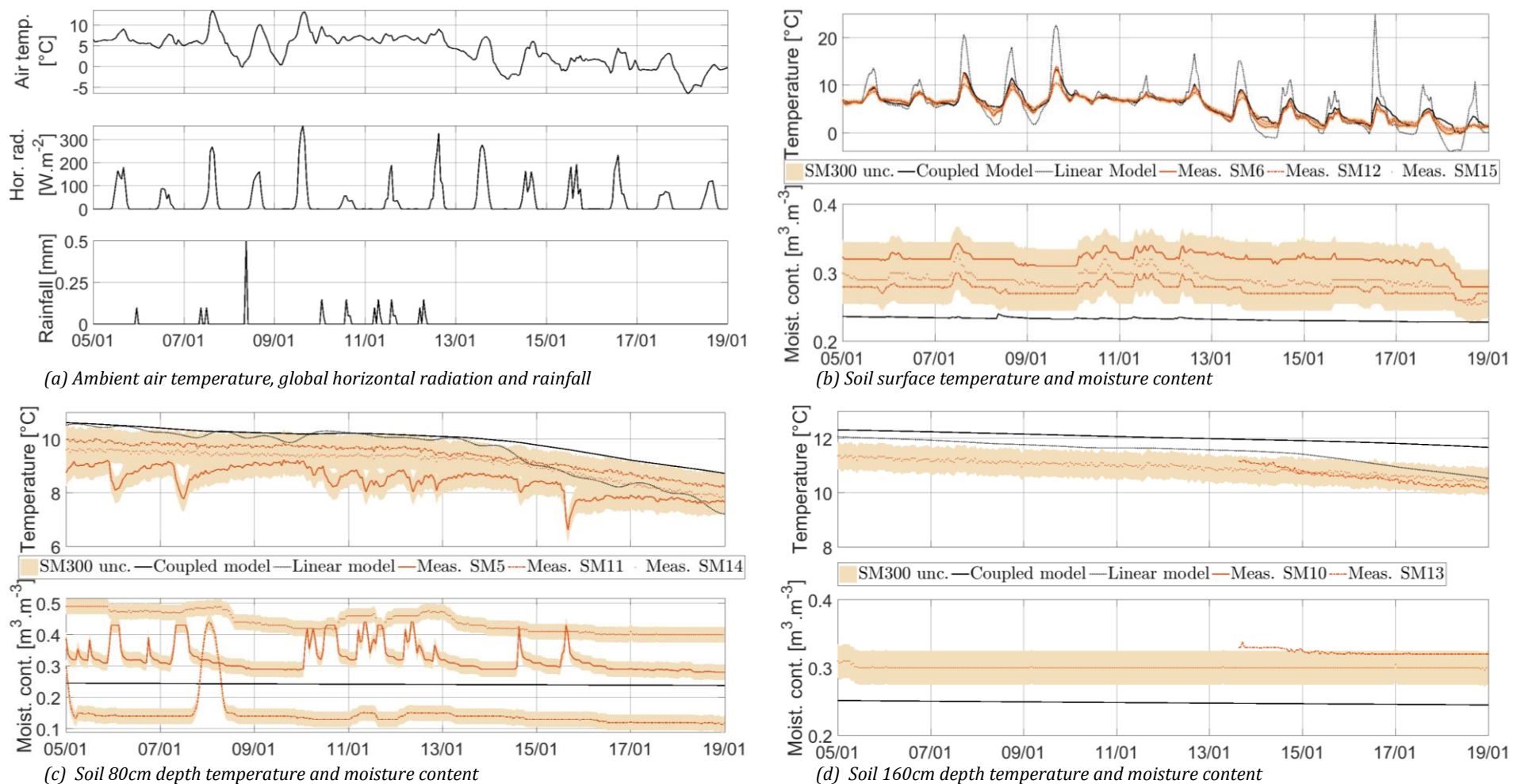


Figure 69: Ground free field measurements and modelling results: (a) Weather data (b) Soil surface (c) Soil 80cm depth (d) Soil 160cm depth

7.2.2.2. Focus on the foundation domain

This subsection represents the main focus of the study: the capacity of the model to accurately reproduce the foundation and the airflow behaviour. Figure 70 focuses on the foundation inlet section of the building west wing. Figure 70 (a) shows the airflow temperature and relative humidity used as input variable of the models. It is important to note that the vertical wall of the soil and the foundation inlet section has been modelled as adiabatic. This could be realistic at the middle section. However in reality, the weather potentially strongly influences this wall. Furthermore, the presence of the inspection manhole accentuates this influence.

Figure 70 (b) is the plot of the inner (i.e. within the cavity) horizontal walls surface temperature. Both upper and lower surface are well reproduced by the coupled model, and a maximal overestimation of 2.5 °C is observed. The differences with the values yields by the linear model are larger. Furthermore, the difference between the upper and the lower walls surface temperature is around 2.5 °C while the measurements show agreement between them. The differences are reasonable considering the modelling simplification cited above.

Figure 70 (c) and (d) are respectively the external and the internal outer walls surface temperature, measured at the same time by Pt-100 and SM300 sensors. The coupled model yields values in accordance with the SM300 sensors (less than 1.5 °C difference), however the linear model overestimates them by around 2.5 / 4.5 °C. The difference observed between the Pt-100 and the SM300 stems from the fact that they are not located exactly at the same place. The SM300 have been buried in the vicinity of the outer walls, while the Pt-100 probe is positioned on the outer wall in a small extension of Fondatherm at its entrance, in the inspection manhole. The influence of the ambient air temperature is thus higher for this probe; the SM300 can thus be considered as more representative of the reality.

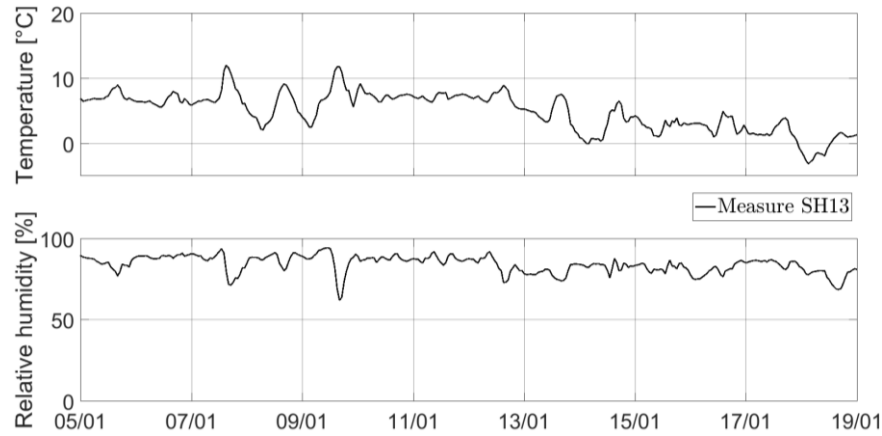
Figure 71 is concerning the foundation middle section. Regarding the airflow, Figure 71 (a) shows a good agreement of the temperature returned by the coupled model with the measurements. It is however slightly over estimated by maximum 1.5 °C. Overestimation from the linear model is more important and around 4 °C. This is in direct relation with the performance of the code at the inlet section since the airflow temperature was already overestimated there. The relative humidity variations are well reproduced by the models especially the coupled model. Nevertheless their values are underestimated by around more than 15 % almost all the time. Part of this difference is the consequence of the overestimation of the temperature values. In this context, it is hard to know if the moisture transfer between the flowing air and the walls surface are well reproduced.

Figure 71 (b), (c) and (d) shows respectively the inner horizontal, the outer vertical and the inner vertical walls surface temperatures. Contrary to the inlet section, the simultaneous temperature measurement of the external outer walls surface by SM300 and Pt-100 sensors is carried out at exactly the same position. This is confirmed by the accordance of the values. However, the position of the probe SM8 and PT19 could not be the same because of the presence of the inspection manhole. The PT19 is well positioned in the outer internal wall surface but in the manhole (see Figure 54). Consequently, it also measures the air

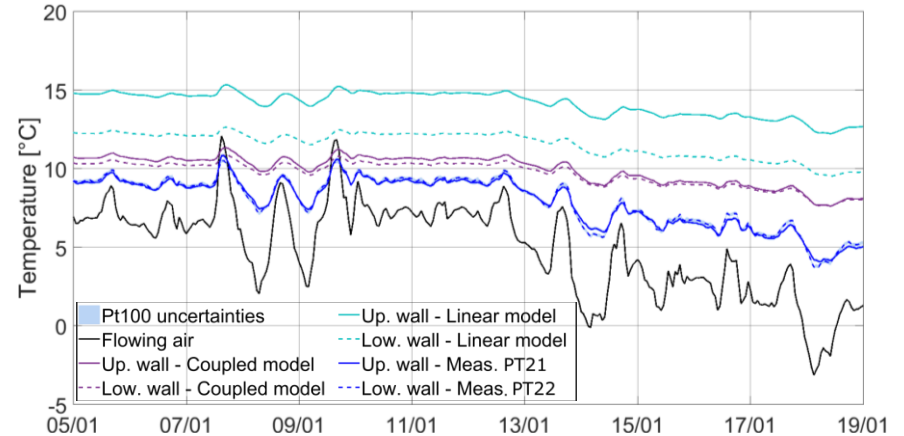
temperature of the crawl space. The values measured by the SM8 will be considered in the following as more representative. The agreement of the coupled model with the measurements is really good, even though it is most of the time beyond the uncertainty spindle. Once again the linear model overestimates the values, especially the upper, the inner and the outer internal walls surface temperature. This is very likely the consequence of the overestimation of the soil temperature of the crawl-space side, as highlighted in the previous sub-section.

Lastly, Figure 72 represents the outlet section of the foundation. Figure 72 (a) shows a really good agreement of the coupled model with both the measurements of air temperature and relative humidity. The yielded values are included in the uncertainty range around the measure. The linear model reproduces well the variations of both variables, but overestimates the temperature and underestimates the relative humidity of about 2.5 °C and up to 15 %. As previously, the relative humidity underestimation is mainly linked to the temperature overestimation. Figure 72 (b) also shows a good agreement of the upper and lower inner walls surface temperature returned by the coupled model with the measurements. The linear model once again overestimates them and differentiates the two walls. As for the middle section, the Pt-100 measuring the outer internal wall surface temperature (PT13) is positioned in the inspection manhole, and therefore is influenced by the crawl-space air. The SM17 probe, assumed to measure the same temperature, will be considered similarly as more representative. The agreement of the coupled model with the outer external wall surface temperature measured by the SM18 probe is quite good (Figure 72 (c)). The PT14 sensor yield really different values, which cannot be explained, except by a potential thermal load from the building north part. The outer internal wall temperature is overestimated by both the model. Potentially the measure is disturbed by an eventual additional thermal load neglected in the model.

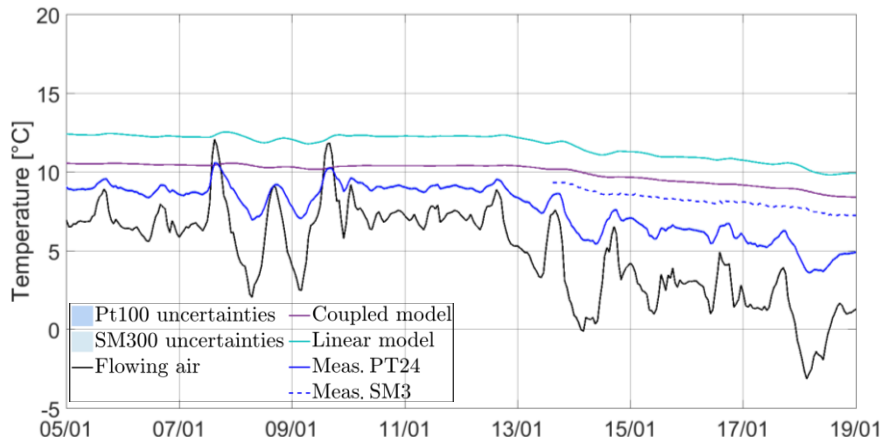
To sum up this sub-section, the ground, the foundation at the middle section and the airflow behaviour is really well reproduced by the coupled model over the considered period. This is especially true while considering the lack of information about the ground. Some additional external loads at the inlet and the outlet section not taken into account by the model can explain the observed discrepancies. The linear model is not as good. The absence of latent heat transfer at the soil surface (both outdoor and beneath the building) induces an overestimation of the influx and consequently of the temperature field. The study of the spring period in the next sub-section will indicate if this could also be due to a residual effect of the initial conditions or a bad estimation of the ground thermal properties.



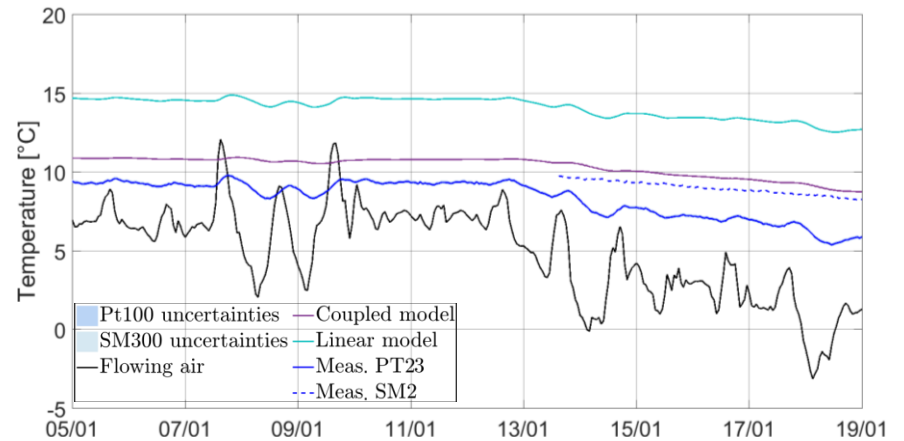
(a) *Flowing air temperature and relative humidity*



(b) *Upper and lower inner walls temperature*



(c) *External outer wall temperature*



(d) *Internal outer wall*

Figure 70: Foundation inlet section (section AA') temperature measurements and modelling results: (a) Flowing air (b) Inner walls (c) External outer wall (d) Internal outer wall

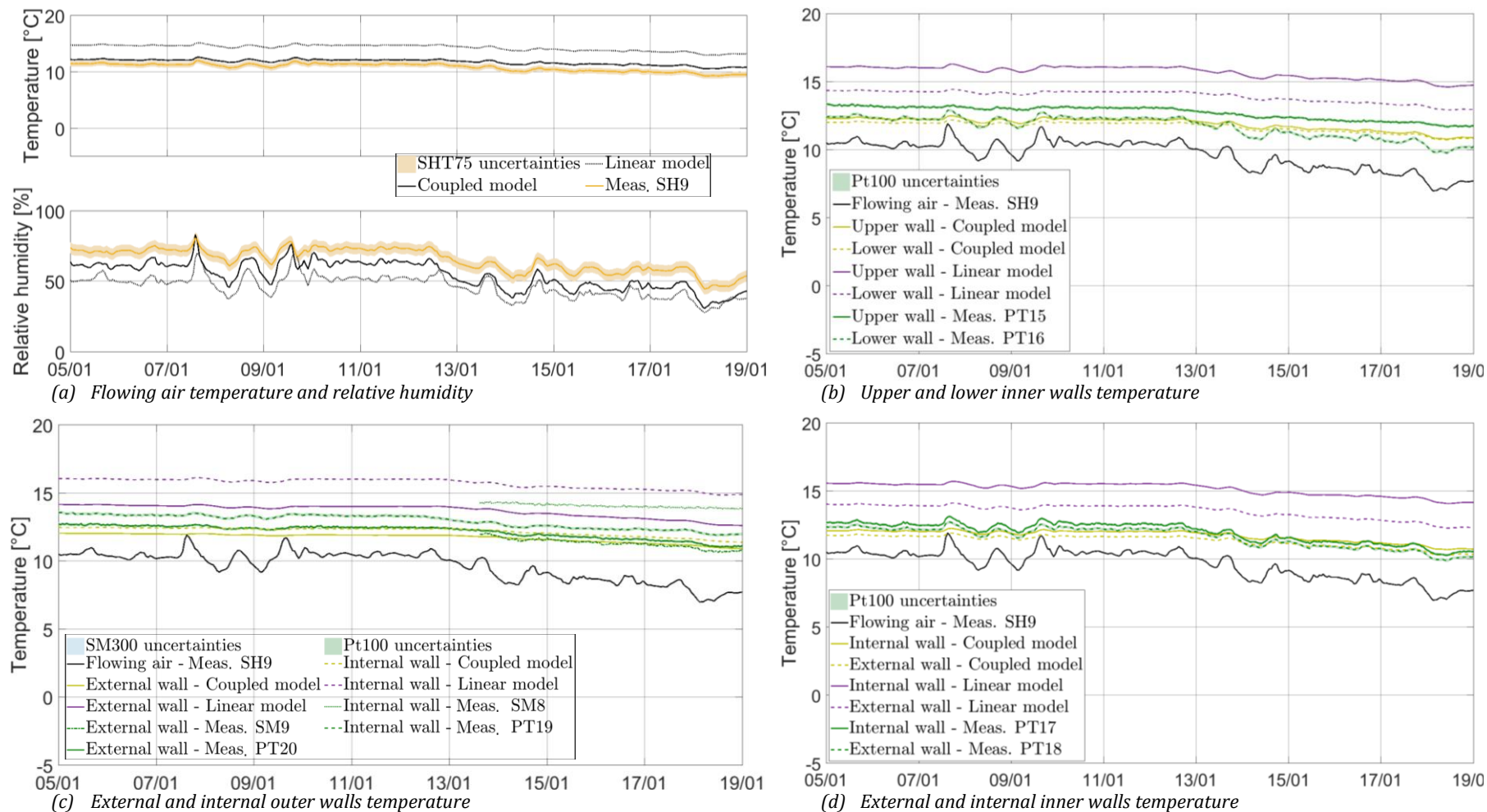


Figure 71: Foundation middle section (section CC') temperature measurements and modelling results: (a) Flowing air (b) and (d) Inner walls (c) Outer wall

TAURINES Kevin

CETHIL - INSA Lyon

2017

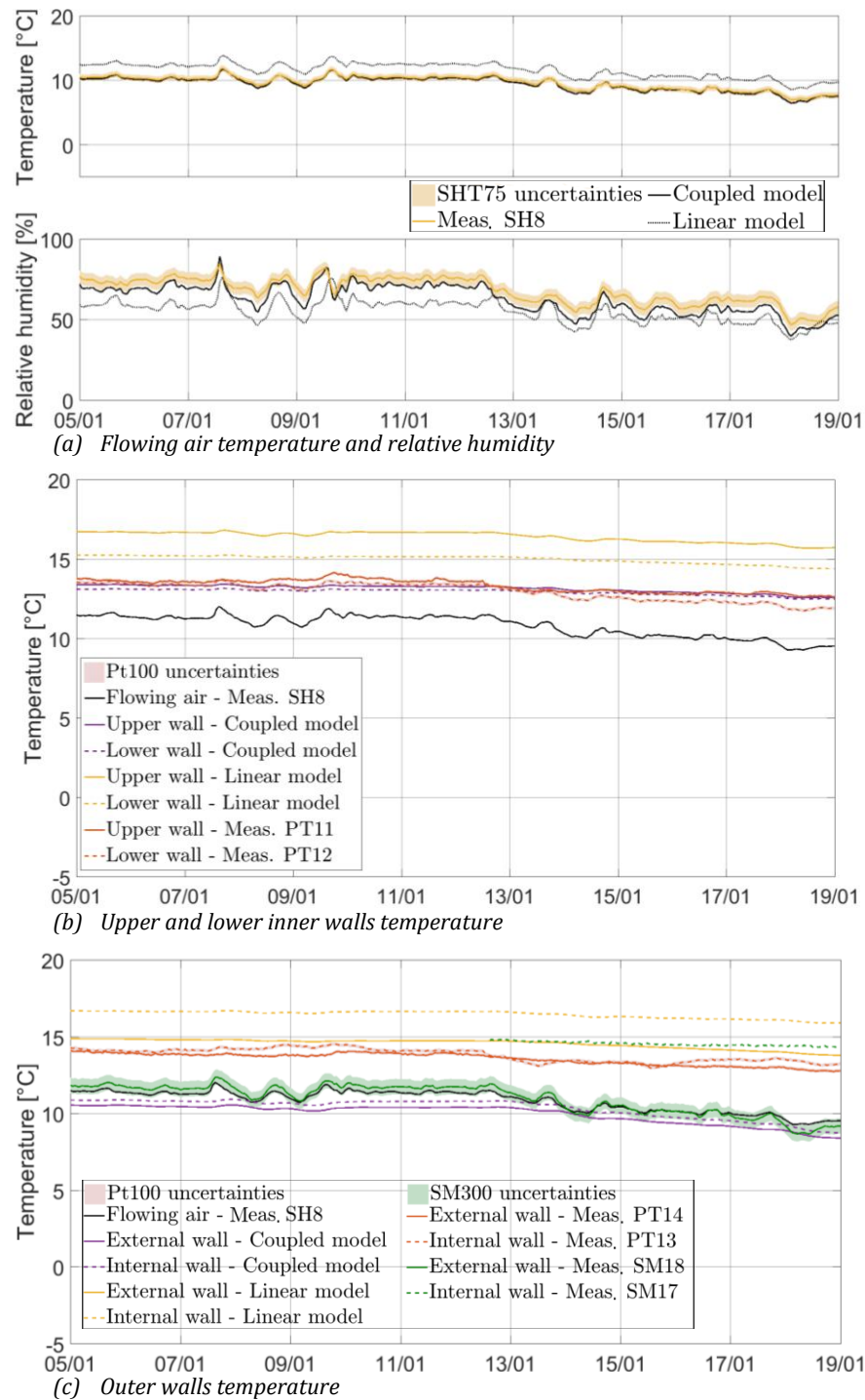


Figure 72: Foundation outlet section (section FF') temperature measurements and modelling results: (a) Flowing air (b) Inner walls (c) Outer walls

7.2.3 TWO SPRING WEEKS

7.2.3.1. Focus on the soil domain

Figure 73 is relative to the ground beneath the building. Figure 73 (a) shows the output of the models concerning the crawl-space air temperature and relative humidity. Their values are once again relevant but cannot be validated without measurements. Figure 73 (b)

indicates that the crawl-space model is quite good since the soil temperature and water content at 40 cm depth are well reproduced by the coupled model. The linear model overestimates the temperature.

Figure 74 is concerning the outdoor soil over two spring weeks from 5 to 25 May, 2016. Figure 74 (a) is about the weather data of this period. Contrary to the previously studied period, the rainfalls are multiples and correspond to moderate rain.

Figure 74 (b) shows that the soil surface temperature is still very well reproduced by the coupled model, but is really overestimated by the linear model when the radiation flux is high. The behaviour of the coupled model during rainfall is this time really good. The amplitude of the variation perfectly follows that of the measurements. They however are slightly underestimated by the model, which can be a default of the hygrothermal properties evaluation (for this period the deviation cannot be attributed to the effect of initial conditions).

In Figure 74 (c) and (d) are respectively plotted the ground state at 80 cm and 160 cm depth. The agreement of the temperature from the coupled model and the measurements is good. As a result of the previous observation for the soil surface, the linear model logically strongly overestimates the temperature in both cases. Similar remarks as mentioned in the previous sub-section can be done for the soil water content measurement. However, during this period, one can note a slight increasing from the 14 May of the water content at 80 cm depth then, with about one day time shift, at 160 cm depth. The coupled model seems to be able to reproduce the slow water movement within the soil, but not the faster ones at 160 cm depth as for example the episode of the 14 May.

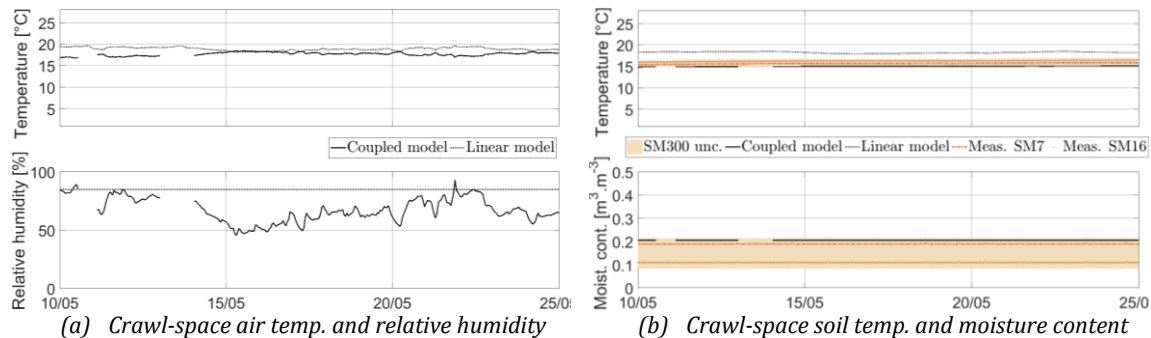
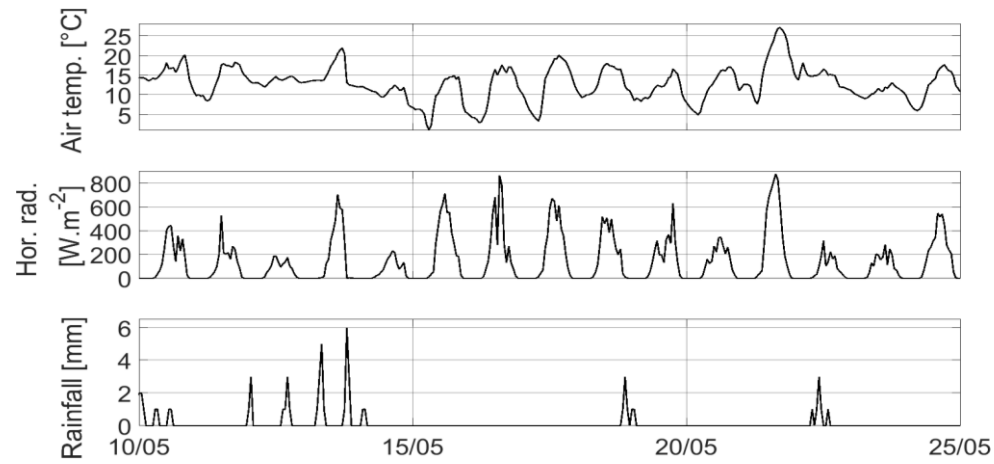


Figure 73: Crawl-space modelling results: (a) Air volume (b) Soil 42cm depth

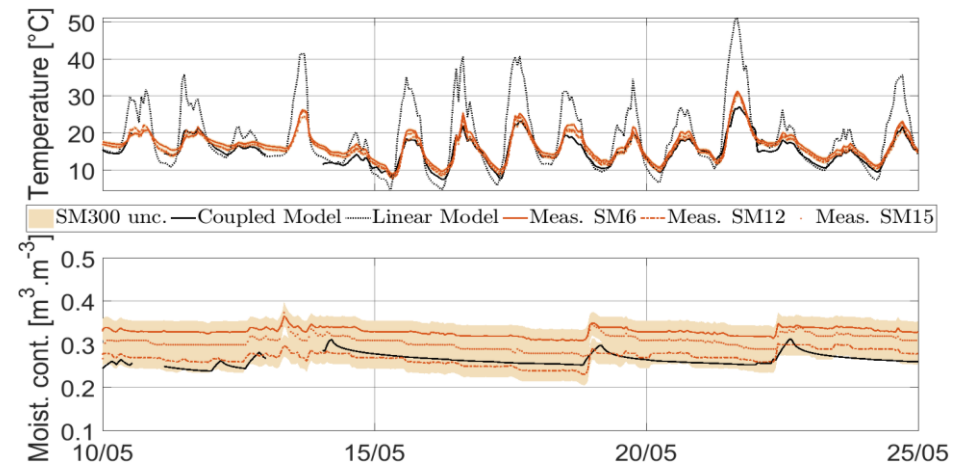
7.2.3.2. Focus on the foundation domain

Figure 75 is concerning the foundation inlet section, with the models input variable shown in Figure 75 (a) namely the flowing air temperature and relative humidity.

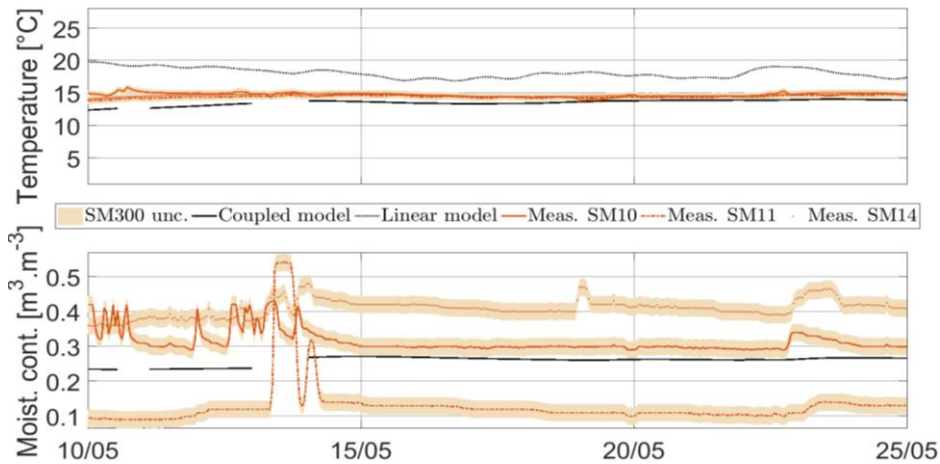
Figure 75 (b) focuses on the upper and lower inner walls surface temperature. The amplitude of their variation is higher than during the winter weeks that have been studied in the previous sub-section. These variations are dampened by the coupled model, even if the temperature range is correct. The linear model likewise dampens the oscillations, but also overestimates the values. It also, as previously, accentuates the difference between the lower and the upper temperature. The previous explanation - the soil temperature beneath the building is overestimated - is still valid.



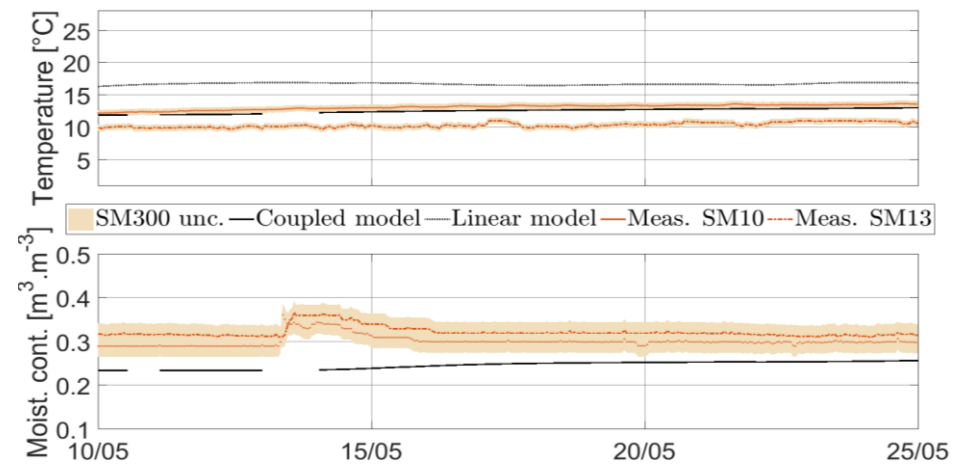
(a) Ambient air temperature, global horizontal radiation and rainfall



(b) Soil surface temperature and moisture content



(c) Soil 80cm depth temperature and moisture content



(d) Soil 160cm depth temperature and moisture content

Figure 74: Ground free field measurements and modelling results: (a) Weather data (b) Soil surface (c) Soil 80cm depth (d) Soil 160cm depth

Figure 75 (c) focuses on the outer external walls surface temperature. The coupled model agrees well with the SM3 measure - less than 1 °C differences are observed whereas the linear model overestimates it. For the other side, the coupled model underestimates the temperature by around 2 °C, but the slight variations are well reproduced. For this latter case, the measure can be questioned instead of the model, since the SM2 was not positioned from the inspection manhole but from the soil surface. It could result in a displacement of several centimetres far from the outer internal wall surface. The linear model is in agreement with the measure at that point, but given the previous explanation, this is not really reliable.

Figure 76 depicts the behaviour of the foundation in its middle section. Figure 75 (a) highlights a really good agreement between the airflow temperature measured and the returned values by the coupled model. The linear model reproduced really well variations but overestimates the measurements by about 2.5 °C. The relative humidity evolution is not really well reproduced by both models especially the linear model. Nevertheless, the values yields by the coupled model are close to the measurements. These discrepancies can hardly be explained.

Concerning the inner walls (Figure 76 (b) and (d)) the coupled model still reproduces reasonably well the measurements, with moderate difference (less than 2 °C), and the linear model overestimates it by about 3 °C / 5 °C. This can be certainly attributed to a combination of a bad estimation of soil thermal properties and crawl-space soil temperature overestimation. Similar remarks can be done for the outer walls as shown in Figure 76 (c).

Figure 77 finally concerns the outlet section. About the airflow (Figure 77 (a)) behaviour reproduction by the models, a similar analysis than for the middle section can be done. The upper and lower inner walls surface temperature (Figure 77 (b)) are well reproduced by the coupled model but are slightly underestimated, while the linear model overestimates it. Finally, the outer external and internal walls surface temperature (Figure 77 (c)) are underestimated by the coupled model and slightly overestimated by the linear model. Regarding the relatively good agreement of the coupled model at the two first sections, the assumption of an additional external load, maybe caused by the presence of the north part of the building and not taken into account in the model, appears as more and more credible.

The long term performance of the model has to complete this short term analysis, in order to obtain a more general understanding of the proposed modelling. This has been carried out in the next sub-section.

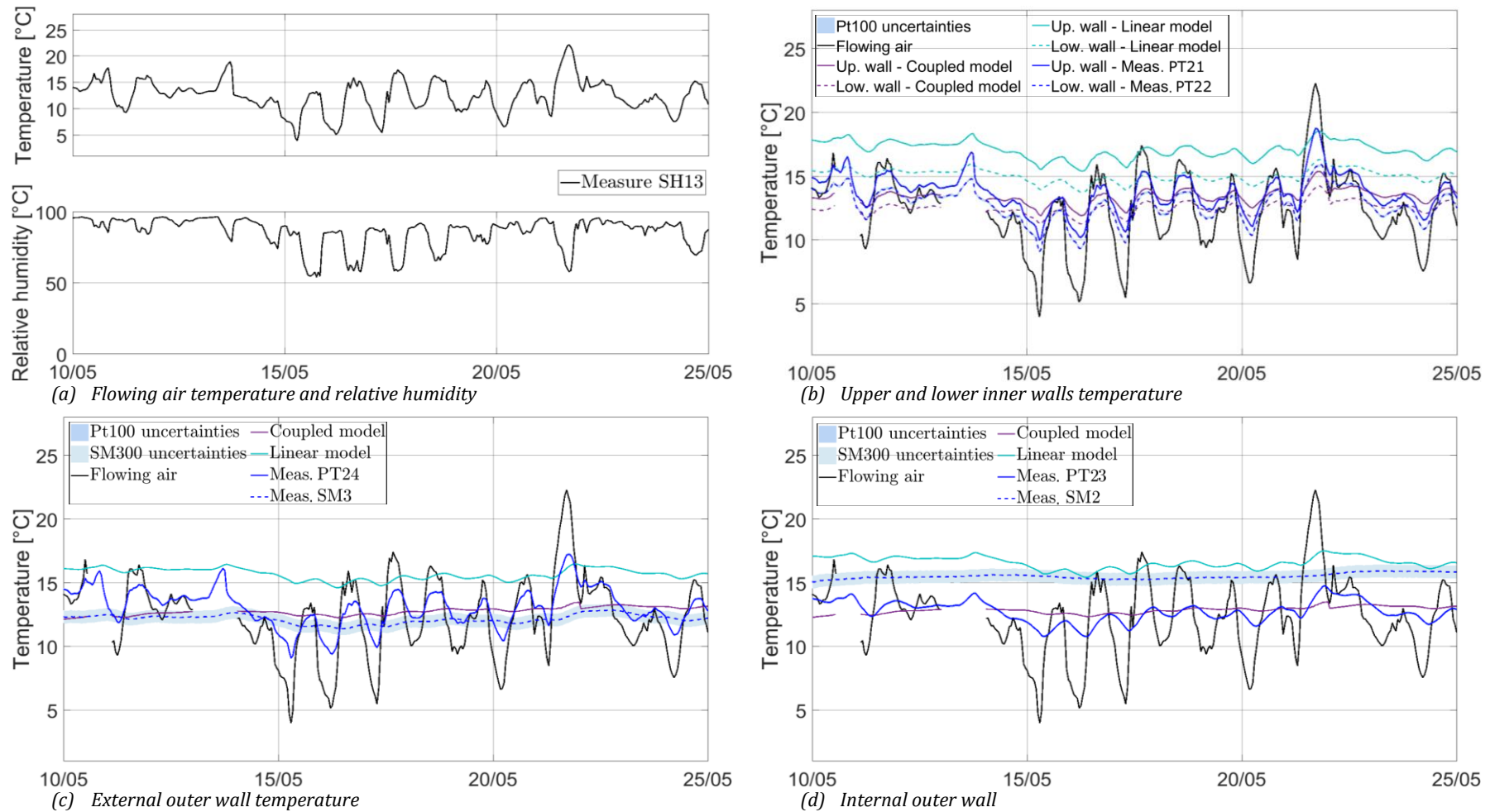


Figure 75: Foundation inlet section (section AA') temp. measurements and modelling results: (a) Flowing air (b) Inner walls (c) External outer wall (d) Internal outer wall

TAURINES Kevin

CETHIL - INSA Lyon

2017

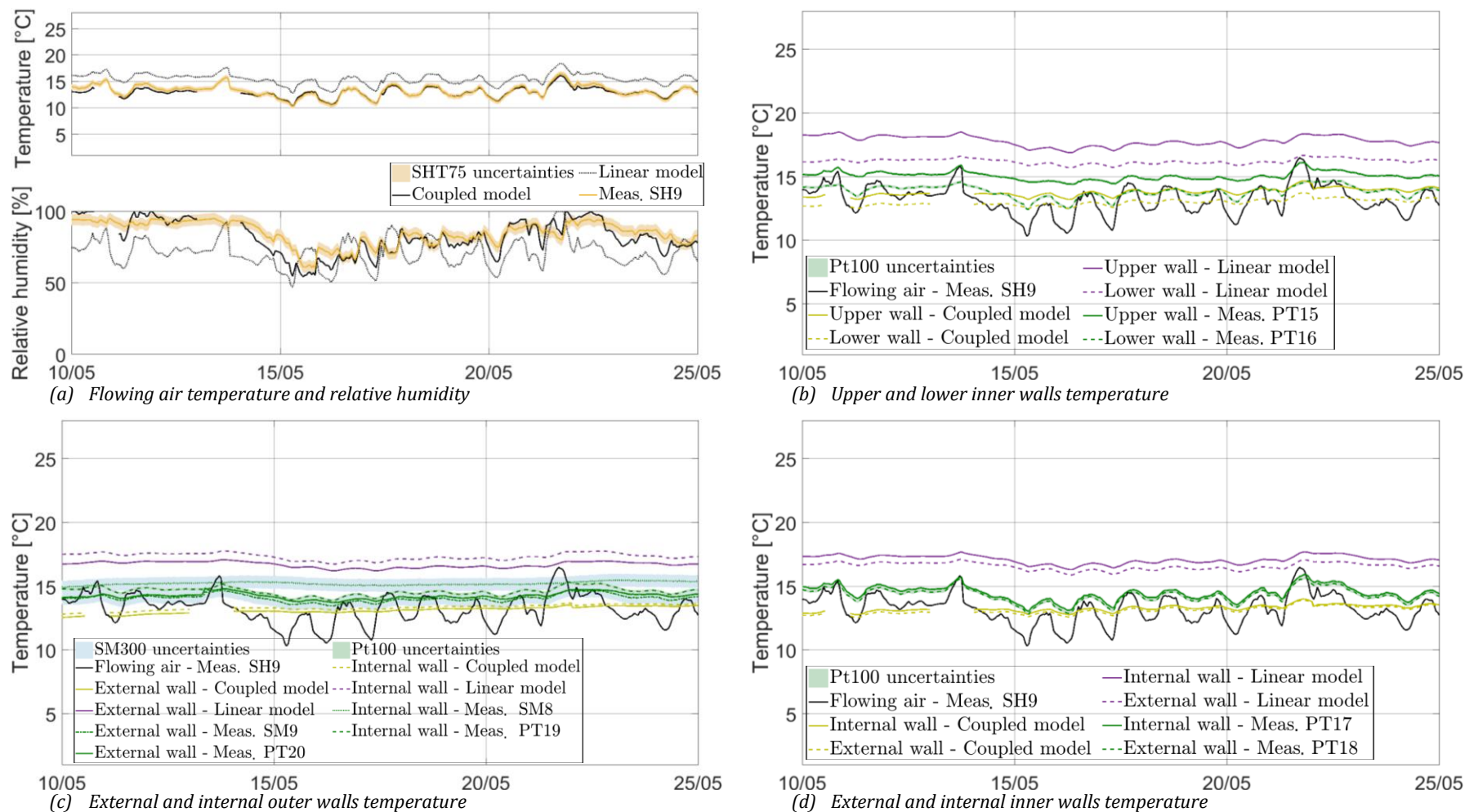


Figure 76: Foundation middle section (section CC') temperature measurements and modelling results: (a) Flowing air (b) and (d) Inner walls (c) Outer wall

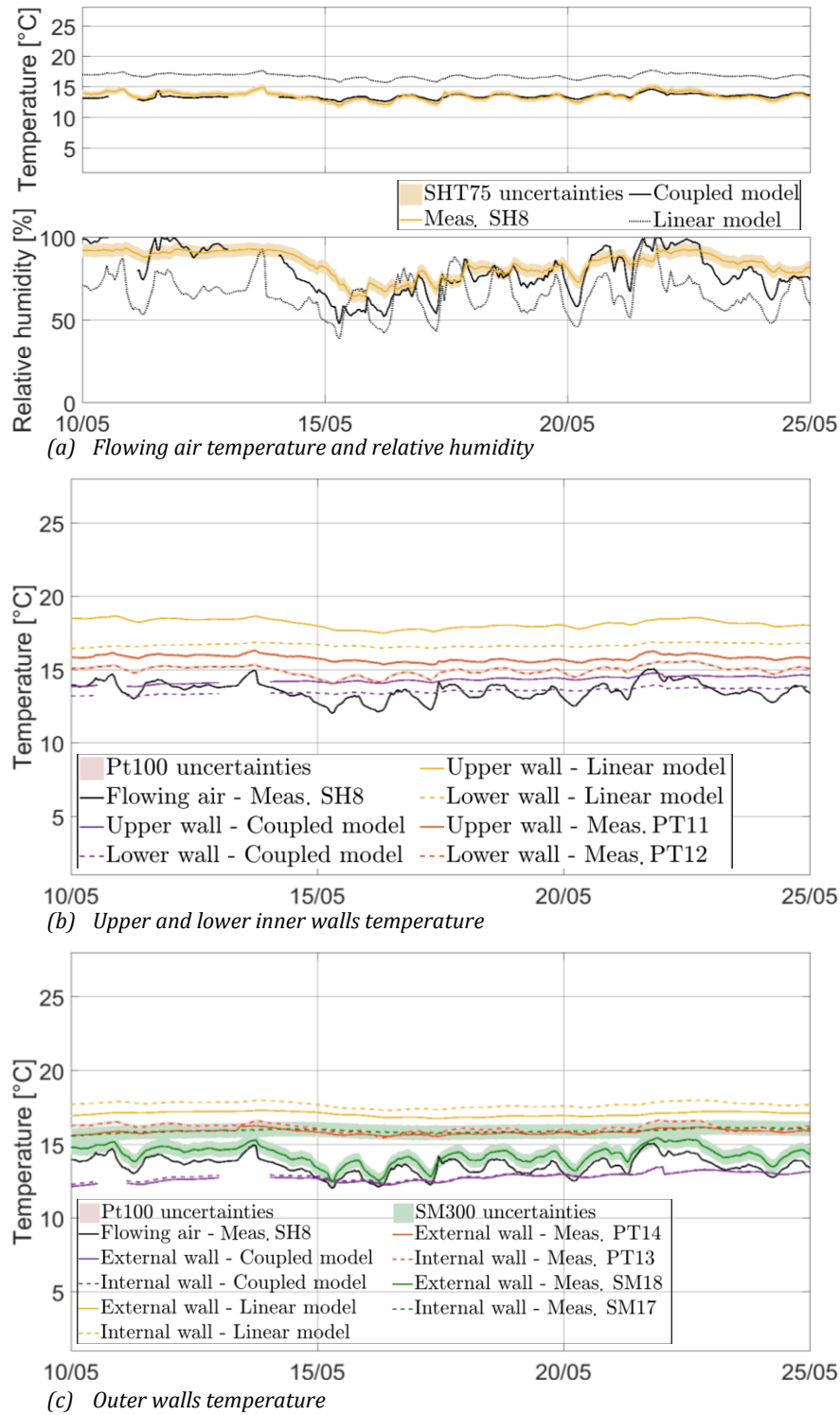


Figure 77: Foundation outlet section (section FF') temperature measurements and modelling results: (a) Flowing air (b) Inner walls (c) Outer walls

7.3. ANALYSIS OVER SIX MONTHS

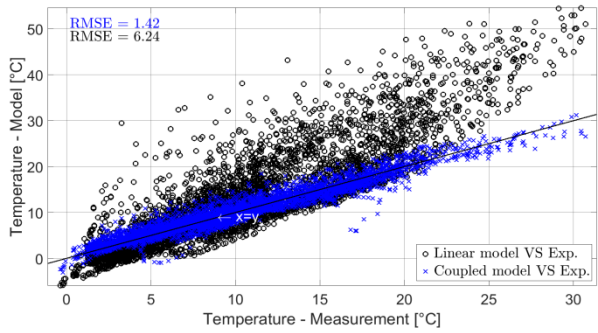
In this section a global analysis over the full simulation period (1 December 2015 to 22 June 2016) is made. The graphs that are representing the measurements on abscissa axis and the corresponding modelled values on ordinate axis are plotted and enable to evaluate the correlation 'Model / Measurements'. The root mean square error (RMSE) is the chosen indicator of the global ability of the model to reproduce the measurements. It is systematically calculated on every figure. Another approach has been proposed and consists in analyzing the difference measurements / numerical results, and is available in Appendix G. As previously, the study will first focus on the soil, then on the foundation.

7.3.1 FOCUS ON THE SOIL RESULTS

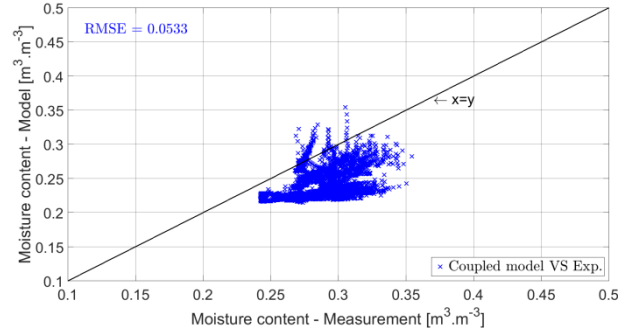
Figure 78 (a) is the numerical versus the measured soil surface temperature. The agreement of the coupled model throughout the (almost) seven considered months is really good. From the lowest temperatures (around 0 °C) to the highest (around 30 °C), the deviation from the $x=y$ straight is low: the RMSE is lower than 1.5 °C. In opposition, the deviation of the linear model from the $x=y$ axis is important and increasing: the higher the measured temperature, the larger the discrepancy. If the measured temperature is around 30 °C, the model yields 50 °C. The RMSE is over 6. The suggestion to explain such difference was the absence of the latent flux, which seems reasonable given the fact that this flux is increasing with solar radiation and temperature. Figure 78 (b) shows the water content modelled versus measured at the same level. It is globally under-predicted but it follows the $x=y$ trend.

At 80 and 160 cm depth (Figure 78 (c), (d), (e) and (f)), the models behaviour are similar. Since the coupled model reproduces correctly the heat and moisture transfer at the surface, the temperature at 80 and 160 cm are also well reproduced. The remaining small deviations (RMSE around 0.9 in both cases) can eventually be explained by an incorrect choice of the soil hygrothermal properties. On the contrary the water content is not well reproduced. The results yield from the model is almost constant around $0.25 \text{ m}^3.\text{m}^{-3}$ over the period, while the measurements vary from 0.25 to $0.5 \text{ m}^3.\text{m}^{-3}$. Since the ability of the model to correctly reproduce liquid and vapour flows within a soil column, the remaining assumptions to explain these discrepancies are a measurement problem or soil thermohygric settings non representative of the soil considered. The linear model results are acceptable but not as good as the coupled model since the RMSE is around 2.5 against about 0.9 for the coupled model.

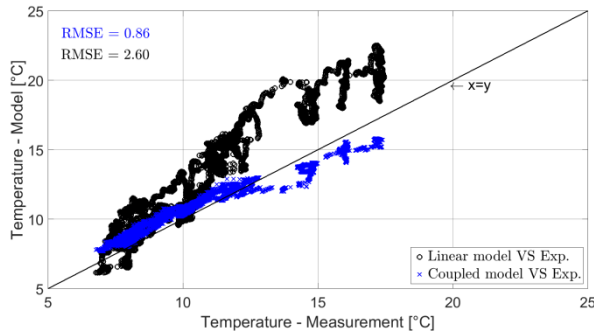
Considering the soil beneath the crawl-space, Figure 78 (g) shows that the slope of the straight created by the point (coupled model, measurements) is higher than that at $x=y$. Nevertheless, the distance to the latter is low, since the RMSE is only about 0.7 against 2.4 for the linear model. The absence of latent transfer can explain the overestimation. About the water content Figure 78 (h), only a few measurements are available and do not enable us to conclude. But since the quantities of liquid water transfers are low, the soil saturation level is potentially constant except close to its surface.



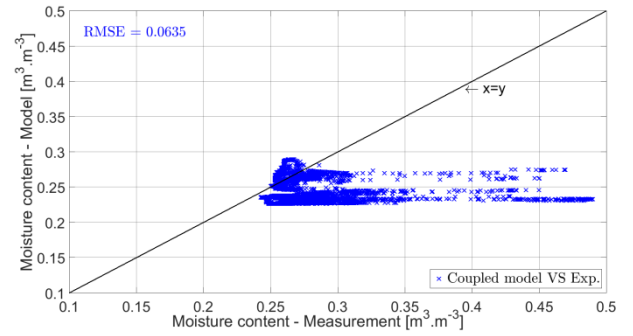
(a) Ground surface temperature



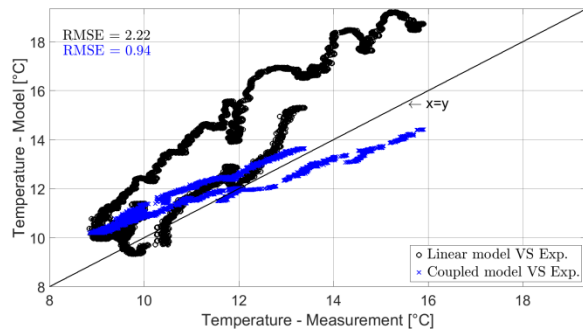
(b) Ground surface moisture content



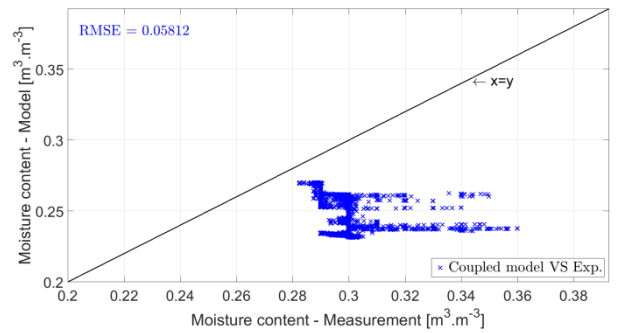
(c) Ground 80 cm depth temperature



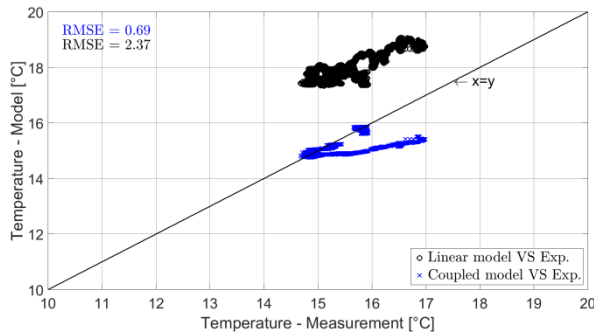
(d) Ground 80 cm depth moisture content



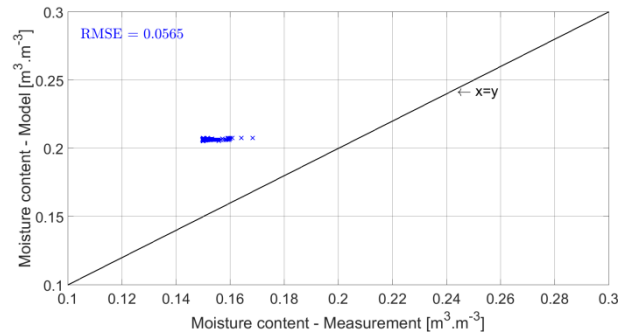
(e) Ground 160 cm depth temperature



(f) Ground 160 cm depth moisture content



(g) Crawl-space soil temperature



(h) Crawl-space soil moisture content

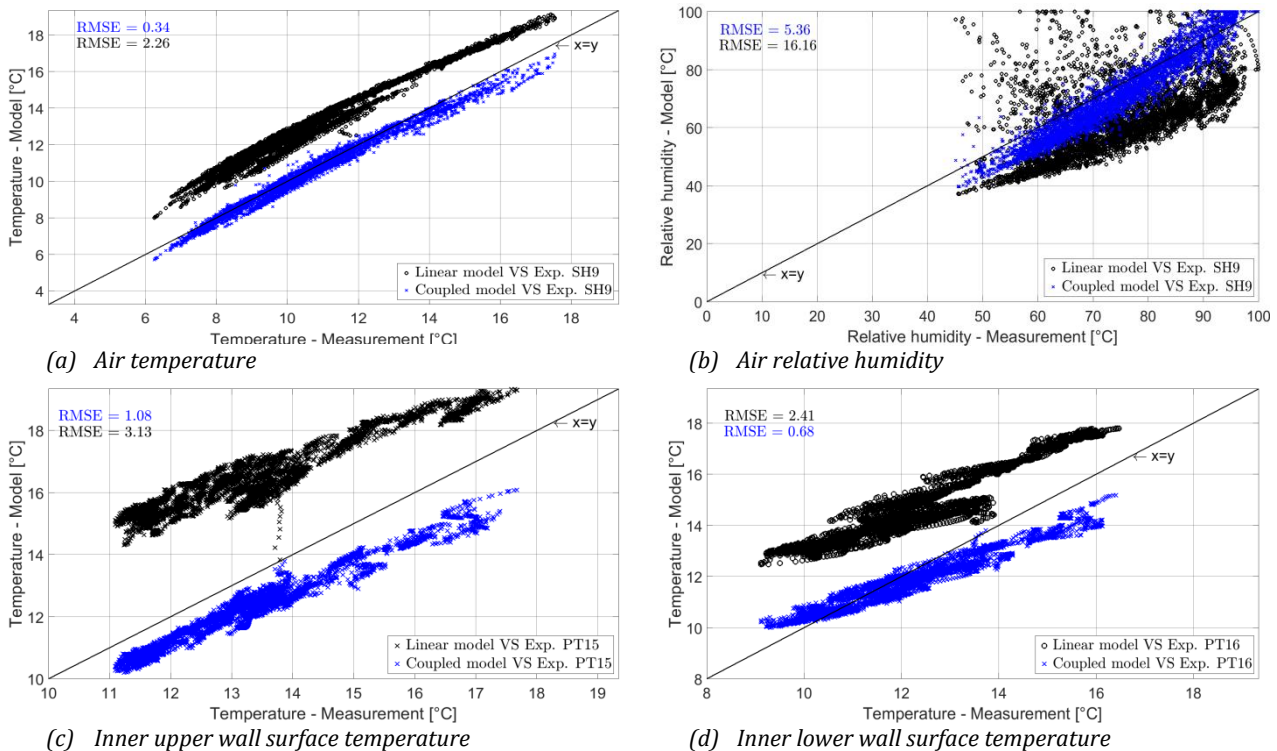
Figure 78: Ground modelling results versus measurements: Surface (a) temp., (b) moist. cont., 80cm depth (c) temp., (d) moist. cont., 160 cm depth (e) temp., (f) moist. cont., Crawl-space soil (g) temp., (h) moist. cont.

7.3.2 FOCUS ON THE FOUNDATION MIDDLE SECTION RESULTS

The analysis of the foundation modelling results only focus on the middle section, since the inlet and the outlet section has been previously identified as potentially affected by the presence of the inspection manhole, the outdoor or the north part of the building. Figure 79 (a) and (b) shows the results concerning the air temperature and relative humidity. The coupled model yield almost perfect results for both. The deviations measured by the RMSE are respectively 0.34 and 5.4, which is in the order of magnitude of the measurement uncertainties. The performances of the linear model are not so good. The temperatures are systematically overestimated but almost constantly. The linear foundation cavity model can thus not be questioned and the problem is certainly linked to the soil modelling. The relative humidity is logically under-predicted most of the time but also strongly over-predicted. The mass transfer model within the cavity should be analyzed in order to explain the observed difference.

Concerning the prediction of the inner walls surface temperature, they are of course correlated to the prediction of the airflow temperature. Figure 79 (c), (d), (e) and (f) shows that all these values are well reproduced by the coupled model with RMSE always around 1, while the linear model over predict it systematically. All these observations confirm the trends shown by the studies over the two fifteen day's periods.

The ability of the model to represent the outer wall surface temperature is finally shown on Figure 80. Once again the coupled model is more trustworthy than the linear model.



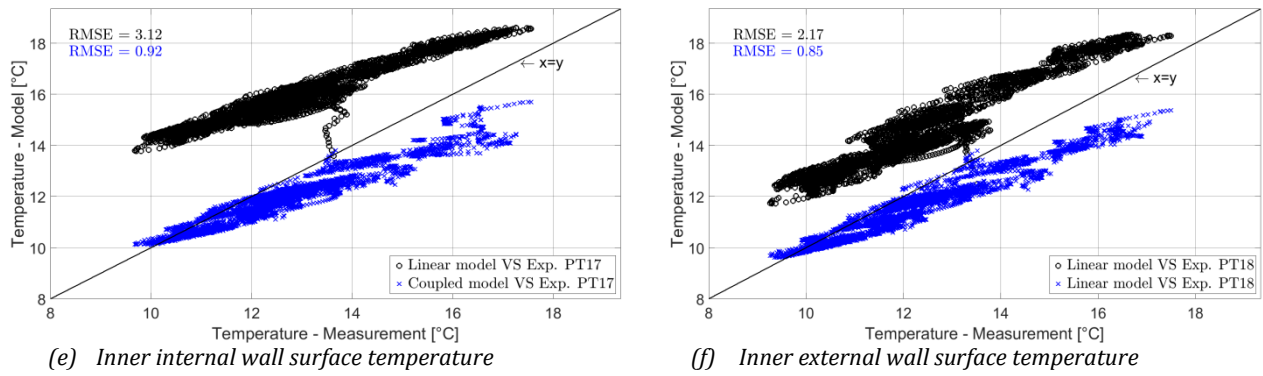


Figure 79: Linear and coupled models results comparison against measurements: Flowing air (a) temp., (b) relative humidity, (c) Inner upper, (d) Inner lower, (e) Inner internal, (f) Inner external wall surface temp.

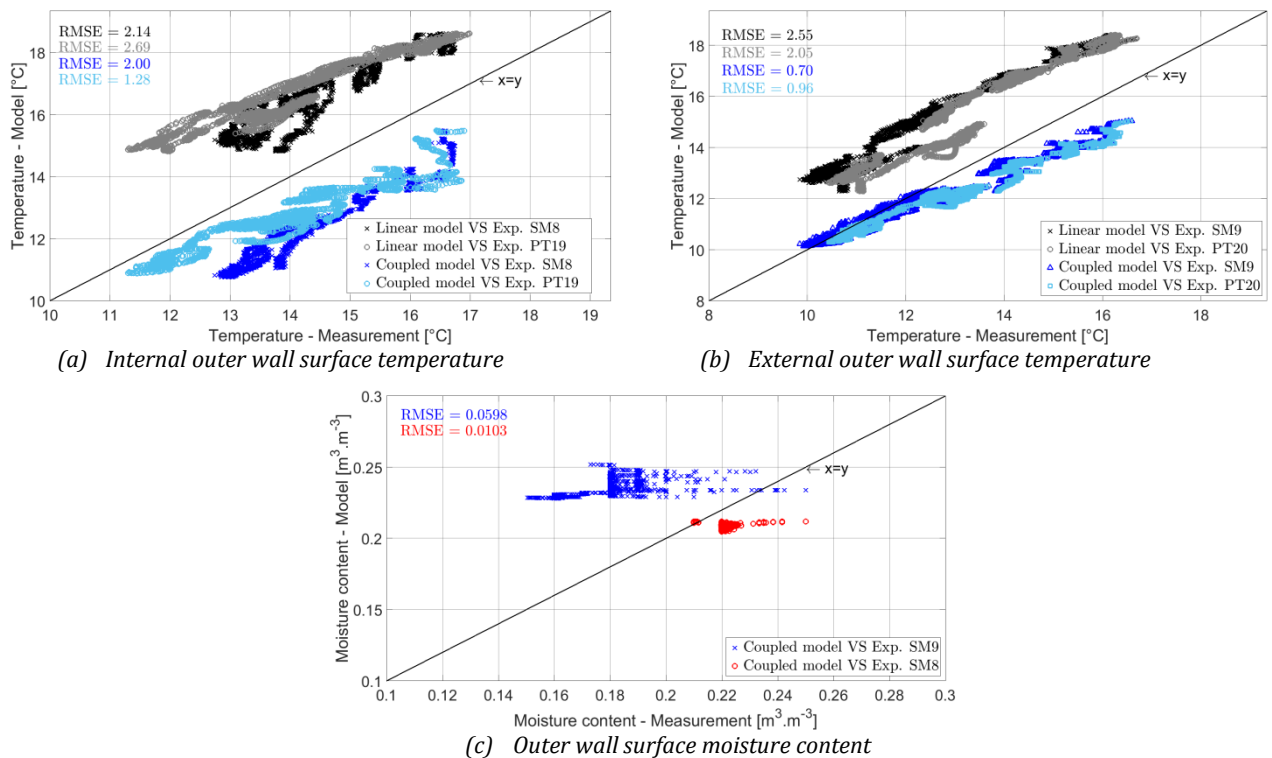


Figure 80: Linear and coupled models results comparison against measurements: (a) Internal outer wall surface temperature, (b) External outer surface wall temperature, (c) Outer walls moisture content

7.4. CONCLUSIONS

Throughout this chapter, the evaluation of the two models performance developed in Chapter 4 & 5 has been carefully analysed. The coupled model clearly appears as an accurate way to study this complex problem. By setting aside the eventual deviations close to the meshing edges – the vertical faces at the inlet and outlet sections are in reality influence by external factors and not adiabatic as assumed in the model – the temperature field is well reproduced. Moreover, it is noticeable that these results have been obtained without any attempt to optimise the choice of the hygrothermal parameters. Considering the water

content, the major effort of development has been made to model the moisture transfer at the ground surface and finally the behaviour of this zone is also well reproduced. The remaining deeper soil is not reproduced very well, but the measurement can also be questioned. Even though a great care was taken to design a set of instrumentation, the presence of the PVC tubes used to bury the SM300 probes could have drain water directly from the surface, and strongly modify the measurements. A calibration of the full acquisition system and the probes would be necessary to determine the origin of the observed discrepancies. Generally speaking, this model could be used to carry out the geothermal foundation. It is nevertheless limited by the high computational time required.

The linear model does not supply really good results for the soil domain, but once again, no attempt to study the impact of the choice of the materials has been done. Indeed, in a real situation the ground characteristics are unknown or necessitate long laboratory tests on soil samples. This model however yields the correct variations of the flowing air temperature, even though they are overestimated. This over-prediction can be corrected for example by modifying the heat transfers at the soil surface in order to incorporate the latent heat flux. This could be realized assuming for example a saturated layer at the ground surface.

Chapter 8. INNOVATIVE COUPLINGS WITH OTHER SYSTEMS

8.1. INTRODUCTION

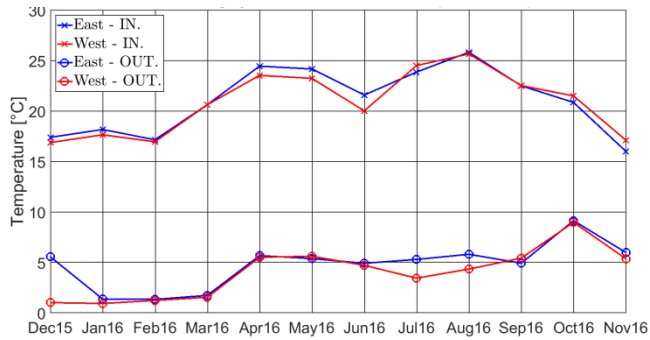
All the previous chapters focused on the Fondatherm heat and mass transfer understanding and none was dedicated its building integration. This chapter proposes to carry out the energy, thermal and aeraulic coupling of the geothermal foundation with the building and its energy systems. Three couplings are investigated.

The first case considers an air handling unit coupling. It is analysed thanks to the experimental measurements on the two AHU introduced in section 6.1. Secondly, since the mechanical fan is the only element that requires electricity, an attempt to replace it by a passive system is proposed: a solar chimney coupling. Finally, a possible solution is introduced for the detrimental periods – heating during cooling periods and reversely – is proposed by the integration of phase change material (PCM) within the cavity. The two further investigations are led using the linear model since it has been proved it can correctly reproduce the airflow temperature evolutions, which is satisfying to compare the two scenarios with / without solar chimney and with / without PCM.

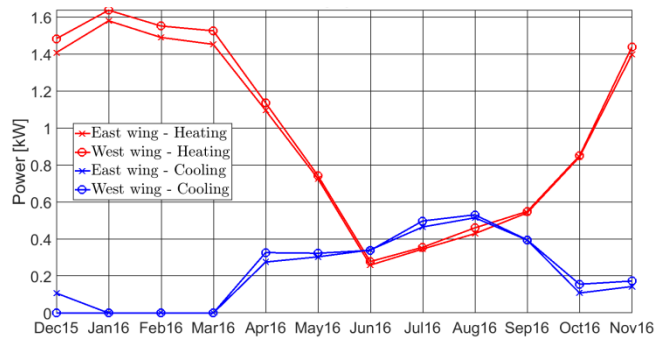
8.2. COUPLING WITH AN AIR HANDLING UNIT

In order to complete the full scale experimental study introduced in Chapter 6, this section discusses the global performance of the coupled {Fondatherm+AHU} system. As a reminder, the air is draft from the foundation outlet to the AHU inlet via an insulated air channel (see Figure 52). Both the air channel and the AHU are located in the crawl space. The AHU includes a heat recovery unit (HRU) of $\varepsilon_{HRU} = 90\%$ efficiency as indicated by the manufacturer. Figure 81 shows the performances of the coupled system, and will allow a comparative analysis with the stand-alone Fondatherm system.

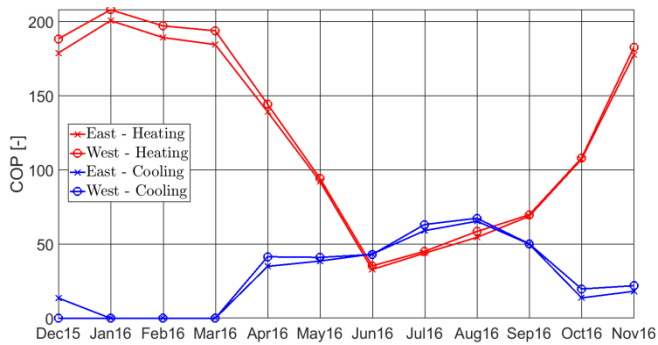
Figure 81 (a) shows that the amplitude dampening during mid-seasons and summer is reduced. Figure 81 (b) shows a slight decreasing of the cooling power in summer. On the contrary, the heating power is increased by more than 2 fold in winter, and around 1.5 during the mid-seasons. The COPs (Figure 81 (c and d)) follow the same tendencies. Regarding cooling mode, the COP is almost unchanged throughout the year while considering the heating mode it is multiplied by more than two for winter time. The same observations can be done about the mean daily energy gains (Figure 81 (g)). Throughout the year, the total energy gain for the heating is multiplied by 2.5, while that for cooling is divided by 1.85.



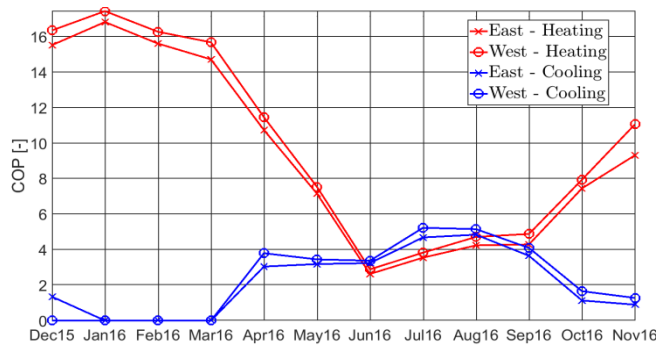
(a) Intake vs. AHU outlet air temperature amplitude



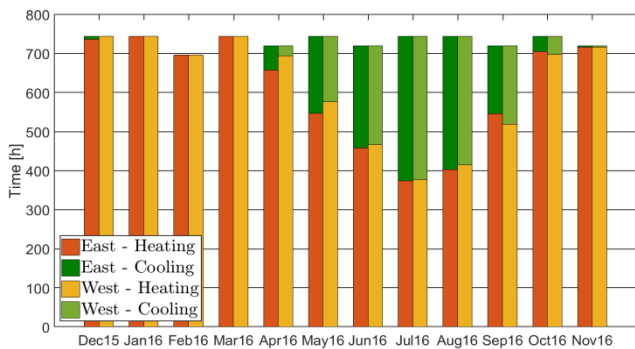
(b) Monthly mean power



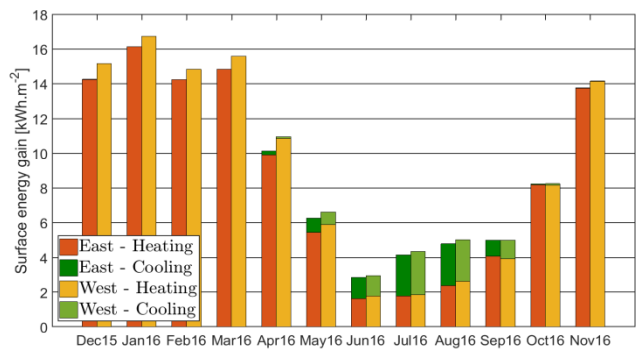
(c) COP_{pl} - calculation based on pressure drop



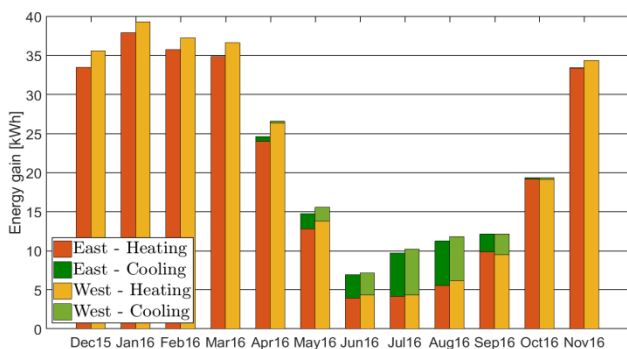
(d) COP - calculation based on AHU electrical consumption



(e) Cumulated heating and cooling operation time



(f) Heating and cooling monthly surface energy gains



(g) Heating and cooling mean daily energy gains

| | Heating | | Cooling | |
|---|---------|-------|---------|------|
| | West | East | West | East |
| <i>Operative hours (h)</i> | 7392 | 7328 | 1392 | 1456 |
| <i>Total energy gain (kWh.m⁻²)</i> | 111,6 | 106,7 | 8,1 | 8,1 |
| <i>Mean daily energy gain (kWh.m⁻².day⁻¹)</i> | 22,2 | 21,3 | 1,6 | 1,6 |
| <i>Annual mean power (kW)</i> | 1,0 | 1,0 | 0,2 | 0,2 |
| <i>Annual max. power (kW)</i> | 2,9 | 2,8 | 1,4 | 1,3 |
| <i>COP_{pl} - pressure drop based (-)</i> | 127,2 | 122,5 | 29,0 | 28,1 |
| <i>COP - AHU elec. cons. based (-)</i> | 10,0 | 9,3 | 2,3 | 2,2 |

(h) Annual summary

Figure 81: Energetic experimental study of the coupling between Fondatherm and the air handling unit

The analysis of the operation time (Figure 81 (e)) shows that contrary to the standing-alone Fondatherm case, there is no cooling during the heating period. In summer, a reduction of the cooling operation time is highlighted: the monthly cooling time switch from around 350/450 h to 250/350 h. The heating operation time is thus increased. Throughout the year, one can note an increase of 1200 h for heating (thus decreasing of 1200 h for cooling).

All the previous observations can be explained by the fact that the temperature at the AHU outlet is both influenced by the foundation outlet and the indoor air temperatures. The inner ambient conditions are almost maintained constant while the outlet air temperature - following the external loads fluctuations - is most of the time lower than the set point temperature. Due to the heat exchanger of the AHU, the air temperature is thus most of the time increasing between the foundation and the AHU outlets. It is related to the temperature difference between the building exhaust air which is almost all the time over 21 °C and the AHU inlet air temperature coming from the foundation most of the time under 20 °C, except during very hot days. Consequently, the air is heated up when it goes through the AHU. It thus improved the heating performance of the foundation, but decreases the cooling performances. A strategy could consist in by-passing the AHU during the cooling time, in order to improve the foundation cooling effect.

Then a question arises:

Is the foundation efficient compared to the HRU performances, and is the coupling {Fondatherm+AHU} relevant?

In order to answer to this issue, the mean daily energy gains due to the HRU when it is coupled to Fondatherm are given by (8.1). This is the part of the total energy saved by the HRU when it is coupled to the foundation.

$$E_{HRU,daily} = \frac{1}{3.6 \cdot 10^6 N} \sum_{i=day 1}^{i=day N} \int_{day i} m_a c_a (T_{HRU,outlet} - T_{HRU,inlet}) dt \quad (8.1)$$

The generated mean daily energy gain when the HRU is operating alone is given by (7.1). Since this latter case has not been studied, it is calculated using the theoretical efficiency ε_{HRU} . Although it can be overestimated by the manufacturer, the yields energy gain values will be analyzed only considering their order of magnitude.

$$E_{HRU,daily}^{standing\ alone} = \frac{1}{3.6 \cdot 10^6 N} \sum_{i=day 1}^{i=day N} \int_{day i} m_a c_a \varepsilon_{HRU} (T_{in} - T^{ext}) dt \quad (8.2)$$

The total energy gain by the coupled system is given by

$$E_{found+HRU,daily} = \frac{1}{3.6 \cdot 10^6 N} \sum_{i=day 1}^{i=day N} \int_{day i} m_a c_a (T_{HRU,outlet} - T^{ext}) dt \quad (8.3)$$

Therefore, the net mean daily energy gain of the foundation can be calculated in two ways. The first is taking the difference between the total energy saved and the part of this energy saved by the HRU. This actually corresponds to the Fondatherm energy supplying and is given by

$$\Delta E_{found,daily} = E_{found+HRU,daily} - E_{HRU,daily} \quad (8.4)$$

The second is taking the difference between the total energy saved and the energy that could be saved by the HRU if it was standing alone (8.5) as proposed by Hollmuller and Lachal (2014). This is a better way to evaluate the Fondatherm contribution. Indeed, the decision-makers usually want to compare the relative performances of systems to choose between several investment opportunities. In our case, the aim is to choose between the coupling {Fondatherm+AHU} and the standing alone HRU.

$$\Delta E_{found,daily}^{standing\ alone} = E_{found+HRU,daily} - E_{HRU,daily}^{standing\ alone} \quad (8.5)$$

Figure 82 shows the part of the heating energy savings with the ventilated foundation ranges between $\frac{1}{3}$ and $\frac{1}{2}$ of the total amount of the energy gains. It can be noticed that for the cooling needs the part of the energy saved thanks to the HRU is negligible. It is consistent with previous observations at the beginning of this section. All the cooling energy gains are thus supplied by the foundation. Figure 82 also highlights that small discrepancies exist between, on the one hand, the sum of the energy saved by the foundation and on the other hand the HRU and the total energy saved (both for heating and cooling). This can be explained by the way to calculate the total energy gain, which takes into account the pipe that drafts the air from the foundation outlet to the AHU inlet. On the contrary, this is not considered in (8.1) and in (6.2). Even if the pipe that goes through the crawl space is insulated, it is around 35 m: the thermal transfers between the flowing air and the crawl space air are not negligible.

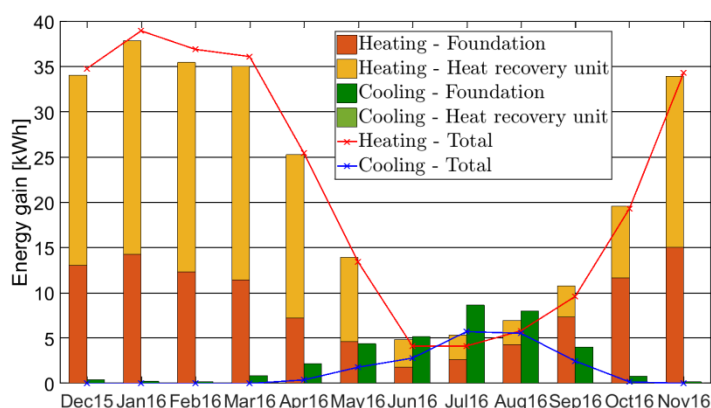


Figure 82: Mean daily energy gains of Fondatherm, of the heat recovery unit of the AHU and of the coupling {Fondatherm+AHU}

Figure 83 shows the net energy gains supplied by Fondatherm. As previously explained, there are two different ways to evaluate them, according to equation (8.4) or (8.5). The results yield by (8.4) are plotted (yellow and clear green bars) to give the Fondatherm energy savings as a comparison point. The total energy saved thanks to Fondatherm appears to be limited

compared to the standing alone HRU energy gains (red and blue curves) except for cooling purposes during summer.

Furthermore, when compared to a standing alone HRU (8.5), Fondatherm appears to have none advantage for heating purposes. On the contrary, the Fondatherm net mean daily energy gains for cooling ranges between 6 kWh.day^{-1} and 10 kWh.day^{-1} .

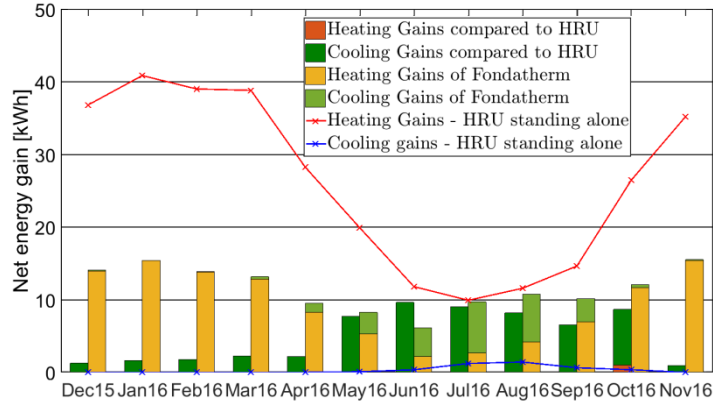


Figure 83: Net mean daily energy gain of Fondatherm when compared to the heat recovery unit (HRU) or considering the coupling with AHU

Given the cost of Fondatherm integration in a new building construction and the energy gains related to this geothermal foundation compared with a heat recovery unit (embedded in an AHU), Fondatherm has almost none advantage for heating compared to a HRU. It is however more efficient for cooling mode. These conclusions have to be taken carefully. First, because they are linked to the local weather: the Fondatherm relative advantage for cooling / heating can be reversed for hot climates. Secondly, because the analysis has been carried out in terms of energy gains only, Fondatherm has however the advantage of removing all the frost problems that can potentially limit the HRU performances.

8.3. COUPLING WITH A SOLAR CHIMNEY

This section provides an analysis of the coupling between Fondatherm and a solar chimney, as illustrated on Figure 84 (a).

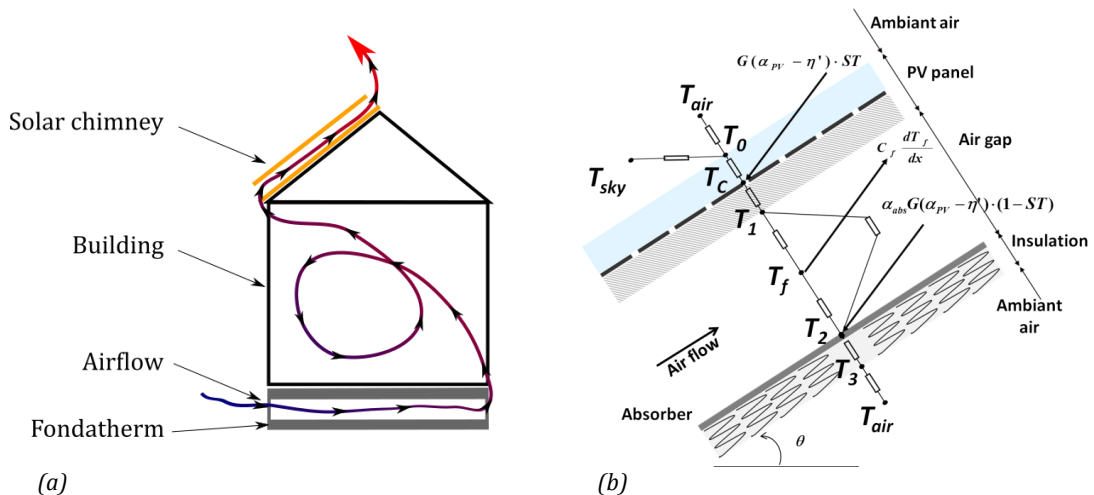


Figure 84: Coupling between a solar chimney and Fondatherm (a) and solar chimney model (b)

The theoretical solar chimney used for the model is schematized on Figure 84 (b) and constituted from top to bottom:

- A semi-transparent solar photovoltaic panel, made of a glazing and a tedlar layer encapsulating spaced out PV cells
- An air layer
- An absorber layer sets on a insulating material.

Heated along the solar chimney, an airflow is governed by thermal buoyancy forces. It affects the stack pressure of the system, which drives the ventilation airflow in the building. These systems have been widely studied as a passive ventilation technique for buildings (Alemu et al., 2012; Bambrook, 2011; Bansal et al., 2005; Bassiouny and Koura, 2008; Mathur et al., 2006). The air flow generated within the solar chimney affect the pressure of the rooms, and can induce an airflow through the earth-to-air heat exchanger connected to the building. Such couplings have been both studied via numerical and experimental approaches (Li et al., 2014; Maerefat and Haghighi, 2010). The objective of this section is to investigate the relevance of the coupling between the solar chimney and Fondatherm. The generation of a natural airflow in the foundation could highly reduce the electric consumption due to mechanical ventilation. It is here assumed that when the flow which is induced by the solar chimney is not sufficient, a mechanical fan is switch on, and imposed an airflow of $0.08 \text{ m}^3 \cdot \text{s}^{-1}$ i.e. an air change per hour of 1 for housing of 100 m^2 and 2.5 m ceiling height. Compared to a traditional solar chimney, the glazing has been replaced by a semi-transparent PV panel. The electricity produced can be stored and used to supply energy to this mechanical fan.

The modelled chimney is 4m long and the air gap is 3m width and 0.125m in depth, with a slope $\theta_{sc} = 45^\circ$. Thermal modelling of this chimney relies on models developed by Bambrook (2011) and Tiwari and Sodha (2007) and is based on an electrical analogy which consider 1D heat flow perpendicular to air gap (Figure 84). Energy balances are calculated for every elementary length of the chimney (along the airflow direction). This enable the computation of every temperature defined on Figure 84. Since the expression of the convective and radiation heat transfer coefficients are depending on the different temperatures, the resolution is iterative until convergence. The air flow is obtained by equation (8.6) proposed by Mathur et al. (2006), where $T_{int} = 20^\circ\text{C}$ is indoor air temperature.

$$\dot{m}_{a,sc} = C_d \rho_a l_{sc} h_{sc} \sqrt{2g L_{sc} \sin(\theta_{sc}) \cdot \frac{T_{sc,outlet} - T_{in}}{2T_{in}}} \text{ [kg} \cdot \text{s}^{-1}] \quad (8.6)$$

The aeraulic coupling between the solar chimney and the building rooms is a very complex problem. The air flow developing in the solar chimney is affected by the air infiltration through the building envelope, by the presence of windows, and by the room air volume. The same problem still occurs for the coupling building / EAHE, such that the air flow in the solar chimney cannot be equal to that in the EAHE. For the sake of simplicity, all of these aeraulic couplings have been neglected in the model: the resulting airflow within the foundation is assumed equal to that in the solar chimney.

Figure 85 (a) shows the airflow evolution with time throughout the year within the chimney. It logically increases in the afternoons and during summers. This airflow rate is around 27 % more than the required threshold of $0.08 \text{ m}^3 \cdot \text{s}^{-1}$. For such periods, the mechanical fan is assumed to be off, and the solar chimney supplying alone the ventilation of the foundation. The remaining time, the mechanical fan is assumed to be on - partially powered by the recovered solar energy - and supplying an airflow of $0.08 \text{ m}^3 \cdot \text{s}^{-1}$.

It has been shown in section 2.1.2. that the airflow increase decreases the cooling/heating potential of an EAHE. This is the case for Fondatherm: it can clearly be observed that the rising of the airflow in summer due to the solar chimney induces an elevation of the outlet air temperature. In winter and mid-seasons, it is slightly lower. These lower thermal performances are offset by an increasing airflow rate. In summer, the mean daily energy gain for cooling is multiply by around 2 with the solar chimney. In winter as well a slight increasing of the heating mean daily energy gain can be noted. It is due to the slight increase of the chimney airflow during the sunniest afternoon.

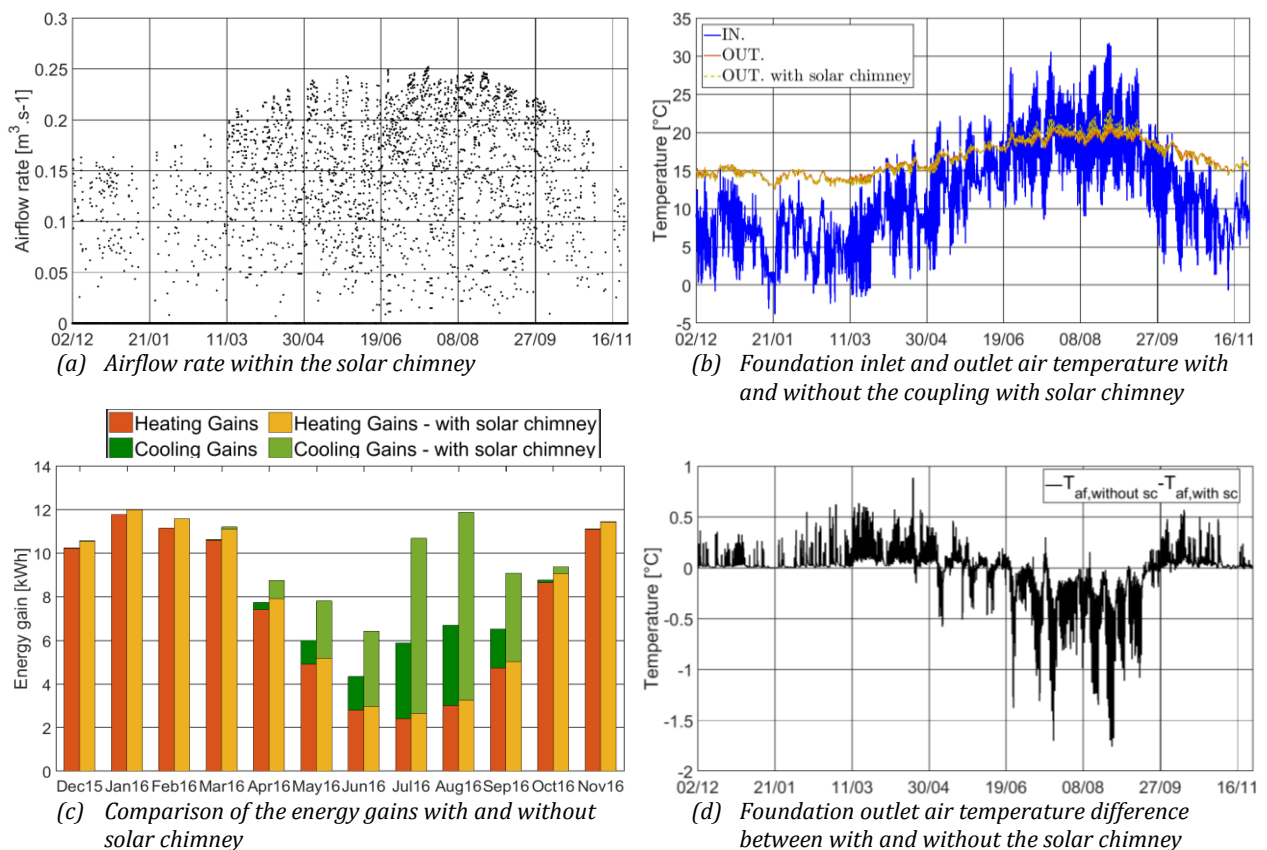


Figure 85: Study of the coupling between Fondatherm and a solar chimney

This study showed that full passive solutions to preheat or cool down the outdoor air for building air renewal could be designed. The coupling between the geothermal foundation and a solar chimney is one of them. Nevertheless, even though the previous results are positive, cautiousness should be exercised for several reasons:

- The complexity of the airflow induced by the chimney into the building rooms and then into the foundation has not been taken into account. In real situations lower airflow rate is therefore more probable, and over reduced time periods,

- The solar chimney installation is complex and potentially costly,
- The generated airflow is sometimes much higher than the requirements, which could considerably increase the heat loss by air renewal. A control is thus mandatory,
- The solar chimney ensures alone the ventilation of the room only 27 % of time at this stage. The design of the chimney (sizes of the air gap, semi-transparency, etc.) has therefore to be optimized.

8.4. PHASE CHANGE MATERIALS COMBINATION

Several journal papers analyzed the integration of PCM within building construction elements or within ventilation systems. Farid et al. (2004) then Soares et al. (2013) made a review about the PCM, more specifically about their uses in building, and it highlighted that they are usually a promising way to improve their energy efficiency. They however pointed out some points of interest, key of the good incorporation of PCM within constructions - that are currently the object of numerous researches:

- The kind of PCM used, mainly characterised by the melting temperature, the thermal conductivity, the density and the specific heat,
- The kind of integration to the construction materials (direct incorporation, immersion, encapsulation),
- The quantity and the position of PCM used.

Considering PCM integration into materials, Hichem et al. (2013) studied their incorporation in common construction brick via both numerical and experimental means. Kuznik et al. (2008) analysed micro-encapsulated PCM in plaster board (manufactured by Dupont de Nemours) used in three walls of a cell under control conditions. Varying the (artificial) solar radiation and outdoor air temperature, they highlighted that the PCM allowed a reduction of 4.5 °C of the indoor peak temperature for summer conditions.

Other studies considered the embedding within ventilation systems. De Gracia et al. (2013) investigated a ventilated façade with micro-encapsulated PCM in blade within the air layer. Rouault et al. (2014) surveyed numerically and experimentally a ventilated heat exchanger-storer supplying conditioned air for building air renewal purposes. Jaworski et al. (2014) proposed to study a heat storage system embedded into ceiling panels, still via both experimental and numerical way. The micro-encapsulated PCM is embedded into the gypsum of the panels. U-shape channels within them allow the circulation of the air from outdoor to the building rooms.

The PCM melting and solidification process is very complicated to model accurately. It indeed implies to consider a moving boundary (fusion front between the solid and the liquid phase). Because of temperature gradients, the liquid is moreover potentially moving, which enhances the heat transfers between the solid and the liquid phases. It is difficult to consider such a complexity at the building scale modelling. Several solutions have been proposed to fix that issue. The two main are the enthalpy method and the equivalent specific heat method. Both are recognized as providing good results (Al-Saadi and Zhai, 2015; de Gracia et al., 2013; Jaworski et al., 2014; Tittlein et al., 2015).

The objective of this section is to embed PCM within the foundation cavity in order to limit the detrimental periods that are characteristics at mid-seasons. More specifically, the PCM could enable to dampen the daily outdoor thermal wave oscillation and to shift it, similarly to what has been introduced in the previously cited papers.

Since it has been observed that the majority of the thermal transfers took place in the first meters of the foundation, PCM have been set in the first section (first 9 meters). The Dupont de Nemours sheets appeared as good candidates to be embedded in the foundation. They can be simply laid on the cavity walls, without modifying the Fondatherm pre-fabrication process. Furthermore, the sheets are only $e_{PCM} = 5 \text{ mm}$ thick, which does not reduce considerably the cross-section area of the cavity. These materials have been used by Kuznik et al. (2008), and the experimental results under controlled conditions proved their efficiency. The authors of this study used an equivalent specific heat method to model it. The PCM equivalent specific heat has thus been determined experimentally by differential scanning calorimeter method (DSC), and is given by

$$C_{PCM}(T) = \begin{cases} 4250 + 10750e^{-\left(\frac{22.6-T}{4}\right)^2} & \text{si } T \leq 22.6 \text{ }^\circ\text{C} \\ 4250 + 10750e^{-\left(\frac{22.6-T}{3}\right)^2} & \text{si } T > 22.6 \text{ }^\circ\text{C} \end{cases} \quad (8.7)$$

According to the authors, the density is equal to $\rho_{PCM} = 1019 \text{ kg} \cdot \text{m}^{-3}$ and the thermal conductivity is obtained by a linear extrapolation of the available measurements, and given by

$$\lambda_{PCM} = 0.22 - \frac{0.04}{26} \times (T - 8) \quad (8.8)$$

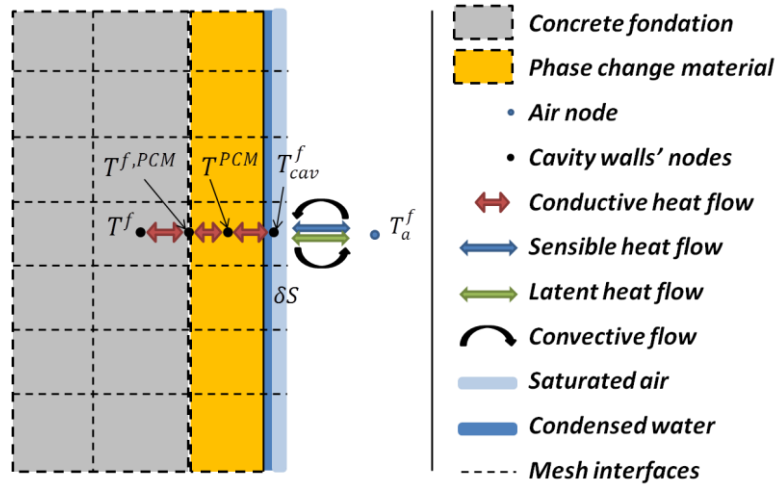


Figure 86: Modelling of the PCM incorporation within the Fondatherm ventilated cavity

As previously said, the PCM coat is assumed to be bonded to the foundation concrete wall without considering any thermal contact resistance. A one-dimensional model heat transfer is used to represent the heat flux perpendicularly to the PCM sheet. One node is used for the whole PCM thickness. At PCM surface facing the flowing air, the boundary condition is similar to that introduced in Chapter 5 for the linear model (the PCM is assumed to be impervious).

This choice will enable a clear comparison between the cases with and without the PCM. This information is summed up on Figure 86.

The heat balances at the core node of the PCM and at the PCM / concrete interface are respectively given by (8.9) and (8.10) where all the quantities have been previously defined. These equations are solved by a Newton-Raphson method at each iteration.

Figure 87 shows the comparison between the foundation outlet air temperature of the normal case and the case where PCM has been set on the first section wall surfaces. The outlet air temperature with PCM is significantly lower in summer, with a difference around 1 °C. Figure 87 (b) highlights that the air temperature amplitude dampening is annual and not daily as initially expected. This can be potentially due to a bad choice of PCM material: the melting temperature is not in the range of the most common airflow temperature at the foundation inlet section, and the phase change does not occur. Figure 87 shows the comparison between the foundation outlet air temperature of the normal case and the case where PCM has been set on the first section wall surfaces. The outlet air temperature with PCM is significantly lower in summer, with a difference around 1 °C. Figure 87 (b) highlights that the air temperature amplitude dampening is annual and not daily as initially expected.

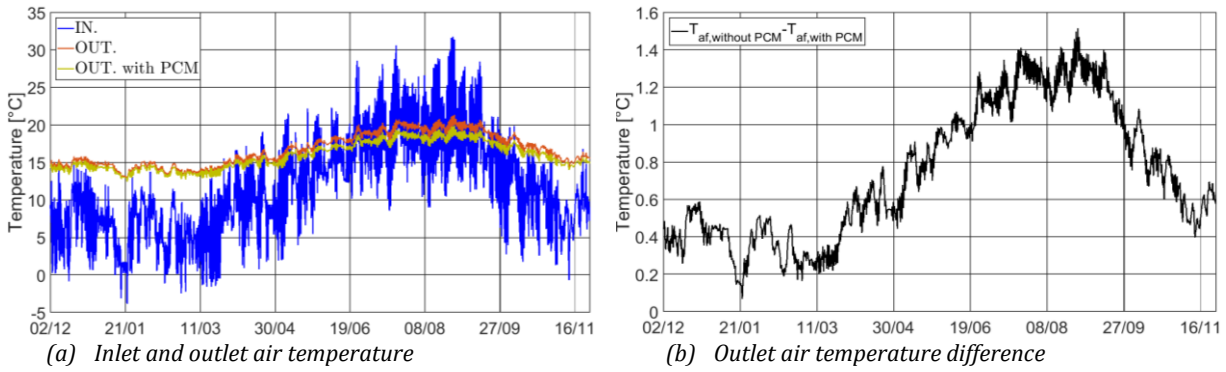


Figure 87: Comparison of the Fondatherm outlet air temperature with and without PCM

$$\begin{aligned} & \frac{C_l m_w^{t-\Delta t}(i, j) \left(T_{cav}^t(i, j) - T_{cav}^{t-\Delta t}(i, j) \right)}{\Delta t} \\ & = A_{cav}(i, j) \left(\phi_{h,sens}^{f,cav}(i, j) + \phi_{h,lat}^{f,cav}(i, j) \right. \\ & \quad \left. + \phi_{h,cond}^{f,cav}(i, j) \right) \end{aligned} \quad (8.9)$$

$$\begin{aligned} & \rho_{PCM} e_{PCM} \delta S_{PCM}(T^{PCM}(i, j)) \frac{\partial T^{PCM}(i, j)}{\partial t} \\ & = \delta S \left[\frac{2\lambda_{PCM}\lambda^f}{\lambda_{PCM}\delta x + \lambda^f e_{PCM}} \left(T^f(i, j) - T^{PCM}(i, j) \right) \right. \\ & \quad \left. + \frac{2\lambda_{PCM}}{e_{PCM}} \left(T_{cav}^f(i, j) - T^{PCM}(i, j) \right) \right] \end{aligned} \quad (8.10)$$

This can be potentially due to a bad choice of PCM material: the melting temperature is not in the range of the most common airflow temperature at the foundation inlet section, and the phase change does not occur. Another explanation could be that a too large and thicker

layer of PCM has been used. The Dupont coats can store a huge quantity of energy and slowly releases it over long time periods.

Ignoring that issue, the analysis of Figure 88 shows a rather low difference between both cases. One can still note that the foundation without PCM incorporation is globally more efficient, due to better heating energy gains that are not off-set by the improved cooling energy gains of the {Fondatherm+PCM} case.

This section put in evidence that a potential improvement of the geothermal foundation is reachable using phase change material, but that a complex parametric analysis is required to select the optimum PCM material (melting temperature and thermal conductivity), thickness, length and position on the cavity. This could involve the use of more accurate PCM layer model, taking into account three-dimensional heat transfers and more discretization nodes.

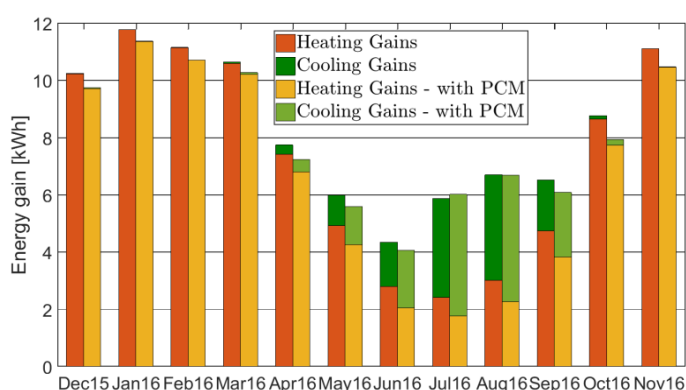


Figure 88: Mean daily energy gains comparison - Fondatherm with and without PCM

8.5. CONCLUSIONS

Throughout this chapter, several solutions have been proposed in order to improve the Fondatherm energy performances, or to simply integrate it into the building. The coupling with the air handling unit showed that Fondatherm could appear to be not relevant in all the cases. Indeed, the heating energy gains are negligible compared to that supplied by a heat recovery unit. On the contrary, Fondatherm is competitive considering the cooling energy gains. This proves again that a careful sizing, taking into account the local climate, the building energy systems and constraints (e.g. airflow rate) is necessary.

The coupling with a solar chimney aiming at removing all dependency to electricity lead to the same conclusion. Even if the solar chimney allows reducing the electric consumption and then improves the energy savings, each element (the foundation and the solar chimney) has to be sized carefully in order to provide both the required sanitary airflow rate and to make the foundation work at an optimum state. Finally, the PCM incorporation is at that stage not very conclusive: this solution appeared to be not efficient, but a wider investigation with other PCM materials, other quantities, set of different location within the foundation could appear more appropriate and convincing. Furthermore, the accuracy of the proposed model can be questioned, and a more detailed level could be necessary.

Chapter 9. GENERAL CONCLUSIONS AND OUTLOOKS

9.1. *CONCLUSIONS OF THIS WORK*

This work is a part of the Fondatherm project involving five partners, and the manuscript is the result of multiple interrelations with them and a part of a global production.

The CSTB worked on the air quality issue, and showed two interesting results. First, the fine particles content (PM 10) of the air is decreased when it goes through the foundation. This was explained by the adsorption onto the cavity walls. A recommendation was therefore to clean it regularly (yearly). A process with an appropriate brush robot has thus been devised. Secondly, the micro-bacteriological results showed a slight increasing of the air bacteria content, but not beyond the health danger threshold. For their part, Industrelec and CIAT developed an appropriate air handling unit including the required control strategy – partially thanks to the CETHIL modelling results - and user dashboard. Finally, the CSTB is currently applying to a ‘Titre V’, which will allow the integration of a Fondatherm model into the French thermal rule RT 2012.

Concerning the tasks carried out within the CETHIL laboratory, it is important to recall here the Fondatherm basic principle and the differences with traditional earth-to-air heat exchanger (EAHE) that have been clearly identified in Chapter 2. As for classical EAHE, a fan forces the circulation of the outdoor air within the cavity over several dozen meters. The main differences with EAHE are the lower burying depth, the wider cross-section area and the material of the channel walls, the coupling with the building above via the concrete beam and the simultaneous influence from the weather and the building. All of these induce a more complex thermal loading of the foundation than in the common EAHE cases. The multi-functionality - since Fondatherm plays a heat exchanger role while it is participating as a building structure element - allows saving materials (mainly concrete) which is better from an embodied energy and carbon balance point of view compared to a traditional EAHE.

From a thermal point of view, as proved by the energy experimental study of Chapter 6, it also allows preheating or cooling down the air with relatively low energy consumption. Therefore, even if the heating or cooling energy produced are modest, the COPs are quite interesting, evolving between 1 and 7 which is in the range of EAHE usual COPs. The raised question is - considering the system costs resulting for instance from the pre-fabricated foundation installation and the fan operation - is that technique supply energy (both for heating and cooling) at a reasonable price compared to gas, fuel or electricity? Is the energy payback time reasonable? The studies cited in the introduction part of this manuscript showed that the development of a competitive EAHE is possible, but required a careful designing process. Similar analysis also appears as crucial for Fondatherm.

The state of the art realized in Chapter 2 highlighted that the thermal performances – linked to the outdoor air temperature wave amplitude dampening and phase shifting - were the results of both:

- The design variables such as the pipe buried depth, diameter, length, number and spacing, the airflow rate or air speed,
- The environmental factors such as the soil hygrothermal properties, the season, the climate, the operation time and more generally the control strategy.

Several modelling approach (numerical, analytical, etc) has been developed in the past to reproduce the EAHE behaviours taking into account the previously cited factors. However, considering the specifications of Fondatherm compared to traditional EAHE, a direct use of the previous conclusions and of the model introduced at the end of Chapter 2 looks not appropriate. Their exploration however gave the best modelling solutions for Fondatherm.

The need for two modelling levels quickly appeared. The first one has a clear objective: improve the knowledge of the Fondatherm operation conditions and of the complex heat transfers involved. This required a detailed model. The second need is a designing tool. A trade-off between accuracy and computational time is this time mandatory.

Concerning the first modelling level, the literature survey showed that a problem close to the analysis of horizontal geothermic for building heating applications is the study of the building ground heat loss via the slab. Resulting from the literature survey carried out about this subject (beginning of Chapter 3) and of EAHE modelling state of art (Chapter 2), it appeared that the most appropriate approach to answer the first modelling needs would be to consider simultaneous heat and moisture transfer (HM) within the soil and the concrete foundation. In Chapter 4, the details about the equations for the HM equations – for both the soil and the concrete porous media - are discussed. It concerns more specifically the water retention curve, the thermal conductivity, the hydraulic conductivity and the vapour diffusivity / permeability. These function required numerous constant to their full determination, depending on the type of soil. The proposed solution from the Janssen (2002) thesis is to build a set of parameters for seven representative soils. This is all the more a relevant solution since most of the time, the soil properties are unknown, and their determination by the measure is impossible. When a study is carried out, the closest kind of soil among the seven proposed is selected. Secondly, the boundary conditions description and implementation has been described. A special effort has been done to accurately reproduce the thermal and moisture load from the outdoor and from the building via the crawl-space. At ground top surface, the boundaries have been implemented in such a way that the reproductions of temperature and water content fields are very satisfactory. This has been possible distinguishing cases for which the evaporation flow rates are important and cases for which infiltration becomes high. Then the numerical methods for the resolution of the conservation equations for both domains (soil and concrete foundation) have been exposed. Finite volume method for the spatial discretization and Newton-Raphson method for the temporal discretization were used. A variable time step method has been implemented for each domain and a global time step govern the progress of the time loop.

In Chapter 5, the second modelling level, i.e. the design tool, is developed. In order to satisfy the computational time requirements, it is reduced by a balanced realization method.

The principle of this reducing technique consists in finding a mathematical base where the state variables are contributing as much to the evolution of observed variables as they are influenced by external loads. This results in saving calculation time while maintaining the level of precision of the detailed model.

The Chapter 6 focus on another approach to understand the Fondatherm behaviour, namely an intensive instrumentation of a building equipped with two 50 *m* long geothermal foundations. First, the energetic survey proved that the Fondatherm performances are interesting both for heating and cooling. The analysis showed that it is as efficient as a traditional EAHE, even more considering only the heating potential. In addition, and in accordance with the results from the literature, the second half is unnecessary for cooling purpose, and can even be slightly detrimental (i.e. heat up the air in cooling mode). On the contrary, the full length is required in heating mode. Secondly, the thermal survey confirmed this later result. Furthermore, it has been proved by a whole year statistic analysis that the exchanges within the cavity are not symmetric at all. In heating mode, the main contribution comes from the upper and the internal walls. In cooling mode, the main contribution comes from the lower and the external walls.

The Chapter 7 proposed an analysis of the ability of the two developed model to reproduce the measurements. Excluding the problem that could arise at the vertical inlet and outlet edges of the studied domain, the performance of the detailed model is really good. The remaining observed differences can be explained by the imprecision of the determination of the soil and concrete thermohygric properties, or by neglected (because unknown) external loads. Nevertheless, a simulation over a long term period is limited by numerical convergence problems. Several of them resulted from a first bad implementation of the boundary conditions. This has been solved by the cases distinction at the soil surface. Unfortunately the origins of the remaining problems could not be identified. The design tool ability to reproduce the measure is lower. A major difference that could explain the deviation is the non-inclusion of latent heat transfers at the soil surface. This strongly modifies the influx, thus the temperature field close to the foundation. In addition, the soil thermal properties have not been measured. Despite all, the airflow temperature variations are well reproduced, even though they are a little bit overestimated.

Finally, the Chapter 8 investigates several innovative coupling with Fondatherm. The objective is to exanimate the opportunities to enhance its performances. Among them, a solar chimney, an air handling unit and phase change material embedding have been carried out. Generally speaking, the results showed that an improvement of Fondatherm was possible but required a careful sizing to optimize the energy saving and the cost of the installation.

9.2. FUTURE OUTLOOKS

Given the work developed in this manuscript and the obtained results, several proposition for future work can be made.

First, the formulation of the boundary conditions at soil top surface should be reworked. The representation of the whole moisture flow by only one variable (matric head or capillary pressure) looks not appropriate for this specific zone. Indeed, if a moist soil is exposed to solar radiation, the matric head vary with several order of magnitude, which induce numerical problem for which solutions has been proposed in this manuscript but that are apparently not sufficient. Instead, it could be relevant to split the moisture equation into two equations: one for the vapour flow and one for the moisture flow – with vapour pressure and liquid water content as driving potential for example. The decoupling of the vapour and the liquid flow could limit the above cited problem.

The previous proposition has a crucial drawback: it increases the number of variables, thus the complexity of the model and consequently the time required for its resolution. The use of the detailed state model code was anyway clearly limited by the computational time. Indeed, it is hard to imagine a parametric analysis with the actual computation performances. The two previous assertions lead us to the second proposition. One possibility to face this trick is to apply reduction methods. Since the coupled model is highly non linear, the method used to reduce the sensible heat transfers model is not appropriate. Several methods accommodate this constraint, as for instance Proper Orthogonal Decomposition (POD) and Proper Generalized Decomposition (PGD). Among both, the PGD has a great advantage considering the previous observations. It is possible to consider a parameter of the model as a variable. Therefore, every parameters planned in a parametric analysis can be easily manipulated. The PGD can be roughly described in three steps. The first is to select the parameters to be varied and to ‘transform’ into variables. The second, which is the key point of the method, is to – mathematically - separate the variables, writing (Chinesta et al. 2013) for example $f^N(x_1, \dots, x_D) = \sum_{i=1}^N F_i^1(x_1) \times \dots \times F_i^D(x_D)$ where D is the number of dimensions, f the unknown field, x_i a space coordinate, time or even a parameter of the model, and the number of terms N and the functions $F_i^j(x_j)$ are a priori unknown. This functions are built by iteration with a successfully enrichment. Thirdly, the (simple and fast) evaluation of this function for each combination of the variables x_1, \dots, x_D enables the creation of a global set of solutions of the problem. Exactly in the same manner as with an abacus reading, the state of the system can be approximate easily.

Thirdly, the moisture transfers between the cavity wall and the airflow could not have been validated. It is nevertheless an important phenomenon that deserves a careful attention: it is involved in mould growth and more generally in the air quality issues. Measurements of the moisture content at the concrete surface could enable to obtain more information to validate the model.

About the foundation designing, the linear model should allow to study potential solutions to improve the system. Since it has been observed that the four walls contribution to heating and cooling of the airflow was different, it could be relevant to put insulation on one side of the foundation according to the dominant operation mode (heating or cooling).

Furthermore, several coupling solutions have been investigated in Chapter 8, but more work is necessary to optimize the global systems and their integration to the buildings. Indeed, it has been highlighted that a given configuration (chimney size, airflow control, heat recovery unit efficiency, PCM quantity, melting temperature and location, etc) could improve as well as inhibit all the geothermal foundation advantages.

Finally, the control strategy of the airflow throughout the foundation should be developed. This could allow the improvement of the foundation performances, especially during the mid-seasons when heating or cooling period is unintended. Premises of such strategy have been explored as illustrated in Appendix H.

REFERENCES

ADEME (2017). Puits climatiques - Les fiches techniques de l'ADEME.

Adjali, M.H., Davies, M., Rees, S.W., and Littler, J. (2000a). Temperatures in and under a slab-on-ground floor: two-and three-dimensional numerical simulations and comparison with experimental data. *Build. Environ.* 35, 655–662.

Adjali, M.H., Davies, M., Riain, C.N., and Littler, J.G. (2000b). In situ measurements and numerical simulation of heat transfer beneath a heated ground floor slab. *Energy Build.* 33, 75–83.

Adjali, M.H., Davies, M., and Rees, S.W. (2004). A comparative study of design guide calculations and measured heat loss through the ground. *Build. Environ.* 39, 1301–1311.

Al-Ajmi, F., Loveday, D.L., and Hanby, V.I. (2006). The cooling potential of earth–air heat exchangers for domestic buildings in a desert climate. *Build. Environ.* 41, 235–244.

Al-Anzi, A., and Krarti, M. (2004). Local/global analysis of transient heat transfer from building foundations. *Build. Environ.* 39, 495–504.

Alemu, A.T., Saman, W., and Belusko, M. (2012). A model for integrating passive and low energy airflow components into low rise buildings. *Energy Build.* 49, 148–157.

Al-Saadi, S.N., and Zhai, Z. (John) (2015). Systematic evaluation of mathematical methods and numerical schemes for modeling PCM-enhanced building enclosure. *Energy Build.* 92, 374–388.

Anderson, B.R. (1991). Calculation of the steady-state heat transfer through a slab-on-ground floor. *Build. Environ.* 26, 405–415.

Ascione, F., Bellia, L., and Minichiello, F. (2011). Earth-to-air heat exchangers for Italian climates. *Renew. Energy* 36, 2177–2188.

ATLANTIC (2016). Puits canadiens.

Badescu, V. (2007). Simple and accurate model for the ground heat exchanger of a passive house. *Renew. Energy* 32, 845–855.

Bambrook, S.M. (2011). Investigation of photovoltaic thermal air systems to create a zero energy house in Sydney. University of New South Wales.

Bansal, N.K., Mathur, J., Mathur, S., and Jain, M. (2005). Modeling of window-sized solar chimneys for ventilation. *Build. Environ.* 40, 1302–1308.

Bansal, V., Misra, R., Agrawal, G.D., and Mathur, J. (2009). Performance analysis of earth–pipe–air heat exchanger for winter heating. *Energy Build.* 41, 1151–1154.

Bansal, V., Misra, R., Agrawal, G.D., and Mathur, J. (2010). Performance analysis of earth–pipe–air heat exchanger for summer cooling. *Energy Build.* 42, 645–648.

Bansal, V., Mishra, R., Agarwal, G.D., and Mathur, J. (2012a). Performance analysis of integrated earth-air-tunnel-evaporative cooling system in hot and dry climate. *Energy Build.* 47, 525–532.

Bansal, V., Misra, R., Agrawal, G.D., and Mathur, J. (2012b). Performance evaluation and economic analysis of integrated earth-air-tunnel heat exchanger-evaporative cooling system. *Energy Build.* 55, 102–108.

Bansal, V., Misra, R., Agarwal, G.D., and Mathur, J. (2013a). 'Derating Factor' new concept for evaluating thermal performance of earth air tunnel heat exchanger: A transient CFD analysis. *Appl. Energy* 102, 418–426.

Bansal, V., Misra, R., Agarwal, G.D., and Mathur, J. (2013b). Transient effect of soil thermal conductivity and duration of operation on performance of Earth Air Tunnel Heat Exchanger. *Appl. Energy* 103, 1–11.

Baroghel-Bouny, V. (2007a). Water vapour sorption experiments on hardened cementitious materials. *Cem. Concr. Res.* 37, 414–437.

Baroghel-Bouny, V. (2007b). Water vapour sorption experiments on hardened cementitious materials. Part II: Essential tool for assessment of transport properties and for durability prediction. *Cem. Concr. Res.* 37, 438–454.

Bassiouny, R., and Koura, N.S.A. (2008). An analytical and numerical study of solar chimney use for room natural ventilation. *Energy Build.* 40, 865–873.

Bauklimatik-Dresden (2017). DELPHIN. Simulation program for the calculation of coupled heat, moisture, air, pollutant, and salt transport.

Berger, J. (2014). Contribution à la modélisation hygrothermique des bâtiments : application des méthodes de réduction de modèle. Civil Engineering. Université de Grenoble.

Bojić, M. (2000). Optimization of heating and cooling of a building by employing refuse and renewable energy. *Renew. Energy* 20, 453–465.

Bojic, M., Trifunovic, N., Papadakis, G., and Kyritsis, S. (1997). Numerical simulation, technical and economic evaluation of air-to-earth heat exchanger coupled to a building. *Energy* 22, 1151–1158.

Bories, S., Mojtabi, A., Prat, M., and Quintard, M. (2008). Transfer de chaleur dans les milieux poreux - Conduction, convection rayonnement.

Breesch, H., Bossaer, A., and Janssens, A. (2005). Passive cooling in a low-energy office building. *Sol. Energy* 79, 682–696.

Burton, S. (2004). Coolhouse - Energie Demonstration Project NNE5.

Campbell, G.S., Jungbauer, W.R., Bidlake, W.R., and Hungerford, R.D. (1994). Predicting the effect of temperature on soil thermal conductivity. *Soil Sci.* 158, 307–313.

Celia, M.A., and Bouloutas, E. (1990). A general mass-conservative numerical solution for the unsaturated flow equation. *Water Resour. Res.* 26, 1483–1496.

Chel, A., and Tiwari, G.N. (2009). Performance evaluation and life cycle cost analysis of earth to air heat exchanger integrated with adobe building for New Delhi composite climate. *Energy Build.* 41, 56–66.

Chlela, F., Husaunndee, A., Riederer, P., and Inard, C. (2007). Numerical Evaluation of Earth to Air Heat Exchangers and Heat Recovery Ventilation Systems. *Int. J. Vent.* 6, 31–42.

Chuangchid, P., and Krarti, M. (2001). Foundation heat loss from heated concrete slab-on-grade floors. *Build. Environ.* 36, 637–655.

Claesson, J., and Hagentoft, C.-E. (1991). Heat loss to the ground from a building - I. General theory. *Build. Environ.* 26, 195–208.

Cucumo, M., Cucumo, S., Montoro, L., and Vulcano, A. (2008). A one-dimensional transient analytical model for earth-to-air heat exchangers, taking into account condensation phenomena and thermal perturbation from the upper free surface as well as around the buried pipes. *Int. J. Heat Mass Transf.* 51, 506–516.

van Dam, J.C., and Feddes, R.C. (2000). Numerical simulation of infiltration, evaporation and shallow groundwater levels with the Richards equation. *J. Hydrol.* 233, 72–85.

Davies, M., Tindale, A., and Littler, J. (1995). Importance of multi-dimensional conductive heat flows in and around buildings. *Build. Serv. Eng. Res. Technol.* 16, 83–90.

De Paepe, M., and Janssens, A. (2003). Thermo-hydraulic design of earth -air heat exchangers. *Energy Build.* 35, 389–397.

De Vries, D.A. (1958). Simultaneous transfer of heat and moisture in porous media. *Trans. Am. Geophys. Union* 39, 909–916.

Deglin, D., Van Caenegem, L., and Dehon, P. (1999). Subsoil Heat Exchangers for the Air Conditioning of Livestock Buildings. *J. Agric. Eng. Res.* 73, 179–188.

Delsante, A.E., Stokes, P.O., and Walsh, P.J. (1983). Application of Fourier transforms to periodic heat flow into the ground under a building. *Int. J. Heat Mass Transf.* 26, 121–132.

Deru, M.P. (2003). A model for Ground-Coupled Heat and Moisture Transfer from Buildings. Technical Report NREL/TP-550-33954. National Renewable Energy Laboratory.

Deru, M.P., and Kirkpatrick, A.T. (2002a). Ground-Coupled Heat and Moisture Transfer from Buildings Part 1–Analysis and Modeling. *J. Sol. Energy Eng.* 124, 10–16.

Deru, M.P., and Kirkpatrick, A.T. (2002b). Ground-Coupled Heat and Moisture Transfer from Buildings Part 2–Application. *J. Sol. Energy Eng.* 124, 17–21.

Eicker, U., Huber, M., Seeberger, P., and Vorschulze, C. (2006). Limits and potentials of office building climatisation with ambient air. *Energy Build.* 38, 574–581.

Eole (2017). Les puits canadiens.

Farid, M.M., Khudhair, A.M., Razack, S.A.K., and Al-Hallaj, S. (2004). A review on phase change energy storage: materials and applications. *Energy Convers. Manag.* 45, 1597–1615.

Farouki, O.T. (1981). Thermal properties of soils (U.S. Army Cold Regions Research and Engineering Laboratory).

Fiabibat SCOP (2017). Le puits canadien à la loupe.

Florides, G., and Kalogirou, S. (2007). Ground heat exchangers—A review of systems, models and applications. *Renew. Energy* 32, 2461–2478.

Gan, G. (2014). Dynamic interactions between the ground heat exchanger and environments in earth–air tunnel ventilation of buildings. *Energy Build.* 85, 12–22.

Gan, G. (2015). Simulation of dynamic interactions of the earth–air heat exchanger with soil and atmosphere for preheating of ventilation air. *Appl. Energy* 158, 118–132.

Gauthier, C., Lacroix, M., and Bernier, H. (1997). Numerical simulation of soil heat exchanger-storage systems for greenhouses. *Sol. Energy* 60, 333–346.

Ghosal, M.K., Tiwari, G.N., and Srivastava, N.S.L. (2004). Thermal modeling of a greenhouse with an integrated earth to air heat exchanger: an experimental validation. *Energy Build.* 36, 219–227.

Gori, F., and Corasaniti, S. (2013). New model to evaluate the effective thermal conductivity of three-phase soils. *Int. Commun. Heat Mass Transf.* 47, 1–6.

de Gracia, A., Navarro, L., Castell, A., and Cabeza, L.F. (2013). Numerical study on the thermal performance of a ventilated facade with PCM. *Appl. Therm. Eng.* 61, 372–380.

Hagentoft, C.-E. (1988). Heat loss to the ground from a building: slab on the ground and cellar. Lund University.

Hagentoft, C.-E. (1996). Heat losses and temperature in the ground under a building with and without ground water flow—I. Infinite ground water flow rate. *Build. Environ.* 31, 3–11.

Hassanizadeh, M., and William G. Gray (1979). General conservation equations for multi-phase systems: 1. Averaging procedure. *Adv. Water Resour.* 2, 131–144.

Hichem, N., Noureddine, S., Nadia, S., and Djamila, D. (2013). Experimental and Numerical Study of a Usual Brick Filled with PCM to Improve the Thermal Inertia of Buildings. *Energy Procedia* 36, 766–775.

Hollmuller, P. (2002). Utilisation des échangeurs air/sol pour le chauffage et le rafraîchissement des bâtiments: mesures in situ, modélisation analytique, simulation numérique et analyse systémique. University of Geneva.

Hollmuller, P. (2003). Analytical characterisation of amplitude-dampening and phase-shifting in air/soil heat-exchangers. *Int. J. Heat Mass Transf.* 46, 4303–4317.

Hollmuller, P., and Lachal, B. (2001). Cooling and preheating with buried pipe systems: monitoring, simulation and economic aspects. *Energy Build.* 33, 509–518.

Hollmuller, P., and Lachal, B. (2014). Air–soil heat exchangers for heating and cooling of buildings: Design guidelines, potentials and constraints, system integration and global energy balance. *Appl. Energy* 119, 476–487.

Hollmuller, P., and Lachal, B.M. (2005). Buried pipe systems with sensible and latent heat exchanges: validation of numerical simulation against analytical solution and long-term monitoring.

Incropera, F.P., and DeWitt, D.P. (1990). *Fundamentals of Heat and Mass Transfer* (John Wiley & Sons).

Janssen, H. (2002). The influence of soil moisture transfer on building heat loss via the ground. Katholieke Universiteit of Leuven.

Janssen, H., Carmeliet, J., and Hens, H. (2004). The influence of soil moisture transfer on building heat loss via the ground. *Build. Environ.* 39, 825–836.

Janssen, H., Blocken, B., and Carmeliet, J. (2007). Conservative modelling of the moisture and heat transfer in building components under atmospheric excitation. *Int. J. Heat Mass Transf.* 50, 1128–1140.

Jaworski, M., Łapka, P., and Furmański, P. (2014). Numerical modelling and experimental studies of thermal behaviour of building integrated thermal energy storage unit in a form of a ceiling panel. *Appl. Energy* 113, 548–557.

Kepes Rodrigues, M., da Silva Brum, R., Vaz, J., Oliveira Rocha, L.A., Domingues dos Santos, E., and Isoldi, L.A. (2015). Numerical investigation about the improvement of the thermal potential of an Earth-Air Heat Exchanger (EAHE) employing the Constructal Design method. *Renew. Energy* 80, 538–551.

Kim, E.-J. (2011). Development of numerical models of vertical ground heat exchangers and experimental verification: domain decomposition and state model reduction approach. INSA de Lyon.

Kim, E.-J., Plessis, G., Hubert, J.-L., and Roux, J.-J. (2014). Urban energy simulation: Simplification and reduction of building envelope models. *Energy Build.* 84, 193–202.

Kopecky, P. (2008). Hygro-thermal performance of earth to air heat exchangers. Numerical model, analytical and experimental validation, measurements in-situ, design. *Disertační práce. ČVUT v Praze.*

Kumar, R., Ramesh, S., and Kaushik, S.C. (2003). Performance evaluation and energy conservation potential of earth-air-tunnel system coupled with non-air-conditioned building. *Build. Environ.* 38, 807–813.

Künzel, H.M. (1995). Simultaneous heat and moisture transport in building components. One- and two- dimensional calculation using simple parameters. (Stuttgart: Fraunhofer IRB).

Kurnitski, J. (2000). Crawl space air change, heat and moisture behaviour. *Energy Build.* 32, 19–39.

Kuznik, F., Virgone, J., and Roux, J.-J. (2008). Energetic efficiency of room wall containing PCM wallboard: A full-scale experimental investigation. *Energy Build.* 40, 148–156.

Labat, M. (2012). Chaleur-Humidité-Air dans les maisons à ossature bois: expérimentation et modélisation. INSA de Lyon.

- Lee, K.H., and Strand, R.K. (2006). Implementation of an earth tube system into EnergyPlus program. In Proceedings of the SimBuild 2006 Conference, Boston MA, USA, p.
- Lee, K.H., and Strand, R.K. (2008). The cooling and heating potential of an earth tube system in buildings. *Energy Build.* *40*, 486–494.
- Li, H., Yu, Y., Niu, F., Shafik, M., and Chen, B. (2014). Performance of a coupled cooling system with earth-to-air heat exchanger and solar chimney. *Renew. Energy* *62*, 468–477.
- Maerefat, M., and Haghighi, A.P. (2010). Passive cooling of buildings by using integrated earth to air heat exchanger and solar chimney. *Renew. Energy* *35*, 2316–2324.
- Mathur, J., Mathur, S., and Anupma (2006). Summer-performance of inclined roof solar chimney for natural ventilation. *Energy Build.* *38*, 1156–1163.
- Mendes, N., and Philippi, P.C. (2005). A method for predicting heat and moisture transfer through multilayered walls based on temperature and moisture content gradients. *Int. J. Heat Mass Transf.* *48*, 37–51.
- Mendes, N., Philippi, P.C., and Lamberts, R. (2002). A new mathematical method to solve highly coupled equations of heat and mass transfer in porous media. *Int. J. Heat Mass Transf.* *45*, 509–518.
- Ménézo, C. (1999). Contribution à la modélisation du comportement thermique des bâtiments par couplage de modèles réduits. INSA de Lyon.
- Mihalakakou, G., Santamouris, M., and Asimakopoulos, D. (1994a). Modelling the thermal performance of earth-to-air heat exchangers. *Sol. Energy* *53*, 301–305.
- Mihalakakou, G., Santamouris, M., Asimakopoulos, D., and Papanikolaou, N. (1994b). Impact of Ground Cover on the Efficiencies of Earth-to-Air Heat Exchangers. *Appl. Energy* *48*, 19–32.
- Mihalakakou, G., Santamouris, M., and Asimakopoulos, D. (1994c). Use of the ground for heat dissipation. *Energy* *19*, 17–25.
- Mihalakakou, G., Lewis, J.O., and Santamouris, M. (1996). The influence of different ground covers on the heating potential of earth-to-air heat exchangers. *Renew. Energy* *7*, 33–46.
- Miller, C.T., Williams, G.A., Kelley, C.T., and Tocci, M.D. (1998). Robust solution of Richards' equation for nonuniform porous media. *Water Resour. Res.* *34*, 2599–2610.
- Milly, P.C.D. (1982). Moisture and heat transport in hysteretic, inhomogeneous porous media: a matric head-based formulation and a numerical model. *Water Resour. Res.* *18*, 489–498.
- Ministère de l'Environnement de l'Energie et de la Mer (2016). Prix du gaz et de l'électricité en France et dans l'Union européenne en 2015 (Commissariat général au développement durable - Service de l'observation et des statistiques).
- Misra, R., Bansal, V., Agarwal, G.D., Mathur, J., and Aseri, T. (2012). Thermal performance investigation of hybrid earth air tunnel heat exchanger. *Energy Build.* *49*, 531–535.
- Mitalas, G.P. (1983). Calculation of basement heat loss. *ASHRAE Trans.* *89*, 420–437.

- Mualem, Y. (1974). A conceptual model for hysteresis. *Water Resour. Res.* *10*, 514–520.
- Mualem, Y. (1976). A New Model for Predicting the Hydraulic Conductivity of Unsaturated Porous Media. *Water Resour. Res.* *12*, 513–522.
- Niu, F., Yu, Y., Yu, D., and Li, H. (2015). Heat and mass transfer performance analysis and cooling capacity prediction of earth to air heat exchanger. *Appl. Energy* *137*, 211–221.
- Ozgener, L. (2011). A review on the experimental and analytical analysis of earth to air heat exchanger (EAHE) systems in Turkey. *Renew. Sustain. Energy Rev.* *15*, 4483–4490.
- Ozgener, L., and Ozgener, O. (2010). An experimental study of the exergetic performance of an underground air tunnel system for greenhouse cooling. *Renew. Energy* *35*, 2804–2811.
- Ozgener, L., and Ozgener, O. (2013). Three heating seasons monitoring of thermo-economic parameters of a prototype EAHE system for technological forecasting and evaluating low grade geothermal resources in Turkey. *Energy Build.* *66*, 346–352.
- Ozgener, O., Ozgener, L., and Goswami, D.Y. (2011). Experimental prediction of total thermal resistance of a closed loop EAHE for greenhouse cooling system. *Int. Commun. Heat Mass Transf.* *38*, 711–716.
- Patankar, S.V. (1980). *Numerical Heat Transfer and Fluid Flow*.
- Pedersen, C.R. (1990). *Combined heat and moisture transfer in building constructions*. Technical University of Denmark.
- Peretti, C., Zarrella, A., De Carli, M., and Zecchin, R. (2013). The design and environmental evaluation of earth-to-air heat exchangers (EAHE). A literature review. *Renew. Sustain. Energy Rev.* *28*, 107–116.
- Pfafferott, J. (2003). Evaluation of earth-to-air heat exchangers with a standardised method to calculate energy efficiency. *Energy Build.* *35*, 971–983.
- Philip, J.R., and De Vries, D.A. (1957). Moisture movement in porous materials under temperature gradients. *Eos Trans. Am. Geophys. Union* *38*, 222–232.
- Priesack, E., and Durner, W. (2006). Closed-Form Expression for the Multi-Modal Unsaturated Conductivity Function. *Vadose Zone J.* *5*, 121–124.
- Rees, S.W., Zhou, Z., and Thomas, H.R. (2007). Ground heat transfer: A numerical simulation of a full-scale experiment. *Build. Environ.* *42*, 1478–1488.
- Rouault, F., Bruneau, D., Sébastien, P., and Lopez, J. (2014). Experimental investigation and modelling of a low temperature PCM thermal energy exchange and storage system. *Energy Build.* *83*, 96–107.
- Rouchier, S. (2012). *Hygrothermal performance assessment of damaged building materials*. Architecture, space management. Université Claude Bernard - Lyon 1.
- Santamouris, M., and Kolokotsa, D. (2013). Passive cooling dissipation techniques for buildings and other structures: The state of the art. *Energy Build.* *57*, 74–94.

Santamouris, M., Argiriou, A., and Vallindras, M. (1994). Design and operation of a low energy consumption passive solar agricultural greenhouse. *Sol. Energy* 52, 371–378.

dos Santos, G.H., and Mendes, N. (2006). Simultaneous heat and moisture transfer in soils combined with building simulation. *Energy Build.* 38, 303–314.

Sawhney, R.L., Buddhi, D., and Thanu, N.M. (1999). An experimental study of summer performance of a recirculation type underground airpipe air conditioning system. *Build. Environ.* 34, 189–196.

Schaap, M.G., and Leij, F.J. (2000). Improved prediction of unsaturated hydraulic conductivity with the Mualem-van Genuchten model. *Soil Sci. Soc. Am. J.* 64, 843–851.

Schaap, M.G., Leij, F.J., and van Genuchten, M.T. (2001). ROSETTA: a computer program for estimating soil hydraulic parameters with hierarchical pedotransfer functions. *J. Hydrol.* 251, 163–176.

Serageldin, A.A., Abdelrahman, A.K., and Ookawara, S. (2016). Earth-Air Heat Exchanger thermal performance in Egyptian conditions: Experimental results, mathematical model, and Computational Fluid Dynamics simulation. *Energy Convers. Manag.* 122, 25–38.

Shen, L.S., and Ramsey, J.W. (1988). An investigation of transient, two-dimensional coupled heat and moisture flow in the soil surrounding a basement wall. *Int. J. Heat Mass Transf.* 31, 1517–1527.

Soares, N., Costa, J.J., Gaspar, A.R., and Santos, P. (2013). Review of passive PCM latent heat thermal energy storage systems towards buildings' energy efficiency. *Energy Build.* 59, 82–103.

Sodha, M.S., Sharma, A.K., Singh, S.P., Bansal, N.K., and Kumar, A. (1985). Evaluation of an earth-air tunnel system for cooling-heating of a hospital complex. *Build. Environ.* 20, 115–122.

Soni, S.K., Pandey, M., and Bartaria, V.N. (2015). Ground coupled heat exchangers: A review and applications. *Renew. Sustain. Energy Rev.* 47, 83–92.

Spieler, A., Wagner, R., Beisel, S., and Vajen, K. (2000). Passive solar office building: First experiences and measurements. In *Proceedings of ISES Europe Solar Congress*, pp. 19–22.

Su, H., Liu, X.-B., Ji, L., and Mu, J.-Y. (2012). A numerical model of a deeply buried air-earth-tunnel heat exchanger. *Energy Build.* 48, 233–239.

Thiers, S., and Peuportier, B. (2008). Thermal and environmental assessment of a passive building equipped with an earth-to-air heat exchanger in France. *Sol. Energy* 82, 820–831.

Thomas, H.R., and Rees, S.W. (2009). Measured and simulated heat transfer to foundation soils. *Géotechnique* 59, 365–375.

Tittlein, P., Achard, G., and Wurtz, E. (2009). Modelling earth-to-air heat exchanger behaviour with the convolutive response factors method. *Appl. Energy* 86, 1683–1691.

Tittlein, P., Gibout, S., Franquet, E., Johannes, K., Zalewski, L., Kuznik, F., Dumas, J.-P., Lassue, S., Bédécarrats, J.-P., and David, D. (2015). Simulation of the thermal and energy behaviour of

a composite material containing encapsulated-PCM: Influence of the thermodynamical modelling. *Appl. Energy* 140, 269–274.

Tiwari, A., and Sodha, M.S. (2007). Parametric study of various configurations of hybrid PV/thermal air collector: Experimental validation of theoretical model. *Sol. Energy Mater. Sol. Cells* 91, 17–28.

Tiwari, G.N., Akhtar, M.A., Shukla, A., and Emran Khan, M. (2006). Annual thermal performance of greenhouse with an earth–air heat exchanger: An experimental validation. *Renew. Energy* 31, 2432–2446.

Trombe, A., and Serres, L. (1994). Air-earth exchanger study in real site experimentation and simulation. *Energy Build.* 21, 155–162.

Trombe, A., Pettit, M., and Bourret, B. (1991). Air cooling by earth tube heat exchanger: experimental approach. *Renew. Energy* 1, 699–707.

Trząski, A., and Zawada, B. (2011). The influence of environmental and geometrical factors on air-ground tube heat exchanger energy efficiency. *Build. Environ.* 46, 1436–1444.

Tzaferis, A., Liparakis, D., Santamouris, M., and Argiriou, A. (1992). Analysis of the accuracy and sensitivity of eight models to predict the performance of earth-to-air heat exchangers. *Energy Build.* 18, 35–43.

Van Genuchten, M.T. (1980). A closed-form equation for predicting the hydraulic conductivity of unsaturated soils. *Soil Sci. Soc. Am. J.* 44, 892–898.

Van Genuchten, M.T., and Nielsen, D.R. (1985). On describing and predicting the hydraulic properties of unsaturated soils. *Ann. Geophys.* 3, 615–628.

Vaz, J., Sattler, M.A., dos Santos, E.D., and Isoldi, L.A. (2011). Experimental and numerical analysis of an earth–air heat exchanger. *Energy Build.* 43, 2476–2482.

Vogel, T., Van Genuchten, M.T., and Cislerova, M. (2001). Effect of the shape of the soil hydraulic functions near saturation on variably-saturated flow predictions. *Adv. Water Resour.* 24, 133–144.

Wagner, R., Beisel, S., Spieler, A., Gerber, A., and Vajen, K. (2000). Measurement, modelling and simulation of an Earth-to-Air Heat Exchanger in Manburg (Germany). In ISES Europe Solar Congress, Copenhagen, Dänemark, p.

Weitzmann, P., Kragh, J., Roots, P., and Svendsen, S. (2005). Modelling floor heating systems using a validated two-dimensional ground-coupled numerical model. *Build. Environ.* 40, 153–163.

Woloszyn, M. (1999). Modélisation hygro-thermo-aéraulique des bâtiments multizones. Proposition d'une stratégie de résolution du système couplé. INSA de Lyon.

Wu, H., Wang, S., and Zhu, D. (2007). Modelling and evaluation of cooling capacity of earth–air–pipe systems. *Energy Convers. Manag.* 48, 1462–1471.

Xiaona, X., Yi, J., and Jianjun, X. (2008). A new approach to compute heat transfer of ground-coupled envelope in building thermal simulation software. *Energy Build.* 40, 476–485.

- Yang, D., Guo, Y., and Zhang, J. (2016). Evaluation of the thermal performance of an earth-to-air heat exchanger (EAHE) in a harmonic thermal environment. *Energy Convers. Manag.* *109*, 184–194.
- Youcef, L. (1991). Two-dimensional model of direct solar slab-on-grade heating floor. *Sol. Energy* *46*, 183–189.
- Zhang, J., and Haghighat, F. (2005). Simulation of earth-to-air heat exchangers in hybrid ventilation systems. In Ninth International IBPSA Conference, Building Simulation 2005, Montreal, Canada, (Citeseer), pp. 1417–1424.
- Zhang, J., and Haghighat, F. (2009). Convective heat transfer prediction in large rectangular cross-sectional area Earth-to-Air Heat Exchangers. *Build. Environ.* *44*, 1892–1898.
- Zhang, H.-F., Ge, X.-S., Ye, H., and Jiao, D.-S. (2007). Heat conduction and heat storage characteristics of soils. *Appl. Therm. Eng.* *27*, 369–373.
- Zhong, Z., and Braun, J.E. (2007). A simple method for estimating transient heat transfer in slab-on-ground floors. *Build. Environ.* *42*, 1071–1080.
- Zoras, S. (2009). A review of building earth-contact heat transfer. *Adv. Build. Energy Res.* *3*, 289–313.

ANNEXES

APPENDIX A: SYSTEMS OF CONSERVATION LAW EQUATIONS FOR SOIL AND CONCRETE

The systems of conservation law equations for soil and concrete as described by Janssen (2002) and Janssen et al. (2007) is given by

$$\begin{cases} c_{TT}^g \frac{\partial T^g}{\partial t} + c_{T\Psi}^g \frac{\partial \Psi^g}{\partial t} = \nabla \cdot (k_{TT}^g \vec{\nabla} T^g + k_{T\Psi}^g \vec{\nabla} \Psi^g + \vec{g}_T) \\ c_{\Psi T}^g \frac{\partial T^g}{\partial t} + c_{\Psi\Psi}^g \frac{\partial \Psi^g}{\partial t} = \nabla \cdot (k_{\Psi T}^g \vec{\nabla} T^g + k_{\Psi\Psi}^g \vec{\nabla} \Psi^g + \vec{g}_\Psi) \end{cases} \quad (A.1)$$

$$\begin{cases} c_{TT}^f \frac{\partial T^f}{\partial t} + c_{TP_c}^f \frac{\partial P_c^f}{\partial t} = \nabla \cdot (k_{TT}^f \vec{\nabla} T^f + k_{TP_c}^f \vec{\nabla} P_c^f) \\ c_{P_c T}^f \frac{\partial T^f}{\partial t} + c_{P_c P_c}^f \frac{\partial P_c^f}{\partial t} = \nabla \cdot (k_{P_c T}^f \vec{\nabla} T^f + k_{P_c P_c}^f \vec{\nabla} P_c^f) \end{cases}$$

where the storage coefficients for the soil are given by

$$c_{TT}^g = C + \theta_a (L_0 + c_v (T^g - T_0)) \frac{\partial \rho_v}{\partial T} + (c_l \rho_l (T^g - T_0) - c_v \rho_v (T^g - T_0) - \rho_v L_0) \frac{\partial \theta}{\partial T} \quad (A.2)$$

$$c_{T\Psi}^g = \theta_a (L_0 + c_v (T^g - T_0)) \frac{\partial \rho_v}{\partial \Psi} + (c_l \rho_l (T^g - T_0) - c_v \rho_v (T^g - T_0) - \rho_v L_0) \frac{\partial \theta}{\partial \Psi} \quad (A.3)$$

$$c_{\Psi T}^g = \left(1 - \frac{\rho_v}{\rho_l}\right) \frac{\partial \theta}{\partial T} + \frac{\theta_a}{\rho_l} \frac{\partial \rho_v}{\partial T} \quad (A.4)$$

$$c_{\Psi\Psi}^g = \left(1 - \frac{\rho_v}{\rho_l}\right) \frac{\partial \theta}{\partial \Psi} + \frac{\theta_a}{\rho_l} \frac{\partial \rho_v}{\partial \Psi} \quad (A.5)$$

the transfer coefficients for the soil by

$$k_{TT}^g = \lambda^* + c_l \rho_l (T^g - T_0) D_{Tv} \quad (A.6)$$

$$k_{T\Psi}^g = \rho_l L D_{\Psi v} + c_l \rho_l (T^g - T_0) (D_{\Psi v} + K_h) \quad (A.7)$$

$$k_{\Psi T}^g = D_{Tv} \quad (A.8)$$

$$k_{\Psi\Psi}^g = K_h + D_{\Psi v} \quad (A.9)$$

the gravitational terms for the soil by

$$\vec{g}_T = \begin{bmatrix} 0 \\ 0 \\ c_l \rho_l (T^g - T_0) K_h \end{bmatrix} \quad (A.10)$$

$$\vec{g}_{\Psi} = \begin{bmatrix} 0 \\ 0 \\ K_h \end{bmatrix} \quad (A.11)$$

the storage coefficients for the concrete foundation by

$$c_{TT}^f = \rho_b C_b + C_l W \quad (A.12)$$

$$c_{TP_c}^f = T^f \frac{\partial w}{\partial P_c} \quad (A.13)$$

$$c_{P_c T}^f = 0 \quad (A.14)$$

$$c_{P_c P_c}^f = \frac{\partial w}{\partial P_c} \quad (A.15)$$

and the transfer coefficients for the concrete foundation by

$$k_{TT}^f = \lambda + (c_v T^f + L_v) \frac{\delta_v P_v}{\rho_l R_v T^f{}^2} (\rho_l L_v + P_c^f (T^f \gamma - 1)) \quad (A.16)$$

$$k_{TP_c}^f = c_l T^f K_p + (c_v T^f + L_v) \frac{\delta_v P_v}{\rho_l R_v T^f} \quad (A.17)$$

$$k_{P_c T}^f = \frac{\delta_v P_v}{\rho_l R_v T^f{}^2} (\rho_l L_v + P_c^f (T^f \gamma - 1)) \quad (A.18)$$

$$k_{P_c P_c}^f = K_p + \frac{\delta_v P_v}{\rho_l R_v T^f} \quad (A.19)$$

APPENDIX B: SET OF THERMO-HYGRIC CHARACTERISTICS FOR SEVEN SOILS

Table 24: Set of parameters for the suction curve, the hydraulic conductivity and the thermal conductivity analytical models, for seven representative soils

| | Loam | Sand | Sand 2 | Silt | Silt 2 | Clay | Heavy clay |
|----------------|--------|---------|----------|---------|---------|---------|---------------|
| Sa | 0.37 | 0.695 | 0.918 | 0.191 | 0.74 | 0.202 | 0.133 |
| θ_{sat} | 0.419 | 0.381 | 0.379 | 0.442 | 0.512 | 0.481 | 0.499 |
| θ_r | 0.072 | 0.051 | 0.05 | 0.057 | 0.05 | 0.096 | 0.101 |
| n | 1.461 | 1.395 | 2.833 | 1.705 | 1.661 | 1.246 | 1.168 |
| α | 1.09 | 3.191 | 3.454 | 0.443 | 0.753 | 1.86 | 2.114 |
| K_0 | 3.7E-7 | 3.94E-6 | 5.219E-5 | 3.36E-6 | 5.12E-6 | 2.17E-6 | 1.9E-6 |
| τ | -0.41 | -1.257 | -0.883 | 0.566 | 0.606 | -1.794 | -3.708 |
| θ_q | 0.44 | 0.619 | 0.753 | 0.401 | 0.368 | 0.28 | 0.19 |
| θ_{nq} | 0.325 | 0.243 | 0.147 | 0.179 | 0.105 | 0.59 | 0.778 |

APPENDIX C: A FINITE VOLUME METHOD

Finite volume method consists in integrate the conservation equations on a control volume. The calculation here are based on the example of the ground heat equation, on a 3D meshing (a 2D example is given on Figure 89 by the sake of simplicity). Note that the choice has been made to set the node in the middle of each meshes, instead to set the interface in the middle of two nodes. Both considerations have advantages and drawbacks according to Patankar (Patankar, 1980), but the solution adopted was easier to code.

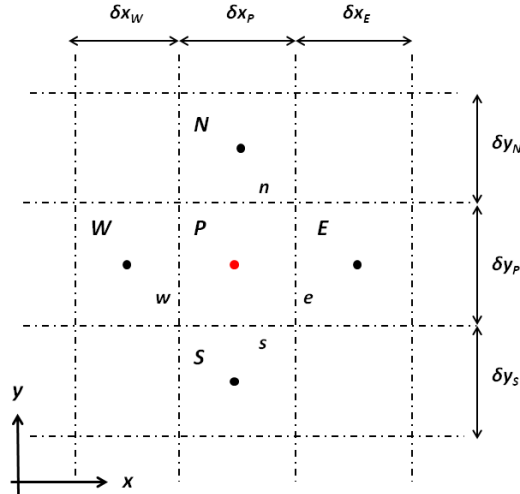


Figure 89: 2D meshing for a finite volume method

Integration of heat equation on the control volume V_c around the node P, delimited by the surface Γ_c - forgetting at the moment the boundary conditions vector and the superscript designating the foundation or the soil for the sake of simplicity - and using the Green-Ostrogradski theorem, we have for example for the heat conservation equation

$$\iiint_{V_c} c_{TT} \frac{\partial T}{\partial t} + c_{T\Psi} \frac{\partial \Psi}{\partial t} = \iint_{\Gamma_c} (k_{TT} \vec{\nabla} T + k_{T\Psi} \vec{\nabla} \Psi + \vec{g}_T) \cdot d\vec{\Gamma}_c \quad (C.1)$$

The first term of the right hand side of this equation (the second term gives a similar expression) becomes

$$\begin{aligned} \iint_{\Gamma_c} (k_{TT} \vec{\nabla} T) d\vec{\Gamma}_c = & (k_{TT} \vec{\nabla} T)_e \cdot \vec{\Gamma}_e - (k_{TT} \vec{\nabla} T)_w \cdot \vec{\Gamma}_w + (k_{TT} \vec{\nabla} T)_n \cdot \vec{\Gamma}_n \\ & - (k_{TT} \vec{\nabla} T)_s \cdot \vec{\Gamma}_s + (k_{TT} \vec{\nabla} T)_t \cdot \vec{\Gamma}_t - (k_{TT} \vec{\nabla} T)_b \cdot \vec{\Gamma}_b \end{aligned} \quad (C.2)$$

The evaluation of the coefficient k_{TT} on the interface e, w, n and s is done thanks to a geometric mean, and the evaluation of the temperature gradient is done by a central difference scheme that finally gives

$$\begin{aligned}
\iint_{\Gamma_c} (k_{TT} \vec{\nabla} T) d\vec{\Gamma}_c = & \frac{2k_{TT_P} k_{TT_E} (T_E - T_P)}{k_{TT_E} \delta x_P + k_{TT_P} \delta x_E} \cdot \delta y_P \delta z_P \\
& - \frac{2k_{TT_W} k_{TT_P} (T_P - T_W)}{k_{TT_P} \delta x_W + k_{TT_W} \delta x_P} \cdot \delta y_P \delta z_P \\
& + \frac{2k_{TT_P} k_{TT_N} (T_N - T_P)}{k_{TT_N} \delta y_P + k_{TT_P} \delta y_N} \cdot \delta x_P \delta z_P \\
& - \frac{2k_{TT_S} k_{TT_P} (T_P - T_S)}{k_{TT_P} \delta y_S + k_{TT_S} \delta y_P} \cdot \delta x_P \delta z_P \\
& + \frac{2k_{TT_P} k_{TT_T} (T_T - T_P)}{k_{TT_T} \delta z_P + k_{TT_P} \delta z_T} \cdot \delta x_P \delta y_P \\
& - \frac{2k_{TT_B} k_{TT_P} (T_P - T_B)}{k_{TT_P} \delta z_B + k_{TT_B} \delta z_P} \cdot \delta x_P \delta y_P
\end{aligned} \tag{C.3}$$

As the vector \vec{g}_T has only a component along the z axis, and using the same geometric mean assumption to compute $g_{T,z}$ on the interfaces t and b, we obtain

$$\iint_{\Gamma_c} \vec{g}_T \cdot d\vec{\Gamma}_c = g_{T,P} \left(\frac{g_{T,T}(\delta z_P + \delta z_T)}{g_{T,P} \delta z_T + g_{T,T} \delta z_P} - \frac{g_{T,B}(\delta z_P + \delta z_B)}{g_{T,P} \delta z_B + g_{T,B} \delta z_P} \right) \delta x_P \delta y_P \tag{C.4}$$

Reinserting the result into the first equation, we have

$$\begin{aligned}
C_{TT} \frac{\partial T}{\partial t} + C_{T\Psi} \frac{\partial \Psi}{\partial t} & = K_{TT,E} T_E + K_{TT,W} T_W + K_{TT,N} T_N + K_{TT,S} T_S + K_{TT,T} T_T \\
& + K_{TT,B} T_B + K_{TT,P} T_P + K_{T\Psi,E} \Psi_E + K_{T\Psi,W} \Psi_W \\
& + K_{T\Psi,N} \Psi_N + K_{T\Psi,S} \Psi_S + K_{T\Psi,T} \Psi_T + K_{T\Psi,B} \Psi_B \\
& + K_{T\Psi,P} \Psi_P \\
& + g_{T,P} \left(\frac{g_{T,T}(\delta z_P + \delta z_T)}{g_{T,P} \delta z_T + g_{T,T} \delta z_P} \right. \\
& \left. - \frac{g_{T,B}(\delta z_P + \delta z_B)}{g_{T,P} \delta z_B + g_{T,B} \delta z_P} \right) \delta x_P \delta y_P
\end{aligned} \tag{C.5}$$

where $K_{TT,E} = \frac{2k_{TT_P} k_{TT_E} \delta y_P \delta z_P}{k_{TT_E} \delta x_P + k_{TT_P} \delta x_E}$ and so on and $K_{TT,P} = -(K_{TT,E} + K_{TT,W} + K_{TT,N} + K_{TT,S} + K_{TT,T} + K_{TT,B})$. Finally, using the same technique for both heat and mass equations, we obtain the following system of matrix equation

$$\begin{aligned}
C_{TT} \frac{\partial T}{\partial t} + C_{T\Psi} \frac{\partial \Psi}{\partial t} & = \mathbf{K}_{TT} T + \mathbf{K}_{T\Psi} \Psi + G_T + B_T \\
C_{\Psi T} \frac{\partial T}{\partial t} + C_{\Psi\Psi} \frac{\partial \Psi}{\partial t} & = \mathbf{K}_{\Psi T} T + \mathbf{K}_{\Psi\Psi} \Psi + G_\Psi + B_\Psi
\end{aligned} \tag{C.6}$$

where C_{TT} , $C_{T\Psi}$, $C_{\Psi T}$ and $C_{\Psi\Psi}$ are diagonal mass matrix, \mathbf{K}_{TT} , $\mathbf{K}_{T\Psi}$, $\mathbf{K}_{\Psi T}$ and $\mathbf{K}_{\Psi\Psi}$ are tridiagonal by bloc stiffness matrixes, G_T and G_Ψ are load vectors and B_T and B_Ψ are boundary vectors. A similar system can also be developed for the foundation model. As all these matrixes of course depend on the variables T and Ψ , it's necessary to write an efficient programme able to compute it quickly for each iteration and time step.

APPENDIX D: A NEWTON-RAPHSON METHOD

For the sake of simplicity and as for the finite volume methods, all the explanation of this appendix is based on the example of the heat equation. For each iteration, the problem is to calculate the unknown $\Delta T^{t+\Delta t, m+1}$ as a solution of the equation (D.1).

$$\frac{\partial \mathcal{L}}{\partial T}(T^{t+\Delta t, m}) \Delta T^{t+\Delta t, m+1} = -\mathcal{L}(T^{t+\Delta t, m}) \quad (D.1)$$

where

$$\begin{aligned} \mathcal{L}(T^{t+\Delta t}) = & \mathbf{C}_{TT}^{t+\Delta t} (T^{t+\Delta t} - T^t) + \mathbf{C}_{T\Psi}^{t+\Delta t} (\Psi^{t+\Delta t} - \Psi^t) - \Delta t \mathbf{K}_{TT}^{t+\Delta t} T^{t+\Delta t} \\ & - \Delta t \mathbf{K}_{T\Psi}^{t+\Delta t} \Psi^{t+\Delta t} - \Delta t (\mathbf{G}_T^{t+\Delta t} + \mathbf{B}_T^{t+\Delta t}) = 0 \end{aligned} \quad (D.2)$$

and the jacobian matrix of the function \mathcal{L} is given by

$$\begin{aligned} \frac{\partial \mathcal{L}}{\partial T}(T^{t+\Delta t, m}) = & \frac{\partial(\mathbf{C}_{TT} T)^{t+\Delta t, m}}{\partial T} + \mathbf{C}_{TT}^{t+\Delta t, m} - \frac{\partial(\mathbf{C}_{TT} T^t)^{t+\Delta t, m}}{\partial T} \\ & + \frac{\partial(\mathbf{C}_{T\Psi} \Psi^{t+\Delta t, m})^{t+\Delta t, m}}{\partial T} - \frac{\partial(\mathbf{C}_{T\Psi} \Psi^t)^{t+\Delta t, m}}{\partial T} \\ & - \Delta t \frac{\partial(\mathbf{K}_{TT} T)^{t+\Delta t, m}}{\partial T} - \Delta t \mathbf{K}_{TT}^{t+\Delta t} - \Delta t \frac{\partial(\mathbf{K}_{T\Psi} \Psi)^{t+\Delta t, m}}{\partial T} \\ & - \Delta t \frac{\partial(\mathbf{G}_T + \mathbf{B}_T)^{t+\Delta t, m}}{\partial T} \end{aligned} \quad (D.3)$$

Neglecting the term of second order $\left(\frac{\partial(\mathbf{C}_{TT} \Delta T^{t+\Delta t})^{t+\Delta t, m}}{\partial T} + \frac{\partial(\mathbf{C}_{T\Psi} \Delta \Psi^{t+\Delta t})^{t+\Delta t, m}}{\partial T} \right) \Delta T^{t+\Delta t, m+1} - \mathbf{C}_{TT}^{t+\Delta t, m} \Delta T^{t+\Delta t} - \mathbf{C}_{T\Psi}^{t+\Delta t, m} \Delta \Psi^{t+\Delta t}$, solve the equation (D.1) is equivalent to solve

$$\begin{aligned} & \left[\mathbf{C}_{TT}^{t+\Delta t, m} - \Delta t \mathbf{K}_{TT}^{t+\Delta t} \right. \\ & \quad \left. - \Delta t \left(\frac{\partial(\mathbf{K}_{TT} T)^{t+\Delta t, m}}{\partial T} + \frac{\partial(\mathbf{K}_{T\Psi} \Psi)^{t+\Delta t, m}}{\partial T} \right. \right. \\ & \quad \left. \left. + \frac{\partial(\mathbf{G}_T + \mathbf{B}_T)^{t+\Delta t, m}}{\partial T} \right) \right] \Delta T^{t+\Delta t, m+1} \\ & = \Delta t (\mathbf{K}_{TT}^{t+\Delta t, m} T^{t+\Delta t, m} + \mathbf{K}_{T\Psi}^{t+\Delta t, m} \Psi^{t+\Delta t, m} + \mathbf{G}_T^{t+\Delta t, m} \\ & \quad + \mathbf{B}_T^{t+\Delta t, m}) \end{aligned} \quad (D.4)$$

where calling $\mathcal{V}(i)$ the neighbourhood of the mesh number i we have for example

$$\left(\frac{\partial(K_{TT}T)^{t+\Delta t,m}}{\partial T}\right)_{i,j} = \begin{cases} 0 & \text{if } j \notin \mathcal{V}(i) \\ \frac{\partial K_{TT}^{t+\Delta t,m}}{\partial T_j} (T_j - T_i) & \text{if } j \in \mathcal{V}(i) \text{ et } j \neq i \\ \sum_{\substack{k \in \mathcal{V}(i) \\ k \neq i}} \frac{\partial K_{TT}^{t+\Delta t,m}}{\partial T_i} (T_k^{t+\Delta t,m} - T_i^{t+\Delta t,m}) & \text{if } i = j \end{cases} \quad (D.5)$$

$$\text{with } \frac{\partial K_{TT}^{t+\Delta t,m}}{\partial T_j} = \frac{\delta x_j (\delta x_j + \delta x_i) \frac{\partial (k_{TT,j}^{t+\Delta t,m})}{\partial T_j} (k_{TT,i}^{t+\Delta t,m})^2}{(\delta x_i k_{TT,j}^{t+\Delta t,m} + \delta x_j k_{TT,i}^{t+\Delta t,m})^2} \quad \text{and} \quad \frac{\partial K_{TT}^{t+\Delta t,m}}{\partial T_i} = \frac{\delta x_i (\delta x_k + \delta x_i) \frac{\partial (k_{TT,i}^{t+\Delta t,m})}{\partial T_i} (k_{TT,k}^{t+\Delta t,m})^2}{(\delta x_i k_{TT,k}^{t+\Delta t,m} + \delta x_k k_{TT,i}^{t+\Delta t,m})^2}$$

Instead of solving two systems of equations, one for the heat conservation and one for the moisture conservation, it has been decided to gathered in one matrix system – the size of which is double – alternating one row for the heat equation of one mesh and one row for the moisture equation which allow a better balance of the matrixes. For example, the ground state

vector that gathers temperature and matric head is written $U^g = \begin{pmatrix} \vdots \\ T_i^g \\ \Psi_i \\ T_{i+1}^g \\ \Psi_{i+1} \\ \vdots \end{pmatrix}$ where i is the mesh

number.

The final matrix system equation is

$$\begin{aligned} & [\mathbf{C}^{t+\Delta t,m} - \Delta t \mathbf{K}^{t+\Delta t,m} \\ & \quad - \Delta t (\partial \mathbf{K}^{t+\Delta t,m} + \partial \mathbf{G}^{t+\Delta t,m} + \partial \mathbf{B}^{t+\Delta t,m})] \Delta U^{t+\Delta t,m+1} \\ & = \Delta t (\mathbf{K}^{t+\Delta t,m} U^{t+\Delta t,m} + \mathbf{G}^{t+\Delta t,m} + \mathbf{B}^{t+\Delta t,m}) \end{aligned} \quad (D.6)$$

APPENDIX E: DESCRIPTION OF THE EXPERIMENTAL ACQUISITION SYSTEM

Figure 90 shows the global architecture of the data acquisition system required by the sensors used and listed in Table 20. The system is divided into 6 boxes distributed over the two building wings in order to limit the wire length from the data logger to the sensors. The content of each box is detailed in Table 25.

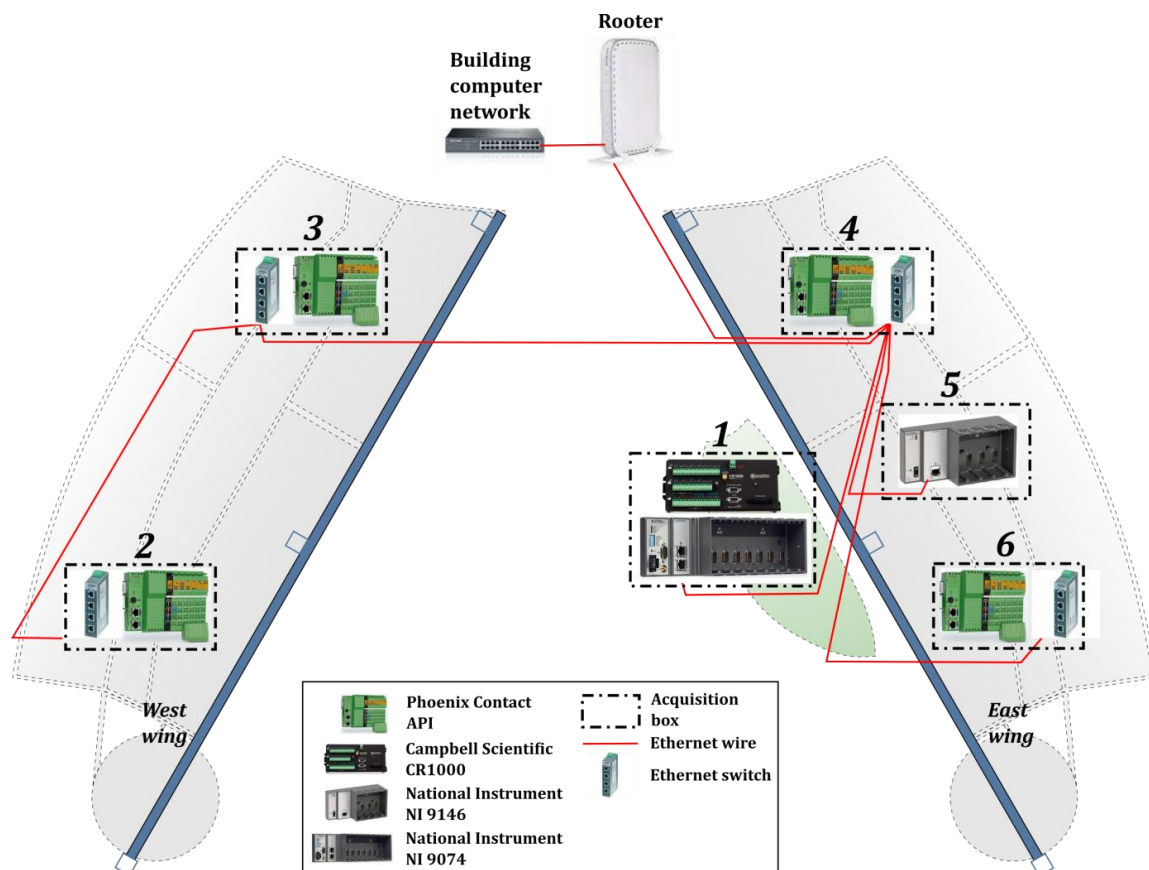


Figure 90: Position of the acquisition boxes and Ethernet connection

Boxes 2, 3, 4 and 6 all contain one data logger API from Phoenix Contact (view of 1 and 5 are available on Figure 93). They are used to recover data send by the 24 RTDs Pt-100. Boxes 2 and 6 also recover data from the electric meter to measure the consumption of the two air handling units. Two data loggers are gathered in box 1. The first is a CR1000 from Campbell Scientific. It is used to recover data from all the weather station sensors, namely the air temperature and relative humidity, the wind speed and direction, and the rainfall. The second one is a Compact RIO 9074 from National Instruments. Several modules are plugged on it and allow the transmission of the measurements from all the thermo-hygrometers 'SHT-75', from the three pyranometers 'LP02', and from eight out of eighteen soil water content and temperature sensors 'SM300'. In addition, the data treated by the CR1000 are sent via a RS-232 wire to the CRIO. Finally the box 5 contains an Ethernet RIO 9146 data logger that allows

the recovering of the data from the rest of the 'SM300'. It sends all the information to the CRIO 9074 via a modbus connection.

On every data loggers, several modules ensure the sensors signal conditioning. They are listed in Table 20. The connection of the SM300 sensors to both the data logger via the module NI 9472 and NI 9205 is not direct and is detailed on Figure 91.

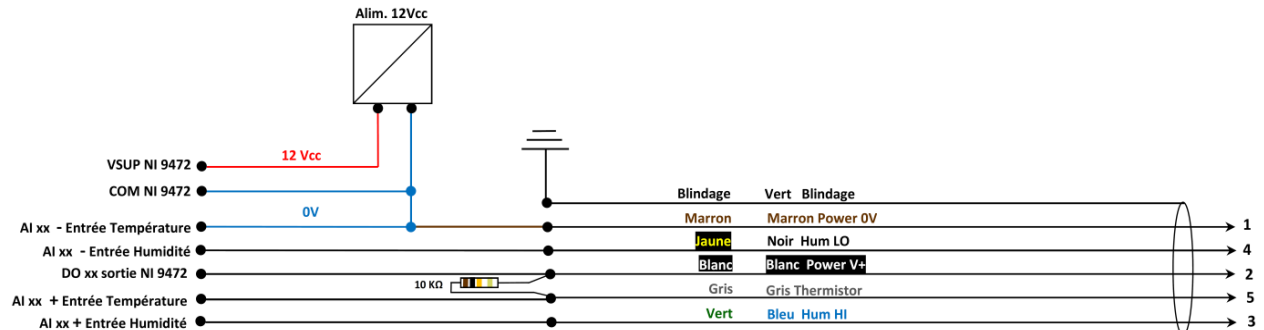


Figure 91: SM300 connection to NI 9472 and NI 9205

All the boxes are connected to a router and to the building computer network via Ethernet. The data logger CRIO 9074, located in box 1, is the master. All the information collected from the other boxes are sent to this data logger and then transmitted to the network. A labview program is written and run on it permanently. Every minute, the values yield by all the sensors are read and stored on the CRIO 9074 hard disk. The data are arranged into a text file which is sent by mail to the administrator of the monitoring based in Lyon. It is also possible to see on real time the information sent by the sensors via the Labview front panel (Figure 92), which allows to detect various problems on sensors or data loggers.

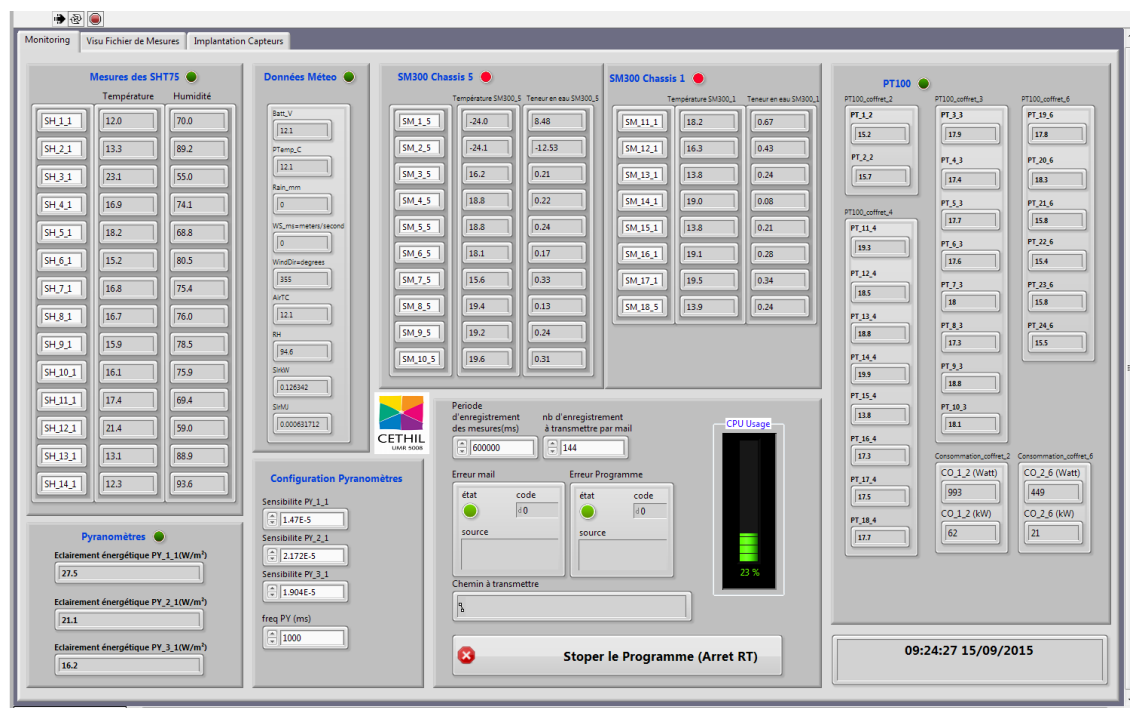































Figure 92: Screenshot of the Labview front panel

Table 25: Details about the box data acquisition system

| | Data logger | Module | | Sensors | |
|-------|--|--|--|---|--|
| | | Reference | Number & Function | Reference | ID |
| Box 1 |  <p>National Instrument - CRIO 9074</p> |  <p>National Instrument - NI 9403</p> | <p>1x communication with CETHIL - BOX SHT-75</p>  |  <p>Sensirion - SHT-75</p> | <p>SH1, SH2, SH3, SH4, SH5, SH6, SH7, SH8, SH9, SH10, SH11, SH12, SH13, SH14</p> |
| | |  <p>National Instrument - NI 9211</p> | <p>1x thermocouple measurement</p> |  <p>Huksflux - LP02</p> | <p>PY</p> |
| | |  <p>National Instrument - NI 9472</p> | <p>1x Power switch</p> | | <p>SM4, SM5, SM6, SM11, SM12, SM13, SM14, SM15</p> |
| | |  <p>National Instrument - NI 9205</p> | <p>1x Voltage measurement ± 200 mV</p> |  <p>Delta T - SM300</p> | |
| | |  <p>TDK LAMBDA - DRB15</p> | <p>1x Power supply 12V/DC 0.63A</p> | | |
| |  <p>Campbell Scientific - CR1000</p> <p>(Connected on CRIO 9074 via RS-232)</p> | - | |  <p>Sensirion - SHT-75</p> <p>Text, RH</p> | |
| | | | |  <p>RM Young - 52203</p> <p>Rain</p> | |
| | | | |  <p>RM Young - 03002 Wind Sentry</p> <p>Wind</p> | |

| | | | | | |
|--------------|---|---|-------------------------------------|--|--|
| <i>Box 2</i> |  | Phoenix Contact - IB IL TEMP 4/8 RTD  | 1x Thermistance measurement | Prosensor - Pt100 SPC 1/3 DIN 3 wires | PT1, PT2 |
| | | - | - | MCI - CONTAX D 031042  | CO Electric meter |
| <i>Box 3</i> |  | Phoenix Contact - IB IL TEMP 4/8 RTD  | 4x Thermistance measurement | Prosensor - Pt100 SPC 1/3 DIN 3 wires | PT3, PT4, PT5, PT6, PT7, PT8, PT9, PT10 |
| <i>Box 4</i> |  | Phoenix Contact - IB IL TEMP 4/8 RTD  | 4x Thermistance measurement | Prosensor - Pt100 SPC 1/3 DIN 3 wires | PT11, PT12, PT13, PT14, PT15, PT16, PT17, PT18 |
| <i>Box 5</i> |  | National Instrument - 9472  | 2x Power switch | Delta T - SM300  | SM1, SM2, SM3, SM7, SM8, SM9, SM10, SM16, SM17, SM18 |
| | | National Instrument - 9205  | 2x Voltage measurement ± 200 mV | | |
| | | TDK LAMBDA - DRB15  | 1x Power supply 12V/DC 0.63A | | |
| <i>Box 6</i> |  | Phoenix Contact - IB IL TEMP 4/8 RTD  | 3x Thermistance measurement | Prosensor - Pt100 SPC 1/3 DIN 3 wires | PT19, PT20, PT21, PT22, PT23, PT24 |
| | | - | - | MCI - CONTAX D 031042  | CO Electric meter |

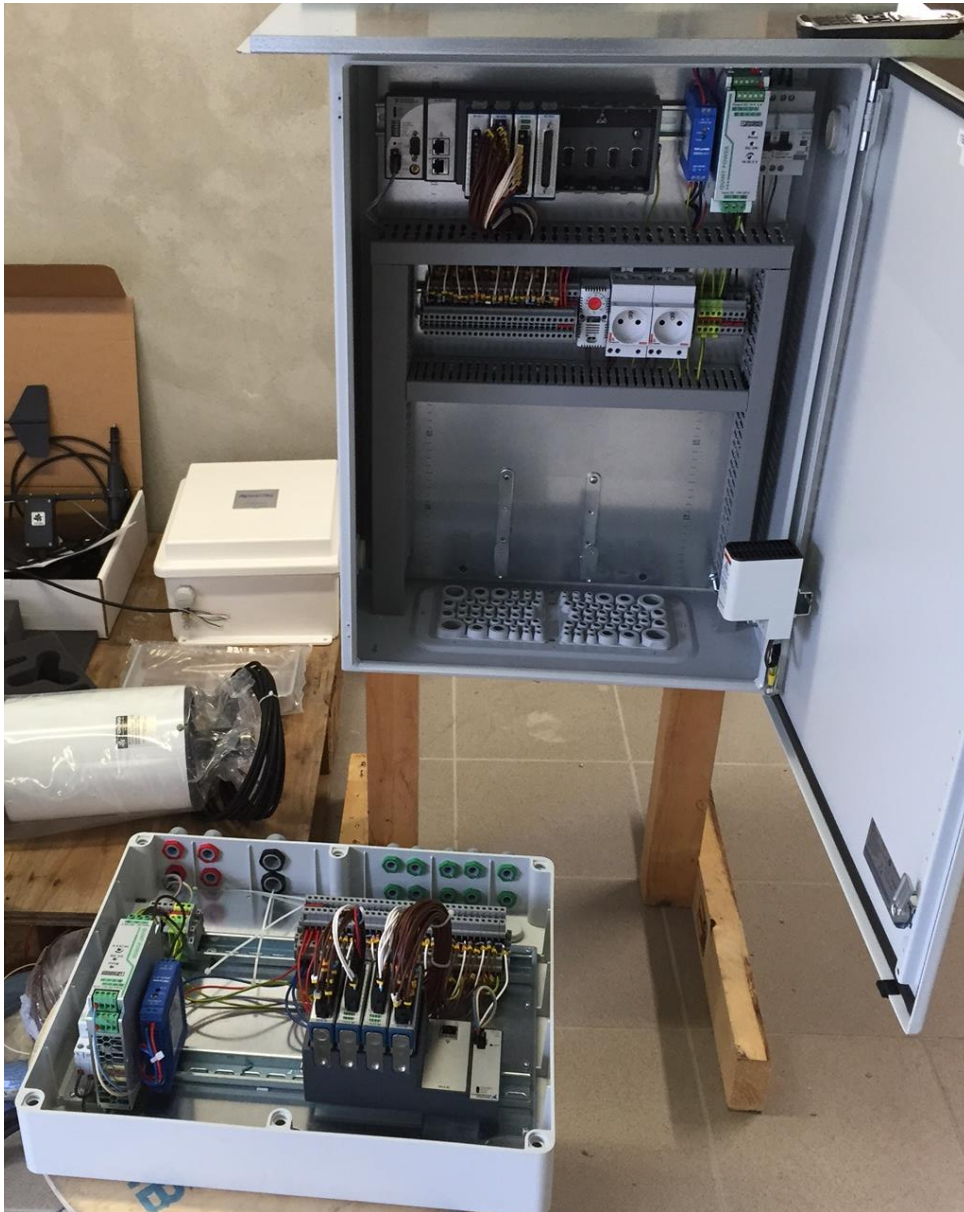


Figure 93: View of box 1 (top right corner) and 5 (bottom left corner)

APPENDIX F: CALCULATION OF THE PRESSURE LOSSES THROUGH THE VENTILATED FOUNDATION

The calculation of the pressure losses through the ventilated foundation is detailed in the Table 26 below. Three sections are considered:

- The first one corresponds to the plastic pipe that drafts the air from the air intake to the foundation entrance. Two circular elbows are considered, as well as a widening located just before the foundation entrance,
- The second corresponds to the foundation cavity,
- The third is the pipe that drafts the air from the foundation outlet section to the air handling unit entrance. Three circular elbows are considered.

The linear pressure losses are considered for the three sections, and calculated assuming that the roughness of all the materials is equal to 0.05 mm. For the singular losses due to the presence of elbows, section widening or reduction, the coefficients used are written down in the table. The total pressure loss of the foundation is about 2 Pa according to the calculation, while it is around 10 Pa according to the measure. Nevertheless, the assumptions about the size and shape of the connecting ducts – involved in the calculation of the singular pressure losses at the foundation ends – as well as the roughness of the surfaces and the airflow rate are approximate because of a lack of data. Despite this, it gives a reasonable value of the total pressure losses, which is only used for the COP_{pl} estimation.

Table 26: Calculation details of the pressure losses through the ventilated foundation

| | Length (m) | Hydraulic diameter (mm) | Airflow rate (m ³ /h) | Type of singularity | ζ | Flow regime | Linear losses (Pa) | Singular losses (Pa) | Total pressure losses (Pa) |
|---|------------|-------------------------|----------------------------------|---|---------|-------------|--------------------|----------------------|----------------------------|
| <i>Section 1 : From air intake to foundation entrance</i> | 10 | 180 | 435 | Circular duct elbow - 90° - sharp edges | 1,2 | Turbulent | 15,02 | 15,99 | 31 |
| | | | | Circular duct elbow - 30° | 0,17 | | | 2,26 | 33,27 |
| | | | | Sharp widening | 0,5 | | | 6,66 | 39,93 |
| <i>Section 2: From foundation entrance to foundation outlet</i> | 46 | 400 | 435 | Sharp reduction | 0,35 | Turbulent | 1,53 | 0,19 | 1,72 |
| <i>Section 3: From foundation outlet to AHU entrance</i> | 30 | 180 | 435 | Circular duct elbow - 45° | 0,23 | Turbulent | 45,05 | 3,06 | 48,12 |
| | | | | Circular duct elbow - 90° | 0,4 | | | 5,33 | 53,45 |
| | | | | Circular duct elbow - 90° | 0,4 | | | 5,33 | 58,78 |
| Total pressure losses (Pa) | | | | | | | | | 100,43 |

APPENDIX G: DIFFERENCES BETWEEN THE MEASUREMENTS AND THE MODELS RESULTS

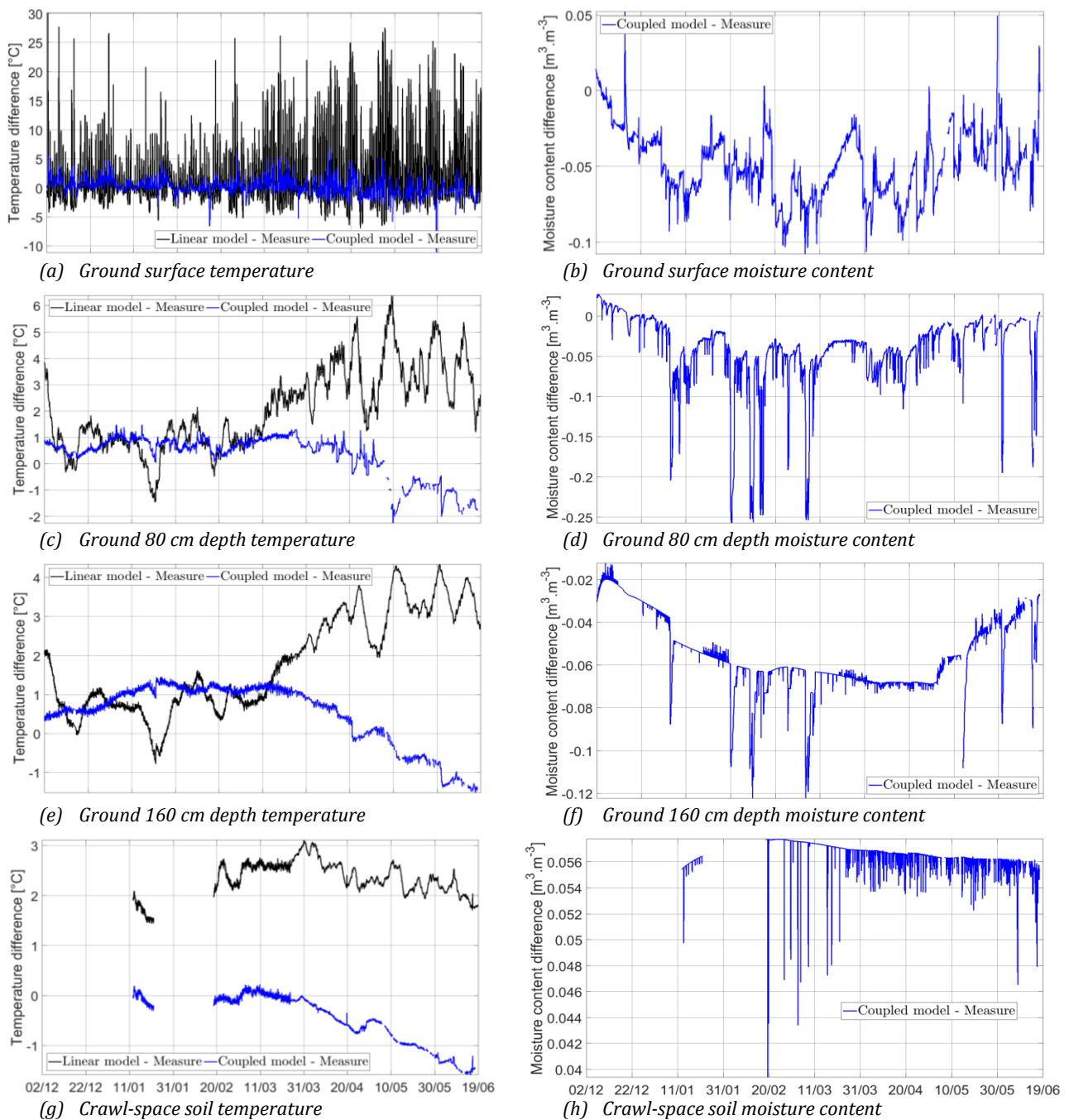


Figure 94: Ground modelling - meas. differences: Surface (a) temp., (b) moist. cont., 80cm depth (c) temp., (d) moist. cont., 160 cm depth (e) temp., (f) moist. cont., Crawl-space soil (g) temp., (h) moist. cont.

TAURINES Kevin

CETHIL - INSA Lyon

2017

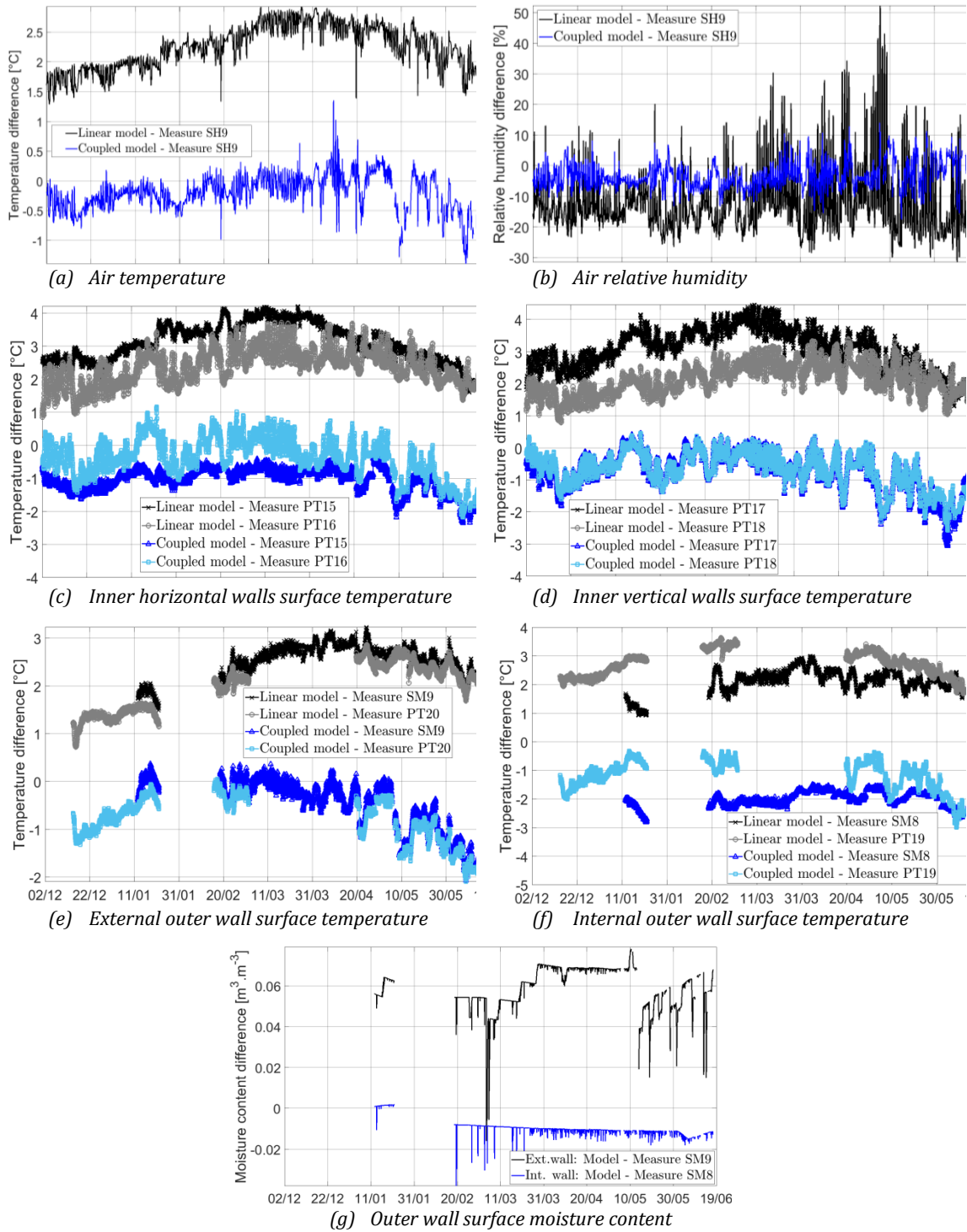


Figure 95: Foundation modelling - measurements difference: Air (a) temp., (b) Rel. humidity, (c) Inner horizontal walls surface temp., (d) Inner vertical walls surface temp., (e) External outer wall surface temp., (f) Internal outer wall surface temp., (g) Outer wall surface moist. cont.

APPENDIX H: FONDATHERM CONTROL STRATEGY: PREMISES

Recording the outdoor and outlet air temperature over long period, as well as the temperature difference between the flowing air and the wall surface, it is possible to build correlation between these two quantities. Therefore, for a given temperature difference measured at the foundation middle section for instance, the cooling or heating effect of the foundation can be anticipated, with statistic margin of errors, as shown on Figure 96. During a 'heating period' for example, if the temperature difference measured is more than 2 °C, Figure 96 (b) shows that the air will be preheat with a high probability. If the temperature difference is lower than 1 °C, the airflow will be cooled down with a high probability too, and consequently, it is better to take this air directly from the outside thanks to a control valve. Over the range [1,2] °C, nothing is done, which corresponds to deadband required for all the mechanical systems control.

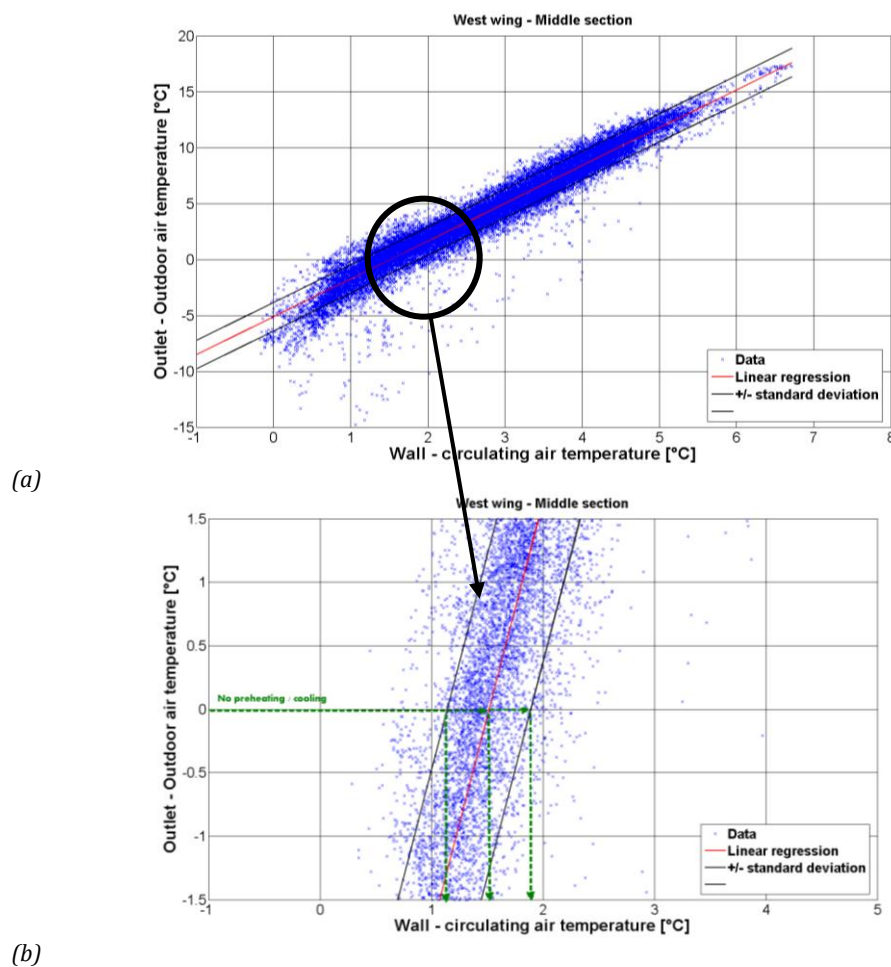


Figure 96: Proposition for a control strategy of the airflow rate



FOLIO ADMINISTRATIF

THESE DE L'UNIVERSITE DE LYON OPEREE AU SEIN DE L'INSA LYON

NOM : TAURINES

DATE de SOUTENANCE : 26/10/2017

Prénoms : Kevin, Antoine, Serge

TITRE : Modelling and experimental analysis of a geothermal ventilated foundation

NATURE : Doctorat

Numéro d'ordre : 2017LYSEI100

Ecole doctorale : Mécanique, Energétique, Génie civil, Acoustique (ED 162)

Spécialité : Génie civil

RESUME : Cette thèse porte sur l'analyse thermique et énergétique d'une fondation géothermique ventilée. A l'instar des échangeurs air-sol classiques (EAHE), celle-ci permet de rafraîchir ou préchauffer selon la saison l'air destiné au renouvellement sanitaire des bâtiments. Face aux contraintes de rationalisation des consommations et aux exigences de confort thermique croissantes, ces systèmes passifs apparaissent comme étant prometteurs.

Le principe de cette fondation est simple et similaire à celui des EAHE : faire circuler de l'air dans une conduite enterrée dans le sol (un à trois mètres) pour qu'il bénéficie - via convection - de l'inertie thermique du sol. La différence réside dans le fait que le canal dans lequel circule l'air n'est pas un tube en PVC ou aluminium mais fait partie intégrante de la structure du bâtiment, à savoir la fondation en béton armé. Ceci présente comme avantage majeur le gain de place lié à l'espace requis pour l'enfouissement des tuyaux. D'un point de vue thermique, la fondation échange non seulement de la chaleur avec le sol exposé aux sollicitations météorologiques mais aussi, et simultanément, aux sollicitations venant du bâtiment. De plus, la profondeur de la fondation – imposée par des raisons structurelles et économiques – est moindre que pour un EAHE traditionnel. Additionné au fait que le béton est poreux, la présence d'humidité peut fortement influencer la performance thermique de la fondation. Le présent travail propose donc d'étudier le comportement thermique complexe de cette fondation par deux approches. La première est expérimentale : un EHPAD équipé de deux fondations a été lourdement instrumenté et des données ont été accumulées sur plus d'un an. L'autre est numérique : deux modèles validés par comparaison avec les données expérimentales ont été développés. Le premier a vocation d'outil de dimensionnement, l'autre de compréhension fine des phénomènes physiques et prends en compte les transferts couplés de chaleur et de masse.

MOTS-CLÉS : géothermie, échangeur air-sol, énergie, thermique, modélisation, volume finis, expérimental, transferts couplés de chaleur et d'humidité.

Laboratoire (s) de recherche : CETHIL (Centre d'Energétique et de Thermique de Lyon) UMR 5008

Directeur de thèse: Christophe MENEZO

Président de jury : Christian GHIAUS

Composition du jury : Christophe MENEZO, Stéphanie GIROUX—JULIEN, Monika WOLOSZYN, Marco FOSSA, Hans JANSSEN, Christian GHIAUS, Guohui GAN